Departamento de Física de Partículas e Instituto Galego de Física de Altas Enerxías

Phenomenological studies of initial state effects and jet quenching in High-Energy Nuclear Collisions at LHC

Carlota Andrés Casas

Santiago de Compostela, setembro de 2017.

USC
UNIVERSIDADE
DE SANTIAGO
DE COMPOSTELA

UNIVERSIDADE DE SANTIAGO DE COMPOSTELA

Departamento de Física de Partículas e Instituto Galego de Física de Altas Enerxías

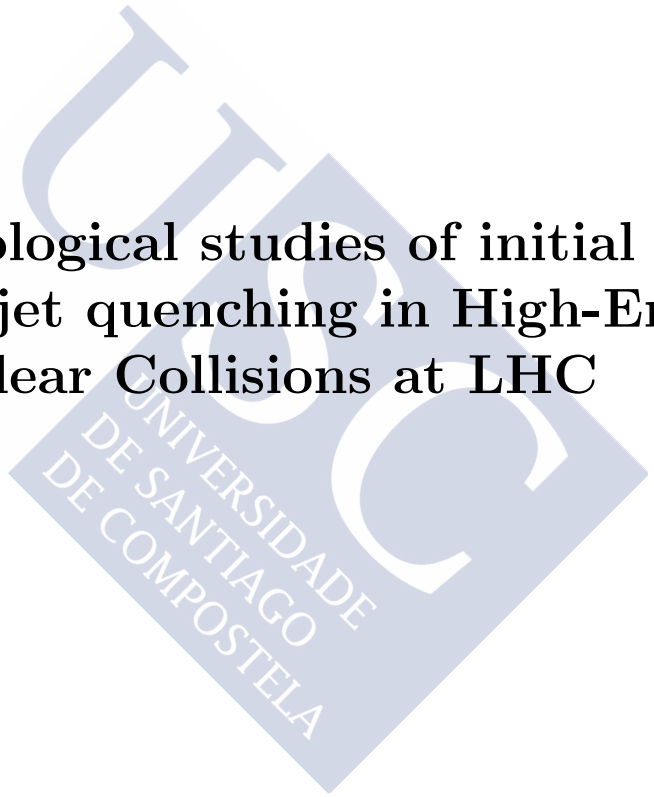

Phenomenological studies of initial state effects and jet quenching in High-Energy Nuclear Collisions at LHC

Carlota Andrés Casas

Santiago de Compostela, setembro de 2017.

USC
UNIVERSIDADE
DE SANTIAGO
DE COMPOSTELA

UNIVERSIDADE DE SANTIAGO DE COMPOSTELA

Departamento de Física de Partículas e Instituto Galego de Física de Altas Enerxías

Phenomenological studies of initial state effects and jet quenching in High-Energy Nuclear Collisions at LHC

Tese presentada para optar ao grao
de Doutora en Física por:

Carlota Andrés Casas

Setembro, 2017

USC
UNIVERSIDADE
DE SANTIAGO
DE COMPOSTELA

UNIVERSIDADE DE SANTIAGO DE COMPOSTELA

Departamento de Física de Partículas e Instituto Galego de Física de Altas Enerxías

Carlos Alberto Salgado López, Profesor Titular de Física Teórica da Universidade de Santiago de Compostela e

Carlos Pajares Vales, Catedrático Emérito de Física Teórica da Universidade de Santiago de Compostela,

CERTIFICAN: que a memoria titulada *Phenomenological studies of initial state effects and jet quenching in High-Energy Nuclear Collisions at LHC* foi realizada, baixo a nosa dirección, por Carlota Andrés Casas, no departamento de Física de Partículas e Instituto Galego de Física de Altas Enerxías desta Universidade e constitúe o traballo de Tese que presenta para optar ao grao de Doutora en Física.

Asinado:

Carlos Alberto Salgado López.

Santiago de Compostela, setembro de 2017.

Asinado:

Carlos Pajares Vales.

Santiago de Compostela, setembro de 2017.

USC
UNIVERSIDADE
DE SANTIAGO
DE COMPOSTELA

A mi familia

"Si en mi tarjeta pusiera Emilio, en lugar de Emilia, qué distinta habría sido mi vida".

Emilia Pardo Bazán

USC
UNIVERSIDADE
DE SANTIAGO
DE COMPOSTELA

Agradecimientos

En primer lugar, quiero agaradecer a Carlos Pajares la oportunidad que me ha dado de trabajar en este campo. Gracias por su dirección, sus explicaciones, sus sugerencias, etc., que no solo han contribuido a que esta tesis sea lo que es, sino a que esta tesis simplemente sea. Agradezco especialmente su apoyo y consejos, tanto en lo personal como en lo profesional, y sus innumerables historias y anécdotas que hacen el trabajo diario mucho más ameno.

Por supuesto, mi más profundo agradecimiento a Carlos Salgado. Trabajar con él es un lujo. Le agradezco especialmente la libertad que siempre me ha dado en mis proyectos, que el trabajo haya sido con él y no para él y que siempre acabe encontrando un hueco en su (más que) imposible agenda para escucharme.

A Pía Zurita le doy las gracias por todo. Por darme la oportunidad de trabajar con ella, por su (duro) trabajo y constancia, por todo lo que me ha enseñado y por todo lo que hemos aprendido juntas. Pero, sobre todo, le doy las gracias por ser mi amiga, por su apoyo y comprensión y por estar siempre ahí, aun cuando un océano nos separa.

Gracias también a toda la gente con la que he colaborado durante mi doctorado. Especialmente a Néstor Armesto por toda la física que me ha enseñado y por tener siempre tiempo para mí y responder a todas mis dudas y preguntas.

Sin duda estos años no habrían sido lo mismo sin mis compañeros de despacho. Gracias a todos, a los que están y a los que ya se han marchado, por los buenos momentos vividos. A toda la gente del departamento y, especialmente, a todos los que me han alejado un poco de la física para tomar café (o cañas). Gracias a Ana y Elvira, por su disposición y por todo el trabajo que hacen, pues sin ellas este departamento no funcionaría. Gracias a Marcos por haberme salvado del pánico con mi portátil y con el cluster en innumerables ocasiones. A Suso de la OIT le debo tener siempre las respuestas a mis incontables problemas burocráticos. Gracias a los (no pocos) post-docs que han pasado por el grupo durante estos años, porque aunque no haya colaborado con todos ellos, con todos he compartido vinos y tapas.

Le doy las gracias a Juan Rojo. Trabajar con él en Oxford ha sido una maravilla. Gracias a él y a su grupo por su hospitalidad, su tiempo, por todo lo aprendido y, en definitiva, por hacer que los tres meses allí fuesen estupendos. Gracias también a los muy buenos amigos que me llevo de esta estancia, por las cenas, por las pintas, por las risas y sobre todo, por seguir estando ahí.

Muchísimas gracias a Charles Gale, a Sangyong Jeon y a todo el grupo de McGill por hacerme sentir como en casa en mi estancia en Montreal. He aprendido muchísimo de todos ellos y espero que en el futuro podamos seguir colaborando. Gracias, especialmente, por el ambiente del grupo, por ser como una familia y por haberme aceptado en ella desde el primer día. No pueden faltar en estas líneas ni mis *colocateurs* ni los amigos, nuevos y no tanto,

con los que he disfrutado de la vida en Montreal y a los que no puedo dejar de echar de menos.

Gracias a mi familia, especialmente a mis padres, por el apoyo que siempre me han dado y porque todo lo bueno que pueda llegar a hacer se lo debo a ellos. A mi hermana le agradezco todas la tonterías (y no tan tonterías) que compartimos en la distancia y que me mantenga actualizada de las cosas de la vida más allá de la física. Gracias a mis perritos, Rufus y Chipi, por se la alegría de la casa y por sacarme una sonrisa hasta en los peores momentos. A Elena, a Eva y a Chus les agradezco todas las comidas que hemos compartido estos años. Creo que no podría haberme reído más de lo que lo he hecho con ellas. A Chus, le estaré eternamente agradecida por cuidar (y malcriar) a Rufus durante todos mis viajes. Gracias a los Brandy, porque son los mejores – y por los cocidos y churrascadas. Gracias también a mi familia al otro lado del Atlántico por ser todos tan lindos.

Mi vida no sería lo mismo sin todos mis amigos. Los de siempre, los que he conocido aquí y allá en estos años, los físicos, los no físicos, los que están cerca, los que están lejos, los que veo a menudo, los que no... A todos, gracias.

Y, por supuesto, gracias a mi *potiron*, por todo.

Pido perdón también a todo aquel que me haya podido olvidar. Si alguien siente que falta en estos agrademientos, estas palabras de gratitud son para él/ella.

And last, but not least, I would like to acknowledge the entire spectrum of feminist movements and all the women that every day fight for their rights. Otherwise, nowadays I would not be allowed to vote, to have a driving license, to open a bank account, to have access to formal education, to use birth control..., and, definitely, I would have never had the opportunity of writing this thesis and these lines. I am really greatful for my freedom and independence. However, much progress still remains to be done, such as destroying the glass ceiling, and ending with sexual harassment and microaggressions women face daily – even in the scientific community. Fortunately, feminism is an unstoppable current and an eventually gender-equal world is not only possible, but unavoidable.

Resumo

As colisións de ións pesados (HICs, polas súas siglas en inglés) son a ferramenta máis axeitada para o estudo da Cromodinámica Cuántica (QCD, polas súas siglas en inglés) baixo condicións extremas de enerxía e densidade, as cales son moi distintas das típicas dos núcleos atómicos. Nas devanditas colisións, acádanse temperaturas e densidades críticas que permiten a formación do chamado quark-gluon plasma (QGP). Esta tese céntrase no estudo de dous tipos de efectos que xorden nestas colisións: os efectos de estado inicial (IS) e os efectos de estado final (FS). Entre os primeiros cabe subliñar as funcións de distribución partónicas nucleares (nPDFs), cuxa determinación precisa é imprescindíbel para a correcta interpretación de calquera observable empregado en HICs. Nesta memoria desenvólvese unha *análise global* de nPDFs a next-to-next-to-leading order en QCD perturbativa (pQCD). Outro asunto moi interesante no tocante ao estado inicial das colisións de ións pesados son os fenómenos colectivos que dan lugar ao QGP. Estos son examinados utilizando o formalismo da percolación de cordas (SPM, polas súas siglas en inglés). Os resultados obtidos mediante este enfoque para diferentes observables son comparados cos datos experimentais dispoñibles. Entre os efectos de estado final cabe salientar as *hard probes*, que son observables caracterizados pola súa alta enerxía ou masa. Preséntase unha análise da supresión *single-inclusive* de partículas con alto momento transverso para diversas enerxías e centralidades. O principal resultado do antedito traballo é a extracción do denominado coeficiente de jet quenching, $\hat{q}$.

PALABRAS CHAVE

Colisións de ións pesados (HICs), QGP, nPDFs, percolación de cordas, supresión de jets

USC
UNIVERSIDADE
DE SANTIAGO
DE COMPOSTELA

Resumen

Las colisiones de iones pesados (HICs, por sus siglas en inglés) son la herrmamienta propicia para el estudio de la Cromodinámica Cuántica (QCD, por sus siglas en inglés) bajo condiciones extremas de energía y densidad, las cuales son muy distintas de las propias de los núcleos atómicos. En dichas colisiones, se alcanzan temperaturas y densidades críticas que perimiten la formación del llamado quark-gluon plasma (QGP). Esta tesis se centra en el análisis de dos tipos de efectos que surgen en HICs: los efectos de estado inicial (IS) y los efectos de estado final (FS). Entre los primeros cabe destacar las funciones de distribución partónicas nucleares (nPDFs), cuya determinación precisa es crucial para la correcta interpretación de cualquier observable empleado en HICs. En esta tesis se desarrolla un *análisis global* de nPDFs a next-to-next-to-leading order en QCD perturbativa (pQCD). Otro tema muy interesante referente al estado inicial de las colisiones de iones pesados son los fenómenos colectivos que dan lugar al QGP. Estos son examinados utilizando el formalismo de percolación de cuerdas (SPM, por sus siglas en inglés). Los resultados obtenidos mediante este enfoque para diferentes observables son comparados con los datos experimentales disponibles. Entre los efectos de estado final cabe citar las *hard probes*, que son observables caracterizados por una alta energía o masa. Se presenta un análisis de la supresión *single-inclusive* de partículas con alto momento transverso para diversas energías y centralidades. El principal resultado de dicho trabajo es la extracción del denominado coeficiente de jet quenching, $\hat{q}$.

PALABRAS CLAVE

Colisiones de iones pesados (HICs), QGP, nPDFs, percolación de cuerdas, supresión de jets

USC
UNIVERSIDADE
DE SANTIAGO
DE COMPOSTELA

Abstract

Heavy ion collisions (HICs) are the appropriate tools to study Quantum Chromodynamics (QCD) under extreme conditions of energy and density, which are very different from those inside the atomic nucleus. In high-energy nuclear collisions critical temperatures and densities that allow the formation of the so-called quark-gluon-plasma (QGP) are reached. This thesis is focused on the analysis of two types of effects arising in HICs: Initial state effects (IS) and Final state effects (FS). Among the former, there are the nuclear parton distribution functions (nPDFs), whose precise determination is crucial for the correct interpretation of any observable used in HICs. In this thesis a global analysis of nPDFs at next-to-next-to-leading order in perturbative QCD (pQCD) is performed. Another very interesting issue regarding the initial stage of HICs are the collective phenomena that give rise to the QGP. These are addressed using an approach denominated percolation of strings (SPM). The results obtained in this framework for different observables are compared to available experimental data. Amongst the FS it is worth stressing *hard probes*, which are observables characterized by a high energy or mass. An analysis of single-inclusive suppression of hard particles at different center of mass energies and centralities in presented. The main result of this work is the extraction of the so-called jet quenching coefficient, $\hat{q}$.

KEYWORDS

Heavy ion collisions (HICs), QGP, nPDFs, percolation of strings, jet quenching

USC
UNIVERSIDADE
DE SANTIAGO
DE COMPOSTELA

List of Papers

List of the papers that were pusblished, or in process of being published, with the work present in this thesis:

1. *Universal geometrical scaling for hadronic interactions*, C. Andrés, A. Moscoso and C. Pajares, Nucl. Phys. A **901** 14 (2013).

2. *Onset of the ridge structure in AA, pA, and pp collisions*, C. Andrés, A. Moscoso and C. Pajares, Phys. Rev. C **90**, 054902 (2014).

3. *Universal geometrical scaling of the elliptic flow*, C. Andrés, A. Moscoso, J. Dias de Deus, C. Pajares and Carlos A. Salgado, Phys. Rev. C **90**, 034901 (2015).

4. *Energy versus centrality dependence of the jet quenching parameter $\hat{q}$ at RHIC and LHC: a new puzzle?*, Carlota Andrés, Néstor Armesto, Matthew Luzum, Carlos A. Salgado and Pía Zurita, Eur. Phys. J. C **76**, 475 (2016).

5. *Energy loss as the origin of a universal scaling law of the elliptic flow*, C. Andrés, Mikhail Braun, C. Pajares, Eur. Phys. J. A **53** no. 3, 41 (2017).

List of proceedings:

1. *High-density QCD and the new LHC data*, A. Moscoso, C. Andrés and C. Pajares, Theor. Math. Phys. **176** 937 (2013).

2. *Universal geometrical scaling in pp, pA and AA collisions and saturation of gluons*, C. Andrés, A. Moscoso and C. Pajares, AIP Conf. Proc. **1606** 283 (2014).

3. *Universal geometrical scaling of the elliptic flow*, C. Andrés, A. Moscoso, J. Dias de Deus, C. Pajares and Carlos A. Salgado, EPJ Web Conf. **90** 08003 (2015).

4. *Modelling jet quenching with Quenching Weights*, C. Andrés, N. Armesto, Carlos A. Salgado and Yan Zhu, J. Phys. Conf. Ser. **612** 012001 (2015).

5. *The onset of the ridge structure in AA, pA and pp collisions*, C. Andrés, A. Moscoso and C. Pajares, Nuclear and Particle Physics Proceedings, **273–275**, 1513 (2016).

6. *Extracting $\hat{q}$ from single inclusive data at RHIC and at the LHC for different centralities: a new puzzle?*, C. Andrés, N. Amesto, M. Luzum, C. A. Salgado and P. Zurita, arXiv:1612.06781 [nucl-th], accepted in Nuclear and Particle Physics Proceedings by Elsevier.

7. *Extracting $\hat{q}$ in event-by-event hydrodynamics and the centrality/energy puzzle*, C. Andrés, N. Armesto, H. Niemi, R. Paatelainen, C. A. Salgado and P. Zurita, arXiv:1705.01493 [nucl-th], accepted in Nuclear Physics A.

I acknowledge the financial support given by the Ministerio Español de Educación, Cultura y Deportes under the grant FPU2013-03558.

USC
UNIVERSIDADE
DE SANTIAGO
DE COMPOSTELA

Contents

Abstract

Heavy ion collisions (HICs) are the fundamental tool to study Quantum Chromodynamics (QCD) under extreme conditions of energy and density, which are very different from those inside the atomic nucleus. In high-energy nuclear collisions critical temperatures and densities that allow the formation of the so-called quark-gluon-plasma (QGP) are reached.

The QGP is composed by deconfined quarks and gluons – the degrees of freedom of the QCD Lagrangian density. This plasma is an almost perfect liquid where its constituents interact strongly. Consequently, its study provides a way to better constrain the non-perturbative regime of QCD, which currently in not very well understood.

Moreover, the QGP is described by present cosmological models as the state of matter during the first microseconds after the Big-Bang. Therefore, the study of the QGP in heavy ion collisions allows us to analyze the evolution from the deconfined state of the matter existing in the early stages of the Universe to the *normal* confined matter. In other words, they may be helpful to disclose the origin of mass and confinement. High-energy nuclear collisions are, definitely, a big window to observe, explore, and understand the origin and evolution of our Universe.

Nonetheless, the mean life of the hot nuclear matter formed in HICs is very small – of around 100 ys = 10^{-22} s – and, hence, it cannot be directly detected. Its properties must be indirectly studied in the final hadronic state of the collision. Usually, distributions of *soft* particles are used to obtain signs of the collective behavior of the QGP and to try to describe it hydrodynamically; while *hard probes* are employed to study the effect of the medium on processes that can be computed perturbatively.

This thesis is focused on the analysis of two types of effects:

- **Initial stage effects (IS)**. These are previous to thermalization.

  A basic ingredient towards the understanding of heavy ion collisions and, hence, the description of the QGP, is the nuclear parton distribution functions (nPDFs). They contain the information about the partonic structure (quarks and gluons) of protons and neutrons bound in the colliding nuclei. They are, consequently, long-distance contributions which are not part of the perturbative domain of QCD. Their precise determination is crucial for the correct interpretation of any observable used in HICs. Thanks to their universality and to the fact that their evolution with respect to a

concrete initial scale can be addressed by perturbative QCD, a technique called global analysis has been developed to extract them. The obtaining of nPDFs at next-to-next-to-leading order in pQCD using global analysis is the subject of chapter 2.

Another very interesting issue regarding HICs are the collective phenomena that give rise to the QGP. These are usually examined within the Color Glass Condensate (CGC) framework. A simplified model which encodes some of the properties of the QGP is percolation of strings (SPM). This approach and some of its results compared to available experimental data are presented in chapter 3.

- **Final state effects (FS)**.

  Amongst them it is worth stressing *hard probes*, which are observables characterized by a high energy or mass. Therefore, they are part of the perturbative sector of QCD.

  Their behavior in vacuum, i.e, in collisions where a plasma is not created, is well known. Thus, their modifications – with respect to the vacuum case – due to the presence of the nuclear medium are analyzed in order to extract the properties of the QGP. Among these hard probes there is *jet quenching*. The suppression of jets, and, particularly, the single-inclusive suppression of particles with high transverse momentum in HICs is addressed in chapter 4.

Chapter 1

Introduction

The existence of a new form of nuclear matter that would be created at very high energies and densities was predicted for the first time in the 1970's [1–5]. Under these extreme conditions, short range interactions dominate over the long range ones which begin to be screened by the color sources nearby. Short-range interactions are characterized by a small coupling constant – due to asymptotic freedom. Therefore, the QCD matter at high energy and density, usually called *quark-gluon plasma* (QGP), is composed by deconfined quarks and gluons. This allows us to study QCD under exceptional conditions which cannot be reached in elementary particle interactions. In addition, the QGP was formed in the very early stages of the Universe, which means that the phase transition from confined to deconfined nuclear matter may provide information about the dynamics of the early Universe. This led to the development of the Heavy-Ion Collisions (HICs) programs: the Alternating Gradient Synchrotron (AGS) at the Brookhaven National Laboratory (BNL), the Super Proton Synchrotron (SPS) at Conseil Européen pour la Recherche Nucléaire (CERN), the Relativistic Heavy Ion Collider (RHIC) at BNL, and the Large Hadron Collider (LHC) at CERN.

According to Lattice QCD calculations, this phase transition is a fast and continuous cross-over at temperatures of $T_c \simeq 154\,\mathrm{MeV}$ (critical temperature), which corresponds to a critical energy density of $\epsilon_c \sim 1\,\mathrm{GeV/fm}^3$ [6]. Experimental data have shown since long time ago that the energy density achieved in ultra-relativistic Heavy-Ion collisions (HICs) is higher than the critical one [7–9]. Therefore, Heavy-Ion Collisions give a window of opportunity to study the properties of the QGP. The systems produced in this kind of collisions expand in time scales $\mathcal{O}\,(10\,\mathrm{fm})$ which are much larger than the typical time scales of individual processes in QCD. During such a long period of time, collective phenomena occur and medium effects are experimentally accessible. The study of processes that are sensitive to the degree of collectiveness of the system is the main purpose of HICs.

As it was just mentioned, the mean life of the QGP is really small, of the order of the transverse size of the atomic nucleus: $\tau_{mean} \sim A^{1/3}$; that is, $\tau_{mean} \sim 6\,\mathrm{fm}$ for lead, the nucleus used in HICs at the LHC. Therefore, a direct observation of it is impossible. Thus, only indirect signals can be used to characterize the properties of the QGP. Usually, these signatures are classified in: *hard probes*, involving scales in the perturbative region of QCD,

and *soft probes*, dominated by non-perturbative scales. The latter are employed to obtain signs of the collective behavior of the QGP and to try to describe it hydrodynamically; while *hard probes* are employed to analyze the effects of the medium on processes that can be computed perturbatively.

Hard probes provide a good connection between the experimental data and the theoretical description of the medium properties. These are particles which are produced at a large energy or mass scale. High-energy partons interact with the hot medium formed in HICs suffering energy loss processes (*jet quenching*), which induce a modification on the final parton shower. The first example of hard probe was proposed in the 80's by Matsui and Satz: the J/Ψ suppression [10]. This suppression as well as the suppression of other charmonia states has been observed experimentally [11, 12]. Some of the most important hard probes at present are those studying the behavior of the spectrum of particles produced with large transverse momentum, generically known as *jet quenching*. Some of the corresponding observables will be studied at lenght in Chapter 4.

Usually, hard probes in HICs are analyzed by evaluating their modifications with respect to vacuum, i.e., w.r.t. proton-proton (pp) collisions. This provides a way to extract transport and dynamical properties of the medium. Nevertheless, the precise knowledge of the initial state of HICs is required in order to differentiate the effects due to it, from those due to the hot and dense QCD matter (final state effects). Here is where nuclear parton distributions (nPDFs) play a key role. The structure of the proton is described in terms of parton distribution functions (PDFs). However, when the proton is not free but bound in a nucleus (as in the case of HICs) the PDFs are modified, giving rise to nPDFs. Any experimental cross section in a nuclear medium can be only described in terms of nuclear parton distribution functions (nPDFs). Therefore, an accurate determination of nPDFs is essential for the understanding of the QGP created in high-energy nuclear collisions. This will be the subject of Chapter 2.

Another important issue in HICs is the description of the collective phenomena that give rise to the QGP. This is usually studied in the context of the *Color Glass Condensate* (CGC) [13–16]. In this picture, the relativistic heavy ions can be viewed, before the collision takes place, as two sheets of longitudinal colored fields, due to Lorentz contraction. These color fields interact forming color flux tubes which eventually materialize into quarks and gluons. An effective way of including some of the most relevant dynamical mechanisms of the CGC approach is the *string fusion* or *string percolation* model [17]. In this framework the interactions among the partons in the nucleons of the two Lorentz-contracted nuclei can be explained in terms of color strings (color flux tubes) that fragment into $q\bar{q}$ or $qq-\bar{q}\bar{q}$ pairs that subsequently hadronize producing the observed hadrons. Some phenomena, as geometric scaling and the near-side ridge structure, will be studied in Chapter 3 in the string percolation approach.

1.1 Quantum Chromodynamics

Quantum Chromodynamics (QCD) is the $SU(3)$ gauge theory of strong interactions. It describes the interactions between the quarks and the gluons, i.e, the inner constituents of the hadrons. Their dynamics is determined by the Lagrangian density

$$\mathcal{L}_{\mathrm{QCD}} \;=\; \bar{\Phi}^k \left(i\gamma^\mu D_\mu - m_k\right) \Phi^k - \frac{1}{4}\, G^a_{\mu\nu} G^{a,\mu\nu} \;\;, \tag{1.1.1}$$

where Φ^k is the quark field with color index k and γ^μ the Dirac matrices. The gauge covariant derivative, D_μ, and the field strength tensor, $G^a_{\mu\nu}$, are respectively:

$$D_\mu \;\equiv\; \partial_\mu - i g_s t^a A^a_\mu \;\;, \tag{1.1.2}$$

$$G^a_{\mu\nu} \;\equiv\; \partial_\mu A^a_\nu - \partial_\nu A^A_\mu + g_s f^{abc} A^b_\mu A^c_\nu \;\;, \tag{1.1.3}$$

where A^a_μ are the gluon vector fields and g_s denotes the strong coupling constant. The t^a are the generators of the color group $SU(3)$ and f^{abc} are the corresponding *structure constants*,

$$[t^a, t^b] \;=\; i f^{abc} t^c \;\;. \tag{1.1.4}$$

Note that in the QCD Lagrangian density, Eq. (1.1.1), nonlinear terms appear. These are the terms proportional to f^{abc} in the field tensor, Eq. (1.1.3), and the ones proportional to t^a in the covariant derivative, Eq. (1.1.2). These expressions, absent in Abelian theories as Quantum Electrodynamics (QED), are necessary to preserve the gauge invariance of a non-Abelian theory, as QCD. In other words, the form of the interactions in a non-Abelian theory is dictated by the gauge symmetry. As these nonlinear self-interactions of the gluon vector field are proportional to f^{abc}, i.e, to the commutators of the – color – symmetry generators, they are the result of the non-Abelian nature of the theory.

One of the striking properties of QCD, which is a direct consequence of the non-Abelian nature of the theory, is *asymptotic freedom* [18]. *Asymptotic freedom* states that the strong coupling constant decreases when the probed distance gets shorter, or equivalently, when the momentum scale of the process is large, $Q^2 \gg 1$ GeV^2. Therefore, in this case, perturbative QCD (pQCD) in terms of quarks and gluons can be used. Nevertheless, when the distance becomes longer – low energies –, the strong coupling increases, *confining* the quarks and the gluons – *partons*– within the hadrons, which are the physical observables of hadronic interactions. How partons are distributed inside the hadrons cannot be ignored when applying pQCD to hadronic interactions. However, *confinement* cannot be studied by applying pQCD. The structure of the hadron should be independent of the collision, rather inherent to the hadron. This is what is called *factorization*: the part of the process involving short distances or large scales – *hard* – is separated from the non-perturbative – *soft* –, which contains the relevant structure of the hadrons and is process-independent. The latter are the *parton distribution functions* (PDFs) and they are universal. Theoretically, PDFs should be computed from the QCD Lagrangian density, Eq. (1.1.1), but this is far from being accomplished. In practice, they are obtained directly from several experiments and evolved

with the pQCD evolution equations – global analysis.

When the interaction takes place in a nuclear medium, i.e, when, for instance, a lepton (or hadron) collides with a parton from a nucleus (instead of a parton from a nucleon) or the collision takes place between two nucleus, the PDFs are modified. The measured experimental cross sections in a nuclear medium can only be described in terms of nuclear parton distribution functions (nPDFs). In consequence, heavy ion collisions require a precise knowledge of the nPDFs. Namely, a reliable description of the partonic behavior in a nuclear medium becomes crucial for the proper interpretation of the nuclear program and benchmarking. The Relativistic Heavy-Ion Collider (RHIC) and the Large Hadron Collider (LHC), in the present and coming runs, and future planned facilities (EIC, LHeC and FCC) make imperative this line of research.

1.2 Factorization and parton distributions

As it was mentioned in Section 1.1, asymptotic freedom allows us to compute many processes, where the energy scale is large enough (hard processes), using perturbative QCD. However, perturbative QCD computations deal only with quarks and gluons, the degrees of freedom of the QCD Lagrangian density, Eq. (1.1.1), rather than with hadrons, the final and initial states that appear in the experiments. Therefore, a way to connect this partonic perturbative expansion to the final and initial state hadrons is needed. Fortunately, different energy scales appear in hard processes, allowing the cross section to be computed at the parton level using pQCD and then convoluted with the large distance information about the structure of initial (or final) state hadrons. This information is given respectively by the parton distribution functions (PDFs) and the fragmentation functions (FFs). The total (hadronic) cross section can be schematically represented by

$$\sigma^{AB\to h+X} \;=\; f_A(x_1,Q^2)\otimes f_B(x_2,Q^2)\otimes \hat{\sigma}(x_1,x_2,Q^2,\alpha_s(Q^2))\otimes D_{i\to h}(z,\mu_F^2)\;, \qquad (1.2.5)$$

where $\hat{\sigma}(x_1,x_2,Q^2,\alpha_s(Q^2))$ is the partonic cross section, illustrated in Fig. 1.1. The partonic cross section is the short distance contribution, $\sim 1/Q$, where Q is the energy scale of the hard process. It can be computed, thanks to asymptotic freedom, using pQCD. The other terms are the long distance non-perturbative contributions, dominated by scales $\sim \Lambda_{QCD}$. $f_A(x,Q^2)$, are the (proton or nuclear) parton distribution functions, (n)PDFs, which contain the partonic structure of the colliding objects. They can be interpreted – at leading order – as the probability of finding a quark or a gluon in a free proton (or bound in a nucleus), with a momentum fraction x of the momentum of the proton at the energy scale Q^2. The fragmentation functions, $D_{i\to h}(z,\mu_F^2)$, describe the hadronization of a parton i into a final hadron h with a momentum fraction z. This convolution is built on the assumption of factorization due to the separation of scales. Factorization has been formally proven for some processes in hadron collisions [19, 20]. However this is not the case for nuclear media, i.e., in heavy ion collisions, where it is a standard assumption that is well supported by numerous studies [21].

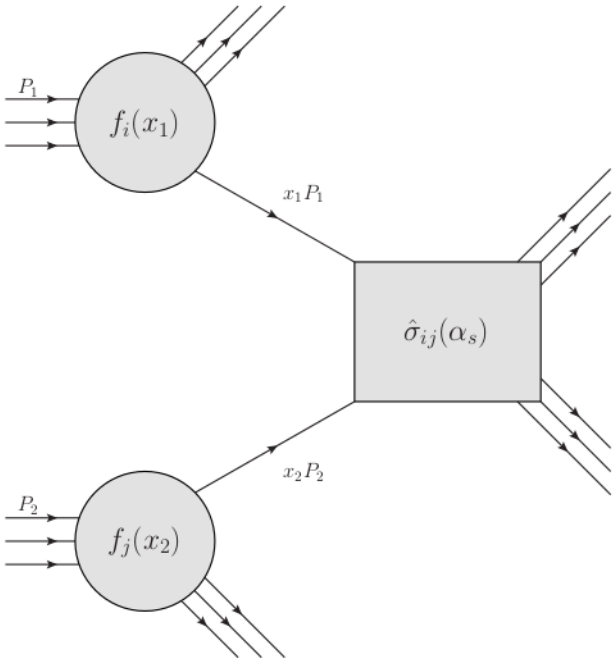

Figure 1.1: Schematic picture of factorization.

As it has already been shown, computing the (n)PDFs (and the FFs) is beyond the scope of pQCD. When calculating their dynamics the so-called collinear divergences show up. To remove this kind of divergences a cut-off scale – the factorization scale – has to be added. Afterwards, the divergent part is absorbed into the parton distribution functions at the factorization scale [1]. This renormalization procedure leads to a set of equations that describe the perturbative evolution of the PDFs once the non-perturbative contribution is absorbed into the initial conditions - Dokshitzer-Gribov-Lipatov-Altarelli-Parisi (DGLAP) [22–24].

Based on the universality of (n)PDFs a technique called global analysis has been developed to obtain the distribution functions. The (n)PDFs are extracted from various experiments (deep inelastic scattering, Drell-Yan, etc.) at their scale and then evolved using the DGLAP evolution equations [22–24]. A global analysis of nPDFs at next-to-next-to leading order in perturbative QCD will be the subject of Chapter 2.

1.3 Hard Probes in Heavy Ion Collisions

During the last fifteen years, the Heavy Ion (HI) program at the Relativistic Heavy-Ion Collider (RHIC) first [3, 7, 8, 25, 26], and, more recently, at the Large Hadron Collider (LHC) [27–30] have provided a great deal of information about ultra-relativistic nuclear

[1]The absorption of the collinear divergence by the distribution functions is probed in the pQCD factorization theorem [19, 20], which is one of the cornerstones of perturbative QCD.

collisions. The study of hard processes (*hard probes)* has become one of the most active fields of research in HICs due to the wide variety of scales that it spans: from a few GeV to the TeV scale. Particles which are produced at a large – energy or mass – scale are designated hard probes (HP). These are originated within the soft bulk in high-energy nucleus-nucleus collisions, so they are an excellent way to describe the properties of the hot nuclear matter. In contrast to the proton-proton case, the particles resulting from the hard process have to traverse the QGP before eventually hadronizing into the observed particles. Colorless particles, as photons or electroweak bosons, do not interact with the surrounding matter, leaving the medium unaffected. However, colored quarks or gluons produced in the elementary hard processes do interact with the QGP and the corresponding signal is modified. Therefore, they can be used to analyze the dynamic behavior of the QGP.

Among hard probes there is *jet quenching*, which is studied in Chapter 4. Jet quenching refers to the effects resulting from the propagation of hard particles through a hot and dense colored medium. In 1982 Bjorken proposed for the first time that high-energy quarks and gluons propagating through a quark-gluon plasma suffer differential energy loss producing, in consequence, a suppression of the inclusive yields at high-p_T [31]. This effect was later observed at RHIC [32]. Nowadays, jet quenching is experimentally well-established. A great amount of data on single-inclusive particle spectra have been provided both from RHIC [33–35], and the LHC [28, 36, 37]. Two-particle correlations have been measured at RHIC [38–40], and at the LHC [41], too. Furthermore, other reflections of this phenomenon have been seen in jets analyses, such as [29, 42, 43] at the LHC and [44] at RHIC. However, from the theoretical point of view, the microscopic mechanisms responsible of jet quenching are not yet fully understood.

In Section 1.2, the factorization theorem was introduced [19, 20]. According to this theorem, the hadronic cross section can be computed, in *vacuum*, in terms of the free-proton PDFs, the partonic cross section, and the (vacuum) fragmentation functions. This partonic cross section, in case of hard probes (large virtualities) can be calculated in pQCD. As it was already mentioned, it has not been theoretically proven rigorously that the same factorization holds in HICs. However, as up to now it is consistent with all the phenomenological analysis, factorization is assumed. In the nuclear case, the free-proton PDFs are replaced by the nPDFs, deeply analyzed in Chapter 2. The partonic cross section takes place in a very short time, $\mathcal{O}(1/Q)$. Consequently, it remains unchanged in the presence of the medium, as partons cannot be resolved by the nuclear matter. Nevertheless, the outgoing partons propagate through the QGP. Hence, the parton branching prior to hadronization in the presence of the medium is modified (jet quenching) and at high enough transverse momentum, the Lorenz boost indicates that hadronization take places in vacuum [2]. The modification of the parton branching can be computed using perturbation theory and the current approaches are based on parton energy loss. The main goal of jet quenching analyses is to characterize the properties of the medium by measuring the modifications in the jet spectrum. One of the most extensive studies of experimental data and its corresponding consequences for the

[2] An experimental signature of this effect is that different hadronic species are affected in the same way by the presence of a medium [45]

medium properties will be presented in Chapter 4.

In order to identify the quenching suffered by the jet or the hard parton, it is worth emphasizing the necessity of a precise knowledge of nPDFs. This allows to identify the effects that are originated at the initial state of an A-A collision, usually called *cold nuclear effects* and deconvolute them from the final state ones (*hot nuclear effects*).

1.4 Percolation of strings

From a theoretical point of view, the Color Glass Condensate (CGC) formalism [13–16], derived from QCD in a semiclassical approach, provides a general framework to compute the initial stages of the collision, from the small-x structure of the nuclei to the approach to the hydrodynamical behavior. The gluon density $xG(x, Q)$ grows rapidly when the fractional momentum x decreases due to the gluon splittings allowed by non-Abelian QCD. Therefore, gluon showers generate more gluon showers giving rise to an exponential growing towards small x.

At small-x the partonic density of gluons grows fast and, at some point, there is a fusion of gluons leading to a limited transverse density of gluons at some fixed momentum resolution, Q_s, the gluon saturation momentum [13]. The distance between these low-x gluons is very small, thus the interaction coupling is weak $\alpha_s \ll 1$. This dense system is called CGC. It has a very high occupation number, $1/\alpha_s(Q_s)$, and corresponds to a coherent state of strong color fields.

High-x gluons can be seen as the sources of the low-x gluons. In the infinite momentum frame, these large momentum gluons travel very fast and, hence, their time scales are Lorentz dilated. Due to Lorentz contraction the collision of two nuclei can be seen as that of two sheets of colored glass where the color field in each point of the sheets is randomly oriented. Between the sheets longitudinal color electric and magnetic fields are formed. The number of these color flux tubes between the two colliding nuclei is $Q_s^2 R^2$, with R the radius of the nuclei, forming Glasma [46], which has been extensively used in comparisons with experimental data.

A simple implementation of these ideas is percolation of strings. Hadron-hadron and heavy ion collisions can be described by the formation of strings linking partons from the projectile and the target. Color strings may be viewed as cylinders expanded in the longitudinal direction, whose interactions with the transverse plane are small areas filled with the color field of the colliding partons. Particles are created via $q\bar{q}$-pair production in this field.

Increasing the energy or/and the centrality or atomic number of the colliding objects, the number of strings grows and they begin to interact forming clusters. These clusters are very similar to disks in two-dimension percolation theory [47]. This cluster formation shows a critical behavior: the cluster size diverges at a certain critical density, η_c, called the

percolation threshold.

The value of the critical density $\eta_c = 1.13$ has been computed by several numerical studies [48–50] using an homogeneous distribution for the colliding nuclei. However, in HICs the distribution of strings in highly non-uniform since there are more nucleons – and, hence, more strings – in the center than in the edge of the nuclei. The results on η_c are higher in this case [51]. This threshold was already reached in Pb-Pb central collisions at the SPS and in semi-peripheral collisions at RHIC energies.

The connection between percolation and QCD has been formally studied. These studies are based on the relation between $SU(N)$ gauge field systems and spin [52], and on Polyakov loops [53].

The addition of some dynamics to this geometric picture is required in order to compare with experimental data. Specifically, a model for the decays of clusters into hadrons is needed. This will be addressed in Chapter 3, where the expressions of the average momentum and average multiplicity of the clusters from the composition of the color fields of the strings will be derived.

Chapter 2

Nuclear parton distribution functions at NNLO

2.1 DGLAP evolution equations

It was already mentioned in the Introduction that parton distribution functions are extracted from experimental data. However, PDFs need to be evaluated at the relevant scale, Q^2, of the experiment. The Q^2-dependence of parton distribution functions can be determined perturbatively as long as Q^2 is large enough.

The transverse resolution of these processes is set by their virtuality, Q^2. Therefore, the Q^2-dependence of parton distribution functions is strictly related to the collinear divergence, a singularity due to the emission of gluons at low transverse momentum. It was already remarked that at leading order (nuclear) parton distributions, $f_i(x, Q^2)$ represent the probability of finding a parton i with fraction of momentum x of the hadron (free or bound in nucleus) at the energy scale Q^2. The Q^2-evolution of the distribution is calculated by considering the probability of emitting a parton with transverse momentum close to Q^2.

The collinear divergences appearing when computing these parton emissions give rise to logarithmic divergences, $\ln(Q^2/\Lambda_{QCD})$. As α_s is small (Q^2 is large), parton emissions are suppressed by powers of the strong coupling constant. Nonetheless, this logarithmic terms can compensate this suppression. These large logarithms are in general obtained from the phase space region where multiple emissions are ordered by transverse momenta, with subsequent emissions having less momenta [1]. This brings on a resummation of large logarithms, as the typical ones in the renormalization group equations approach.

The Dokshitzer-Gribov-Lipatov-Altarelli-Parisi (DGLAP) evolution equations are [22–24]

$$\frac{d}{d\ln Q^2} f_i(x,Q) \;=\; \frac{\alpha_s\left(Q\right)}{2\pi} \int_x^1 \frac{dz}{z}\, P_{ij}\left(z, \alpha_s\left(Q\right)\right)\, f_j\left(\frac{x}{z}, Q\right) \quad , \tag{2.1.1}$$

[1] This is the case of PDFs, which are *space-like* (DIS, $q^2 < 0$). On the contrary, FFs are *time-like* ($q^2 > 0$ for e^+e^- annihilation).

where i and j run over all the possible parton flavors ($2n_f + 1$ equations, n_f being the number of quark flavors). The splitting functions are denoted by P_{ij}. They can be computed in perturbation theory and they describe the probability of the evolution of a parton j into a parton i. In consequence, in general, they are not symmetric, $P_{ij} \neq P_{ji}$.

The splitting functions themselves can be expressed as a perturbative expansion in powers of α_s:

$$P_{ij}(x, \alpha_s(Q)) = P_{ij}^{(0)}(x) + \frac{\alpha_s(Q)}{2\pi} P_{ij}^{(1)}(x) + \left(\frac{\alpha_s(Q)}{2\pi}\right)^2 P_{ij}^{(2)}(x) + ... \tag{2.1.2}$$

Due to charge conjugation invariance and flavor symmetry their number can be reduced significantly:

$$\begin{aligned}
P_{\mathrm{q}_i\mathrm{q}_j} &= P_{\bar{\mathrm{q}}_i\bar{\mathrm{q}}_j} = \delta_{ik} P_{\mathrm{qq}}^{\mathrm{v}} + P_{\mathrm{qq}}^{\mathrm{s}} \ , \\
P_{\mathrm{q}_i\bar{\mathrm{q}}_j} &= P_{\bar{\mathrm{q}}_i\mathrm{q}_j} = \delta_{ik} P_{\mathrm{q\bar{q}}}^{\mathrm{v}} + P_{\mathrm{q\bar{q}}}^{\mathrm{s}} \ , \\
2n_f\, P_{\mathrm{q}_i\mathrm{g}} &= 2n_f\, P_{\bar{\mathrm{q}}_i\mathrm{g}} = P_{\mathrm{qg}} \ , \\
P_{\mathrm{gq}_i} &= P_{\mathrm{g}\bar{\mathrm{q}}_i} = P_{\mathrm{gq}} \ ,
\end{aligned} \tag{2.1.3}$$

where v stands for the flavor-diagonal valence quantity, and s for the flavor-independent *sea* contribution.

The LO splitting functions are [23]

$$\begin{aligned}
P_{\mathrm{qq}} &= C_F \frac{1+x^2}{(1-x)_+} + 2\delta(1-x) \ , \\
P_{\mathrm{qg}} &= \frac{1}{2}\left[x^2 + (1-x)^2\right] \ , \\
P_{\mathrm{gq}} &= C_F \left[\frac{1+(1-x)^2}{x}\right] \ , \\
P_{\mathrm{gg}} &= 2N_c \left[\frac{x}{(1-x)_+} + \frac{1-x}{x} + x(1-x)\right] + \left(\frac{11N_c - 2n_f}{6}\right)\delta(1-x) \ ,
\end{aligned} \tag{2.1.4}$$

where n_f stands for the number of flavors, N_c for the number of colors and $C_F = (N_c^2 - 1)/2N_c$. The "+" prescription is defined by

$$\int_0^1 dx \, \frac{f(x)}{(1-x)_+} = \int_0^1 dx \, \frac{f(x) - f(1)}{1-x} \ . \tag{2.1.5}$$

Higher order contributions to the splitting functions have already been calculated. The splitting functions at NLO can be found in [54,55] . For the NNLO splitting functions see [56,57].

Often, the physical basis of the PDFs is modified to a more appropriate one, which decouples the non-singlet distributions from the gluon. This basis is formed by the aforementioned singlet, non-singlet, valence, and gluon, the three former being, suppressing the functional dependencies, respectively [58]

$$\Sigma \;=\; \sum_{i}^{n_f} \left(q_i + \bar{q}_i\right) \;, \tag{2.1.6}$$

$$q_{ij}^{\pm} \;=\; \left(q_i \pm \bar{q}_i\right) - \left(\bar{q}_j \pm q_j\right) \;\;, \tag{2.1.7}$$

$$q_{ns}^{\mathrm{v}} \;=\; \sum_{i}^{n_f} \left(q_i - \bar{q}_i\right) \;. \tag{2.1.8}$$

It can be demonstrated that in this basis the splitting functions are for the non-singlet and the valence, respectively [58]:

$$P_{\mathrm{ns}}^{\pm} \;=\; P_{\mathrm{qq}}^{\mathrm{v}} \pm P_{\mathrm{q\bar{q}}}^{\mathrm{v}} \;, \tag{2.1.9}$$

$$P_{\mathrm{ns}}^{\mathrm{v}} \;=\; P_{\mathrm{qq}}^{\mathrm{v}} - P_{\mathrm{q\bar{q}}}^{\mathrm{v}} + n_f(P_{\mathrm{qq}}^{\mathrm{s}} - P_{\mathrm{q\bar{q}}}^{\mathrm{s}}) \equiv \; P_{\mathrm{ns}}^{-} + P_{\mathrm{ns}}^{\mathrm{s}} \;. \tag{2.1.10}$$

Regarding the singlet and the gluon, the expression for the quark-quark splitting function is needed [57]

$$P_{\mathrm{qq}} \;=\; P_{\mathrm{ns}}^{+} + n_f(P_{\mathrm{qq}}^{\mathrm{s}} + P_{\mathrm{\bar{q}q}}^{\mathrm{s}}) \equiv \; P_{\mathrm{ns}}^{+} + P_{\mathrm{ps}} \;. \tag{2.1.11}$$

The DGLAP equations in this basis, suppressing the functional dependencies, are

$$\frac{d}{d\ln Q^2}\, q_{\mathrm{ns}}^{i} \;=\; \sum_{n=0} \left(\frac{\alpha_s}{4\pi}\right)^{n+1} P_{\mathrm{ns}}^{(n)i} \otimes q_{\mathrm{ns}}^{i} \qquad (i = \pm, \mathrm{v}) \;\;, \tag{2.1.12}$$

$$\frac{d}{d\ln Q^2} \begin{pmatrix} \Sigma \\ g \end{pmatrix} \;=\; \frac{\alpha_s}{2\pi} \begin{pmatrix} P_{\mathrm{qq}} & P_{\mathrm{qg}} \\ P_{\mathrm{gq}} & P_{\mathrm{gg}} \end{pmatrix} \otimes \begin{pmatrix} \Sigma \\ g \end{pmatrix} \;\;, \tag{2.1.13}$$

where $\otimes$ stands for the Mellin convolution,

$$[a \otimes b](x) \;\equiv\; \int_x^1 \frac{dy}{y}\, a(y)\, b\!\left(\frac{x}{y}\right) \;. \tag{2.1.14}$$

Using these equations, the Q^2-evolution with respect to an initial scale Q_0 of the parton distribution functions is predicted. However, PDFs are unknown *a priori* at any initial scale, hence, they have to be extracted from a global analysis of (DIS, Drell-Yan...) data.

The procedure is as follows, first of all, among all the experimental data available, those which are in the kinematic region where pQCD is valid are selected. Then, all the selected observables are computed at parton level at the order desired in pQCD, in this case, at NNLO. Next, the parton distribution functions are parametrized at the initial scale, Q_0. For

each data point, the PDFs are evolved using the DGLAP equations (including the splitting functions up to NNLO) from the initial scale to the scale of the process, $Q > Q_0$, and, then, the soft part is convoluted with the hard one to obtain the theoretical prediction for the observable. Then a χ^2-distribution is built and the value of the parameters is found minimizing iteratively the χ^2. It is important to highlight that if the observables are computed including NNLO corrections in QCD, the splitting function up to order α_s^2 have to be included in the evolution giving rise to terms of order α_s^3 in the DGLAP equations.

In principle, the number of parameters given to the functional form of the PDFs at the initial scale is arbitrary. The value of Q_0 is also arbitrary and each nPDFs collaboration chooses it according to different criteria. At the initial scale, some of the parameters can be fixed by the proton sum rules, related with the baryon number conservation,

$$\int_0^1 dx\, u_v\left(x, Q_0^2\right) \;=\; 2\int_0^1 dx\, d_v\left(x, Q_0^2\right) \;=\; 2\ , \qquad \int_0^1 dx\, s_v\left(x, Q_0^2\right) \;=\; 0\ , \tag{2.1.15}$$

and the momentum sum rule,

$$\int_0^1 \quad dx\, x\left(\Sigma\left(x, Q_0^2\right) + g\left(x, Q_0^2\right)\right) \;=\; 1\ . \tag{2.1.16}$$

2.2 Deep inelastic scattering

As it has been already outlined in the previous sections both PDFs and nPDFs are obtained from several experimental data and then evolved using the DGLAP evolution equations – global analysis. In this section we will discuss the case of lepton-proton(nucleus) collisions involving a large momentum exchange: Deep Inelastic Scattering (DIS) experiments. These experiments usually provide the strongest constraints to PDFs in global PDF fits and one of the most rigorous tests of perturbative QCD, in general.

In this process, illustrated in Fig. 2.1, the projectile is a high-energy lepton which scatters off a hadron target: $lN \to l'X$. The four-momentum of the incoming lepton is denoted by $k^\mu = (E, \vec{k})$ and the momentum of the outgoing lepton by $k'^\mu = (E', \vec{k'})$. The momentum of the hadron is $p^\mu = (E_N, \vec{p})$, which can be written as $p^\mu = (M, \vec{0})$ in the hadron rest frame. The momentum transfer is given by $q^\mu = k^\mu - k'^\mu$. In the simplest case both the incoming and the outgoing leptons are charged leptons (an electron or a muon) and the interaction is dominated by the exchange of a virtual photon, i.e, the interaction is mainly electromagnetic. However, corrections by the exchange of a Z^0 boson, i.e, *neutral current* (NC) interaction, might be relevant, see left panel of Fig. 2.1. (Anti)neutrinos have no electric charge so do not interact electromagnetically, but they do interact with quarks through week interactions. Neutrino DIS refers to the scattering process that involves the conversion of a(n) (anti)neutrino to its associated charged lepton, exchanging a virtual massive vector boson, the $W^\pm$. In this case, the interaction is called *charged current* (CC) and it is represented, at leading order (LO), on the right panel of Fig. 2.1 .

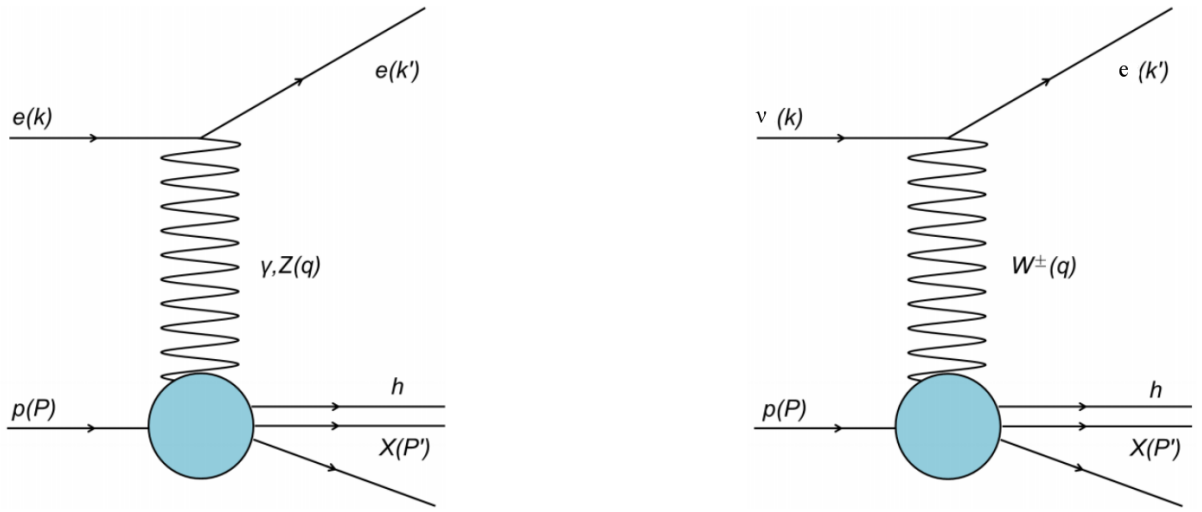

Figure 2.1: Feynman diagram of the electron-proton NC ($ep \to eX$, left panel) and CC ($\nu_e p \to eX$, right panel) at leading order.

The standard DIS invariant variables are defined by:

$$Q^2 \equiv -q^2 \ , \qquad x \equiv \frac{Q^2}{2p\cdot q} = \frac{Q^2}{2M\nu} \ , \qquad y \equiv \frac{p\cdot q}{p\cdot k} = \frac{\nu}{E'} \ , \tag{2.2.17}$$

where the latter equalities refer to the target rest frame. M denotes the rest mass of the nucleon, $\nu = E - E'$ is the energy transfer to the target nucleon. The invariant Q^2 is called *virtuality* and it is related to the scale of distances involved in the interaction. The Björken scaling variable x is the fraction of momentum from the proton (free or bound) carried by the interacting quark. The invariant y represents the fraction of the energy of the ingoing lepton transferred to the virtual photon.

The unpolarized cross section for both charged-lepton and neutrino DIS can be written in terms of the *structure functions*. These are adimensional functions which parametrize the structure of the target as 'seen' by the virtual photon (or, in general, gauge boson). These functions are F_2, F_L and F_3 [2]. In the electromagnetic case – interaction mediated by a virtual photon – only F_2 and F_L appear. F_2^{em} dominates the cross section and, for this reason, it is the best known of the structure functions, as F_L^{em} appears at higher orders in perturbation theory. In the case of charged current (or neutrino) DIS the structure functions involved are F_2 and F_3, which describe the interaction with (anti)neutrinos. Due to the weak nature of the neutrino interaction the use of heavy nuclear targets is unavoidable.

[2]Sometimes instead of F_L, F_1 is used which is just a combination of F_2 and F_L

2.2.1 Deep inelastic scattering at LO

The charged-lepton electromagnetic DIS cross section, neglecting the contribution of the exchange of a Z^0 boson, can be written as:

$$\frac{d^2\sigma}{dxdQ^2} = \frac{4\pi\alpha_{em}^2}{xQ^4}\left[\left(1-y+\frac{y^2}{2}\right)F_2^{em}(x,Q^2)-\frac{y^2}{2}F_L^{em}(x,Q^2)\right] , \tag{2.2.18}$$

where $\alpha_{em} \equiv e^2/4\pi$ stands for the fine structure constant and F_L is given by

$$F_L^{em}(x,Q^2) = F_2^{em}(x,Q^2)\left(1+\frac{4x^2M^2}{Q^2}\right) - 2xF_1^{em}(x,Q^2) . \tag{2.2.19}$$

At very high energies, in particular for $Q^2 \sim M_Z^2$, the contribution to the charged-lepton DIS from the boson Z exchange cannot be neglected. Eq. (2.2.18) can be generalized including both γ and Z exchanges to:

$$\frac{d^2\sigma}{dxdQ^2} = \frac{4\pi\alpha_{em}^2}{xQ^4}\left[xy^2F_1(x,Q^2)+(1-y)F_2(x,Q^2)+y(1-\frac{y}{2})F_3(x,Q^2)\right] , \tag{2.2.20}$$

where now the parity-violating structure function F_3 appears.

The unpolarized neutrino (antineutrino) DIS cross section for $\nu p \to lX$ can be written as:

$$\frac{d^2\sigma^{\nu(\bar\nu)}}{dxdy} = \frac{G_F^2ME}{\pi}\left[\left(1-y-\frac{M}{2E}xy\right)F_2^{\nu(\bar\nu)}+y^2xF_1^{\nu(\bar\nu)}+(-)\,y\left(1-\frac{y}{2}\right)xF_3^{\nu(\bar\nu)}\right] , \tag{2.2.21}$$

where G_F is the *Fermi constant* defined as

$$\frac{G_F}{\sqrt{2}} = \frac{g^2}{8m_W^2} . \tag{2.2.22}$$

Let us discuss now the electromagnetic DIS interaction in the naive parton model. The parton model approximation states that for hard enough interactions, the virtual photon interacts only with a single point-like parton inside the target proton and these partons can be treated approximately as free particles. In this model, considering point-like (massless) and spin 1/2 partons (quarks) moving parallel to the hadron (with $p_T = 0$) the EM longitudinal structure functions are exactly zero: $F_L^{em} = 0$. Hence, in the limit $M^2/Q^2 \to 0$, the Callan-Gross relation is satisfied [59]:

$$2xF_1(x) = F_2(x) . \tag{2.2.23}$$

This relation illustrates a fundamental property of spin-1/2 particles, that they cannot absorb a longitudinally polarized photon [60]. The electromagnetic F_1 and F_2 in the parton model are, respectively,

$$\begin{aligned} F_1^{em}(x,Q^2) &= \sum_i e_i^2\,\left[q_i(x,Q^2)\right] \\ F_2^{em}(x,Q^2) &= \sum_i 2xe_i^2\,\left[q_i(x,Q^2)\right] , \end{aligned} \qquad (i=1,2,L) \tag{2.2.24}$$

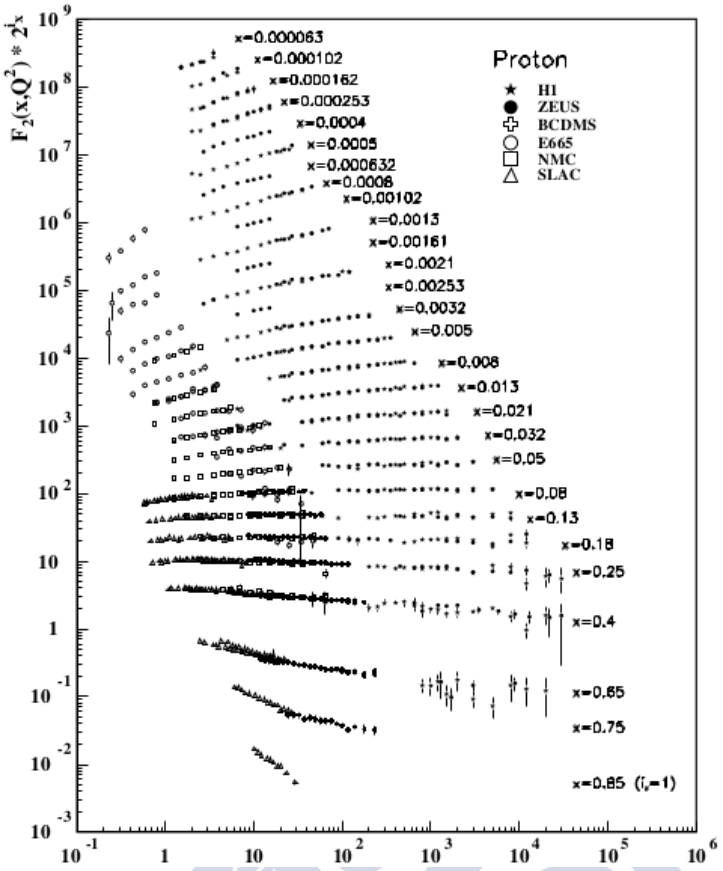

Figure 2.2: Björken scaling: F_2 versus Q^2 for different values of x. Courtesy of the Particle Data Group [65].

where i represents the sum over all partons and e_i are their fractional electric charges.

Some comments are in order. First of all, in this approximation the structure functions are independent of the virtuality of the process, Q^2. They only depend on one dimensionless variable x. This phenomenon is known as *Björken-scaling* [61] and was a remarkable success of the original parton model. It was observed for the first time in the SLAC experiments [62] giving direct evidence of the constituents of the nucleon. The data showing this approximate behavior span two decades of experiments, from the early SLAC measurements to the more recent experiments at HERA [63, 64], see Fig. 2.2. The lack of any scale dependence in the structure functions is a consequence of the parton model's assumptions: partons are treated as point-like particles, and consequently having no characteristic length scale.

The simple parton model provided a good phenomenological description of early DIS measurements. The asymptotic freedom of QCD allows for a consistent description of Björken-scaling, where the constituents of the hadron can be treated as independent, non-interacting point-like particles at high virtuality Q^2. The partons in this model were therefore rapidly

associated with the quarks and gluons of QCD.

However, as it can be seen in Fig. 2.2, the Q^2-independence of the structure functions is a good approximation, but it is not completely exact. Some deviations from the scaling law appear. These are called *scaling violations* and they can be perfectly understood by the DGLAP equations. These higher-order corrections to the point vertex cross section introduce logarithms of Q^2 which break the Björken scaling of the structure functions. In fact, the observation of such scaling violations was considered as one of the most robust experimental validations of QCD.

For the neutrino scattering, the interaction is mediated by the electroweak charged-current, CC, so the quark distributions (PDFs) are weighted by their corresponding weak charges. It has to be taken into account whether the interacting lepton is a neutrino or an antineutrino and the mixture of flavors in the quark sector given by the CKM matrix. When the interacting lepton is a neutrino, $\nu p \to lX$, the structure function F_2^ν at LO is [66]:

$$F_2^\nu(x,Q^2) \;=\; 2x\left[d'(x,Q^2)+s'(x,Q^2)+\bar{u}(x,Q^2)+\bar{c}(x,Q^2)\right] \;\;, \tag{2.2.25}$$

with

$$\begin{aligned} d'(x,Q^2) \;&=\; |V_{ud}|^2\, d(x,Q^2)+|V_{us}|^2\, s(x,Q^2) \\ s'(x,Q^2) \;&=\; |V_{cd}|^2\, d(x,Q^2)+|V_{cs}|^2\, s(x,Q^2) \;\;, \end{aligned} \tag{2.2.26}$$

where V_{ij} is the element ij of the CKM matrix [3].

The structure function F_3 at LO is given by [66]:

$$F_3^\nu(x,Q^2) \;=\; 2\,\left[d'(x,Q^2)+s'(x,Q^2)-\bar{u}(x,Q^2)-\bar{c}(x,Q^2)\right] \;\;. \tag{2.2.27}$$

2.2.2 Deep inelastic scattering at NLO

In this section the diagrams that contribute at next-to-leading order (in QCD) to the one studied in the previous section will be summarized.

At $\mathcal{O}(\alpha_s)$ in QCD the structure functions are modified by two kind of processes: initial (or final) state radiation and virtual corrections. The initial (final) state radiation consists of having extra QCD particles in the initial (final) state; i.e, in the radiation of an extra real gluon, as it can be seen in Fig. 2.3. The virtual corrections correspond to the emission and then absorption of a virtual gluon. This can be due to the self-energy corrections of the external legs (see right panel of Fig. 2.4) or to the loop correction to the quark-photon vertex (see left panel of Fig. 2.4).

[3] When the interacting lepton is an antineutrino, $\bar{\nu}p \to lX$, $F_2^{\bar{\nu}}$ can be obtained from Eq. (2.2.25) changing the PDF of each particle by the PDF or its antiparticle.

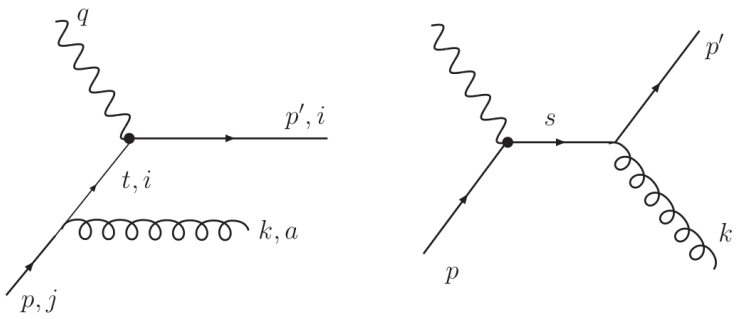

Figure 2.3: Feynman diagrams corresponding to the real-gluon emission process $\gamma * q \to qg$.

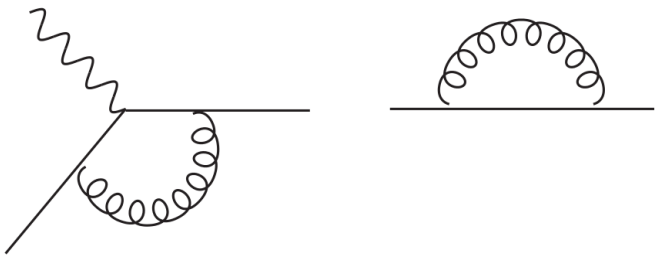

Figure 2.4: Virtual corrections to DIS.

Collinear, *infrared* (IR) and *ultraviolet* (UV), divergences show up when trying to compute the QCD corrections to DIS (at any order in perturbation theory). For instance, in the case of initial state radiation, see Fig. 2.3, collinear divergences appear when the emission is parallel to the direction of the incoming or outgoing quark and infrared divergences happen if the momentum of the emitted particle goes to zero. These divergences can be regulated in a gauge-invariant way using the dimensional regularization methods [67]. All these calculations can be performed in $N = 4 - \epsilon$ space-time dimensions. Then, all the divergences appear as $1/\epsilon^n$-poles. When regularization is appropriately performed, all the divergences, except of the collinear ones, turn out to cancel as a consequence of the IR safety of QCD yielding a finite contribution to the cross section. The latter singularities need to be removed by absorbing them into the parton densities.

Including all the contributions both at LO and NLO, the full F_2^{em} structure function can be written as:

$$F_2^{em}(x,Q^2) = \sum_i x e_i^2 \Bigg[f_i(x) + \frac{\alpha_s}{2\pi} \int_0^1 \frac{d\xi}{\xi} \sum_j \left(P_{ij}\left(\frac{x}{\xi}\right) \log \frac{Q^2}{\kappa^2} + W_{ij}(x) \right) f_j(\xi) + \mathcal{O}(\alpha_s^2) \Bigg] \quad . \tag{2.2.28}$$

where an infrared cutoff, κ, has been introduced to regulate the parton splitting. P_{ij} are the splitting functions, known at leading and next-to-leading order accuracy for some time [56, 57], and W_{ij} is the hadronic tensor, which can be written in terms of the structure functions and contains all the (NLO) finite contributions from the above-shown diagrams. This expression still suffers from the IR divergence when the limit $\kappa \to 0$ is considered. This divergence needs to be absorbed into the parton distribution functions by replacing the *bare* quantities $f(x)$ by a physically accessible quantity measured at the factorization scale μ_F. This can be expressed as an expansion of the bare PDFs

$$f_i(x,\mu_F^2) \;=\; f_i(x) + \frac{\alpha_s}{2\pi}\int_0^1 \frac{d\xi}{\xi}\,\Delta_{ij}^{(1)}\left(\frac{x}{\xi},\frac{\mu_F}{\kappa}\right) f_j(\xi) + \mathcal{O}(\alpha_s^2)\;, \tag{2.2.29}$$

where the counter-terms $\Delta_{ij}^{(n)}$ are the sum of a regular part $\Delta_{r,ij}^{(n)}$ and a singular one $\Delta_{s,ij}^{(n)}$, and the sum over j is implicit. The singular part is defined by removing the divergence present in the structure functions. Comparing to Eq. (2.2.28), this divergence may be subtracted by setting

$$\Delta_{s,ij}^{(1)} \;=\; P_{ij}\left(\frac{x}{\xi}\right)\log\frac{\mu_F^2}{\kappa^2}\;. \tag{2.2.30}$$

The regular part of the counter-term is not uniquely specified by the factorization procedure. The choice of a specific counter-term gives rise to different *factorization schemes*. For example, one may make a process-specific choice where all of the regular coefficients are absorbed into the PDF definition.

- **DIS-scheme**. In this scheme, all the regular coefficients are absorbed into the definition of the PDF [68]. In this case, $\Delta_{r,ij}^{(1)} = W_{ij}(x)$ and, therefore:

$$F_2^{em}(x,Q^2) \;=\; x\sum_i e_i^2\, f_i^{\rm DIS}(\xi)\;. \tag{2.2.31}$$

  The expression is particularly simple. However, in this scheme, the definition of the PDFs is process-dependent.

- $\overline{\rm MS}$**-scheme**. The minimal subtraction scheme allows a consistent definition of the PDFs for all kind of processes. The regular part of the counterpart is set to $\Delta_{r,ij}^{(1)} = \log 4\pi - \gamma_E$, so, it is process independent. In the $\overline{\rm MS}$-scheme the factorized PDFs are given by

$$f_i(x,\mu_F^2) = f_i(x) + \frac{\alpha_s}{2\pi}\sum_j\left[\left(P_{ij}\,(x)\log\frac{\mu_F^2}{\kappa^2} + \log 4\pi - \gamma_E\right)\right]\otimes f_j(x) + \mathcal{O}(\alpha_s^2)\,, \tag{2.2.32}$$

  and the electromagnetic F_2^{em} becomes

$$F_2(x,Q^2) \;=\; x\sum_i e_i^2\left\{f_i(x,\mu_F^2) + \frac{\alpha_s}{2\pi}\int_x^1\frac{d\xi}{\xi}\,f_i(\xi,\mu_F^2)\,\widetilde{W}_i\left(\frac{x}{\xi},\frac{Q^2}{\mu_F^2},\alpha_s\right)\right\}\;, \tag{2.2.33}$$

where the $\widetilde{W_i}$ are the finite contributions remaining after factorization. Note that the relation between the PDFs at the factorization scale and the bare distributions is now divergent. However, the renormalized distributions can be measured at some scale. In general, for a universal factorization scheme such as $\overline{\text{MS}}$, structure functions can be computed as

$$F_j(x,Q^2) = \sum_i \int_x^1 \frac{d\xi}{\xi} C_i\left(\frac{x}{\xi}, \frac{Q^2}{\mu_F^2}, \alpha_S\right) f_i(\xi, \mu_F^2) \qquad (i = 1, 2, L) \ , \tag{2.2.34}$$

where the C_i are the finite Wilson coefficients determined perturbatively and the PDFs f_i encode the non-perturbative structure of the calculation.

In our global analysis the $\overline{\text{MS}}$-scheme is used, so all the expressions hereinafter will be written for this scheme.

In the $\overline{\text{MS}}$-scheme, the electromagnetic proton F_2 at NLO taking the factorization and renormalization scales equal to Q^2 can be written as [69]:

$$\begin{aligned}\frac{F_2^{em}(x,Q^2)}{x} \ = \ \int_x^1 \frac{dx'}{x'} \Bigg\{ \sum_i e_i^2 \, q_i\left(\frac{x}{x'}, Q^2\right) \left[C_{2,q}^{(0)}(x') + \frac{\alpha_s\left(Q^2\right)}{4\pi} C_{2,q}^{(1)}(x') \right] + \\ + \frac{\alpha_s\left(Q^2\right)}{4\pi} g\left(\frac{x}{x'}, Q^2\right) C_{2,g}^{(1)}\left(x'\right) \Bigg\} \ ,\end{aligned} \tag{2.2.35}$$

where $g(x,Q^2)$ is the gluon PDF and $C_{2,q}^{(0)}(x')$ is the LO coefficient:

$$C_{2,q}^{(0)}(x') = \delta(1-x). \tag{2.2.36}$$

By integrating the part corresponding to this coefficient Eq. (2.2.24), as expected, is obtained. The first order correction coefficient to the quark is given by [69]

$$\begin{aligned}C_{2,q}^{(1)}(x') \ = \ C_F \Bigg[4 \left(\frac{\ln\left(1-x\right)}{1-x} \right)_+ - \frac{3}{\left(1-x\right)_+} - 2\left(1+x\right)\ln\left(1-x\right) \\ - 2\,\frac{1+x^2}{1-x}\ln\left(x\right) + 6 + 4x - \delta\left(1-x\right)\left(9 - 4\zeta_2\right) \Bigg] \ ,\end{aligned} \tag{2.2.37}$$

with $\zeta_2 = \pi^2/6$ and $C_F = 4/3$. The "+" prescription is defined as usual as Eq. (2.1.5).

The NLO gluon coefficient of the F_2^{em} is [69]

$$C_{2,g}^{(1)}(x') \ = \ T_f \, n_f \left\{ 4\left(1 - 2x + 2x^2\right) \left[\ln\left(1-x\right) - \ln\left(x\right)\right] - 4 + 32x\left(1-x\right) \right\} \ , \tag{2.2.38}$$

with $T_f = 1/2$ and n_f the number of active flavors.

For more detailed information about the computation of these diagrams and the different schemes see Chapter 3 of [70]. In [70] the relation between the PDFs in both schemes and the expressions of the structure functions in the DIS-scheme – that here are omitted – can be found.

For completeness, the proton structure functions, F_2 and F_3, for the neutrino DIS at NLO are now presented. The structure function F_2, that is, for $\nu p \to lX$ is

$$\begin{aligned}\frac{F_2^{\nu}\left(x,Q^2\right)}{2x} \;=\; \int_x^1 \frac{dx'}{x'}\; \Big\{ \Big[d'\left(\frac{x}{x'},Q^2\right) + s'\left(\frac{x}{x'},Q^2\right) + \bar{u}\left(\frac{x}{x'},Q^2\right) \;+ \\ + \bar{c}\left(\frac{x}{x'},Q^2\right)\Big] \left[C_{2,q}^{(0)}(x') + \frac{\alpha_s\left(Q^2\right)}{4\pi} C_{2,q}^{(1)}(x') \right] + \\ + \frac{\alpha_s\left(Q^2\right)}{4\pi}\, C_{2,g}^{(1)}(x') g\left(\frac{x}{x'},Q^2\right) \Big\} \;\;, \end{aligned} \tag{2.2.39}$$

where the coefficients are the same as the ones that appeared in the electromagnetic case, Eqs. (2.2.36), (2.2.37) and (2.2.38). The quark distributions d' and s' are given by Eq. (2.2.26). The proton structure function F_3 – for $\nu p \to lX$ – at NLO can be written as [71]

$$\begin{aligned}\frac{F_3^{\nu}\left(x,Q^2\right)}{x} \;=\; \int_x^1 \frac{dx'}{x'}\; \Big[d'\left(\frac{x}{x'},Q^2\right) + s'\left(\frac{x}{x'},Q^2\right) - \bar{u}\left(\frac{x}{x'},Q^2\right) - \\ - \bar{c}\left(\frac{x}{x'},Q^2\right)\Big] \left[C_{3,q}^{(0)}(x') + \frac{\alpha_s\left(Q^2\right)}{4\pi}\, C_{3,q}^{(1)}(x') \right] \;\;, \end{aligned} \tag{2.2.40}$$

where $C_{3,q}^{(0)}(x) = C_{2,q}^{(0)}(x)$ and

$$C_{3,q}^{(1)}(x) \;=\; C_{2,q}^{(1)}(x) - 2C_F\left(1+x\right) \;\;. \tag{2.2.41}$$

2.2.3 Deep inelastic scattering at NNLO

In this section, an outline of the calculation of the second order QCD corrections to deep inelastic scattering will be given.

Let us start by the electromagnetic interaction: the process $l + p \to l + X$ $(l = e, \mu)$ and its QCD corrections up to NNLO, neglecting the contribution given by the exchange of a Z^0 boson. In Table 2.1 the parton subprocesses that contribute to the proton structure function up to order α_s^2 are presented. The corresponding Feynman diagrams contributing to this processes can be found in [69]. As it was already mentioned in the NLO section, when computing these diagrams three type of divergences are found: infrared, ultraviolet, and collinear. They are regularized using n-dimensional regularization with $\epsilon = n - 4$. For further information about the computation of this diagrams see [69] and references therein.

DIS subprocesses		
α_s^0	$\gamma^* + q(\bar{q}) \to q(\bar{q})$	
α_s^1	$\gamma^* + q(\bar{q}) \to q(\bar{q})$	one-loop correction
	$\gamma^* + q(\bar{q}) \to q(\bar{q}) + g$	
	$\gamma^* + g \to q + \bar{q}$	
α_s^2	$\gamma^* + q(\bar{q}) \to q(\bar{q})$	two-loop correction
	$\gamma^* + q(\bar{q}) \to q(\bar{q}) + g$	one-loop correction
	$\gamma^* + q(\bar{q}) \to q(\bar{q}) + g + g$	
	$\gamma^* + q(\bar{q}) \to q(\bar{q}) + q(\bar{q}) + \bar{q}(q)$	
	$\gamma^* + g \to q + \bar{q}$	one-loop correction
	$\gamma^* + g \to q + \bar{q} + g$	

Table 2.1: List of charged-lepton DIS subprocesses up to NNLO.

The structure functions of the proton F_1, F_2, and F_L restricting ourselves to the photon exchange reaction can be written as

$$\frac{F_i\left(x,Q^2\right)}{a_i\left(x\right)} = \int_x^1 \frac{dx'}{x'}\left\{\frac{5}{18}\left[\Sigma\left(\frac{x}{x'},Q^2\right)C_{i,q}^S(x') + G\left(\frac{x}{x'},Q^2\right)C_{i,g}^G(x')\right] + \frac{1}{6}\Delta\left(\frac{x}{x'},Q^2\right)C_{3,q}^{NS}\left(x'\right)\right\}, \qquad (i=1,2,L)\ , \tag{2.2.42}$$

where the renormalization and factorization scales are taken as Q^2 and $a_2(x) = a_L(x) = 1$ and $a_1(x) = 1/2$. Here $G(x)$ stands for the gluon density and $\Delta(x)$ and $\Sigma(x)$ denote the non-singlet (NS) and singlet (S) quark densities [72]

$$\Delta_{ij}(x) = \left(q_i(x) \pm \bar{q}_i(x)\right) - \left(\bar{q}_j(x) \pm q_j(x)\right)\ , \tag{2.2.43}$$

$$\Sigma(x) = \sum_i^{n_f}\left(q_i(x) + \bar{q}_i(x)\right)\ , \tag{2.2.44}$$

where n_f is the number of lights quarks. C_i^G, C_i^{NS}, C_i^S are their corresponding Wilson coefficients. The details of their computation and their expressions up to α_s^2, both in the $\overline{\text{MS}}$-scheme and in the DIS-scheme, for the photon exchange reaction – ignoring the Z^0 contribution – can be found in [69].

The NNLO QCD corrections to charged-lepton deep inelastic scattering turned out to be remarkable. In the case of the proton F_2 structure function, they can amount for more than a 10% depending on the phase space region. For the F_L they are much larger, specially for the small-x region [73,74]. This highlights the necessity of extracting the parton distribution functions at NNLO to have the precision required by the present and new experiments (LHC, LHeC, EIC...).

The structure functions presented for $l + p \to l + X$ were limited to the electromagnetic interaction, i.e, to the photon exchange only. I will briefly describe now the case of the

structure function F_3 that appears in the charged current reaction $\nu + p \to l + X$ and also in the above-mentioned neutral reaction, when the Z-boson exchange is taken into account.

In the case of the charged current reaction the structures functions for a proton or, in general, for any isoscalar target are [71]

$$\begin{aligned}
\frac{F_i\left(x,Q^2\right)}{x} &= \int_x^1 \frac{dx'}{x'}\left[\Sigma\left(\frac{x}{x'},Q^2\right)C_{i,q}^S(x') + G\left(\frac{x}{x'},Q^2\right)C_{i,g}^G(x')\right] \qquad (i=2,L)\\
\frac{F_3\left(x,Q^2\right)}{x} &= \int_x^1 \frac{dx'}{x'}\, q_{ns}^v\left(\frac{x}{x'},Q^2\right)C_{3,q}^{NS}\left(x'\right) \ , \qquad (2.2.45)
\end{aligned}$$

where the renormalization and factorization scale have been taken equal to Q^2. $G(x)$ stands for the gluon density and $\Sigma(x)$ and $q_{ns}^v(x)$ denote the singlet, Eq. (2.2.44), and valence, Eq. (2.2.46), quark distribution functions, respectively [72]:

$$q_{ns}^v(x) \ = \ \sum_i^{n_f}\left(q_i(x) - \bar{q}_i(x)\right) \ . \qquad (2.2.46)$$

The coefficient functions follow the same notation. The gluon and singlet coefficients, $C_{i,g}^G(x')$ and $C_{i,q}^S(x')$, up to order α_s^2, are the same as those for the charged-lepton DIS with only electromagnetic interaction (for massless quarks) and can be found in [69, 75, 76]. For the expression of the first order correction to $C_{3,q}^{NS}$ see [77, 78]. Regarding the NNLO QCD corrections to this coefficient, the subprocesses contributing to the order α_s^2, where V denotes the intermediate vector boson $W^{+/-}$ or Z^0, are presented in Table 2.2.

NNLO DIS subprocesses		
α_s^2	$V + q(\bar{q}) \to q(\bar{q})$	two-loop correction
	$V + q(\bar{q}) \to q(\bar{q}) + g$	one-loop correction
	$V + q(\bar{q}) \to q(\bar{q}) + g + g$	
	$V + q(\bar{q}) \to q(\bar{q}) + q + \bar{q}$	

Table 2.2: List of subprocesses contributing to $C_{3,q}^{NS}$ at NNLO.

In the same way as for the computation of the NLO and NNLO QCD corrections of the structure functions in charged-lepton DIS, ultraviolet, infrared, and collinear divergences will show up in this calculation and they are regularized using n-dimensional regularization. The expression of the Wilson coefficient $C_{3,q}^{NS}$ is obtained in [71].

The structure function F_3 is of particular interest, since it only has contributions from the valence parton densities, which are well known from the precise charged-lepton DIS data, and from the non-singlet Wilson coefficient functions, see Eq. (2.2.45). Namely, it does not contain any information from the sea-quarks and gluons, which are less known. In consequence, it can be used as a test of perturbative QCD.

The structure functions in DIS allow us to determine the strong coupling constant and the parton distribution functions (PDFs) in a exceptionally precise way. The order α_s^2 in QCD corrections to the DIS structure functions reduce notably the theoretical uncertainties in the determination of the strong coupling constant, α_s, and the parton distributions. A precise knowledge of these quantities, is mandatory in the present and future hadron collider experiments. In summary, with the NNLO perturbative corrections of DIS structure functions, F_2, F_L and F_3, a new level of precision, in comparing theory and experiments, is achieved.

2.3 Drell-Yan

Another process that is often employed to extract the parton distribution functions is Drell-Yan dilepton production. This process consists in the collision of two hadrons decaying into two leptons and its name is given in honor to Sydney Drell and Tung-Mow Yan, who first computed the Drell-Yan cross section [79]. Usually, Drell-Yan refers to the production of two muons, because this is the most easily experimental accessible observable.

A very useful property of Drell-Yan dilepton production resides in the nature of its final state. The Drell-Yan process consists, at leading order, in the production of a lepton pair through a γ or Z^0, after a quark-antiquark annihilation. In consequence, the final state has no colored particles and, therefore, no uncertainties regarding the fragmentation functions.

This kind of reaction is illustrated at LO in Fig. 2.5. Here the role played by the virtuality Q^2 in DIS is played by the invariant mass of the lepton pair, M^2.

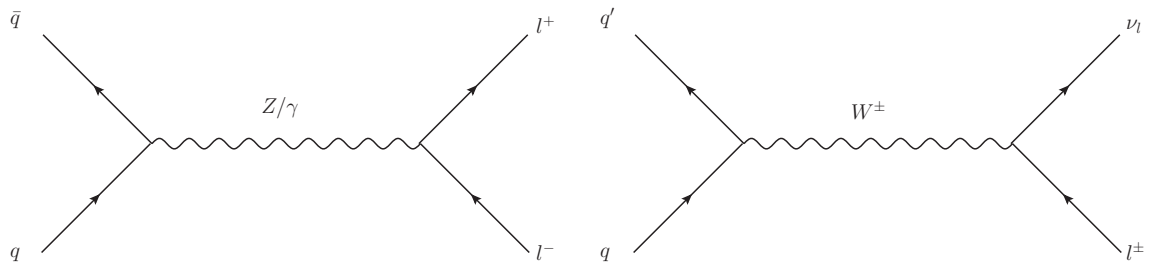

Figure 2.5: Feynman diagrams of Drell-Yan dilepton production at leading order. The neutral current process is shown on the left, and the charged current process on the right.

The cross section in Drell-Yan production is a double-differential cross section, $d^2\sigma/dM^2dy_R$, where M and y_R stand, respectively, for the invariant mass and the rapidity of the lepton pair. At LO and taking in consideration only the photon exchange (Born-level) this cross section is given by [80]:

$$\frac{d^2\sigma}{dM^2dy_R} = \frac{4\pi\alpha^2}{9sM}\left[q^{(1)}(x_1)\bar{q}^{(2)}(x_2) + (1 \leftrightarrow 2)\right] \tag{2.3.47}$$

where

$$x_1 \equiv \sqrt{\tau}e^{y_R}, \qquad x_2 \equiv \sqrt{\tau}e^{-y_R}, \qquad \tau \equiv \frac{M^2}{s} \ , \tag{2.3.48}$$

$\sqrt{s}$ being the center of mass energy of the two hadrons system. As usual, $q^{(i)}(x_i)$ is the parton distribution function.

NLO QCD corrections are added to the Born-level Drell-Yan cross section. There are two type of corrections: having a quark and antiquark in the initial state or having a quark (antiquark) and a gluon. In the first case, $\mathcal{O}(\alpha_s)$ QCD corrections come from gluon radiation, the emission of an additional unobserved gluon off the quark or the antiquark before the annihilation, see Fig 2.6, or from virtual corrections, one-loop diagrams equivalent to the ones in DIS, see Fig 2.7. On the other hand, we have initial state gluons: instead of having a quark and a antiquark in the initial state, we have a quark (antiquark) and a gluon. This gluon decays into a quark-antiquark pair, and the quark (antiquark) is annihilated with the antiquark (quark) from the other hadron into a virtual photon which decays into the dilepton pair, see Fig. 2.8. All the subprocesses corresponding to the NLO QCD corrections to Drell-Yan dilepton production are summarized in Table 2.3.

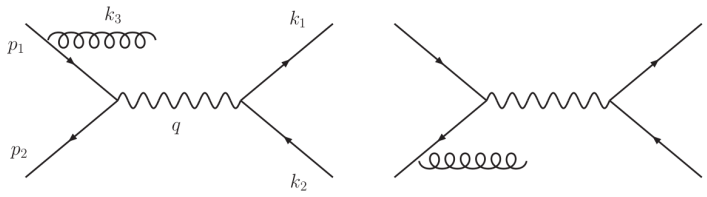

Figure 2.6: NLO gluon radiation in Drell-Yan dilepton production. Process $q + \bar{q} \to \mu^+ + \mu^- + g$.

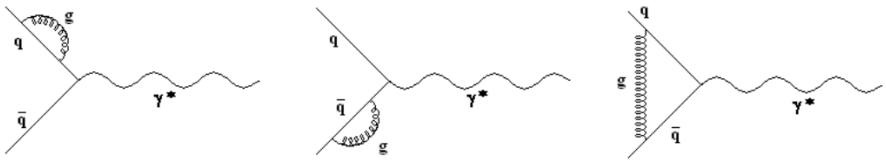

Figure 2.7: NLO Virtual corrections to the Born term: $q + (\bar{q}) \to \gamma^*$.

The LO cross section is finite, however NLO QCD corrections give rise to infrared, ultraviolet, and collinear singularities. To handle them a regularization procedure is needed. The detailed computation of the NLO Drell-Yan cross section can be found in [81]. The full expression for the Drell-Yan cross section at NLO is given in [82].

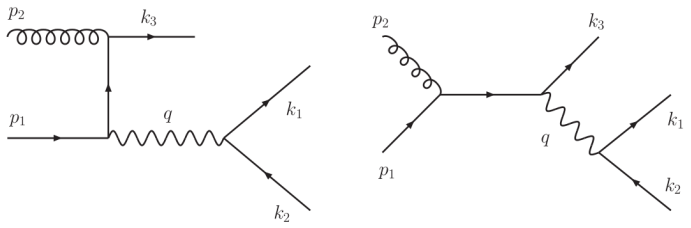

Figure 2.8: Gluon-quark subprocess at NLO in pQCD, $g+q(\bar{q}) \to \mu^+ + \mu + q(\bar{q})$, in Drell-Yan dilepton production.

Drell-Yan NLO subprocesses		
	$q + (\bar{q}) \to \gamma^*$	one-loop (virtual) correction
α_s	$q + \bar{q} \to \gamma^* + g$	
	$g + q(\bar{q}) \to \gamma^* + q(\bar{q})$	

Table 2.3: List of subprocesses in Drell-Yan dilepton production at NLO.

Drell-Yan dilepton production is an essential process to test the Standard Model (SM) in an accurate way at hadron colliders, since it has a large cross section, a clean experimental signature, and it is very sensitive to the properties of the gauge bosons. It is also a fundamental tool for the extraction of the (n)PDFs. Thus, the QCD corrections at NNLO to Drell-Yan are essential to have the precision required for present and future colliders.

The processes which contribute to the Drell-Yan cross section at NNLO in pQCD are listed in Table 2.4, where V stands for the vector boson exchanged, γ or Z^0 boson. As in the case of the NLO corrections, infrared, ultraviolet, and collinear poles show up. A regularization procedure is used and the divergent part is absorbed into the parton densities. For the results for Drell-Yan dilepton production at NNLO see [83, 84].

Drell-Yan NNLO subprocesses		
	$q + (\bar{q}) \to V$	two-loop (virtual) correction
	$q + \bar{q} \to V + g$	one-loop correction
	$q + \bar{q} \to V + g + g$	
α_s^2	$q + \bar{q} \to V + q + \bar{q}$	
	$g + q(\bar{q}) \to V + q(\bar{q})$	one-loop correction
	$g + q(\bar{q}) \to V + q(\bar{q}) + g$	
	$q(\bar{q}) + q(\bar{q}) \to V + q(\bar{q}) + q(\bar{q})$	
	$g + g + \to V + q + \bar{q}$	

Table 2.4: List of subprocesses in Drell-Yan dilepton production at NNLO.

2.4 Treatment of heavy-flavor

So far in this thesis, the assumption that all the quarks are massless has been made. Nonetheless, the appropriate treatment of heavy quarks in global analysis is essential for the precision demanded by current hadron colliders [95].

The zero-mass limit for all the partons is considered a good approximation at virtualities far above all quark mass thresholds, denoted by m_i: $Q \gg m_i$. This obviously does not hold when $Q \leq m_i$. A consistent treatment of heavy quark mass effects in pQCD over the whole energy range, from $Q \leq m_i$ to $Q \gg m_i$, is mandatory.

Dealing with heavy quarks in pQCD is a delicate task. Traditionally, there have been two kinematical regimes where this treatment could be simplified: the regime where $Q^2 \leq m_Q$ and the one where $Q^2 \geq m_Q$, being m_Q the mass of the heavy quark. These two regions correspond to the two bounded regimes between which all the current heavy quark schemes try to interpolate. These are, respectively the *Fixed Flavor Number scheme* (FFNS) and the *Zero-Mass Variable Flavor Number scheme* (ZM-VFNS). For simplicity, a theory with n_f light flavors and a single heavy quark with mass m_Q will be considered.

2.4.1 The FFN and ZM-VFN schemes

The simplest scheme adopted to include heavy quark effects in global analysis is the *Fixed Flavor Number scheme* (FFNS). The assumption made is that all the partons in the theory are the n_f light quarks, considered as massless, and the gluons. Indeed, the initial state nucleon is assumed to not to have heavy quark component, which is treated as a final state particle. Unfortunately, this model becomes unreliable when the scale of the hard process, Q, becomes larger than the mass of the heavy quark, m_Q. In this scheme, when the factorization and the renormalization scales are $\mu_r = \mu_f = \mu$, the DIS structure function in the $\overline{\text{MS}}$ factorization scheme can be written as,

$$F^{\lambda}\left(n_f, m_H^2, Q^2\right) = \sum_i^{n_f} C_i^{\lambda}\left(n_f, \frac{Q^2}{m_Q^2}, \frac{\mu^2}{m_Q^2}, \frac{Q^2}{\mu^2}\right) , \tag{2.4.49}$$

where the sum is only over light quark flavors. This structure function can be divided in two components: F^L, the one where only light flavors are present, and F^H, which includes the contribution of the final state heavy quark.

$$F(n_f, Q^2, m_Q^2) = F^L(n_f, Q^2) + F^H(n_f, Q^2, m_Q^2) , \tag{2.4.50}$$

where

$$F^L(n_f, Q^2) = \sum_i^{n_f} L_i\left(n_l, \frac{Q^2}{\mu^2}\right) \otimes f_i(n_f, \mu^2) , \tag{2.4.51}$$

$$F^H(n_f, Q^2, m_Q^2) = \sum_i^{n_f} H_i\left(n_f, \frac{Q^2}{m_Q^2}, \frac{\mu^2}{m_Q^2}, \frac{Q^2}{\mu^2}\right) \otimes f_i(n_f, \mu^2) . \tag{2.4.52}$$

Here the Wilson coefficients including heavy quark lines are denoted by H, and L are the diagrams that do not.

The expression (2.4.49) is reliable in the heavy quark mass threshold region and below. In this scheme, the Wilson coefficients contain unresummed logarithms of the ratio Q^2/m_Q^2 which can become large at scales much larger than the heavy quark mass.

In the *Zero-Mass Variable Flavor Number* (ZM-VFN) prescription these problems are solved by treating the heavy quark as a massless parton above its mass threshold. That is that the parton distribution of the heavy quark remains zero if $Q^2 \leq m_Q^2$, but it follows DGLAP evolution when $Q^2 > m_Q^2$. The renormalization of the heavy quark PDF resums all the logarithms via the DGLAP equations. Thus, the number of flavors is increased by one when crossing the heavy quark mass threshold in this approach. In the ZM-VFN the structure function is

$$F(n_f+1,x,Q^2) \;=\; \sum_i^{n_f+1} C_i\left(n_f+1,\frac{Q^2}{\mu^2}\right)\otimes f_i(n_f+1,\mu^2)\;. \tag{2.4.53}$$

This method solves the problems that arises at large scales in FFNS. However, the treatment of heavy quarks is made only in terms of massless partons: it completely ignores the massive contributions to the Wilson coefficients. Hence, it is not accurate when the powers m_Q^2/Q^2 are significant. Despite the simplicity of the procedure, it has been used in several global analysis [90, 96].

2.4.2 GM-VFN schemes

The *General Mass Variable Flavor Number schemes* (GM-VFNS) have been developed in order to avoid the shortcomings of both the FFN and ZM-VFN schemes. In such approaches the treatment of heavy quarks is usually reduced to the FFN scheme at low scales and the ZM-VFNS procedure at high scales, with some interpolation between these two regions. The GM-VFN schemes require that the ZM-VFN and FFN calculations coincide at large scales, where the heavy quark mass dependence of the FFN Wilson coefficients can be neglected,

$$F^L(n_f,Q^2)+\lim_{Q^2\gg m_Q^2}\left[F^H(n_f,Q^2,m_Q^2)\right] \;=\; F(n_f+1,x,Q^2)\;. \tag{2.4.54}$$

This constraint implies that the PDFs in the two schemes need to be related by a perturbatively computable transformation:

$$f_i(n_f+1,\mu^2)=\sum_j^{n_f} A_{ij}\left(n_f,\frac{\mu^2}{m_Q^2}\right)\otimes f_j(n_f,\mu^2)\;, \tag{2.4.55}$$

where the A's are not square matrices: i runs over the n_f+1 partons in the ZM-VFNS, and j runs over the n_f partons in the FFNS. These matrices have been determined up to NNLO

in α_S in Refs. [97, 98].

In practice, the GM-VFN schemes are chains of FFN-type schemes with increasing n_f as the scale increases over each quark mass threshold, requiring the physical observables to be continuous across these thresholds. The matching condition at the heavy quark mass threshold for the structure function is

$$F^{\rm GM}(m_Q^2) \;=\; \sum_j^{n_l} C_j^{\rm FF}\left(n_f, m_Q^2\right) \otimes f_j(n_f) \;=\; \sum_i^{n_f+1} C_i^{\rm VF}\left(n_f+1, m_Q^2\right) \otimes f_i(n_f+1) \;. \quad (2.4.56)$$

Introducing Eq. (2.4.55) in Eq. (2.4.56) one gets:

$$C_j^{\rm FF}\left(n_f, m_Q^2\right) \;=\; \sum_i^{n_f+1} C_i^{\rm VF}\left(n_f+1, m_Q^2\right) \otimes A_{ij}\left(n_f, m_Q^2\right) \quad , \quad (2.4.57)$$

which is the minimal GM-VFN scheme [99]. This last relation has to be satisfied order by order in α_s. To illustrate this, let us consider Eq. (2.4.57) at NLO for the gluon:

$$C_g^{\rm NLO}(n_f+1, m_Q) \;=\; C_g^{\rm NLO}(n_f, m_Q) - C_H^{\rm LO}(n_f+1, m_Q) \otimes A_{Hg}^{\rm LO}(n_f, m_Q^2) \;. \quad (2.4.58)$$

This is the expression used to define the original ACOT (M. A. G Aivazis, J. C. Collins, F. I. Olness, and W. K. Tung) scheme [100]. The rightmost term on the r.h.s. of Eq. (2.4.58) when moved to the l.h.s. is known as the *subtraction term* and allows to define the coefficient $C_g^{\rm NLO}(n_f, m_Q)$ in the ACOT scheme. The subtraction term allows the elimination of the IR-unsafe logarithms present in the FFN approach.

However, there is ambiguity to define different GM-VFNS, which has resulted in the existence of several prescriptions. This freedom of definition comes from the existence of terms proportional to powers of m_Q/Q that can be interchanged between the Wilson coefficients in Eq. (2.4.58) without changing the final value of the physical observable, i.e., of the structure function. The already-mentioned ACOT scheme does not try to exploit this degeneracy. The Simplified ACOT scheme, or S-ACOT [101, 102], chooses a much simpler prescription of the GM-VFNS. In the S-ACOT calculation the heavy-quark-initiated subprocesses are chosen to be equal to the ZM formulae. Therefore, only the full m_Q-dependent contributions from the light-parton-initiated contributions have to be computed. Another choice is the TR type schemes by R. S. Thorne and R. G. Roberts [103, 104], which also require the scale derivatives of heavy flavor structure functions, $dF_2/d\ln Q^2$, to be continuous at the transition point. More recent refinements to this prescription can be found in Refs. [105–107].

Let us summarize the TR prescription in [107] since it is the one implemented in our global analysis. It has been shown that the choice of coefficient functions removes the ambiguity in defining a GM-VFNS. However, there are additional ambiguities: the ordering of $F_2^H(x, Q^2)$ is different for the n_f and n_f+1 regions. This is illustrated in the following table where the

expressions order by order both below and above the heavy quark mass threshold are shown.

	n_f-flavor	n_f+1-flavor
LO	$\frac{\alpha_s}{4\pi} C_{2,Hg}^{FF,1} \otimes g^{n_f}$	$C_{2,HH}^{VF,0} \otimes (h+\bar{h})$
NLO	$\left(\frac{\alpha_s}{4\pi}\right)^2 (C_{2,Hg}^{FF,2} \otimes g^{n_f} + C_{2,Hq}^{FF,2} \otimes \Sigma^{n_f})$	$\frac{\alpha_s}{4\pi} (C_{2,HH}^{VF,1} \otimes (h+\bar{h}) + C_{2,Hg}^{VF,1} \otimes g^{n_f+1})$
NNLO	$\left(\frac{\alpha_s}{4\pi}\right)^3 \sum_i C_{2,Hi}^{FF,3} \otimes f_i^{n_f}$	$\left(\frac{\alpha_s}{4\pi}\right)^2 \sum_j C_{2,Hj}^{VF,2} \otimes f_j^{n_f+1}$

Being h the parton distribution function of the heavy quark. This means that switching directly from a fixed order with n_f active quarks to a fixed order with n_f+1 active quarks leads to a discontinuity in $F_2^H(x,Q^2)$. ACOT scheme uses the same order of α_s above and below the transition point, for instance, at NLO

$$\frac{\alpha_s}{4\pi} C_{2,Hg}^{FF,1} \otimes g^{n_f} \to C_{2,HH}^{VF,0} \otimes (h+\bar{h}) + \frac{\alpha_s}{4\pi} (C_{2,HH}^{VF,1} \otimes (h+\bar{h}) + C_{2,Hg}^{FF,1} \otimes g^{n_f+1}) \ . \quad (2.4.59)$$

Then, the structure function is automatically continuous. However, as $C_{2,Hg}^{FF,1}$ contains only information on P_{qg}^0 not on P_{qg}^1, there is effectively LO evolution below the heavy quark mass threshold and NLO evolution above it. Hence, the slope $d\,F_2^H(x,Q^2)/d\,\ln Q^2$ is discontinuous. In the TR scheme [103, 104] – and all its revisions – has the same order above and below the transition point is used, but it adds a term independent of Q^2 above the transition point to preserve the continuity of the structure function

$$\frac{\alpha_s(Q^2)}{4\pi} C_{2,Hg}^{FF,1}(Q^2/m_Q^2) \otimes g^{n_f}(Q^2) \to \frac{\alpha_s(M^2)}{4\pi} C_{2,Hg}^{FF,1}(1) \otimes g^{n_f}(M^2) + C_{2,HH}^{VF,0}(Q^2/m_Q^2) \otimes (h+\bar{h})(Q^2) \ . \quad (2.4.60)$$

The $\mathcal{O}(\alpha_s)$ term is frozen through $Q^2 = m_Q^2$. Consequently, the definition of the ordering is consistent within each region, except for the addition of a constant term above $Q^2 = m_Q^2$ which does not affect the evolution. This implies that in order to implement a GM-VFNS at NNLO ,$\mathcal{O}(\alpha_s^3)$ heavy-flavor coefficient functions are needed for $Q^2 \leq m_Q^2$ and that their contribution will be frozen for $Q^2 \geq m_Q^2$.

The heavy-flavor Wilson coefficients for DIS have been computed up to two-loop order in [108–110]. Recently, $\mathcal{O}(\alpha_s^3)$ contributions to these coefficients have been computed in the asymptotic region of large momentum transfer, i.e. for $Q^2 \gg m_Q^2$ [111, 112]. The full expressions up to two-loop corrections and the asymptotic ones at three loops have been implemented in our code. The massive Wilson coefficients of F_2, F_L and F_3 for charged-current DIS in the same limit can be found in [113, 114]. Most of the expressions regarding the heavy-quark treatment cannot be analytically transformed into Mellin space, hence, we have pre-evaluated their momenta and saved them in grids to be read as needed.

2.5 Mellin evolution

In Section 2.1, the DGLAP evolution equations, Eqs. (2.1.13) and (2.1.12), were presented. These integro-differential equations cannot be solved analytically in the x-space. Because of

this, several techniques to accomplish a numerical solution have been developed.

Some of the most common methods employed to solve numerically the DGLAP equations in the x-space will be introduced in the following, playing special attention to the Mellin-evolution, that is the approach used in this thesis.

As it was already indicated, solving the DGLAP equations in the x-space analytically is impossible. One way to deal with this in the *force-brute* method [85, 86]. This consists in discretizing the equation by a finite difference method. The code is very simple, however, the computation time is large due to the large number of steps (in x and in t) required in order to obtain an accurate evolution. This method was very popular in the 90's.

The Laguerre technique [87] is one of the fastest methods. Splitting functions and PDFs are expanded in terms of Laguerre polynomials. The DGLAP equations turn out to be a simple summation of Laguerre-expansion coefficients, so, it is a very efficient numerical method. This method has some disadvantages. First, obtaining an accurate evolution at large x is not easy. And, second, since the Laguerre polynomials $L_n(-\ln x)$ diverge when x goes to zero, it could have convergence issues in the small x region, which is an important region in high-energy physics.

One of the most established approaches nowadays in the x-space is given by the QCD evolution package HOPPET [88]. The splitting functions are represented by their convolution with a set of piecewise polynomial basis functions. Then, Runge-Kutta techniques are used for the evolution in Q^2. Good speed and accuracy are obtained by this method. Another popular method is a semianalytical one involving the construction of an evolution operator expressed in form of a rapidly convergent series of matrices, depending only on the splitting functions [89]. This technique is used, for example, in EPS09 NLO nPDFs [90].

The Mellin transformation method is one of the most popular evolution techniques. As it was said in the previous section, the DGLAP equations, Eqs. (2.1.13) and (2.1.12), contain a Mellin convolution. When a Mellin transform is applied to these equations, their right-hand side becomes a simple multiplication of two (Mellin) moments: the moment of the splitting functions, and the moment of the distribution functions (see Appendix A). Therefore, using the Mellin technique, the DGLAP integro-differential equations in x-space are converted into ordinary differential equations that can be solved analytically to all orders. The main inconvenient of this method is that the functional form of the parton distribution functions at the initial scale, Q_0, is restricted to have an easily computed Mellin moment.

In general lines the application of this method to global analysis is the following:

- The (n)PDFs at the initial scale are parametrized in x-space and then the Mellin transform is performed. Flexible polynomial forms are used for the parton distributions at the initial scale in order to be able to calculate their Mellin moments easily.

- The evolution of the (n)PDFs from the initial scale, Q_0, to the scale of the experiment, $Q > Q_0$, is also done in the moment-space. The moment of the splitting functions – *anomalous dimensions* – are well known up to NNLO [56,57]. Then, obtaining an analytic solution for the DGLAP evolution equations in the Mellin-space is straightforward.

- Once the data to be used have been chosen, the corresponding observables (cross-sections or structure functions) are computed in Mellin space. In the particular case of contributions that cannot be analytically transformed into momentum space, we pre-evaluated the momenta and saved them in grids to be read as needed. The principal advantage of this is that all the time-consuming integrations are already dealt with in the determination of the perturbative cross sections. Then, thanks to factorization (see Section 1.2) the theoretical observable can be calculated (in moment-space). Usually, DIS experimental data are in terms of the structure functions, so, instead of the cross sections, the structure functions are used. As it was shown in previous sections, the structure functions are written in terms of the Wilson coefficients and the parton distribution functions. Because of this, the expressions at NNLO for the Wilson coefficients in Mellin-space have to be computed.

- A Mellin inversion of the total cross section is performed to go back to x-space and obtain the theoretical prediction of the observable.

- Finally, a χ^2-distribution is built and the value of the parameters is found iteratively minimizing the χ^2.

In Appendix A, further details about the Wilson coefficients in moment-space and the anomalous dimensions can be found. The Mellin inversion is also explained in this appendix.

As it was mentioned, the DGLAP equations can be solved analytically in Mellin-space. The non-singlet DGLAP equation has an analytical exact solution at NNLO, which is derived in Section 8 of [91]. Regarding the singlet (and gluon) equations, there are no exact solutions in moment-space beyond those known at LO. However, a solution can be constructed using a logarithmic ansatz. This logarithmic series can be improved in order to capture higher order contributions in the truncated solution, a feature that can be very appealing for phenomenological purposes [91]. In our case, the higher order logarithmic approximation of the NNLO singlet solution is used, see Section 10 of [91]. This solution has corrections of $\mathcal{O}(\alpha_s^3)$ in the evolution, but the anomalous dimensions used go up only to $\mathcal{O}(\alpha_s^2)$. Using $\mathcal{O}(\alpha_s^3)$-terms in the evolution improves the result comparing to the one truncated at $\mathcal{O}(\alpha_s^2)$. To see the expression of this solution see Section 10 of [91]. In summary, we have implemented from scratch in our code the exact solution of the DGLAP equations at NNLO in pQCD for the non-singlet and the truncated evolution of the singlet including these $\mathcal{O}(\alpha_s^3)$-terms. This implies that all the expressions of the anomalous dimensions at NNLO in pQCD have also

been implemented.

Our evolution, both for the non-singlet and the singlet sectors, has been successfully cross-checked with the evolution code QCD-PEGASUS [92]. QCD-PEGASUS results have been carefully cross-checked up to $Q^2 = 10000\,\mathrm{GeV}^2$ with [93]. In Figs. 2.9, 2.10, 2.11, and 2.12, free-proton PDFs are plotted versus x for $Q^2 = 1\,\mathrm{GeV}^2$, $Q^2 = 10\,\mathrm{GeV}^2$, $Q^2 = 100\,\mathrm{GeV}^2$, and $Q^2 = 10000\,\mathrm{GeV}^2$, respectively. Black points correspond to MMHT2014 NNLO free-proton PDFs [94], whose evolution is given by QCD-PEGASUS [92]. The different curves represent our evolution for $A = 1$, that is, for the proton, whose PDFs have been parametrized according to MMHT2014 at the initial scale $Q_0^2 = 1\,\mathrm{GeV}^2$. Dashed lines correspond to a Mellin contour given by 144 moments and $\phi = 3\pi/4$. The different colors stand for the different values of the parameter c: black $c = 1$, red $c = 0.9$, green $c = 0.8$, and blue $c = 0.7$ (see Appendix A). For continuous lines, the same criteria apply, but, in this case, the contour is given by 136 Mellin-moments. As it can be seen in these figures, there is a good agreement between our evolution and the one given by QCD-PEGASUS [92] in the wide range in virtuality considered [4].

In order to choose the most appropriate Mellin contour, we plot in Fig. 2.13 the ratio of the curves in Fig. 2.9. The same color criterion has been employed. As it can be seen in Fig. 2.13 the agreement between our evolution and that of QCD-PEGASUS [92] is excellent. Only at very large and very low x, some discrepancies arise. On the one hand, in the (very) large-x region, parton densities are numerically very small, typically falling as $(1-x)^\beta$ with $\beta \geq 3$. Moreover, in this region there are not any experimental data which could constrain the PDFs. On the other hand, at low-x, deviations show up for $x \leq 10^{-4}$. However, there are no data constrains at all in nPDFs fits for $x \leq 10^{-3}$. Hence, all the available sets in this region are model-dependent, since the nPDFs at low-x are mostly extrapolations which depend on the chosen parametrization. Taking into account the current level of precision of nPDF analysis, the differences that arise in the evolution in this region are negligible. The Mellin contour that was finally implemented in our code is that corresponding to the dashed blue line, i.e., the values $\phi = 3\pi/4$ and $c = 0.8$ and 144 Mellin-moments are taken.

[4] In Figs. 2.9, 2.10, 2.11, and 2.12, our evolution of charm and bottom PDFs are plotted compared to that obtained by MMHT2014 global analysis [94], where the GM-VFNS in the TR scheme was also employed.

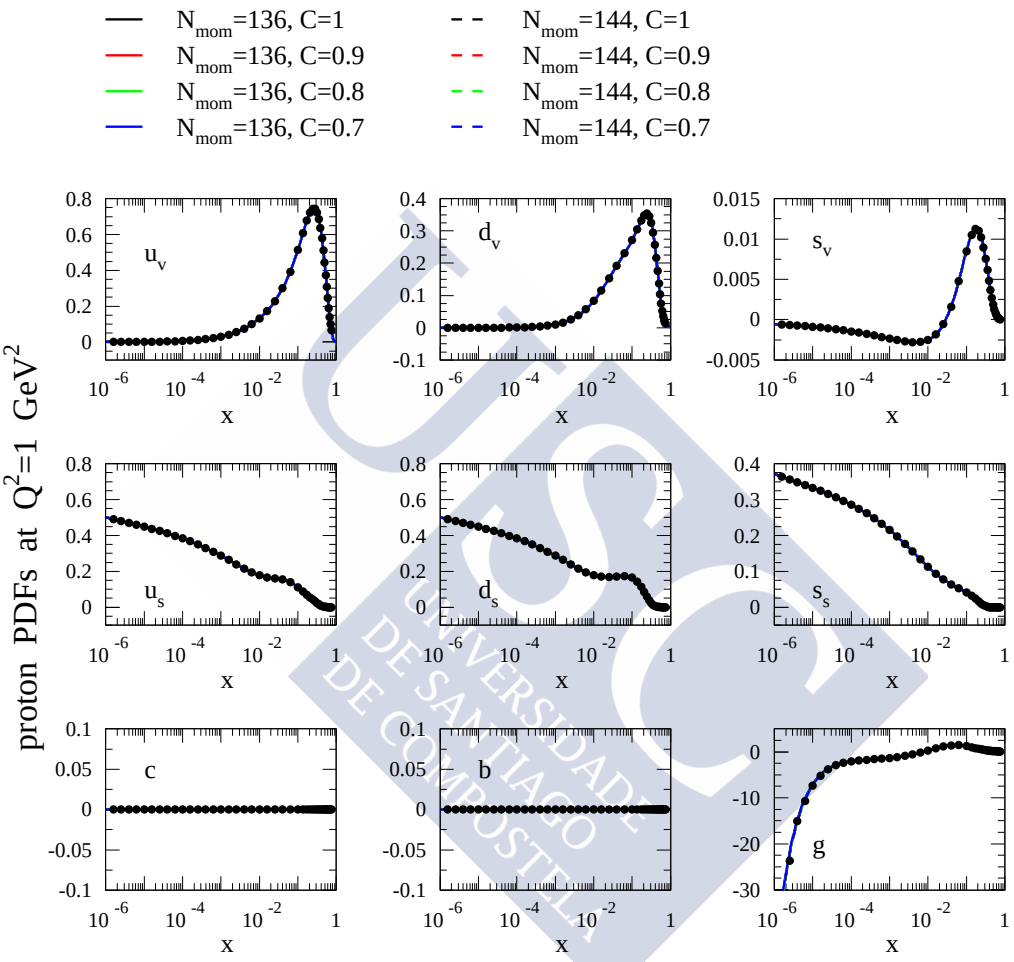

Figure 2.9: NNLO-evolution at $Q^2 = 1\,\mathrm{GeV}^2$ for the different PDFs versus x. Dashed lines correspond to 144 Mellin-moments and continuous lines to 136. Different colors correspond to the different values of the parameter c: black $c = 1$, red $c = 0.9$, green $c = 0.8$, and blue $c = 0.7$ (see Appendix A). Black points correspond to MMHT2014 NNLO free-proton PDFs [94].

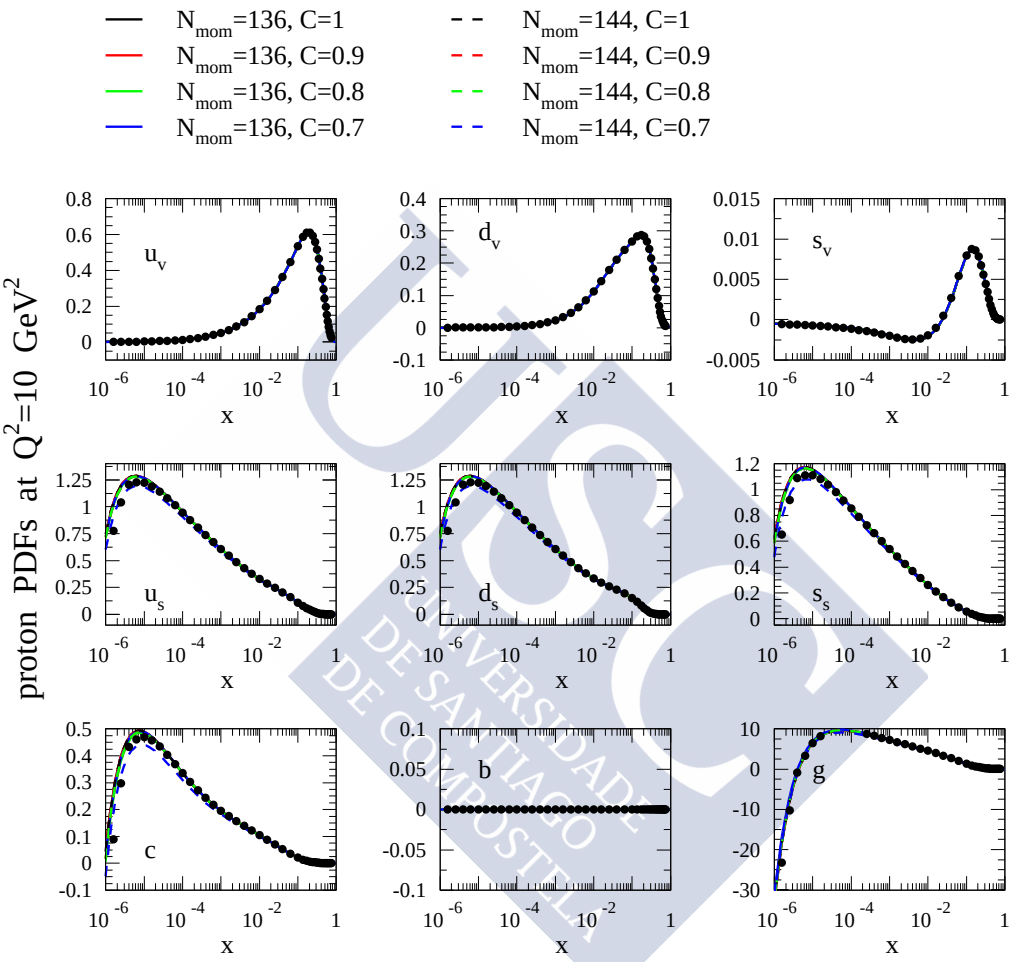

Figure 2.10: NNLO-evolution at $Q^2 = 10\,\mathrm{GeV}^2$ for the different PDFs versus x. Dashed lines correspond to 144 Mellin-moments and continuous lines to 136. Different colors correspond to the different values of the parameter c: black $c = 1$, red $c = 0.9$, green $c = 0.8$, and blue $c = 0.7$ (see Appendix A). Black points correspond to MMHT2014 NNLO free-proton PDFs [94].

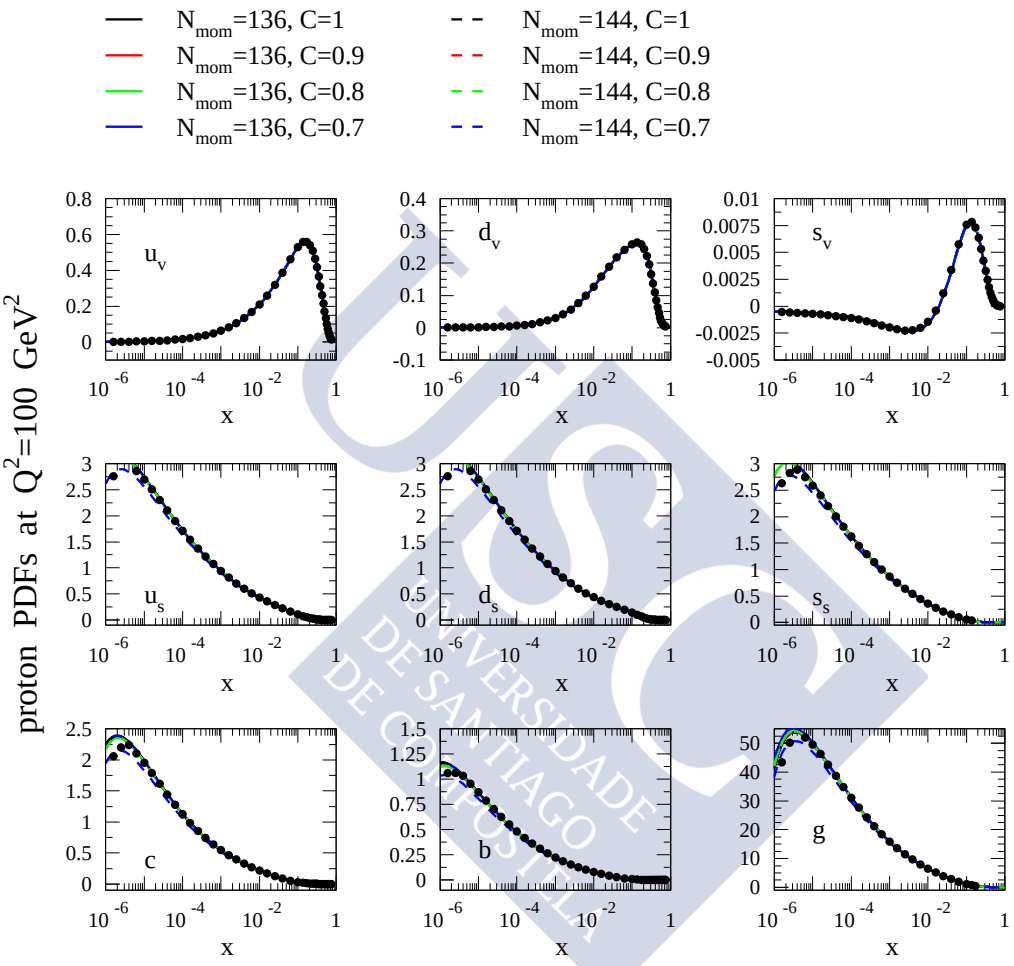

Figure 2.11: NNLO-evolution at $Q^2 = 100\,\mathrm{GeV}^2$ for the different PDFs versus x. Dashed lines correspond to 144 Mellin-moments and continuous lines to 136. Different colors correspond to the different values of the parameter c: black $c = 1$, red $c = 0.9$, green $c = 0.8$, and blue $c = 0.7$ (see Appendix A). Black points correspond to MMHT2014 NNLO free-proton PDFs [94].

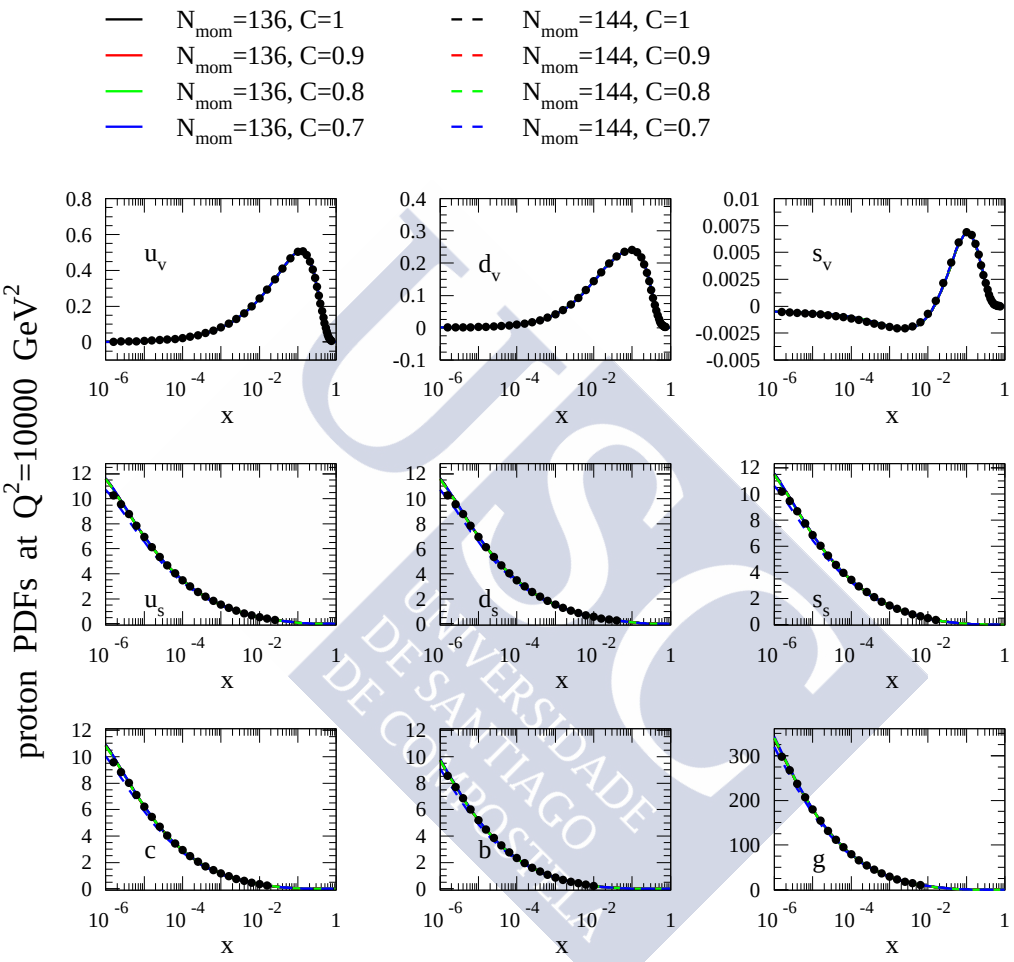

Figure 2.12: NNLO-evolution at $Q^2 = 10000\,\mathrm{GeV}^2$ for the different PDFs versus x. Dashed lines correspond to 144 Mellin-moments and continuous lines to 136. Different colors correspond to the different values of the parameter c: black $c = 1$, red $c = 0.9$, green $c = 0.8$, and blue $c = 0.7$ (see Appendix A). Black points correspond to MMHT2014 NNLO free-proton PDFs [94].

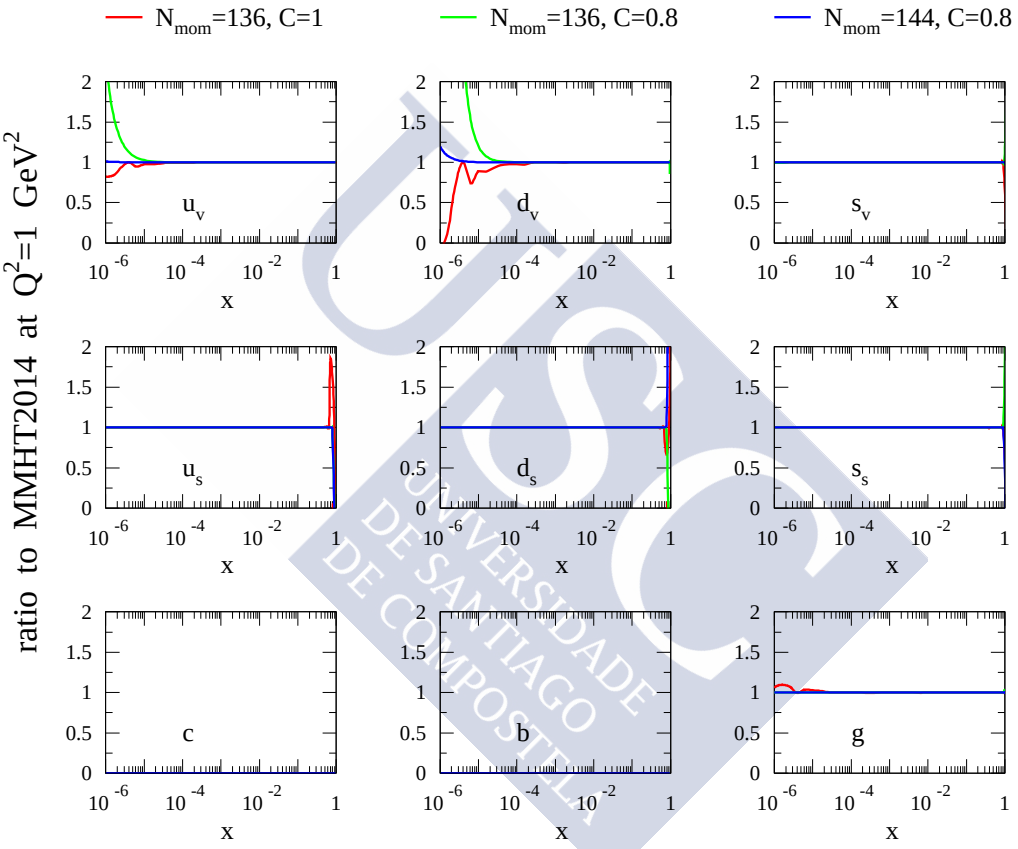

Figure 2.13: Ratios of NNLO-evolution at $Q^2 = 1\,\mathrm{GeV}^2$ for the different PDFs – same order than in previous plots – versus x. The red curve corresponds to $c = 1$ and $N = 136$, the green curve to $c = 0.8$ and $N = 136$, and the blue one to $c = 0.8$ and $N = 144$. (see Appendix A). Black points correspond to MMHT2014 NNLO free-proton PDFs [94].

2.6 Nuclear parton distribution functions

So far in this thesis, all the formalism presented – except if indicated – was valid both for free parton distribution functions (PDFs) and parton distribution functions in nuclear media (nPDFs). However, are the nuclear bounding effects in nPDFs significant? Could the nucleus be considered as a sum of almost free nucleons and therefore the quarks (and gluon) distributions almost unmodified by the nuclear medium? Until the 1980's the bounding effects due to the nuclear medium were considered negligible, especially because the energy scale of the DIS experiments at that time was much higher than the characteristic nuclear scales. Nevertheless, in the 1982 the European Muon Collaboration presented the data on F_2^{Fe}/F_2^d changing radically this perception [115], see Fig. 2.14.

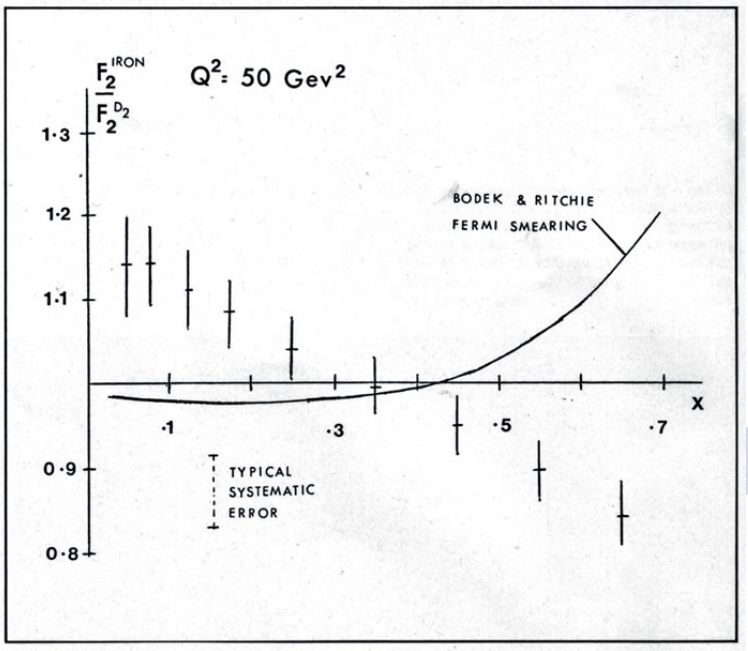

Figure 2.14: F_2^{Fe}/F_2^d vs. x measured by the European Muon Collaboration [115].

Nuclear effects in DIS are often studied by comparing the structure function of the nucleons in the nucleus A, F_2^A, with respect to deuterium, F_2^d. Nucleons in deuterium are usually considered as approximately free, although some nuclear effects exist [116]. The EMC collaboration showed that F_2^{Fe} was different from F_2^d and, hence, nuclear effects in nPDFs cannot be neglected, as it can be seen in Fig. 2.14. This compelling breakthrough was confirmed by many collaborations; for instance, SLAC [117], Fermilab [118] and the New Muon collaboration (NMC) at CERN [119, 120]. The conclusions from the combined experiments were: the shape of the effect was universal, independent of the virtuality of the process Q^2, increased with the nuclear mass number A, and scaled with the average nuclear density. The typical shape for F_2^A/F_2^d is illustrated in Fig. 2.15.

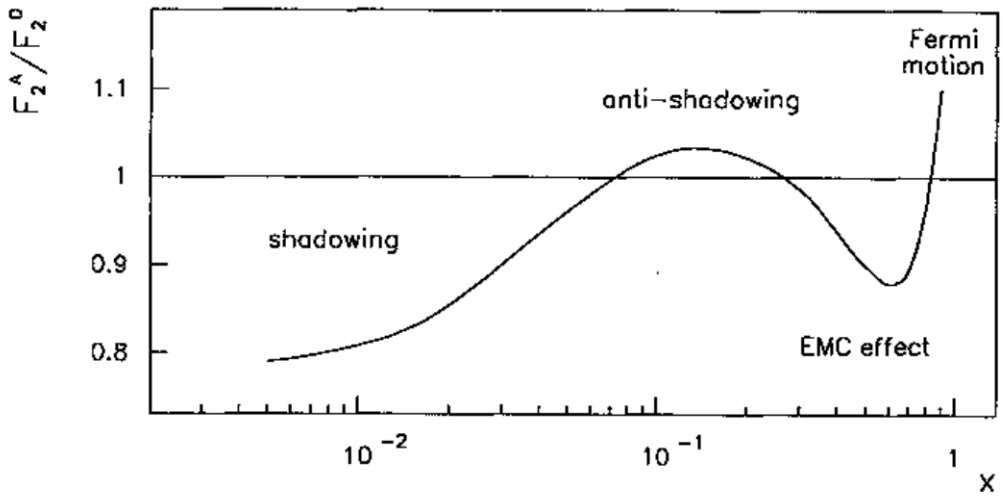

Figure 2.15: Schematic representation of F_2^A/F_2^d vs. x.

As it can be seen in Fig. 2.15, the nuclear effects can be classified in different x-regions:

- *Shadowing.* It is the reduction of the ratio F_2^A/F_2^d with respect to 1 that appears at low x, $x \lesssim 0.07$.

  Partonic distributions are dominated in this region by sea quarks and gluons. The depletion of the nuclear ratios is often related with the hadronic behavior of the virtual photon [121]. This resolved hadronic component of the photon wave function at high collision energies – or, equivalently, small-x –, interacts several times with the different nucleons in the nucleus, i.e., experiences *multiple scattering*. This results into a reduction of the corresponding cross sections – shadowing – and, therefore in the structure functions. For a review of multiple scattering as the underlying mechanism of shadowing see [122] and references therein.

  Other models that try to explain this effects, are the *partonic models*. In these frameworks the shadowing is considered as the consequence of the decrease of the total number of partons at low x, see, for example [123]. In the Breit or infinite momentum frame, the low-x partons are dispersed at large distances – according to the uncertainty principle. Thus, the fusion among partons from different nucleons decreases the number of partons at low x – and increases the number at high x.

- *Anti-shadowing.* It is the region $0.05 \lesssim x \lesssim 0.3$ where $F_2^A > F_2^d$.

  The phenomenon of anti-shadowing is less understood than the one of shadowing. In some models, it is a direct consequence of shadowing (see for instance [124]), in others, it is discussed as coming from the application of sum rules for momentum [125].

- *EMC effect.* For $0.3 \lesssim x \lesssim 0.8$, F_2^A/F_2^d decreases reaching a minimum at $x \sim 0.6$ and then increases again.

  The EMC effect suggests that in the region where $0.3 \lesssim x \lesssim 0.8$ – dominated by valence quark distributions for DIS – the valence quark distribution of free nucleons is larger than the one of bound nucleons. Many models successfully explain this phenomenon: nuclear binding or pion cloud effects [126, 127]; combinations of various different models [128]; and two-nucleon short-range correlations [129].

- *Fermi-motion.* For $x \gtrsim 0.8$, $F_2^A/F_2^d > 1$.

  Nucleons in nuclei move with an average momentum of k_F. For nuclear experimental data, the x variable is determined in the approximation that the nucleon is at rest. In consequence, the experimental measured structure function F_2 in case of nuclear DIS is the convolution of the structure function, F_2, of a free nucleon and the momentum distribution of the nucleon in the nucleus. However, since there are no data in the region of high x, global analysis impose to the nuclear parton distributions, f_i^A: $f_i^A \to 0$ and $f_i^A/f_i \to L$, where $L \gg 1$ when $x \to 1$.

2.7 A-Z Global analysis

In this section my work in collaboration with Dr. Pia Zurita (Brookhaven National Laboratory, Upton, NY) is presented. We have performed a global analysis in QCD of collinearly factorized nuclear parton distribution functions and their uncertainties. In this analysis, available data of charged-lepton deep inelastic scattering as well as neutrino deep inelastic scattering are included. The global fit is done at NNLO in pQCD, which means that all the observables are calculated at NNLO, as explained in Section 2.2, and that also the evolution is performed at NNLO in QCD, see Sections 2.1 and 2.5. LHC data are not included in this study. However, several articles have indicated the constraining power of these recent measurements at the LHC [130, 131] in the context of reweighting [132–135], and a new global analysis of nPDFs at NLO, EPPS16, has recently incorporated them [136]. In the present work, Drell-Yan experimental results on the structure functions are being implemented and will be presented in a forthcoming publication. The treatment of heavy quarks follows the GM-VFNS approach explained in Section 2.4. This is the first global analysis of nPDFs performed at NNLO within the GM-VFN scheme [5]. The analysis is performed using the Hessian method, that will be explained, together with the estimation of the uncertainties, in Subsection 2.7.3.

The extraction of nPDFs from experimental data is fundamental for the understanding of nuclear modifications outlined in the previous section. On the other hand, nuclear parton distributions are essential for the analysis of a wide variety of nuclear experiments, such as heavy ion collisions at the Large Hadron Collider (LHC) and at the Relativistic Heavy-Ion

[5] There is a previous set of NNLO nPDFs [96], but the simplistic ZM-VFNS is used.

Collider (RHIC). Moreover, the precise knowledge of nPDFs will be mandatory for future colliders, as the EIC and the LHeC. In the last few years, there has been a lot of improvement on the determination of nPDFs, both from the experimental and the theoretical sides. Furthermore, global fits also permit to study the range of applicability of the factorization theorems [19, 20] and the universality of nPDFs. Finally, free-proton global fits make use of neutrino-nucleus DIS data in order to study flavor decomposition, hence, nPDFs are needed also in free-proton PDFs analysis.

However, nPDFs are much less known than free proton PDFs, especially due to the wider diversity of data – that cover a larger kinematical range – available for the proton community, as it can be seen in Fig. 2.16. Nowadays, the available nuclear (charged-lepton) DIS data go from $x \approx 0.01$ to $x \approx 1$ and they are often a ratio of the structure function of the studied nucleus, A, with respect to the structure function of deuterium – or sometimes from another nucleus B. These data are basically sensitive to the valence quarks, though for $x \lesssim 0.01$ some sensitivity to the sea quarks arises. Gluons are almost not constrained by DIS – and DY – experiments. Many analysis such as HKN07 [137], EPS09 [90], DSSZ12 [138], nCTEQ15 [139], and the recent EPPS16 [136], have included among their data inclusive pion production in d-Au collisions at RHIC [140, 141], since this observable has a potential to better constrain the gluon distribution. However, inclusive pion data are different to the previous mentioned sets – DY, and neutral and charged current DIS – in the sense that they have an additional dependence on the fragmentation functions. As the parton-to-pion fragmentation functions may experience a nuclear modification [21], the interpretation of the inclusive pion production observable is nowadays ambiguous. That is the reason why this observable has not been included in our analysis so far.

With respect to neutrino DIS experiments, they may be helpful to constrain light quark flavor, since they provide an electroweak observable. These data have been controversial in the past, as it appeared to show some tension with (charged-lepton NC) DIS data [143]. Nonetheless, this seemed to be mostly a normalization issue and neutrino data have been employed in DSSZ12 [138] and EPPS16 [136] with no difficulties.

This section is organized as follows: the parametrization employed for the nuclear modifications of PDFs is described in the next section. Then, the experimental data used in our analysis are presented. In Subsection 2.7.3 the analysis procedure is summarized and, finally, in subsection 2.7.4 our results are presented and discussed.

2.7.1 Parametrization of nPDFs

Following the typical framework used in most of the nPDFs global fits, the bound proton PDF for a mass number A and parton species i, $f_i^A(x, Q^2)$, is defined relative to the corresponding free proton PDF, $f_i^p(x, Q^2)$, as

$$f_i^A(x, Q_0^2) \;=\; R_i^A(x, Q_0^2)\, f_i^p(x, Q_0^2) \;\;, \tag{2.7.61}$$

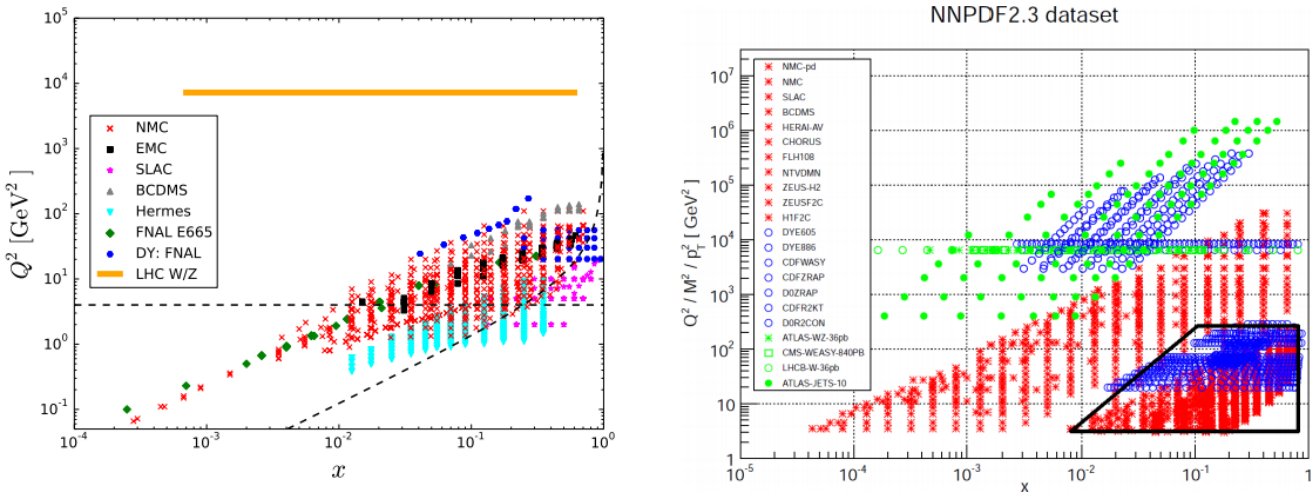

Figure 2.16: (Left panel) Typical kinematic range of data used in nPDFs global analysis. (Right panel) Typical kinematic range employed in free-proton global analysis. Figures taken from [142].

where $R_i^A(x, Q_0^2)$ denotes the nuclear modification. Our free proton baseline is MMHT2014 NNLO [94], which is defined in a GM-VFNS to deal with heavy quark mass effects. Consistently, we adopt the same prescription for the treatment of heavy quark effects.

The nPDFs are then obtained by Eq. (2.7.61) at an initial scale of Q_0 by determining the nuclear modification factors, $R_i^A(x, Q_0^2)$, from the experimental data. In order to parametrize the $R_i^A(x, Q_0^2)$ in Eq. (2.7.61), we assume isospin invariance for bound protons and neutrons, that is, $u^p = d^n$, and $d^p = u^n$. Therefore, the u quark density in a nucleus A with Z protons – and $A - Z$ nucleons – at a scale Q^2 is given by

$$u_A(x, Q^2) \;=\; \frac{Z}{A}\, f_u^A(x, Q^2) + \frac{Z - A}{A}\, f_d^A(x, Q^2) \;, \tag{2.7.62}$$

and similarly for d_A , $\bar{u}_A$, and $\bar{d}_A$. In contrast to all the nPDFs sets available, except for HKN07 [137], nuclear effects in deuterium are considered here.

Due to the lack of diversity of the experimental data available, nuclear modifications for each parton flavor cannot be independently determined. At this stage, as only charged lepton and neutrino DIS data are employed in our fit, we define only three nuclear corrections at the parametrization scale Q_0: R_V^A for both valence quark distributions, R_S^A for all the sea quarks, and R_g^A for gluons. This is a standard way to proceed that has been used in many nuclear global fits, such as EPS09 [90], and DSSZ12 [138]. However, the most recent analyses, nCTEQ15 [139] and EPPS16 [136], allow some flavor separation for the valence quark distributions in the case of nCTEQ15 [139], and complete separation for the valence and some separation for the sea quarks in the case of EPPS16 [136]. Considering flavor

separation in our fit would imply a larger number of parameters and, at this stage, due to the lack of sensitivity of the implemented data, they would not be well-determined making the uncertainties huge.

Our parametrization of the nuclear corrections at the initial scale Q_0 is given by

$$\begin{aligned} R_V^A &= N_V(A) + (1 - A^{a_V})\,(1-x)^{\beta_V}\left[b(A)\,x^{\alpha_V} + c(A)\,x^{2\alpha_V} + d(A)\,x^{3\alpha_V}\right] \ , \\ R_S^A &= N_S(A) + (1 - A^{a_S})\,(1-x)^{\beta_S}\left[b(A)\,x^{\alpha_S} + c(A)\,x^{2\alpha_S} + d(A)\,x^{3\alpha_S}\right] \ , \\ R_g^A &= N_g(A) + (1 - A^{a_g})\,(1-x)^{\beta_g}\left[b_g\,x + c_g\,x^2\right] \ , \end{aligned} \tag{2.7.63}$$

where the dependencies on A of the parameters are indicated and β_g is fixed to $\beta_g = 0.1$.

In the case of $N_V(A)$, $N_S(A)$, and $N_g(A)$, the A dependencies are

$$N_i(A) \ = \ A^{\gamma_i} \qquad (i = V, S, g) \ . \tag{2.7.64}$$

The coefficients $b(A)$, $c(A)$ and $d(A)$ depend on A. The dependence on A of $d(A)$ is given by

$$d(A) \ = \ d_1\,A^{d_2} \ . \tag{2.7.65}$$

The baryon number and momentum sum rules given by Eq. (2.1.15) and Eq. (2.1.16), respectively, allows us to determine b, c, N_V, and N_g for each nucleus separately. Therefore, the latter quantities are not parametrized. Thus, we have in total 12 free parameters.

Above the initial scale, $Q > Q_0$, nuclear PDFs are obtained solving the DGLAP evolution equations with 3-loop splitting functions in the Mellin space, as explained in Sections 2.1 and 2.5. Our initial scale is $Q_0^2 = 1\,\mathrm{GeV}^2$, consistently with that of MMHT2014 NNLO [94]. The charm and bottom quark masses are respectively: $m_b = 4.75$ GeV, and $m_c = 1.4$ GeV. The factorization, μ_F, and renormalization, μ_R, scales are taken to be $\mu_F^2 = \mu_R^2 = Q^2$. The value of the strong coupling constant is set at the renormalization scale as $\alpha_s(Q_0) = 0.46797$.

2.7.2 Experimental data

In this first study we restrict ourselves to fixed-target neutral and charged current lepton-nuclei deep-inelastic scattering structure functions (or cross sections).

Regarding charged-lepton DIS, measurements from a wide variety of experiments, such as NMC [119, 120, 144, 145], SLAC139 [117], and EMC [146] are incorporated in this analysis. Guided by the free-proton baseline fit MMHT2014 [94], the kinematical cuts applied on these data are: $Q^2 \geq 2$ GeV^2 and $W^2 \geq 15\,\mathrm{GeV}^2$. These data sets – except of those referring to deuteron targets – are listed in Table 2.5, as well as the number of data points that survive our kinematical cuts and the corresponding publication reference. As it was said in the previous section, deuterium is usually considered as approximately free. In fact, only HKN07 nPDFs global analysis [137] have considered any nuclear correction to deuterium.

However, some nuclear effects exist [116] and, deuterium data have been incorporated in several free-proton PDF global fits, such as MMHT2014 [94], and NNPDF3.0 and subsequent analysis [147]. These analysis have shown the power of using deuterium data in order to separate the u and d distributions at moderate values of x [94]. Therefore, in this study, DIS on deuteron targets measurements have been incorporated. These data are shown in Table 2.6.

On the other hand, results on neutrino DIS using either lead or iron targets from CDHS [148] and CHORUS [149] collaborations, respectively, are also included. The kinematical cuts set on these data are: $Q^2 \geq 5\,\mathrm{GeV}^2$ and $W^2 \geq 25\,\mathrm{GeV}^2$, according to MMHT2014 [94]. These data are summarized in Table 2.5.

In Tables 2.5 and 2.6 the data sets employed are listed. In most of the cases the observable used is a ratio of the structure function F_2 of the nucleus A – or cross-section – with respect to that of deuterium or that of a lighter nucleus B. However, for neutrino DIS and, occasionally, for charged-lepton DIS, only measurements of the absolute structure function F_2 – or cross section – are available. This is the reason why the cuts imposed here are more restrictive – especially for charged-lepton DIS – than those used in other nPDFs global analysis which only include observables in form of ratios where higher-twist effects may cancel. The notations R^A and R'^A used in these tables designate the following observables

$$R^A = \frac{F_L^A + F_2^A \frac{4M^2x^2}{Q^2}}{F_2^A - F_L^A}\,, \tag{2.7.66}$$

$$R'^A = \frac{F_L^A}{F_2^A(1+\frac{4M^2x^2}{Q^2}) - F_L^A}\,, \tag{2.7.67}$$

where M is the mass of the nucleon.

Table 2.5: Data sets included in the present analysis (except deuterium data), listed in order of growing nuclear mass number. In the second column the observable used in our analysis is indicated, when needed the nuclear mass number is as well specified. In the third and fourth columns the number of data points that survive our kinematical cuts and their contribution to the χ^2 are – respectively – shown. In the last column the corresponding publication reference is indicated.

Experiment	Observable	N_{dat}	χ^2	Reference
DESY HERMES	$\sigma^{He(3)}/\sigma^d$	43	48.6	[150]
SLAC E-139	$\sigma^{He(4)}/\sigma^d$	2	0.7	[117]
CERN NMC 95, re.	$F_2^{He(4)}/F_2^d$	15	13.9	[119]
CERN NMC 95	$F_2^{Li(6)}/F_2^d$	14	15.8	[144]
CERN NMC 95, Q^2 dependence	$F_2^{Li(6)}/F_2^d$	132	151.0	[144]
SLAC E-139	$\sigma^{Be(9)}/\sigma^d$	2	0.3	[117]
CERN NMC 96	$F_2^{Be(9)}/F_2^{C(12)}$	15	4.5	[120]
CERN BCDMS	$F_2^{C(12)}$	162	422.0	[151]
CERN EMC	$F_2^{C(12)}/F_2^d$	9	8.5	[152]

Experiment	Observable	$N_{\rm dat}$	χ^2	Reference
CERN EMC	$\sigma^{C(12)}/\sigma^d$	8	20.5	[153]
CERN EMC	$F_2^{C(12)}$	31	37.3	[154]
SLAC E-139	$\sigma^{C(12)}/\sigma^d$	1	0.1	[117]
Fermilab E665	$\sigma^{C(12)}/\sigma^d$	4	8.6	[118]
CERN NMC 95, re.	$F_2^{C(12)}/F_2^d$	15	23.0	[119]
CERN NMC 95	$F_2^{C(12)}/F_2^d$	15	20.6	[144]
CERN NMC 95, Q^2 dependence	$F_2^{C(12)}/F_2^d$	145	149.8	[144]
CERN NMC 95, re.	$F_2^{C(12)}/F_2^{Li(6)}$	18	18.7	[119]
SLAC E-143	$R'^{C(12)}$	5	2.8	[155]
CERN BCDMS	$F_2^{N(14)}/F_2^d$	9	26.8	[156]
DESY HERMES	$\sigma^{N(14)}/\sigma^d$	42	36.0	[150]
SLAC E-049	$\sigma^{Al(27)}/\sigma^d$	3	2.0	[157]
SLAC E-139	$\sigma^{Al(27)}/\sigma^d$	2	0.1	[117]
CERN NMC 96	$F_2^{Al(27)}/F_2^{C(12)}$	15	7.1	[120]
CERN EMC	$\sigma^{Ca(40)}/\sigma^d$	8	8.5	[153]
CERN EMC	$F_2^{Ca(40)}$	32	24.2	[154]
SLAC E-139	$\sigma^{Ca(40)}/\sigma^d$	1	$0.001 \sim 0$	[117]
Fermilab E665	$\sigma^{Ca(40)}/\sigma^d$	4	7.7	[118]
CERN NMC 92	$R^{Ca(40)} - R^{C(12)}$	4	1.4	[158]
CERN NMC 95, re.	$F_2^{Ca(40)}/F_2^d$	14	17.6	[119]
CERN NMC 95, re.	$F_2^{Ca(40)}/F_2^{Li}$	18	11.0	[119]
CERN NMC 95, re.	$F_2^{Ca(40)}/F_2^{C(12)}$	18	20.5	[119]
CERN NMC 96	$F_2^{Ca(40)}/F_2^{C(12)}$	15	9.2	[120]
CERN BCDMS	$F_2^{Fe(56)}/F_2^d$	6	14.7	[156]
CERN BCDMS	$F_2^{Fe(56)}/F_2^d$	10	25.0	[159]
CERN EMC	$F_2^{Fe(56)}$	195	352.5	[161]
SLAC E-087	$\sigma^{Fe(56)}/\sigma^d$	1	0.3	[160]
SLAC E-139	$\sigma^{Fe(56)}/\sigma^d$	5	2.3	[117]
CERN NMC 96	$F_2^{Fe(56)}/F_2^{C(12)}$	15	14.3	[120]
CERN EMC	$F_2^{Cu(64)}/F_2^d$	9	4.7	[152]
CERN EMC	$F_2^{Cu(64)}/F_2^d$	19	13.8	[146]
DESY HERMES	$\sigma^{Kr(84)}/\sigma^d$	34	35.8	[150]
SLAC E-139	$\sigma^{Ag(108)}/\sigma^d$	1	0.1	[117]
CERN EMC	$F_2^{Sn(117)}/F_2^d$	8	17.6	[152]
CERN NMC 96	$F_2^{Sn(117)}/F_2^{C(12)}$	15	6.2	[120]
CERN NMC 96, Q^2 dependence	$F_2^{Sn(117)}/F_2^{C(12)}$	138	108.0	[145]
CERN NMC 96	$R'^{Sn(117)} - R'^{C(12)}$	13	4.7	[145]
Fermilab E665	$\sigma^{Xe(132)}/\sigma^d$	3	1.4	[162]
SLAC E-139	$\sigma^{Au(197)}/\sigma^d$	2	0.5	[117]

Experiment	Observable	$N_{\rm dat}$	χ^2	Reference
CERN CDHS	$\sigma^{\nu Fe(56)}$	300	256.1	[148]
CERN CDHS	$\sigma^{\bar{\nu} Fe(56)}$	302	256.3	[148]
CERN NMC 96	$F_2^{Pb(208)}/F_2^{C(12)}$	15	6.1	[120]
Fermilab E665	$\sigma^{Pb(208)}/\sigma^d$	4	15.9	[118]
CERN CHORUS	$\sigma^{\nu Pb(208)}$	292	196.7	[149]
CERN CHORUS	$\sigma^{\bar{\nu} Pb(208)}$	292	287.5	[149]

Table 2.6: DIS on deuteron targets data sets included in the present analysis. In the second column the observable used in our fit is indicated. In the third and fourth columns the number of data points that survive our kinematical cuts and their contribution to the χ^2 are – respectively – shown. In the last column the corresponding publication reference is indicated.

Experiment	Observable	$N_{\rm dat}$	χ^2	Reference
CERN EMC	$2F_2^d/F_2^p$	66	19.2	[163]
CERN EMC	$2F_2^d$	35	34.5	[154]
CERN BCDMS	R^d	9	6.8	[164]
CERN BCDMS	F_2^d	246	114.5	[164]
CERN BCDMS	$2F_2^d/F_2^p - 1$	11	21.3	[165]
Fermilab E665	σ^d/σ^p	4	3.9	[166]
Fermilab E665	$2F_2^d/F_2^p - 1$	7	3.4	[167]
Fermilab E665	F_2^d/F_2^p	53	44.3	[168]
SLAC E-140	R'^d	1	2.8	[169]
SLAC E-140	F_2^d	1	$0.005 \sim 0$	[169]
CERN NMC	F_2^d/F_2^p	148	175.6	[170]
CERN NMC	R^d/R^p	13	13.3	[170]
DESY HERMES	σ^d/σ^p	21	9.5	[171]
Total (of both tables)		3115	3188.4	

Charged-lepton DIS

The structure function F_2^A of a nucleus with atomic number Z and mass number A is given by

$$F_2^A \;=\; \frac{Z}{A}F_2^{p,A} + \frac{A-Z}{A}F_2^{n,A} \;, \tag{2.7.68}$$

where $F_2^{p,A}$ and $F_2^{n,A}$ are the structure functions of the bound protons and neutrons. However, this is not the observable reported in the original publications of charged-lepton DIS. Instead, the *isoscalar corrected* structure function was defined as that containing equal number of protons and neutrons:

$$\hat{F}_2^A \;=\; \frac{1}{2}F_2^{p,A} + \frac{1}{2}F_2^{n,A} \;. \tag{2.7.69}$$

The leading cause of using this definition was to eliminate the effects arising for the different number of protons and neutrons of the considered nucleus A when comparing to deuteron structure functions in such a way that $\hat{F}_2^A/F_2^d$ directly illustrated nuclear effects on the PDFs.

The structure function F_2 can be expressed in terms of the *isoscalar corrected* structure function as

$$F_2^A \;=\; \hat{F}_2^A \delta \;, \tag{2.7.70}$$

where

$$\delta \;=\; \frac{2}{A}\,\frac{Z+(A-Z)\,\frac{F_2^{n,A}}{F_2^{p,A}}}{1+\frac{F_2^{n,A}}{F_2^{p,A}}} \;. \tag{2.7.71}$$

The ratio $F_2^{n,A}/F_2^{p,A}$ is considered to be free of nuclear effects and parametrized by the different collaborations according to the DIS measurements on proton and deuterium.

Using Eq. (2.7.70) we compute from the *isoscalar corrected* structure function, $\hat{F}_2^A$, published by the different collaborations, the structure function F_2^A, which is the one employed in this work.

Finally, in the case of neutrino DIS, both target-mass [172] and radiative [173] corrections to the cross-section have been included.

2.7.3 Analysis method

The typical procedure to extract the optimal values of the parameters that fit the experimental data is to minimize the global χ^2-function. We use for this purpose the routine MINUIT [174] from CERNLIB library. The χ^2 is defined as

$$\chi^2(\{a_j\}) \;\equiv\; \sum_i \frac{[D_i - T_i(\{a_j\})]^2}{\sigma_i^2} \;, \tag{2.7.72}$$

where D_i are the measured experimental values, T_i are the corresponding theoretical predictions, and σ_i^2 are the experimental errors. In fact, σ_i^2. are the systematic and statistical uncertainties added in quadrature, since in most of the cases the correlation matrices are not available. The parameters $\{a_j\}$ are the set of parameters – 12 in our case – that define the nuclear modification at the initial scale.

We define our central fit as that corresponding to the minimum value of the global χ^2 obtained using our set of free parameters $\{a_j\}$,

$$\chi^2(\{a_j^0\}) \;\equiv\; \min\left[\chi^2(\{a_j\})\right] \;. \tag{2.7.73}$$

Estimation of the uncertainties

The set of parameters $\{a_j^0\}$ represent our best estimate of nPDFs. However, due to the existence of experimental uncertainties, we can move along the neighborhood of $\{a_j^0\}$ having still a good agreement with data. The main goal of this subsection is to quantify the uncertainties of the nPDFs and also their propagation to any hard process quantity X. The Hessian approach [175], which will be briefly described in the following, is used for this purpose.

The basic assumption of the Hessian method is that the dominant behavior of the χ^2-function near the fitted minimum can be approximated by a quadratic form of the fitting parameters, $\{a_j\}$,

$$\chi^2(\{a_j\}) \approx \chi_0^2 + \sum_{i,j} H_{ij}\, y_i\, y_j \ , \tag{2.7.74}$$

where $y_i = a_i - a_i^0$ are the parameters shifts from their best-fit values, $\chi_0^2 = \chi^2(\{a_j^0\})$ is the value of the χ^2-function in the minimum, and H_{ij} is the Hessian matrix, defined as

$$H_{ij} \equiv \frac{1}{2}\left(\frac{\partial^2 \chi^2}{\partial y_i \partial y_j}\right)\bigg|_{a_i = a_i^0} \ . \tag{2.7.75}$$

Being a real and symmetric matrix, H_{ij}, has a complete set of n – 12 in our case – orthonormal eigenvectors $v_i^{(k)}$ with eigenvalues ϵ_k such that

$$\begin{aligned} \sum_j H_{ij} v_j^{(k)} &= \epsilon_k\, v_i^{(k)} \quad . \\ \sum_i v_i^{(j)}\, v_i^{(k)} &= \delta_{jk} \end{aligned} \tag{2.7.76}$$

We can define a new set of parameters $\{z_j\}$ replacing our parameters $\{y_j\}$ by

$$z_i \equiv \sqrt{\epsilon_i} \sum_j v_j^{(i)} y_j \ . \tag{2.7.77}$$

In these new coordinates, Eq. (2.7.74) reduces to

$$\Delta\chi^2 \equiv \chi^2 - \chi_0^2 \approx \sum_i z_i^2 \ . \tag{2.7.78}$$

In other words, the surfaces of constant χ^2 are – in the quadratic approximation – hyperspheres in z-space, with distance to the minimum given by Eq. (2.7.78).

Now let us consider any physical quantity X which depends on the PDFs, i.e, which is a function of the parameters $\{a_j\}$. Assuming that the linear term of Taylor expansion of X around its central value $X_0 \equiv X(a_i^0) \equiv X(z_i = 0)$ gives an adequate approximation, one has

$$\Delta X \equiv X - X_0 \approx \sum_j \frac{\partial X}{\partial z_i} z_i \ , \tag{2.7.79}$$

where the z-gradient of X is evaluated at the global minimum, that is, at the origin in z-space.

Since χ^2 increases uniformly in all z-space directions, the vector in this space that maximizes ΔX for a given $\Delta\chi^2$ is that in the direction of the gradient of X with length of $\sqrt{\Delta\chi^2}$. For the square deviation we obtain

$$(\Delta X)^2 \approx \Delta\chi^2 \sum_i \left(\frac{\partial X}{\partial z_i}\right)^2 . \tag{2.7.80}$$

In order to compute the partial derivatives in Eq. (2.7.80), a set of $2n - 24$ in our case – auxiliary PDFs, $S_i^{\pm}$, in the z-space are defined as

$$\begin{aligned} S_1^{\pm} &= \pm\sqrt{\Delta\chi^2}\,(1,0,...0) \\ S_2^{\pm} &= \pm\sqrt{\Delta\chi^2}\,(0,1,...0) \\ &\vdots \\ S_N^{\pm} &= \pm\sqrt{\Delta\chi^2}\,(0,0,...N) \ , \end{aligned} \tag{2.7.81}$$

where n is the original number of parameters a_j. These $S_i^{\pm}$ PDFs, usually known as error sets, are those in which the fit parameters are changed by a fixed amount in the z-space direction separately. The central set, $S_0 = (0, 0, ..., 0)$, is the set giving the minimum χ^2.

Using these PDF error sets, the derivatives in Eq. (2.7.80) can be approximated by

$$\frac{\partial X}{\partial z_i} \approx \frac{X(S_i^+) - X(S_i^-)}{2\sqrt{\Delta\chi^2}} \tag{2.7.82}$$

Inserting this expression in Eq. (2.7.80) we get

$$\Delta X \approx \frac{1}{2}\sqrt{\sum_i \left[X(S_i^+) - X(S_i^-)\right]^2} . \tag{2.7.83}$$

How to choose $\Delta\chi^2$?

Ideally, one would expect the errors to be given by $\Delta\chi^2 = 1$ for one standard deviation (90 % C.L. limit). This is adequate when fitting consisting data with ideal Gaussian uncertainties to a well-defined theory. However, global analysis combine data from a wide variety of independent experiments, where there are unknown experimental and theoretical uncertainties. Therefore, the situation is far from being ideal. So, how to determine $\Delta\chi^2$ in global analysis?

The 90 % C.L. limit can be computed for each data set k with N_k data points. Then, $\Delta\chi^2$ can be chosen to ensure that each data set is described within its 90 % C.L. limit. The 90 % C.L. limit for each data set k is defined by [176]

$$\int_0^{\xi_k} \frac{d\chi^2}{2\,\Gamma(N_k/2)} \left(\frac{\chi^2}{2}\right)^{N_k/2-1} e^{-\chi^2/2} = 0.90 \ , \tag{2.7.84}$$

where

$$\xi_k \;=\; \chi^2_{k,max}\,\frac{N_k-2}{\chi^2_{k,0}}\;, \tag{2.7.85}$$

$\chi^2_{k,0}$ being the value of the χ^2 for the kth data set at the global minimum.

For each eigenvector direction, z_i, we move our parameters from the global minimum until any of the data sets exceeds its 90 % C.L. limit, i.e, until $\chi^2_k > \chi^2_{k,max}$ for any k. At this point, we check the value of the global χ^2, $\chi^2(S_i^{\pm})$, and compute $\Delta\chi^2(S_i^{\pm}) = \chi^2(S_i^{\pm}) - \chi^2_0$. This is repeated for all the eigenvectors in both directions (positive and negative). The average of these $2n$ individual $\Delta\chi^2(S_i^{\pm})$ is our final average tolerance, $\Delta\chi^2$,

$$\Delta\chi^2 \;\equiv\; \sum_i \frac{\Delta\chi^2(S_i^+)+\Delta\chi^2(S_i^-)}{2n}\;. \tag{2.7.86}$$

For the present fit of data, we find $\Delta\chi^2 = 78$. This averaging process is illustrated in Fig. 2.17, where the individual differences, $\chi^2(S_i^+)-\chi^2_0$, and $\chi^2(S_i^-)-\chi^2_0$ are shown together with the obtained average.

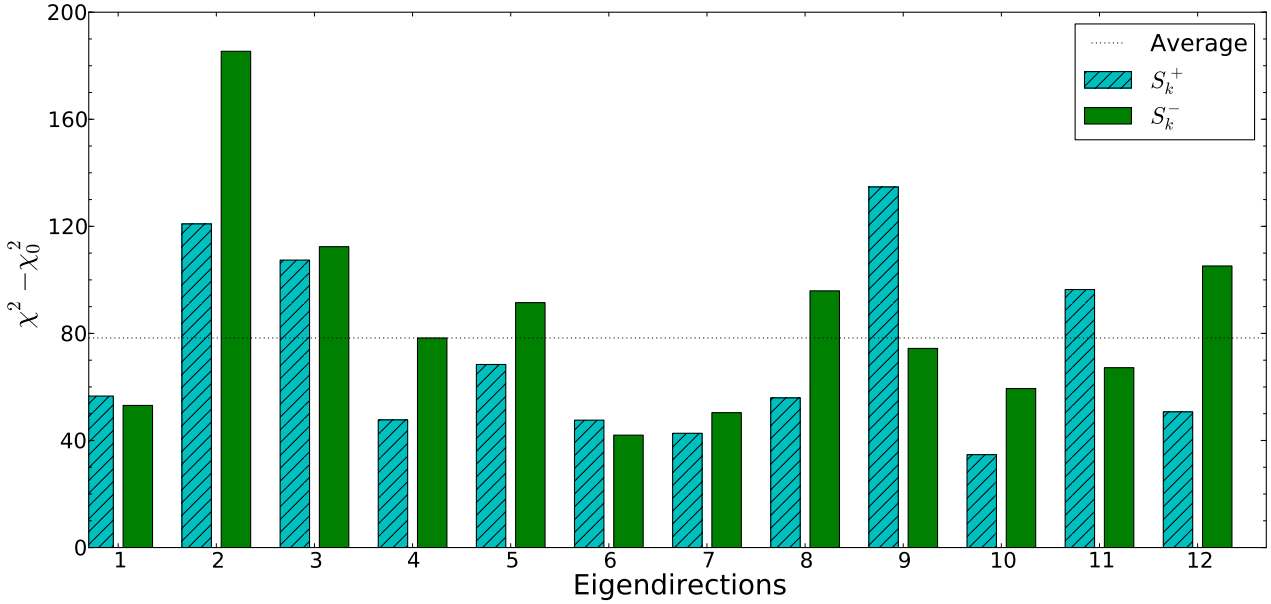

Figure 2.17: The individual values $\chi^2(S_i^{\pm}) - \chi^2_0$ compared with their average $\Delta\chi^2 = 78$.

2.7.4 Results

In Table 2.7 the values of the 12 free parameters of the nuclear modifications R_i^A in Eq. (2.7.63) resulting from the χ^2 minimization are listed. We also present in this table those parameters that were fixed.

Valence R_V^A	Sea R_S^A	Gluon R_g^A
γ_V: sum rule	$\gamma_S = \mathbf{0.11497}$	γ_g: sum rule
$a_V = \mathbf{0.13661 \times 10^{-2}}$	$a_S = \mathbf{0.10942 \times 10^{-3}}$	$a_g = \mathbf{-2.7286}$
$\beta_V = \mathbf{0.32662}$	$\beta_S = \mathbf{0.26067}$	β_g = -0.1, fixed
$\alpha_V = \mathbf{0.1648}$	$\alpha_S = \mathbf{-0.4596 \times 10^{-1}}$	—
b: sum rule	as R_V^A	$b_g = \mathbf{-5.7769}$
c: sum rule	as R_V^A	$c_g = \mathbf{9.6361}$
$d = \mathbf{3782.7}\, A^{\mathbf{0.06297}}$	as R_V^A	—

Table 2.7: List of parameters defining the modifications R_V^A, R_S^A, R_g^A through Eq. (2.7.63) at our initial scale $Q_0 = 1$ GeV. The values of the 12 parameters that were free in the fit are shown in bold face.

The nuclear modifications, R_i^A, the error sets given by Eq. (2.7.81) and the uncertainty bands of Eq. (2.7.83) are plotted in Fig. 2.18 for deuterium, carbon, and lead at $Q^2 = 2\,\mathrm{GeV}^2$. Fig. 2.19 is the same as Fig. 2.18 but for $Q^2 = 10\,\mathrm{GeV}^2$.

The valence quark modifications are well under control at $x \geq 0.07$, thanks to the constraining power of the DIS data. At low-x there are no data constraints and the uncertainty band is wider. However, the baryon number sum rule prevents the uncertainty at small-x to be (even) larger.

The uncertainty band of the sea quark is narrow around $x \sim 0.1$ due to the DIS data probing the sea quarks in this region. Towards smaller and higher x the uncertainty increases due to the lack of data constraining these regions.

Due to the sum rules and to the chosen parametrization, the uncertainties of the gluon are unrealistically small, since the are only some indirect constraints over the gluon distribution at moderate x.

A global analysis of the nuclear corrections to the free proton PDFs at NNLO accuracy in pQCD has been presented. We have implemented a complete treatment of heavy quarks following the GM-VFNS at NNLO. In this preliminary fit only charged-lepton DIS and neutrino DIS data have been implemented. We have also quantified the uncertainties arising from the experimental errors by providing 24+1 nPDF sets. The extension of this nPDFs global analysis to that including Drell-Yan experimental results remains as a future task.

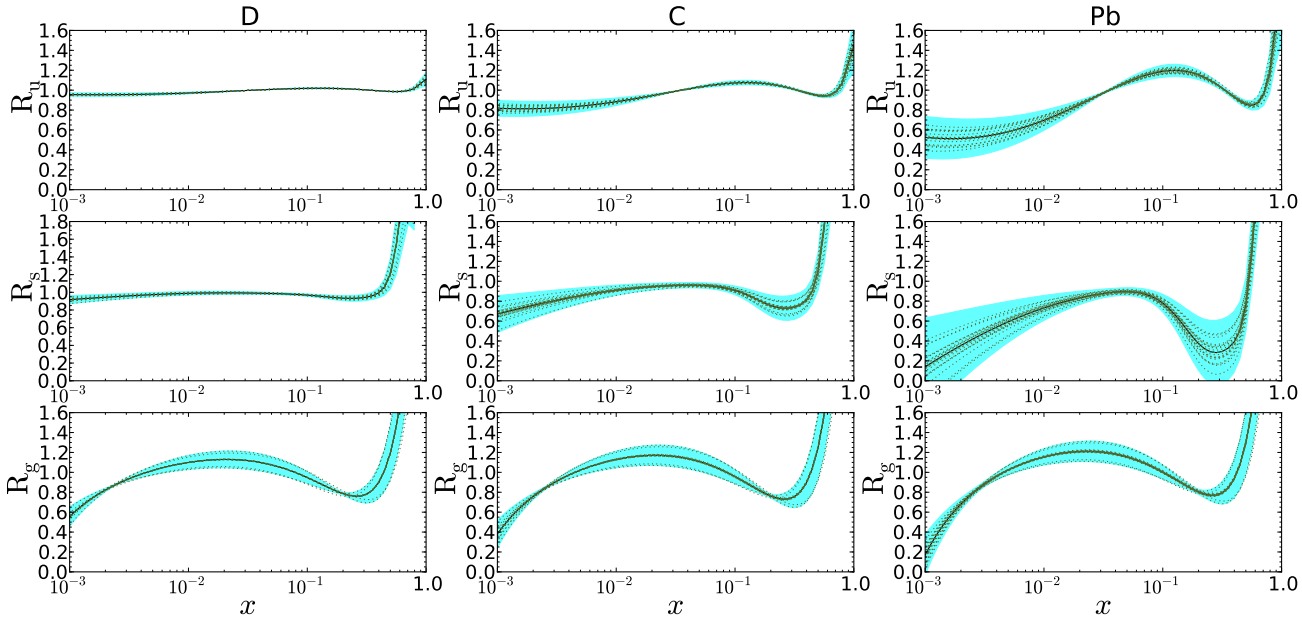

Figure 2.18: Nuclear modifications for deuterium (leftmost column), carbon (central column), and lead (rightmost column) at $Q^2 = 2\,\mathrm{GeV}^2$. The black curves correspond to the central fit, S_0, and the dotted green curves to the error sets $S_i^{\pm}$. The total uncertainties are shown as blue bands.

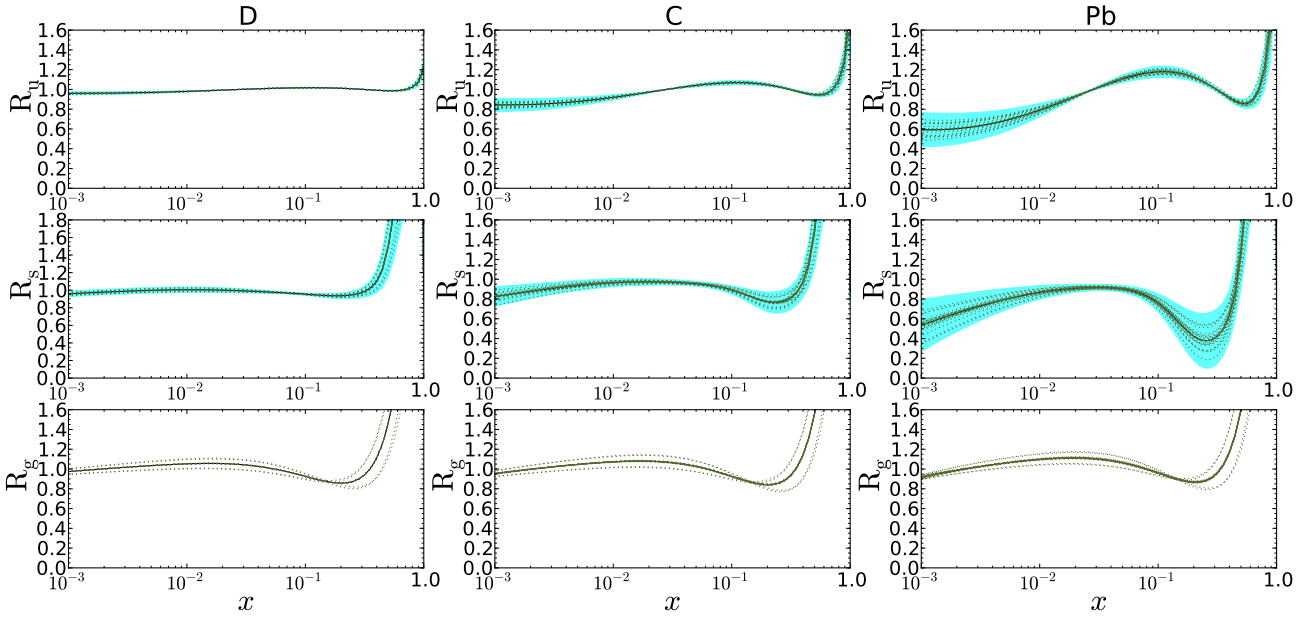

Figure 2.19: Nuclear modifications for deuterium (leftmost column), carbon (central column), and lead (rightmost column) at $Q^2 = 10\,\mathrm{GeV}^2$. The black curves correspond to the central fit, S_0, and the dotted green curves to the error sets $S_i^{\pm}$. The total uncertainties are shown as blue bands.

USC
UNIVERSIDADE
DE SANTIAGO
DE COMPOSTELA

Chapter 3

Percolation of strings

The Color Glass Condensate (CGC) [13–16], derived from QCD in a semiclassical way, provides a suitable generic formalism to explain the collective phenomena appearing in heavy-ion collisions and eventually leading to the formation of a QGP. A simpler model, capturing some of the main features of the CGC is the string percolation model (SPM) [17]. Percolation of strings is not directly obtained from QCD, but QCD inspired. In this framework, multiparticle production is described in terms of color strings stretched between the partons of the projectile and target. Due to color confinement, each string has a transverse size $S_1 = \pi r_0^2$ with $r_0 = 0.2 - 0.3$ fm [177], dictated by the color fields between the color charges of the partons at the end of each string. These strings decay into $q - \bar{q}$ and $qq - \bar{q}\bar{q}$ pairs, which subsequently hadronize producing the observed hadrons. The mechanism of pair production is analogue to the well-known Schwinger mechanism [178–181], but in a finite space:

$$W_f(\vec{Q},\vec{C}) = \frac{1}{4} S_1 \left(b\,\vec{Q}\cdot\vec{C}\right) e^{-\pi M_f^2/\left(b\,\vec{Q}\cdot\vec{C}\right)} \tag{3.0.1}$$

is the probability for a string of transverse area S_1 and tension $K = \pi b Q^2/2$ of producing a pair of flavor, f, with transverse mass M_f, and color charge $\vec{C}$. For high color values, $\vec{Q}$, the most probable situation is the full screening of the field with the creation of a pair with color charge $\vec{C} = \vec{Q}$.

In general, interactions between strings are not considered in string models [182]. Strings are generated in an initial state according to Gribov-Regge-Theory (GRT) [183–185] and then they decay into hadrons according to different fragmentation models. However, this kind of models were unable to explain strangeness enhancement [186] and the saturation of the multiplicity per participant [187, 188]. Some collective behavior is required in order to explain both phenomena. The interaction among strings is incorporated in the SPM.

At low energies and peripheral collisions, the fact that strings have finite dimension has no influence on the results. Therefore, in this case, the scenario where the strings are independent is applicable. Nevertheless, when increasing the energy or/and the size (or centrality) of the colliding objects, the number of strings grows and then they begin to interact, being no longer independent. They overlap forming clusters, which are very similar to 2-dimensional

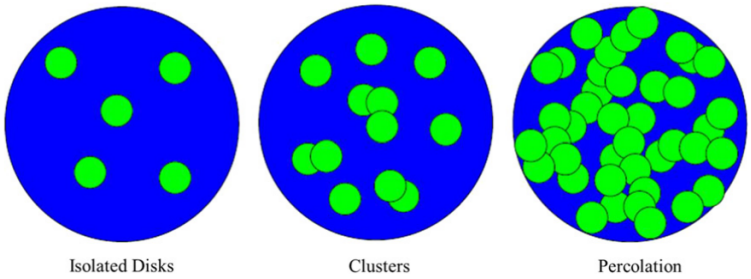

Figure 3.1: Overlapping discs up to the percolation phase transition. Figure taken from [52].

discs in percolation theory. A cluster of strings has an homogeneous color field which is the result of the vectorial sum of those of the original strings. At a given critical density, η_c, a macroscopic cluster appears across the collision surface. This marks the percolation phase transition. Hence, the nature of this transition is geometrical. Consider a flat large 2-dimensional surface, $S_A = \pi R^2$, which is the total nuclear overlapping area. On this surface, n discs of area $S_1 = \pi r_0^2$ are randomly distributed, allowing overlap between them. If the number of discs grows, clusters of overlapping discs start to form. The density of discs is given by $\rho = n/S_A = n/\pi R^2$. When this density increases, the average cluster size increases and at a certain critical density, ρ_c, the cluster occupies the whole surface. This is known as percolation and it is shown in Fig. 3.1.

The percolation threshold, η_c, that is, the onset of continuum percolation, is related to the critical density, ρ_c, by

$$\eta_c \;=\; \rho_c S_1 \;=\; \rho_c \pi r_0^2 \;. \tag{3.0.2}$$

η_c has been computed using numerical simulations for different systems [48–50]. The results are in the range $\eta_c = 1.12 - 1.5$ depending on the profile function used for the colliding nuclei – homogeneous or a 3-parameter Fermi distribution. When the percolation point has been reached, i.e., when the largest cluster expands over the entire surface, there is still a considerable fraction of the surface which is empty. Indeed, at the threshold, only $1 - exp(\eta_c) \sim 2/3$ of the surface is covered by discs.

The expressions of the average transverse momentum, $\langle p_T \rangle$, and average multiplicity, $\langle \mu \rangle$, of the particles produced in a cluster can be derived from the composition of the color fields of its strings. Let us consider a cluster made of n strings, with area S_n and color charge $\vec{Q}_n$. $\vec{Q}_n$ is the vectorial sum of the color charges of each individual string, $\vec{Q}_i$,

$$\vec{Q}_n^2 \;=\; \left(\sum_1^n \vec{Q}_i \right)^2 \;. \tag{3.0.3}$$

Since strings colors are arbitrarily oriented, in the limit of large n, the average of $\vec{Q}_i \cdot \vec{Q}_j$

(with $i \neq j$) is zero. Hence, $\vec{Q}_n^2 = n\vec{Q}_1^2$. Due to the Gauss theorem,

$$Q_n \;=\; \sqrt{\frac{nS_n}{S_1}}\, Q_1 \;. \tag{3.0.4}$$

This approximate equation will be used as a smooth interpolation between the non-overlapping and the total overlapping extreme cases.

From the color charge in Eq. (3.0.4) and applying the Schwinger formula Eq. (3.0.1) the expressions for the average multiplicity and the average transverse momentum of a cluster can be obtained:

$$\langle \mu_n \rangle \;=\; \sqrt{\frac{nS_n}{S_1}}\, \langle \mu_1 \rangle \,, \qquad\qquad \langle p_{Tn}^2 \rangle \;=\; \sqrt{\frac{nS_1}{S_n}}\, \langle p_{T1}^2 \rangle \;, \tag{3.0.5}$$

where $\langle \mu_1 \rangle$ and $\langle p_{T1} \rangle$ stand, respectively, for the average multiplicity and transverse momentum of the particles produced in a single string. Note that a kind of conservation law of the total transverse momentum produced, holds

$$\frac{1}{n} \langle \mu_n \rangle \langle p_{Tn}^2 \rangle \;=\; \langle \mu_1 \rangle \langle p_{T1}^2 \rangle \;. \tag{3.0.6}$$

In low energy peripheral HICs the number of nucleon-nucleon interactions is small and so is the number of strings formed. Thus, in this case, strings act as independent sources and, so, $S_n = nS_1$. Then, from Eq. (3.0.5), the total average multiplicity and transverse momentum are: $\langle \mu_n \rangle = n \langle \mu_1 \rangle$ and $\langle p_{Tn} \rangle = \langle p_{T1} \rangle$. On the contrary, in the total overlapping limit case, $S_n = S_1$ and, then, $Q_n = \sqrt{n}\, Q_1$, $\langle \mu_n \rangle = \sqrt{n}\, \langle \mu_1 \rangle$, and, $\langle p_{Tn}^2 \rangle = \sqrt{n}\, \langle p_{T1}^2 \rangle$.

To obtain the mean p_T and the mean multiplicity of a collision at a given centrality, one needs to sum over all formed clusters and to average over all events,

$$\langle \mu \rangle \;=\; \frac{\sum_{i=1}^{N_{events}} \sum_j \langle \mu_{nj} \rangle}{N_{events}} \,, \qquad\qquad \langle p_T \rangle \;=\; \frac{\sum_{i=1}^{N_{events}} \sum_j \langle \mu_{nj} \rangle \langle p_{T\,nj} \rangle}{\sum_{i=1}^{N_{events}} \sum_j \langle \mu_{nj} \rangle} \;, \tag{3.0.7}$$

where the sum over j goes over all individual clusters (j), each one constituted by n_j strings and occupying an area S_{nj}.

These expressions show a good agreement with experimental data. For instance, as it can be seen in Fig 3.2, when clustering is included, there is a prefect agreement of the multiplicity of negatively charged particles in Pb-Pb collisions with the data from NA49 Collaboration [189].

Let us consider now the "thermodynamic limit", i.e., the limit where the number of strings goes to infinity, $n \to \infty$, keeping the *percolation parameter*, $\eta = \rho S_1$, fixed. In this limit, the distribution of the overlaps is Poissonian, $P_n = \eta^n e^{-\eta}/n!$, and [191]

$$\langle \mu_n \rangle \;=\; nF(\eta)\, \langle \mu_1 \rangle \,, \qquad\qquad \langle p_{Tn}^2 \rangle \;=\; \frac{\langle p_{T1}^2 \rangle}{F(\eta)} \;, \tag{3.0.8}$$

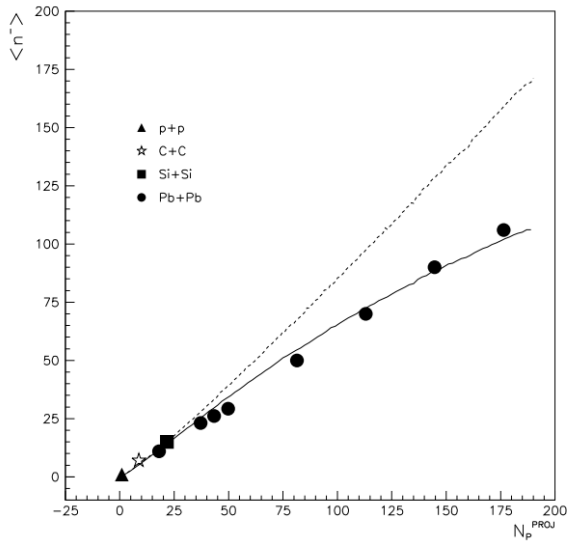

Figure 3.2: Mean multiplicity of negatively charged particles in Pb-Pb collisions at $P_{lab} = 158A$ GeV/c not including clustering (dashed line) and including it (continuous line) compared to NA49 experimental data [189]. Figure taken from [190].

where

$$F(\eta) \;=\; \sqrt{\frac{1-e^{-\eta}}{\eta}} \tag{3.0.9}$$

is a continuous geometric saturation function whose value is close to unity at low η and to zero at very high ones. In Eq. (3.0.9), the numerator, $1-e^{-\eta}$, represents the fraction of the area covered by the strings. A more realistic implementation implies a modification of this area in Eq. (3.0.9).

In HICs experimental data on the multiplicity are known to be well described by a negative binomial distribution

$$P(\mu,k) \;=\; \frac{\gamma^k}{\Gamma(k)\mu!}\,\frac{\Gamma(\mu+k)}{(1+\gamma)^{\mu+k}}\;, \tag{3.0.10}$$

where k stands for

$$\frac{1}{k} \;\equiv\; \frac{\langle\mu^2\rangle - \langle\mu\rangle^2 - \langle\mu\rangle}{\langle\mu\rangle^2}\;, \tag{3.0.11}$$

and $\gamma = k/\langle\mu\rangle$.

$P(\mu,k)$ can be written as a convolution of the probability of having a cluster composed by n strings, $W(n)$, and the probability for that cluster to fragment into μ particles, $G(n,\mu)$, [192]

$$P(\mu,k) \;=\; \int_0^\infty dn\, W(n)G(n,\mu)\;. \tag{3.0.12}$$

$G(n,\mu)$ is taken Poissonian,

$$G(n,\mu) \;=\; e^{-n}\frac{n^{\mu}}{\mu!} \;\;, \tag{3.0.13}$$

and $W(n)$ is taken as a Gamma distribution,

$$W(n) \;=\; \frac{\gamma}{\Gamma(k)}(\gamma n)^{k-1}e^{-\gamma n} \;\;, \tag{3.0.14}$$

with k given by

$$\frac{1}{k} \;=\; \frac{\langle n^2\rangle - \langle n\rangle^2}{\langle n\rangle^2} \;\;. \tag{3.0.15}$$

There are several reasons for this choice. First, the gamma distribution reproduces to a good approximation the cluster size distributions at different centralities. Indeed, in peripheral collisions the density of strings is small and there are only very few overlapping strings. In this case, the cluster size is peaked at low values of the number of strings of the cluster. As the centrality increases, so does the density of strings, and there are more and more overlapping strings. The cluster size distribution becomes strongly modified. Second, there is a more technical reason related to the renormalization group [193].

$\mathcal{R} \equiv 1/k$ can be interpreted as the fluctuations on the number of strings in the clusters. Note that, on the one hand, in the large density limit, η large, $\langle n^2\rangle - \langle n\rangle^2 \sim \langle n\rangle$, then $k \to \langle n\rangle \to \infty$ [192, 194]. On the other hand, in the low density limit, $\eta \ll 1$, the multiplicity, μ, is Poisson-like, hence, its variance coincides whith its mean value, and $k \to \infty$, see Eq. (3.0.11). At intermediate energy densities, k must have a minimum close to the critical density.

In the following sections, some of the results of this model and their comparison with the available experimental data will be discussed.

3.1 Geometric scaling for hadronic interactions

It has been recently shown that the p_T-spectra of charged particles in p-p collisions exhibit geometric scaling [195, 196]. Indeed, the p_T-spectra in p-p collisions in the broad range of energies from 0.9 to 7 TeV, scale in a single variable $\tau \equiv p_T^2/Q_s^{p2}$, where the proton saturation momentum Q_s^p is given by

$$(Q_s^p)^2 \;\equiv\; Q_0^2\left(\frac{W}{p_T}\right)^{\lambda} \;\;, \tag{3.1.16}$$

where $W = \sqrt{s}$ and $\lambda = 0.27$.

An extension of this geometric scaling to A-A collisions, for both RHIC and LHC energies, at different centralities, and different nuclei is considered here. It is shown that this scaling is not only valid for each collision at fixed centrality separately, but also for any

centrality for $\tau < 1$. Furthermore, the hard spectrum, i.e., the spectrum for $\tau > 1$ is also analyzed. The hard multiplicity turns out to decrease with the size of the participant nuclei – as it would be expected from jet quenching.

3.1.1 The saturation momentum

The saturation momentum, Q_s^A, in A-A collisions is defined as,

$$\left(Q_s^A\right)^2 \;=\; \left(Q_s^p\right)^2 \; N_A^{\beta(s)/2} \, A^{1/6} \left(\frac{A}{N_A}\right)^{1/3} \quad , \tag{3.1.17}$$

where

$$\beta(s) = \frac{1}{3}\left(1 - \frac{1}{1+\ln\left(\sqrt{s/s_0}+1\right)}\right) \quad , \tag{3.1.18}$$

N_A being the number of participant nucleons divided by two and A the mass number.

At high energy, $\beta(s) = 1/3$. With this value, for $N_A = A$ the well-known behavior of Q_s^A for central collisions $\left(Q_s^A\right)^2 = \left(Q_s^p\right)^2 A^{1/3}$ is recovered.

The parametrization of Eq. (3.1.17) is based on the description of the experimental data on dN/dy for p-p and A-A collisions at all centralities, rapidities, and energies using the framework of percolation of strings [197, 198]. The dependence of the charged particle multiplicity on the center of mass energy is the same in p-p and A-A collisions, as it is shown in reference [197]. The observed differences are due to the energy conservation effect that can be incorporated in $\beta(s)$. In fact,

$$\left.\frac{dn^{AA}}{dy}\right|_{y=0} \;\sim\; N_A\left(N_A^{\beta(s)} - 1\right)\left.\frac{dn^{pp}}{dy}\right|_{y=0} \quad , \tag{3.1.19}$$

where $\beta(s)$ is given by Eq. (3.1.18).

As it was already explained, the string percolation can be regarded as a simpler implementation of the CGC [199]. Therefore, the number of color flux tubes of the glasma, $(Q_s^A)^2 R_A^2$, corresponds to the number of clusters of strings (effective number of sources), $\eta^{1/2} R_A^2$, in SPM. In this way, the dependence of the string density, η, on s, A and N_A is translated into $(Q_s^A)^2$, resulting in Eq. (3.1.17).

The values of the parameters $\lambda = 0.27$ and $Q_0 = 1$ GeV/c are taken from the reference [195]. A slightly worse scaling has been obtained with $\lambda = 0.30$. The value of $\sqrt{s_0} = 245$ GeV was obtained in references [197, 198] and indicates the energy scale of the energy conservation effect.

$(Q_s^A)^2$ in Eq. (3.1.17) does not depend on the rapidity. Nevertheless, only the central pseudorapidity region will be used. In most of the string models, strings stretching among sea quarks and antiquarks are expanded only in the central pseudorapidity range. This fact changes the dependence of strings on N_A. For central pseudorapidity, $N_s \sim N_A^{4/3}$ and outside this range $N_s \sim N_A$. This change gives rise to a smoother dependence of $(Q_s^A)^2$ on N_A outside the central pseudorapidity region.

3.1.2 Comparison with experimental data

In Fig. 3.3, the multiplicities for Cu-Cu $0-6$ % at 62.4 and 200 GeV, and Au-Au $0-6$ % at 62.4 and 200 GeV [203, 204], together with Pb-Pb $40-50$ %, $5-10$ %, and $0-5$ % at 2.76 TeV [205] as a function of $\tau \equiv p_T^2/\left(Q_s^A\right)^2$, in the pseudorapidity range $0.2 < \eta < 1.4$ are plotted. The number of participants used is the mean value corresponding to the given centrality. Experimental data taken from ALICE [205] correspond to a pseudorapidity range – including the $\eta = 0$ region –, in which $dn/d\eta$ is smaller than in the pseudorapidity range considered here. Because of this a 15 % correction was applied to the normalization [198].

It can be seen that Pb-Pb $0-5$ %, and $5-10$ % data points lie in the same line for $\tau < 1$. Also the Cu-Cu, and the Au-Au data at both energies are approximately in the same curve for $\tau < 1$. Only Pb-Pb $40-50$ % present some departure around 1. For $\tau > 1$ a suppression for the heavy nuclei is shown.

In order to see the differences between the different sizes of projectile and target, Fig. 3.4 in presented. In this figure, data for p-p collisions at 0.9, 2.36, and 7 TeV [206, 207] are plotted together with the recent p-Pb data at 5.02 TeV [208]. Au-Au central data at 62.4 GeV [203], and Pb-Pb central data at 2.76 TeV [205], already shown in Fig. 3.3, are also plotted here. In the case of p-Pb, $\langle N_{part} \rangle = 7.9$ is used, according to reference [209].

It is observed that p-p data at different energies are all in the same line, satisfying geometric scaling, as it was shown in reference [195]. Moreover, p-Pb, Pb-Pb and Au-Au central data at low τ are very close to these p-p data. When τ becomes larger the difference between these sets of data increases. For $\tau > 1$ the suppression is larger for Pb-Pb $0-5$ % central than for p-Pb, and the latter are more suppressed than the p-p sets.

The scaling for $Q^2 < Q_s^2$ was predicted by CGC and by phenomenological saturation models [210–213]. The HERA data on DIS at low x show scaling even for very high Q^2, $Q^2 < 400\,\mathrm{GeV}^2/\mathrm{c}^2$ [214]. Indeed, the solution of the BFKL evolution equation shows that the scaling can be extended to intermediate Q^2, $1 \lesssim ln(Q^2/Q_s^2) \ll ln(Q_s^2/\Lambda_{QCD}^2)$ [215]. Our comparison with data shows that p-p collisions present geometric scaling even for $\tau > 1$. However, this is not true for A-A collisions. Notice that in the p-p case, jet quenching is not expected, since a high density medium is not formed. On the contrary, in A-A collisions, at high LHC energies and high multiplicity events, jet quenching has been predicted [216, 217]; but the weight of these events compared to minimum bias is negligible.

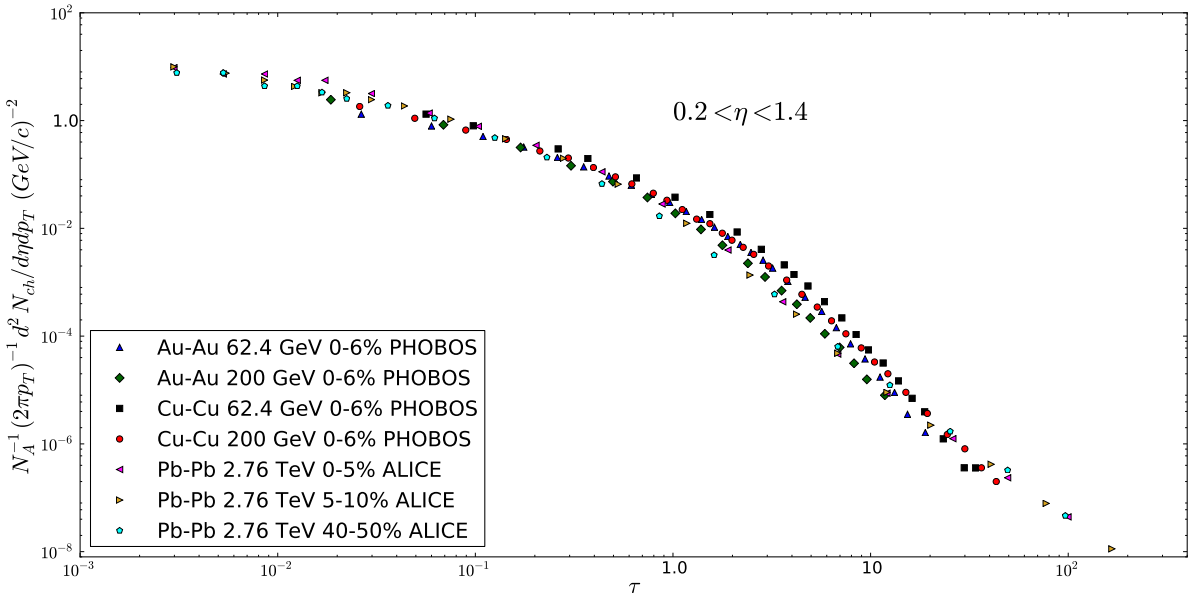

Figure 3.3: Charged particle multiplicity per participant at pseudorapidity $0.2 < \eta < 1.4$ for Au-Au and Cu-Cu central collisions at two RHIC energies 62.4 and 200 GeV [203, 204], and for Pb-Pb collisions at 2.76 TeV [205] versus τ.

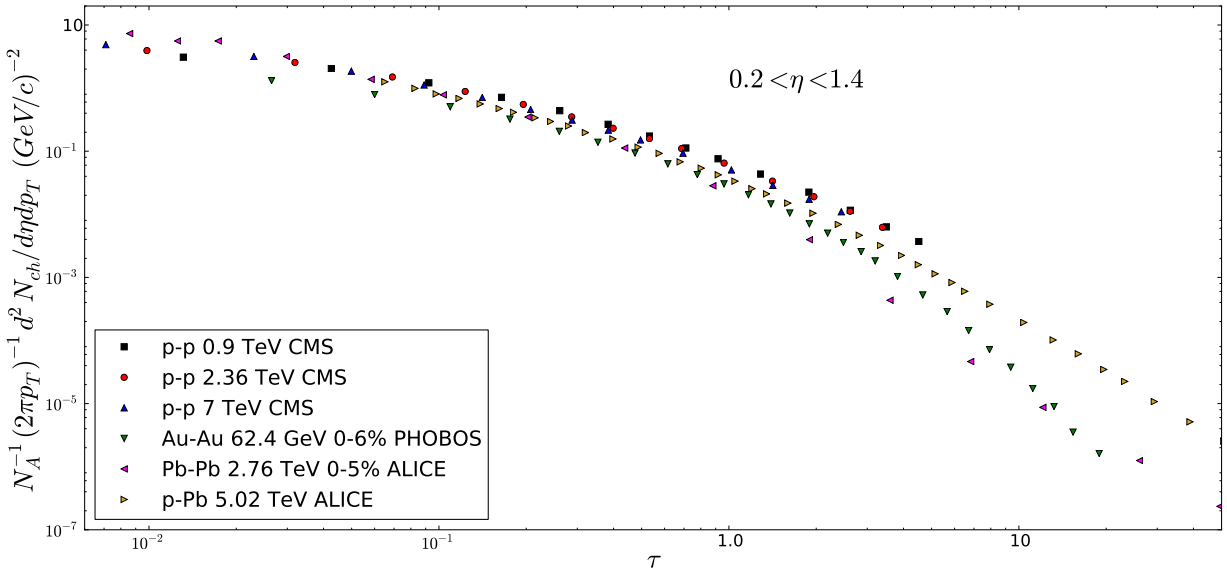

Figure 3.4: Charged particle multiplicity per at pseudorapidity $0.2 < \eta < 1.4$ for p-p collisions [206, 207], Au-Au $0 - 6$ % central collisions at 62.4 GeV [203], Pb-Pb $0 - 5$ % collisions at 2.76 TeV [205], and p-Pb data at 5.02 TeV [208] versus τ.

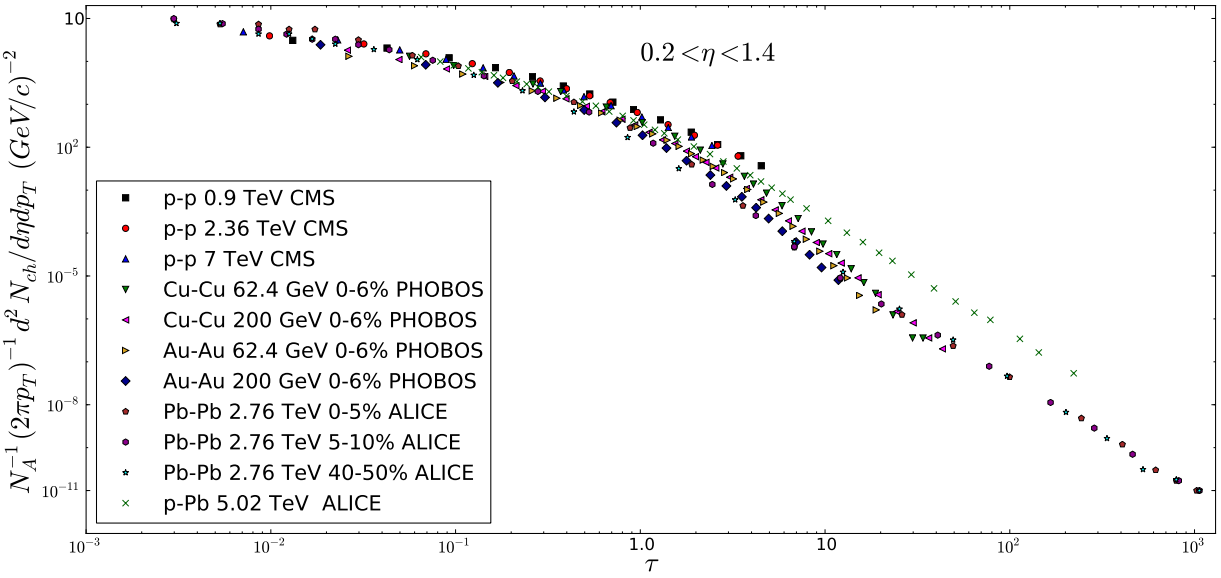

Figure 3.5: Charged particle multiplicity per participant in the pseudorapidity range $0.2 < \eta < 1.4$ for all the heavy ion collisions considered versus τ.

In Fig. 3.5, all previous data were plotted together to show that for $\tau < 1$ there are not many differences among them. This does not occur for $\tau > 1$ region, where suppression is larger for larger sizes of nuclei.

It is worth emphasizing that the parametrization in Eq. (3.1.17) allows us to deal with all type of collisions at any energy. For that purpose, the introduction of the $\beta(s)$ function is required, which implies a different power for different number of participants. In reference [196] the geometric scaling was shown for p-p collisions at LHC and A-A collisions at RHIC using an energy independent exponent λ, but this exponent for p-p was different that the one from A-A. If an energy independent exponent is used for both, p-p and A-A collisions, the scaling is spoiled as it can be seen in Fig. 3.6, where p-p and several A-A transverse momentum distributions using $\beta(s) = 1/3$ are plotted.

In order to see the quality of this extended scaling, the ratio of Pb-Pb $0-5$ % at 2.76 TeV, Au-Au $0-6$ % at 200 GeV, Cu-Cu $0-6$ % at 62.4 GeV, p-Pb at 5.02 TeV over Cu-Cu $0-6$ % at 200 GeV as a function of τ is shown in Fig. 3.7. Even for such different projectiles and targets and also in the broad range of energies considered, an approximate scaling at low τ is observed. Notice that for $\tau < 1$ the data extend over three orders of magnitude. Excluding Cu-Cu data, ratios vary between 0.7 and 1.3 in the range $0.2 < \tau < 1$ [1]. The violation of the scaling is clear for $\tau > 1$, showing a higher suppression for heavier nuclei. The hierarchy of the scaling violations for $\tau > 1$ agree with the expected suppression due to

[1]Note that for $p_T < \Lambda_{QCD}$ or, equivalently, $\tau < 0.1 - 0.2$, there is no reason to expect geometric scaling.

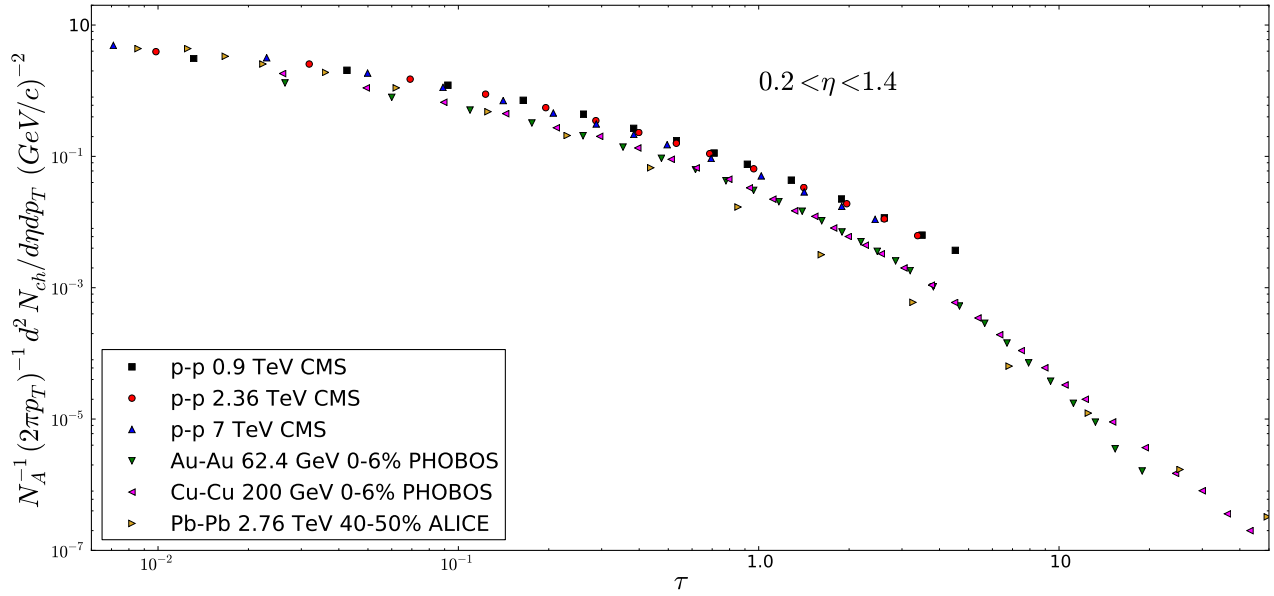

Figure 3.6: Charged particle multiplicity per participant in the pseudorapidity range $0.2 < \eta < 1.4$ for p-p collisions [206, 207], Au-Au $0-6$ % at 62.4 GeV [203], Cu-Cu $0-6$ % at 200 GeV [204], and Pb-Pb $40-50$ % at 2.76 TeV [205] versus τ using $\beta(s) = 1/3$.

jet quenching.

Based on this approximate scaling, the multiplicity of soft and hard particles per participant, defining soft particles as those with $p_T < Q_s$ and hard as those with $p_T > Q_s$, can be computed. In fact,

$$\frac{1}{N_A}\frac{dN_{ch}^{soft}}{d\eta} = \frac{1}{N_A}\int_0^{Q_s^2} \mathrm{d}p_T^2\,\frac{dN_{ch}^2}{d\eta dp_T^2} = \frac{1}{N_A}\int_0^{Q_s^2} \mathrm{d}p_T^2\,\frac{1}{Q_0^2}\,F(\tau)\ , \tag{3.1.20}$$

and with the following change of variables

$$\frac{dp_T^2}{Q_0^2} = \frac{2}{2+\lambda}\left(\frac{W}{Q_0}\right)^{\frac{2\lambda}{2+\lambda}} \tau^{-\frac{\lambda}{2+\lambda}}\,N_A^{\beta(s)/2}\,A^{1/6}\left(\frac{A}{N_A}\right)^{1/3} d\tau\ , \tag{3.1.21}$$

the fraction of soft and hard multiplicities over the total multiplicity results

$$R_s \equiv \frac{dN_{ch}^{soft}/d\eta}{dN_{ch}^{tot}/d\eta} = \frac{\int_0^1 \mathrm{d}\tau\,\tau^{-\frac{\lambda}{2+\lambda}}\,F(\tau)}{\int_0^\infty \mathrm{d}\tau\,\tau^{-\frac{\lambda}{2+\lambda}}\,F(\tau)}\ , \qquad R_h \equiv \frac{dN_{ch}^{hard}/d\eta}{dN_{ch}^{tot}/d\eta} = \frac{\int_1^\infty \mathrm{d}\tau\,\tau^{-\frac{\lambda}{2+\lambda}}\,F(\tau)}{\int_0^\infty \mathrm{d}\tau\,\tau^{-\frac{\lambda}{2+\lambda}}\,F(\tau)}\ . \tag{3.1.22}$$

In Table 3.1, the fractions of soft and hard multiplicities for the centralities, energies, and collisions considered are presented. In order to do the integration in Eq. (3.1.22), first a fit to each p_T-distribution separately is done, and, afterwards, this is integrated.

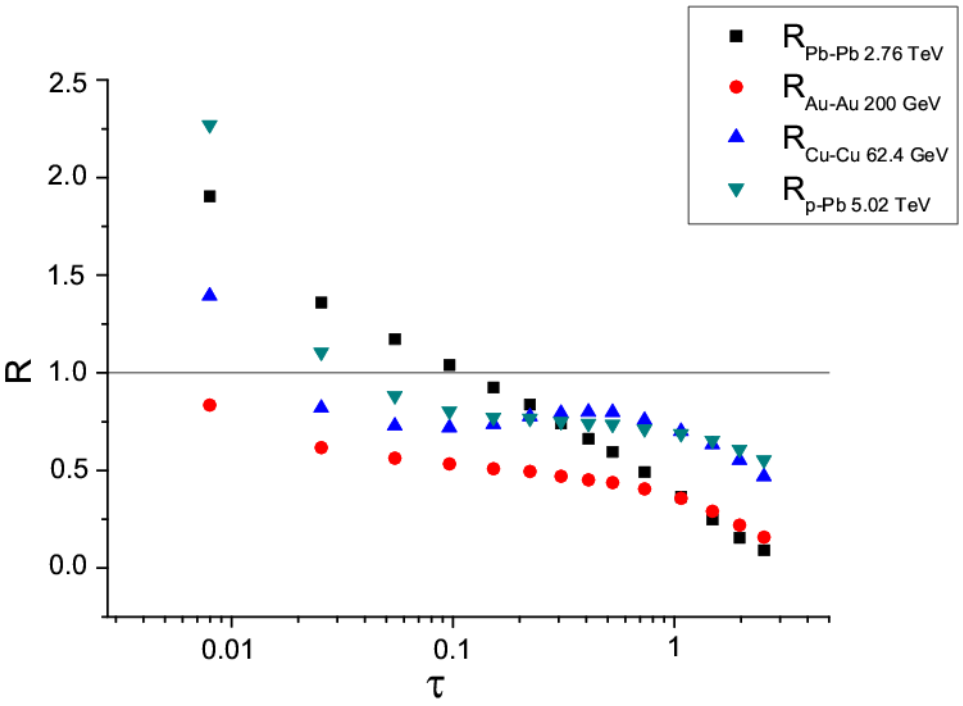

Figure 3.7: Ratio of Pb-Pb $0-5$ % at 2.76 TeV [205], Au-Au $0-6$ % at 200 GeV [203], Cu-Cu $0-6$ % at 62.4 GeV [204], and p-Pb at 5.02 TeV [208] w.r.t. Cu-Cu $0-6$ % at 200 GeV [204] versus τ.

The hard fraction decreases slowly with center of mass energy and with the size of the participant nuclei, as it can be seen in Table 3.1. In the case of p-p collisions the dependence of the energy is very weak, varying from 9 % to 8 % in the broad range $0.9-7$ TeV. However, larger differences between Au-Au central collisions at 62.4 GeV and Pb-Pb central collisions at 2.76 TeV are observed: their hard fractions are, respectively, 7 % and 2 %. The hard fraction of Pb-Pb is the same for peripheral $(40-50$ %) and central $(0-5$ %) collisions.

In summary, the weight of the hard collisions – and, hence, the weight of the hard multiplicities – is believed to increase when the energy or the size of the participant nuclei grow; however, the opposite is observed here, within our definition of hard and soft collisions. This result was also pointed out by ALICE Collaboration data on the sphericity as a function of the energy and the charge multiplicity in p-p collisions at 0.9, 2.36, and 7 TeV [218]. The sphericity measures the jet activity, in such a way that one event with dijet back-to-back implies sphericity zero. On the contrary, an event where all the produced particles are distributed isotropically in phase space implies sphericity one. Most of the Monte Carlo codes (Pythia 8, Perugia-0, Phojet, Atlas-CSC) predict a decreasing of the sphericity with energy and charged multiplicity, whereas the data show the opposite trend. In the CGC [15,16,219] the more the saturation momentum grows with the energy and the number of participants, the smaller is the room for hard collisions. This also happens in the framework of percolation

	Energy (TeV)	Centrality	R_s	R_h
p-p	0.9	minb	0.91	0.09
p-p	2.36	minb	0.90	0.10
p-p	7	minb	0.92	0.08
p-Pb	5.02	minb	0.93	0.07
Cu-Cu	0.0624	$0-6$ %	0.93	0.07
Cu-Cu	0.2	$0-6$ %	0.94	0.06
Au-Au	0.0624	$0-6$ %	0.93	0.07
Au-Au	0.2	$0-6$ %	0.96	0.04
Pb-Pb	2.76	$40-50$ %	0.98	0.02
Pb-Pb	2.76	$0-5$ %	0.98	0.02

Table 3.1: Values of the fractions of soft and hard multiplicities for different nuclei, centralities and energies.

of strings [192,220] where the area covered by strings increases with the energy and the size of the nuclei leaving less room for hard scatterings.

Let us mention that the scaling found is naturally incorporated in the CGC [15,16,219], where the p_T spectrum depends only on p_T^2/Q_s^2. In the model of percolation of strings [192,220] a scaling law is also obtained for the p_T-dependence. Now the role of Q_s^2 is played by $\sqrt{\eta}$. Indeed, the parametrization in Eq. (3.1.17) has its origin in the parametrization of $\sqrt{\eta}$ [197].

In conclusion, it has been shown that the geometric scaling seen previously in p-p collisions holds for A-A collisions, being satisfied also at different centralities. For different projectiles and targets an approximate scaling is also satisfied although in this case some differences occur. The departure of the scaling for $\tau > 1$ follows the expected hierarchy in jet quenching, namely, the suppression is larger for larger participant nuclei.

3.2 The near-side ridge structure

Correlations between pairs of hadrons that are collimated in their relative azimuthal angle and are long range in relative rapidity were observed in heavy ion collisions first at RHIC [40,221–225] and later at the LHC [226]. These ridge-like correlations have also been seen in proton-proton collisions at $\sqrt{s} = 7$ TeV and at $\sqrt{s} = 13$ TeV for high multiplicity events [227, 228]. More recently, a sizable ridge has been observed in p-Pb collisions at $\sqrt{s} = 5.02$ TeV [229–233]. Much attention has been paid to understanding whether these structures are due to initial state or to final state effects that are amenable to a hydrodynamic description [199,216,234–245].

The origin of long range rapidity correlations is similar in heavy ion and proton-proton collisions. It is due, in the glasma picture of the Color Glass Condensate (CGC), to the saturation of color flux tubes correlated in the transverse space with a length, $1/Q_s$, determined by the saturation momentum Q_s [237–243]. On the contrary, not much attention has been paid to the onset of the ridge structure. In p-p collisions at $\sqrt{s} = 7$ TeV the structure is only observed for $N_{ch} > 110$, and in p-Pb collisions at $\sqrt{s} = 5.02$ TeV for $N_{ch} \gtrsim 50$ [2]. Moreover, in Au-Au collisions at $\sqrt{s} = 200$ GeV and $\sqrt{s} = 62$ GeV an anomalous centrality dependence of the correlation is observed: the strength of the near-side ridge as a function of multiplicity presents a change on the behavior of the slope for $N_{ch} = 120$ and $N_{ch} = 130$, respectively [246].

All these features can be understood in the framework of percolation of strings, as it will be shown in this section. As the number of strings formed in a collision reaches the universal critical density, η_c, a macroscopic cluster of strings appears covering around 2/3 of the total collision area [177]. As the density approaches the critical value the ridge structure begins to unfold. The dependence of the strength of the near-side ridge on the multiplicity in a given collision reflects the fraction of the collision area covered by strings which is related to the profile function of the colliding objects.

The goal of this section is not to give a detailed description of the azimuthal dependence of the ridge structure, but to show that its onset can be explained in the framwork of percolation of strings. Nevertheless, a brief discussion on how the collimated ϕ-distribution of the near-side ridge arises in our approach is included.

3.2.1 The near-side ridge in the SPM

As it has been seen, the strings are the basic ingredients of the SP models. It is necessary to know their number, rapidity extension, fragmentation, and probability distribution, which depend on the chosen model. This model dependence is not strong because in most of the color exchange string models, as dual parton model (DPM) [247, 248], quark-gluon string model [249], VENUS [185] or EPOS [250], the results for the mentioned observables are very similar. In this section the DPM is used. In this model, $2k$ strings are produced in p-p collisions. Two of them stretched between a valence diquark of the projectile (target) and a valence quark of the target (projectile) and $2k-2$ strings stretched between sea quarks and antiquarks. Due to the momentum distribution functions of the valence diquarks, valence quarks, and sea quarks or antiquarks, $x^{3/2}$, $x^{-1/2}$ and x^{-1}, respectively, the rapidity extension of the $(qq)_v - q_v$ strings is in between one edge of the rapidity range and the central rapidity region. On the contrary the $q_s - \bar{q}_s$ strings are in the central rapidity region which approximately grows – in rapidity extension – proportional to the longitudinal phase space, that is, proportional to $\ln s$. The mean number of strings at a given energy is determined by the cross section of producing $2k$ strings, σ_{2k}, corresponding to cut k Pomerons. At not very high energy, there are only contributions from the two $(qq)_v - q_v$ strings. As the energy

[2] N_{ch} is the number of charged particles created in a particular collision.

increases, there are more and more contributions of the $q_s - \bar{q}_s$ type. In the case of A-A collisions, the rapidity distribution is approximately given by [248]

$$\begin{aligned}\frac{dN}{dy} &\approx \langle N_A \rangle \left[2N^{(qq)_v - q_v}(y) + 2(\langle k \rangle - 2) N^{q_s - \bar{q}_s}(y) \right] \\ &+ (\langle N_C \rangle - \langle N_A \rangle)\, 2 \langle k \rangle\, N^{q_s - \bar{q}_s}(y) \ , \end{aligned} \tag{3.2.23}$$

where $\langle N_A \rangle$ and $\langle N_C \rangle$ are the mean number of participants (divided by two) and collisions, obtained in the Glauber-Gribov model [251]. $N^{(qq)_v - q_v}(y)$ and $N^{q_s - \bar{q}_s}(y)$ are the rapidity distributions of the corresponding $(qq)_v - q_v$ and $q_s - \bar{q}_s$ strings.

As we have seen, the strings decay into new ones by $q - \bar{q}$ and $qq - \bar{q}\bar{q}$ pair production and, subsequently, hadronize producing the observed particles. At high energies the strings overlap forming clusters. The behavior of a cluster of n strings has already been explained in the beginning of this chapter. The multiplicity and transverse momentum of the particles produced by a cluster in the high density limit are given by Eq. (3.0.8), where $F(\eta)$ is given by Eq. (3.0.9).

The area covered by clusters divided by the area of an effective cluster gives the effective average number $\langle N \rangle$ of clusters,

$$\langle N \rangle \ = \ \frac{(1 - e^{-\eta}) R^2}{r_0^2 F(\eta)} \ = \ \sqrt{1 - e^{-\eta}}\, \sqrt{\eta} \left(\frac{R}{r_0} \right)^2 \ , \tag{3.2.24}$$

where R is the radius of the collision area [3].

The energy-momentum of the cluster of strings is the sum of the energy-momentum of the individual strings. As in the central rapidity region the main contribution, according to the Eq. (3.2.23), comes from the $q_s - \bar{q}_s$ strings, whose number is proportional to $(N_C - N_A)$, the mean rapidity extension of one string should be

$$\Delta y_1 \ = \ c_1 \left(1 - \frac{N_A}{N_C} \right) \ln \left(\frac{s}{s_0} \right) \ , \tag{3.2.25}$$

where s_0 is the minimum energy required for the creation of a single string able to decay into two particles. We take $s_0 = 1$ GeV^2.

As each cluster contains, on average, $N_s/N = 1/F(\eta)$ strings, the rapidity length of these effective clusters is

$$\begin{aligned}\sigma_{\Delta y} &= \Delta y_1 - \ln F(\eta) \ = \\ & c_1 \left(1 - \frac{N_A}{N_C} \right) \ln \left(\frac{s}{s_0} \right) + \ln \left(\sqrt{\frac{\eta}{1 - e^{-\eta}}} \right) \ . \end{aligned} \tag{3.2.26}$$

[3] For non central collisions, the corresponding area S of the almond shape should be used. In this case, instead of $(R/r_0)^2$, S/S_1 should be employed.

This is the rapidity width of the near-side ridge. The constant c_1 does not depend neither on N_A, N_C, nor on the center of mass energy.

The normalized two-particle correlation function, $\mathcal{R} = 1/k$, was written in terms of the multiplicity in Eq. (3.0.11) and in terms of the number of strings in Eq. (3.0.15). It was already discussed that in both the large density and small density limits $k \to \infty$, and that k has a minimum close to the critical string density, η_c. A parametrization of k satisfying these requirements is [199]

$$k \;=\; \frac{\sqrt{\eta}\,(R/r_0)^2}{1-e^{-\eta}} \;=\; \frac{\langle N\rangle}{(1-e^{-\eta})^{3/2}} \;. \tag{3.2.27}$$

Any other possible parametrization with the above requirements cannot be very different from Eq. (3.2.27) in the η range around the critical value.

The experimental data on Au-Au at 62 GeV and 200 GeV measure $\Delta\eta/\sqrt{\eta_{ref}}$, where $\Delta\eta$ is the difference between the pair distribution of the same collision and the uncorrelated pair distribution, η_{ref}, obtained from mixed events. It has been shown that this quantity is proportional to $\mathcal{R}\,dn/dy$ (see appendix C of reference [246]). The data on the near-side ridge structure are fitted, obtaining the value of its strength, A_1, for different centralities at the two different energies by STAR Collaboration. Hence, we can write

$$\frac{\Delta\eta}{\sqrt{\eta_{ref}}} = \mathcal{R}\,\frac{dn}{dy}\,G(\phi) \;, \tag{3.2.28}$$

where $G(\phi)$ encodes all the azimuthal dependence. This factorized form was used before in the framework of the CGC [230, 252].

From equations (3.0.15), (3.2.24), (3.2.26), and (3.2.27) we deduce

$$\mathcal{R}\frac{dn}{dy} \;=\; \frac{\langle N\rangle}{k} \;=\; \left(1-e^{-\eta}\right)^{3/2} \;. \tag{3.2.29}$$

As previously mentioned, the factor $1-e^{-\eta}$ is the fraction of the collision surface covered by strings, assuming a homogeneous profile [191]. For more realistic profiles this shape is modified. For Gaussian and Wood-Saxon profiles, the critical density is not $\eta_c \approx 1.2$, but $\eta_c \approx 1.5$, and the fraction of the collision area covered by strings is more similar to [51]

$$A(\eta) \;=\; \frac{1}{1+a\,e^{-(\eta-\eta_c)/b}} \;, \tag{3.2.30}$$

where $\eta_c = 1.5$. The parameter b controls the ratio between the edge, $2\pi R$, and the total surface, πR^2, and, therefore, is proportional to the inverse of the radius. Thus, instead of using $1-e^{-\eta}$ in Eq. (3.2.29), $A(\eta)$ is used, and from Eq. (3.2.28) we have

$$A_1 \;=\; c\,A^{3/2}(\eta) \;. \tag{3.2.31}$$

The conventional understanding of the ridge is simply related to flow harmonics in a fluid dynamic scenario, where the inclusion of the p-p and p-A ridges has been a challenge. In string percolation, the fragmentation of a single string gives a rather flat ϕ-distribution. In the 3-dimensional space the string becomes non orthogonal to the transverse plane and one may expect an anisotropic emission of particles in this plane, though this anisotropy is very small [253]. However, a cluster of overlapping strings has an asymmetric form in the transverse plane and the partons emitted at the same point inside the cluster have to pass through a certain length before appearing outside – and being observed. Along this path, they interact with the strong color field inside the cluster and their energy decreases. As a result, an observed particle with transverse momentum p_T was born inside the cluster with a higher momentum, whose value depends on the path length travelled inside the cluster. Consequently, this moment is different for the different directions of emission. As the transverse distribution of the strings depends on the form of the nuclear overlapping, so does the azimuthal distribution of strings and of the cluster of strings. These two anisotropies lead to the anisotropy of the spectrum of emitted particles. In this way, a reasonable agreement is obtained with the experimental data on v_2 [253] and higher harmonics [254]. The role of energy loss in the understanding of flow harmonics will be addressed in Section 3.3.

The narrow structure in the azimuthal dependence of the near-side ridge is determined by the transverse correlation length which, according to Eq. (3.0.8), is $r_0 F(\eta)^{1/2}$. Hence, the width of the azimuthal angle is

$$\sigma_{\Delta\phi} = c_2 \left(\frac{1 - e^{-\eta}}{\eta} \right)^{1/4} . \tag{3.2.32}$$

Eq. (3.2.32) is only a rough evaluation of the width of the ridge structure and, hence, the comparison with data should be considered carefully. In order to do a more detailed comparison a Monte Carlo simulation is necessary. The first results of this simulation agree with the experimental data on the near-side width for p-p, p-Pb and Au-Au collisions [255].

3.2.2 Results

In order to compare with the experimental data on the strength of the near-side ridge Eq. (3.2.30) is used. The expression $A_1 = cA(\eta)^{3/2}$ is fitted to the data on Au-Au collisions at $\sqrt{s} = 200$ GeV and $\sqrt{s} = 62$ GeV, and p-Pb and p-p collisions at $\sqrt{s} = 5.02$ TeV and $\sqrt{s} = 7$ TeV, respectively. To do this, the values of η are needed. These are taken from a previous study in the framework of string percolation of dN/dy at SPS, RHIC and LHC energies for p-p and A-A at different centralities [197, 198]. In the case of p-p and p-Pb to compute η the collision area of references [243] and [244] are used. The values of η for Au-Au collisions at $\sqrt{s} = 200$ GeV for the different centralities are in the range $0.6 - 3.0$. For p-Pb at $\sqrt{s} = 5.02$ TeV these values go from $\eta = 0.8$ and $\eta = 2.3$, corresponding to $N_{ch} = 50$ and $N_{ch} = 330$, respectively. Finally, for p-p collisions at $\sqrt{s} = 7$ TeV the values are between $0.25 - 0.7$, corresponding to $N_{ch} = 18$ (minumum bias) and $N_{ch} = 110$, respectively. In high multiplicity p-p collisions at the LHC, the values of η are close to the values obtained in peripheral Cu-Cu collisions at RHIC energies, where a ridge structure was observed. This

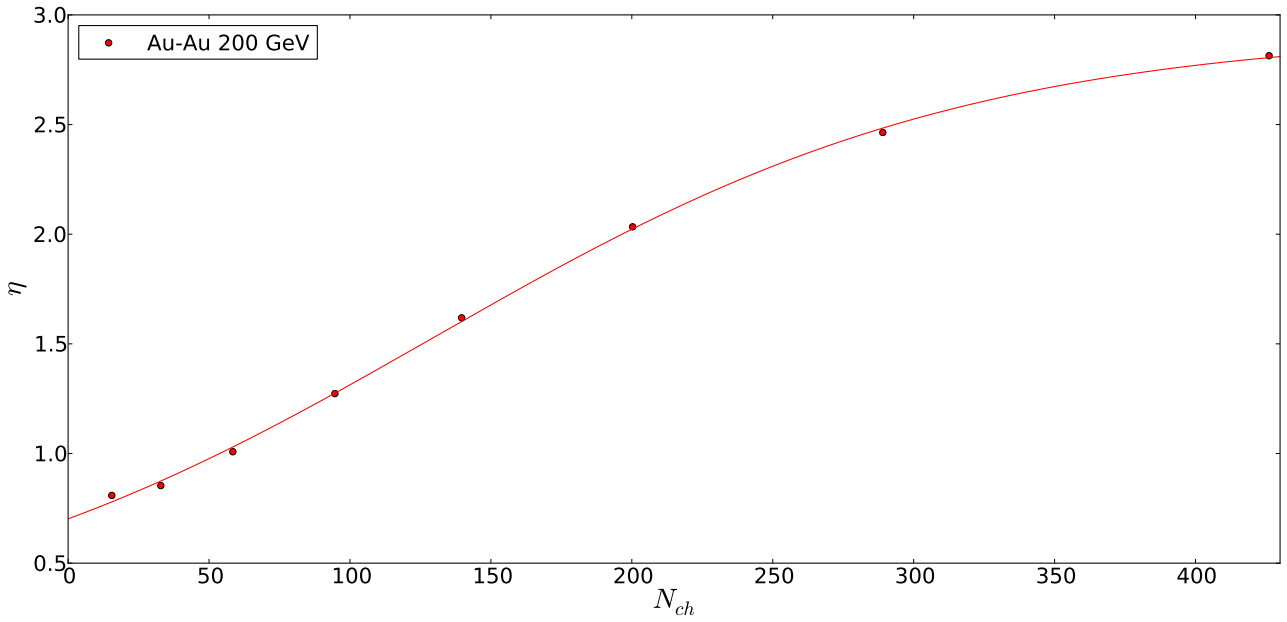

Figure 3.8: String density η versus N_{ch} for Au-Au collisions at $\sqrt{s} = 200$ GeV.

	Au-Au 200 GeV	Au-Au 62 GeV	pPb	p-p
a	1.5	1.5	1.5	1.5
b	0.75	0.75	0.35	0.35
c	0.93	0.80	0.21	0.57

Table 3.2: Values of parameters a, b and c for the different collisions.

fact was the main reason to predict [216] the near-side ridge later observed. An example of the dependence of η on centrality is shown in Fig. 3.8 for Au-Au collisions at $\sqrt{s} = 200$ GeV.

In Fig. 3.9 the strength, A_1, of the near-side ridge versus the number of charged particles for Au-Au collisions at $\sqrt{s} = 200$ GeV and $\sqrt{s} = 62$ GeV is shown. The parameter a is fixed, $a = 1.5$. The value of b obtained is $b = 0.75$. In Fig. 3.10 the corresponding results for p-Pb and p-p collisions are plotted. In this case, the parameters are $a = 1.5$ and $b = 0.35$. The values of a, b and c for the different collisions are summarized in Table 3.2.

The values of b obtained for the p-Pb and p-p cases are much smaller than for Au-Au collisions, as expected. The string density in p-Pb at $N_{ch} = 50$ – where the near-side ridge structure emerges – is $\eta = 0.8$. In the p-p case the near-side ridge structure unfolds at $N_{ch} = 100$, corresponding to $\eta = 0.7$, very close to the one obtained for p-Pb collisions. Notice that, apart from the normalization constant c, different for the three type of collisions, the parameters $\eta_c = 1.5$ and $a = 1.5$ are fixed for all the considered collisions, keeping b as the only fitting parameter. Even this parameter is not fully free because its dependence on

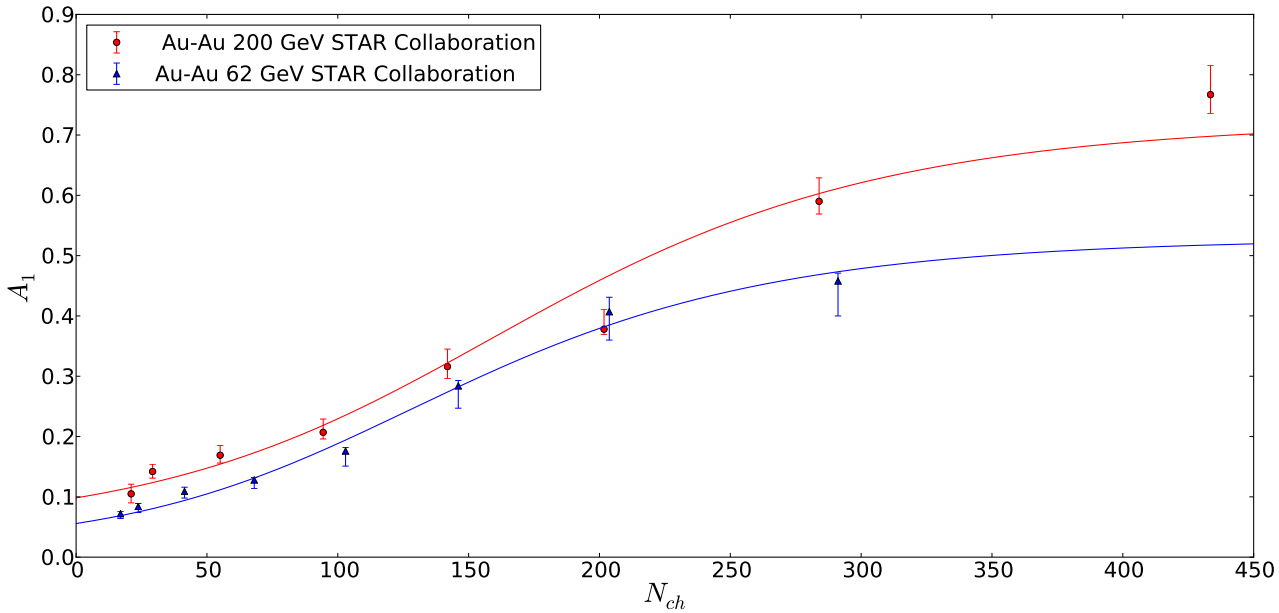

Figure 3.9: Comparison between our results on the strength of the near-side ridge for Au-Au collisions at two RHIC energies $\sqrt{s} = 200$ GeV (red line) and $\sqrt{s} = 62$ GeV (blue line) with experimental data [246] versus N_{ch}.

the nucleus radius should be similar to $1/R$, as it is obtained.

The pseudorapidity width, obtained from Eq. (3.2.26), compared with the experimental data on Au-Au at $\sqrt{s} = 200$ GeV and $\sqrt{s} = 62$ GeV [246] is shown in Fig. 3.11. The value of c_1 is 0.23. N_A and N_C are taken from the quoted experimental analysis [256]. It is observed that our result for $\sqrt{s} = 200$ GeV is slightly larger than the corresponding one at $\sqrt{s} = 62$ GeV. Experimental data are very close at both energies.

In Fig. 3.12 experimental data on the azimuthal width for Au-Au collisions at $\sqrt{s} = 200$ GeV and $\sqrt{s} = 62$ GeV [246] are compared to our model. The values of c_2 are: $c_2 = 0.866$ for Au-Au at $\sqrt{s} = 200$ GeV, and $c_2 = 0.890$ for Au-Au at $\sqrt{s} = 62$ GeV. Increasing energy and centrality, the azimuthal width decreases, in agreement with the trend of the experimental data. For both widths a qualitative agreement is obtained.

The dependence of A_1, $\sigma_{\Delta\eta}$, and $\sigma_{\Delta\phi}$ on energy and centrality, resulting from equations (3.2.29) and (3.2.30), is very similar to the one obtained in the glasma picture. In this approach, $\mathcal{R}dN/dy$ and $\sigma_{\Delta\eta}$ are proportional to $1/\alpha_s(Q_s)$ and $\sigma_{\Delta\phi}$ is proportional to $1/Q_s$. Hence, both $\mathcal{R}dN/dy$ and $\sigma_{\Delta\eta}$ grow with $\ln s$ and $\ln N_A$. In the high density limit, the same dependence on the center of mass energy and on the number of participants for both observables is obtained in percolation . In the case of $\sigma_{\Delta\phi}$, as $1/Q_s \sim N_A^{1/6} s^{\Delta/2}$ and $r_0 F(\eta)^{1/2} \sim r_0 \eta^{1/4} \sim r_0 N_A^{1/6} s^{\Delta/2}$.

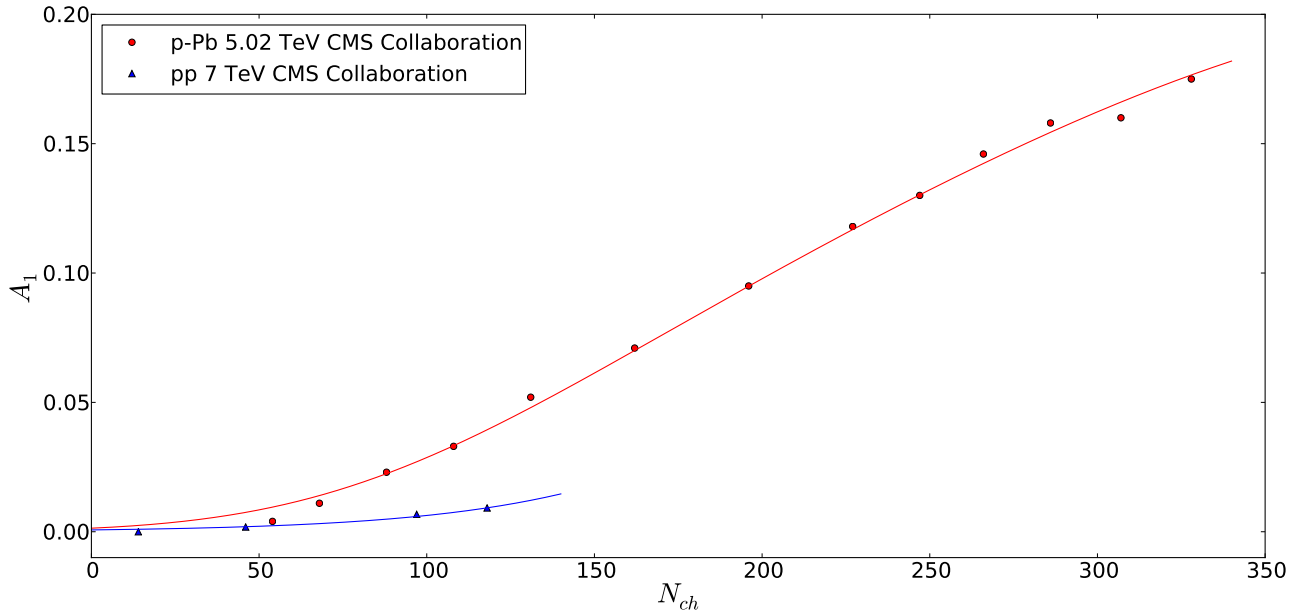

Figure 3.10: Comparison between our results on the strength of the near-side ridge for p-p collisions at $\sqrt{s} = 7$ TeV (blue line) and p-Pb collisions $\sqrt{s} = 5.02$ TeV (red line) with experimental data [229] versus N_{ch}.

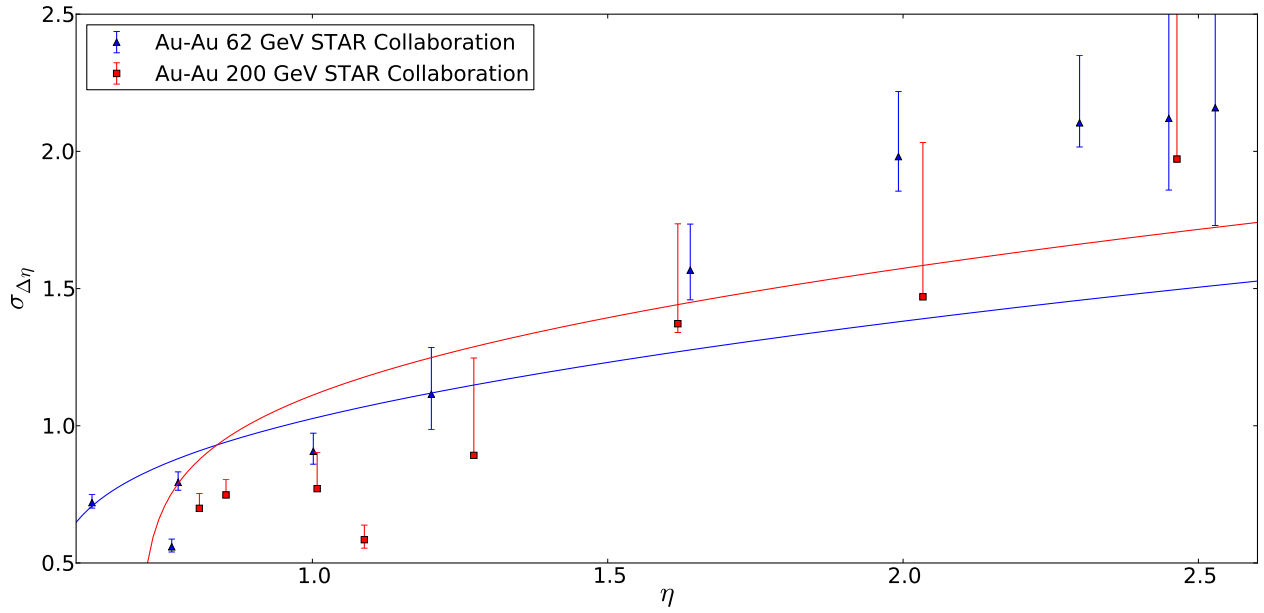

Figure 3.11: Pseudorapidity width of the near-side ridge for Au-Au collisions at two RHIC energies $\sqrt{s} = 200$ GeV and $\sqrt{s} = 62$ GeV [246] versus η. Curves obtained from Eq. (3.2.26) for Au-Au collisions at $\sqrt{s} = 200$ GeV (red) and $\sqrt{s} = 62$ GeV (blue).

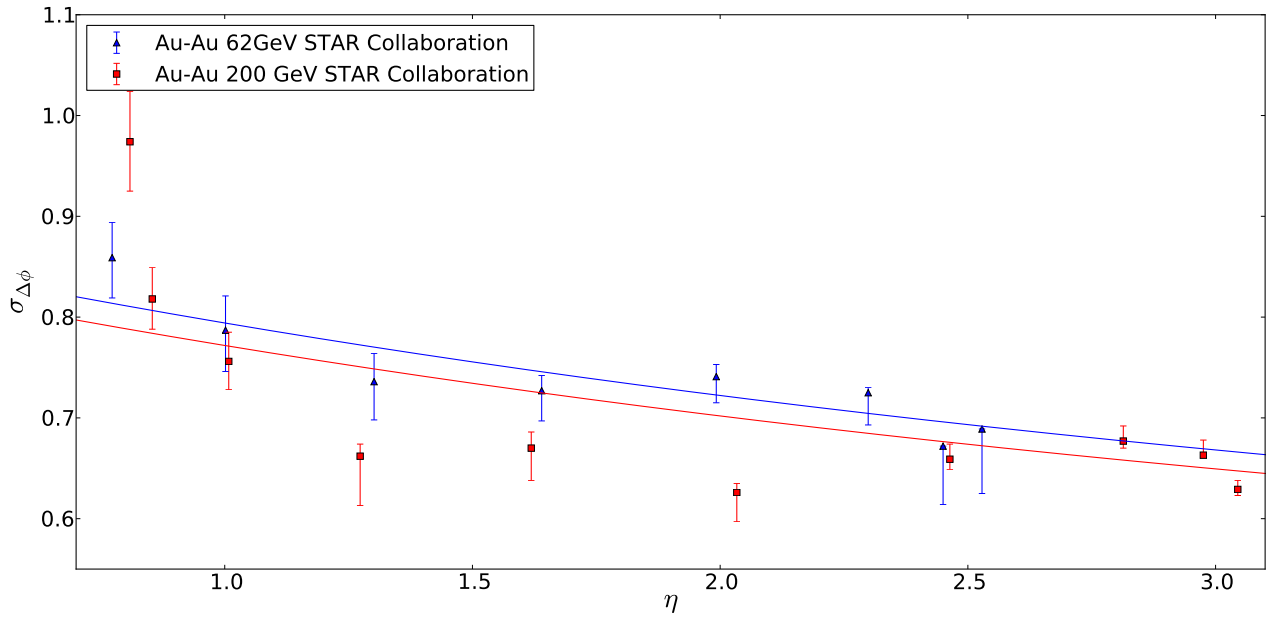

Figure 3.12: Azimuthal width of the near-side ridge for Au-Au collisions at $\sqrt{s} = 200$ GeV and $\sqrt{s} = 62$ GeV [246] versus η. Curves obtained from Eq. (3.2.32) for Au-Au collisions at $\sqrt{s} = 200$ GeV (red) and $\sqrt{s} = 62$ GeV (blue).

To conclude, it has been shown that percolation of strings may naturally explain the anomalous dependence of the near-side ridge structure correlation on the multiplicity observed in Au-Au collisions at $\sqrt{s} = 200$ GeV and $\sqrt{s} = 62$ GeV. The onset of the ridge structure in high multiplicity p-p events at $\sqrt{s} = 7$ TeV and in high multiplicity p-Pb at $\sqrt{s} = 5.02$ TeV is also explained. Furthermore, our model qualitatively describes the dependence of the azimuthal and pseudorapidity widths on multiplicity. Our framework can be regarded as a complementary picture to the glasma in the description of the initial state, able to explore the transition from low to high density. Most of the ingredients used here can be considered initial state effects, although the quenching of the partons produced in the cluster of strings is a final state effect.

3.3 Geometric scaling of elliptic flow

The discovery of a sizable elliptic flow in A-A collisions, first observed at RHIC [7, 8] and later at the LHC [257], turned up as an experimental major breakthrough. The observed anisotropic flow can be exclusively understood if the measured particles in the final state depend not only on the physical conditions realized locally at their production point, but also on the global geometry of the event. This non-local information can solely emerge as a collective effect, requiring strong interactions among the relevant degrees of freedom, i.e. quarks

and gluons. The study of higher harmonics has also shown very interesting features, including the ridge structure seen in A-A collisions [221, 222, 225, 226], p-Pb collisions [229, 230] and also in high multiplicity p-p collisions [227], which was analyzed in Section 3.2.

Along these lines, it is pointed out that some scaling laws satisfied by the elliptic flow could be very useful to determine some properties of the initial stage of the collision which should be preserved by the hydrodynamic evolution [258]. The experimental data on the elliptic flow of charged particles showed up a universal scaling law related to the gluon saturation momentum. This scaling law is also satisfied by the photon data, suggesting that the elliptic flow of charged particles and photons should have a common origin.

3.3.1 Universal scaling law

The experimental data for v_2 at RHIC and at the LHC normalized to the saturation momentum, eccentricity, and radius of the collision area satisfy geometric scaling:

$$\frac{v_2(p_T)}{\epsilon_1 Q_s^A L} \;=\; f(\tau) \;, \tag{3.3.33}$$

where

$$\epsilon_1 \;=\; \frac{2}{\pi}\int_0^{\pi/2} d\varphi\, \cos 2\varphi \frac{R^2 - R_\varphi^2}{R^2} \;, \quad R_\varphi \;=\; \frac{R_A \sin(\varphi-\alpha)}{\sin\varphi} \;, \tag{3.3.34}$$

$$\alpha \;=\; \arcsin(\frac{b}{2R_A}\sin\varphi) \;, \quad R^2 \;=\; \langle R_\varphi^2\rangle \;=\; \frac{2}{\pi}\int_0^{\pi/2} d\varphi\, R_\varphi^2 \;, \tag{3.3.35}$$

and

$$\tau = \frac{p_T^2}{(Q_s^A)^2} \;, \tag{3.3.36}$$

being Q_s^A the saturation momentum, R_A the radius of the nucleus, and L the length associated to the size of the collision area at a given impact parameter and energy. Indeed, the product $Q_s^A L$ is the inverse of the Knudsen number, i.e., the mean free path normalized to the length measured as the number of scattering centers. The scaling law (3.3.33) is tested in the range $0 < \tau < 1$.

ϵ_1 is a measurement of the eccentricity of the collision. It does not depend on the distribution of scattering centers – partons or nucleons in the transverse plane. It is only determined by the almond shape of the collision at a given impact parameter.

The scaling variable τ is known from the geometric scaling verified in DIS, p-p, p-A, and A-A collisions [195, 196, 259–261]. That is, $\tau = p_T^2/\left(Q_s^A\right)^2$, where, now,

$$\left(Q_s^A\right)^2 \;=\; (Q_s^p)^2\, A^{\beta(s)/2}\, N_A^{1/6} \;, \tag{3.3.37}$$

being N_A the number of wounded nucleons. $\beta(s)$ and the proton saturation momentum, Q_s^p, are given, respectively, by equations (3.1.18) and (3.1.16)[4].

[4]Note that the definition of Q_s^A has been slightly modified from the one given in 3.1.17.

3.3.2 Discussion

In Fig. 3.13 (a), $v_2(p_T)$ for Au-Au collisions for different centralities at RHIC [262], and for Pb-Pb collisions at LHC [257] divided by the product $\epsilon_1 Q_s^A L$ computed for each centrality and energy is plotted. The usual values of b and N_A for each centrality are taken, in order to compute ϵ_1 and Q_s^A using Eqs. (3.3.34) and (3.3.35), and Eq. (3.3.37), respectively. The length, L, measures the number of longitudinal scatterings, which in the Glauber model is proportional to $N_A^{1/3}$. Nevertheless, $(1 + N_A^{1/3})/2$ is employed, as in most of the strings models, DPM [247, 248], quark gluon string model [249], Venus [185], and EPOS [250]. The values of b, N_A and ϵ_1 for each centrality and energy are shown in Table 3.3.

$\sqrt{s}$	200 GeV (PHENIX)				2.76 TeV (ALICE)			
Centrality	10-20 %	20-30 %	30-40 %	40-50 %	10-20 %	20-30 %	30-40 %	40-50 %
$b\ (fm)$	5.7	7.4	8.7	9.9	5.6	7.4	8.9	10.1
N_A	117.3	83.3	57.1	37.2	130.05	92.9	64.25	42.35
ϵ_1	0.208	0.286	0.356	0.436	0.172	0.238	0.300	0.357

Table 3.3: Values of the impact parameter, $N_A = N_{part}/2$ and ϵ_1 for PHENIX [256] and ALICE [263] at different centralities.

The solid black line in this figures corresponds to a fit to these data, given by

$$\frac{v_2}{\epsilon_1 Q_s^A L} = a\tau^b \ , \tag{3.3.38}$$

where $a = 0.1264 \pm 0.0076$ and $b = 0.404 \pm 0.025$. Fig 3.13 shows that this scaling is satisfied.

In order to see the quality of this scaling, the ratio of Pb-Pb $10-20$ % at 2.76 TeV, Pb-Pb $40-50$ % at 2.76 TeV, Au-Au $20-30$ % at 200 GeV and Au-Au $30-40$ % at 200 GeV over Pb-Pb $30-40$ % at 2.76 TeV as a function of τ is shown in Fig. 3.13 (b) . All the ratios lie in the range $0.8-1.15$ for the whole τ considered, showing that the scaling is quite good [5].

The experimental data used in Fig. 3.13 correspond to event plane [262] and 4-particle cumulant measurements and, therefore, include some amount of fluctuations. As in the scaling law of Eq. (3.3.33) the quantities ε_1, Q_s^A, and L have nothing to do with fluctuations, the latter could give rise to the residual differences between the experimental data and the function $f(\tau)$ of Eq. (3.3.33).

Changing the eccentricity, ϵ_1, by the usual eccentricity, $\epsilon = \langle y^2 - x^2 \rangle / \langle y^2 + x^2 \rangle$, or by the participant eccentricity, the scaling is not satisfied for both Monte-Carlo Glauber and Color Glass distributions. This fact does not mean that the initial state should give the

[5] Most of the experimental error data are of the order of 10 %.

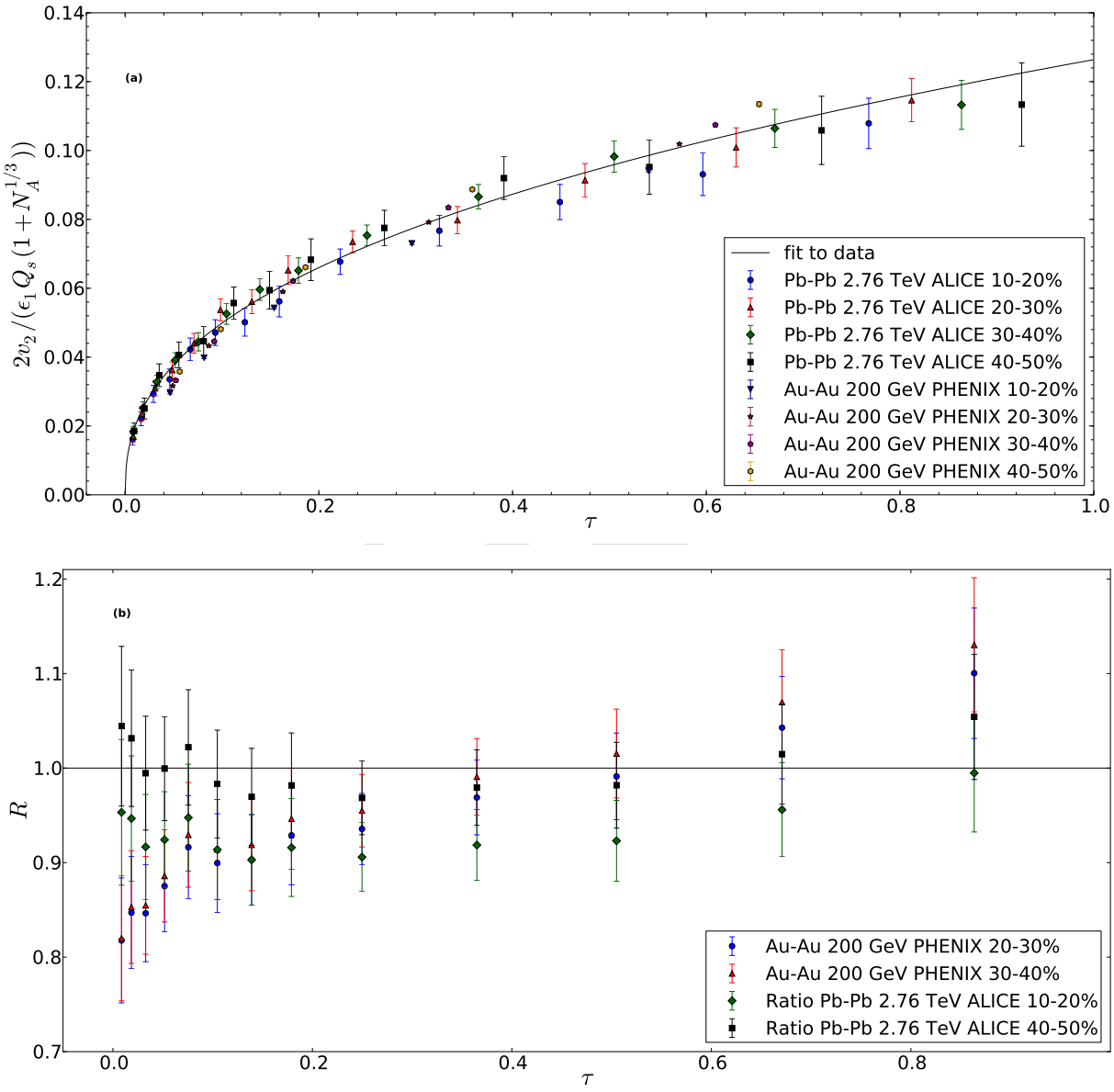

Figure 3.13: **(a)** v_2 divided by the product $\epsilon_1 Q_s^A L$ for $10-20$ %, $20-30$ %, $30-40$ % and $40-50$ % Au-Au collisions at 200 GeV [262], and for $10-20$ %, $20-30$ %, $30-40$ % and $40-50$ % Pb-Pb collisions at 2.76 TeV [257] versus τ. The solid black line is a fit to data according to Eq. (3.3.38). **(b)** Ratio of Pb-Pb $10-20$ %, Pb-Pb $40-50$ % at 2.76 TeV [257] , Au-Au $20-30$ %, and Au-Au $30-40$ % at 200 GeV [262] over Pb-Pb $30-40$ % at 2.76 TeV [257] versus τ.

corresponding eccentricity of a hard profile, such as it is defined in Eq. (3.3.34). Probably, the scaling law could be preserved using other eccentricities, but in this case some changes in the dependence of L and N_A are necessary.

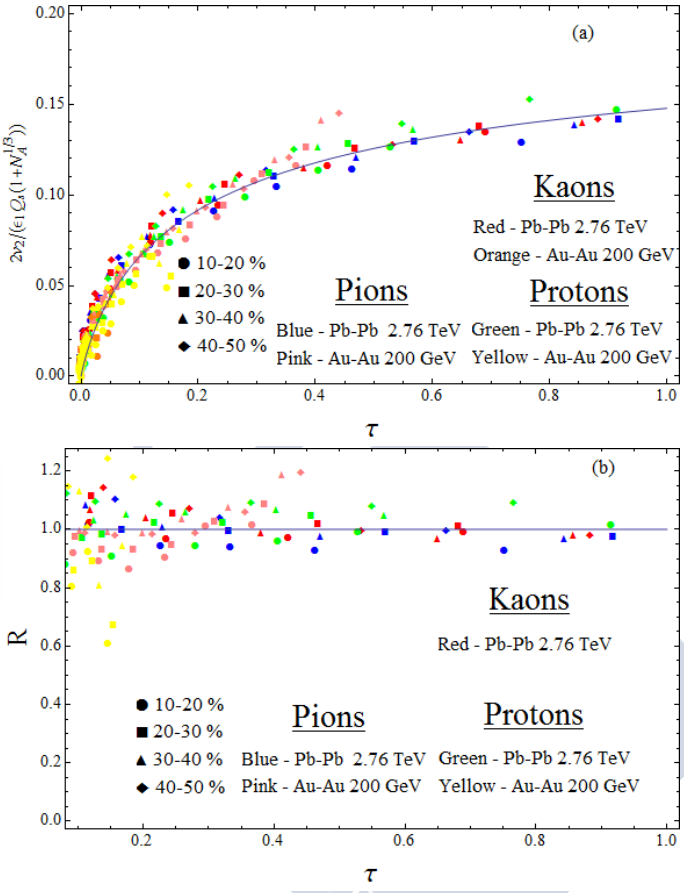

Figure 3.14: **(a)** v_2 of π, k and p divided by the product $\epsilon_1 Q_s^A L$ for $10-20$ %, $20-30$ %, $30-40$ % and $40-50$% Au-Au collisions at 200 GeV [269], and for $10-20$ %, $20-30$ %, $30-40$ % and $40-50$ % Pb-Pb collisions at 2.76 TeV [271] versus τ, for $\tau < 1$. The solid line is a fit to Eq. (3.3.39). **(b)** Ratio of the experimental points over the fitting function Eq. (3.3.39) versus τ, for $0.1 < \tau < 1$.

The scaling law is also satisfied for specified particles, such as pions, kaons, and protons, as it can be seen in Fig. 3.14. In the proton case, an effective transverse momentum, $Q_s'^A$, instead of Q_s^A, $\left(Q_s'^A\right)^2 = N_s^{0.045}\left(Q_s^A\right)^2$, where N_s is the number of strings, has been used. It is known that for central collisions the ratio baryon/meson increases with p_T up to a moderate value of transverse momentum. In central collisions, due to the strong color field formed, the color flux tubes in the glasma picture or the cluster of strings in the SPM have a larger string tension, producing high mass particles more efficiently. In addition to that, inside a cluster of many strings the flavor of each single string recombines with the flavor

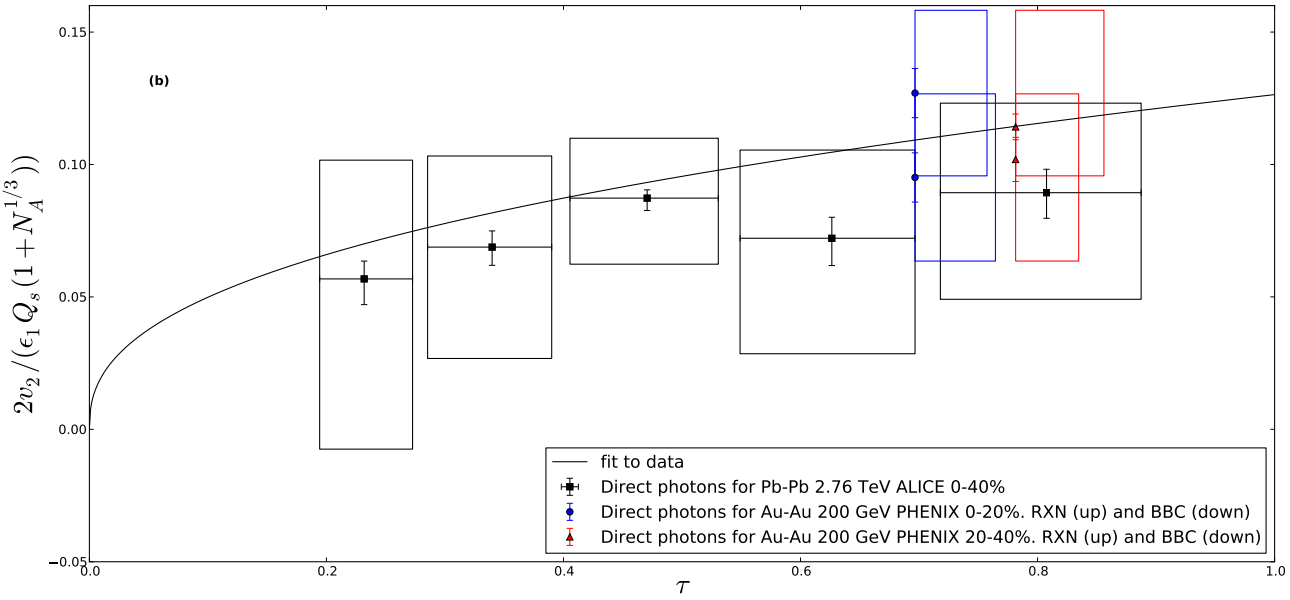

Figure 3.15: v_2 divided by the product $\epsilon_1 Q_s^A L$ for direct photons at $0-20$ % and $20-40$ % Au-Au collisions at 200 GeV [269] and direct photons at $0-40$ % Pb-Pb collisions at 2.76 TeV [270] versus τ. The solid black line is the scaling curve of Fig. (3.13). All the data with $p_T < Q_s$ have been included.

of other strings, producing also baryons more efficiently. Concerning the p_T-distributions, these two effects can be taken into account in an effective way, defining a $Q_s'^A$ for baryon production, related to Q_s^A by a factor which was obtained in [264]. This was done by fitting the dependence of the ratio of the p_T-integrated nucleon distribution over the p_T-integrated pion distribution on the number of collisions, and, so, on the number of strings, N_s. For this study data from PHENIX are used [265], resulting in a $N_s^{0.09}$ dependence which, in terms of Q_s^2, is $N_s^{0.045}$ [199]. It is observed in Fig. 3.14 that all the data lie, approximately, in the same curve, parametrized by

$$\frac{v_2}{\epsilon_1 Q_s^A L} = \frac{\tau}{a + b\tau + c\sqrt{\tau}} \ , \tag{3.3.39}$$

with $a = 0.573 \pm 0.011$, $b = 4.76 \pm 0.23$ and $c = 1.52 \pm 0.34$.

Although in this case the scaling is not as accurate as the obtained for charged particles, a good agreement for $\tau > 0.1$ is obtained. The discrepancies are not higher than 20 % for most of the experimental points. For $\tau < 0.1$ a great departure occurs, probably motivated by the precision of our fit in this low τ region and the proximity with Λ_{QCD}. Points in this region are not shown in Fig. 3.14 (**b**) in order to keep a good visibility of the remaining points to evaluate the scaling law.

Data on v_2 for p-Pb collisions have not been included in these analysis due to the uncer-

tainties in the values of N_A at a given impact parameter.

In addition, since direct photon production satisfies geometric scaling [261], its elliptic flow may be of the same size and p_T shape of the rest of particles. In order to check this point, in Fig. 3.15, ALICE data [270] and the PHENIX data [269] at different centralities are plotted. PHENIX Collaboration quote two different points at the same p_T and centrality obtained by different analysis methods (BBC and RXN detectors). In any case, data are close to the scaling curve.

The scaling law of elliptic flow cannot be derived from the geometric scaling of the multiplicities in a simple way [272]. Thus, it would be interesting to know the origin of the v_2-scaling law and the role played by saturation on it. Moreover, it would be also worth looking at the possibility of a scaling law similar to Eq. (3.3.33) for higher harmonics. These will be the subjects of the next section.

In summary, it has been shown that experimental data on the elliptic flow of charged particles for Au-Au and Pb-Pb collisions for different centralities at RHIC and LHC energies satisfy a scaling law. The elliptic flow for identified particles, π, k, and p, lies in the same curve. The photon data, despite their large uncertainties, also verify this scaling. Other than the eccentricity, this scaling law involves the number of scatterings and a function which depends only on $p_T^2/\left(Q_s^A\right)^2$. The number of scatterings is the only involved quantity related to final state effects, since the rest of variables have to do with the geometry and the gluon saturation.

3.4 Energy loss as the origin of the scaling law of v_2

In the previous section, Section 3.3, a scaling law for the elliptic flow was obtained, see Eq. (3.3.33). Nonetheless, this scaling could not be derived from the geometric scaling of the transverse momentum distributions described in Section 3.1. The origin of this scaling is the subject of this section. It will be shown here that the interaction of the partons produced in the collision with the color field gives rise to this scaling. Furthermore, a detailed functional form of the scaling which shows a very good agreement with data is obtained.

3.4.1 Energy Loss

To describe the dynamics of particle production at high energies in the soft domain the model of color strings with fusion and percolation [17] is used. As it was already explained, string decays are assumed to follow the Schwinger mechanism of pair production in the strong external field. The momentum distribution of these initial partons is azimuthally isotropic,

$$P(p_0) \;=\; Ce^{-p_0^2/\sigma} \;, \tag{3.4.40}$$

where p_0 is the initial transverse momentum, σ is the string tension, and C the normalization factor. It is important to stress again that p_0 is different from the observed particle transverse momentum, p_T, since the parton has to traverse the cluster area emitting gluons on its way out. Hence, in fact, the momentum distribution of the observed particles has the following form

$$P(p,\phi) \;=\; C\, e^{-p_0^2(p,l(\phi))/\sigma} \;\;, \tag{3.4.41}$$

where ϕ is the azimuthal angle and $l(\phi)$ is the path length inside the nuclear overlap through which the observed particle has passed before being detected.

Note that due to string tension fluctuations, the distribution in Eq. (3.4.40) is transformed into the thermal one

$$P(p_0) \;=\; Ce^{-p_0/T} \;\;, \tag{3.4.42}$$

where the temperature is $T = \sqrt{\sigma/2}$ [273, 274]. In this calculation, the latter thermal distribution is employed.

Radiative energy loss has been extensively studied in the framework of perturbative QCD for a parton traversing the QGP as a result of multiple collisions with the medium scattering centers [275–279] and it will be explained in detail and used in a phenomenological analysis of single-inclusive production in the following chapter. In this case, the physical picture is different: the created parton, with a relatively small transverse momentum, moves in the external gluon field of the string or cluster of strings, which, approximately, can be taken as constant and orthogonal to the direction of the parton. This precludes from application of the perturbative QCD. In the same vein as the mechanism of pair creation, one may assume that the reaction force due to radiation is similar to the QED case, where a charged particle is moving in an external electromagnetic field E. For an ultra-relativistic particle in a very strong field, this force causes an energy loss given by [280]

$$\frac{dp(l)}{dl} \;=\; -012\, e^2\, \left(eEp(l)\right)^{2/3} \;\;, \tag{3.4.43}$$

By integrating this equation, the dependence $p(l)$ on the path length, l, is found. This leads to our quenching formula,

$$p_0\left(p, l(\phi)\right) \;=\; p\, \left(1 + \kappa p^{-1/3} T^{4/3} l(\phi)\right)^3 \;\;, \tag{3.4.44}$$

where the string tension, $eE/\pi = \sigma$, has been identified by comparison with Eq. (3.4.40) and the Schwinger equation for pair creation in a constant electric field. It has also been introduced the dimensionless quenching coefficient κ, taking the role of $0.12e^2$.

The validity of using the QED equation for the QCD case may raise certain doubts. However, it was found using the AdS/CFT correspondence that for the $N = 4$ SUSY Yang-Mills theory the energy loss of a colored charge moving in the external chromodynamic field is essentially given by the same equation as in QED case (see reference [281]).

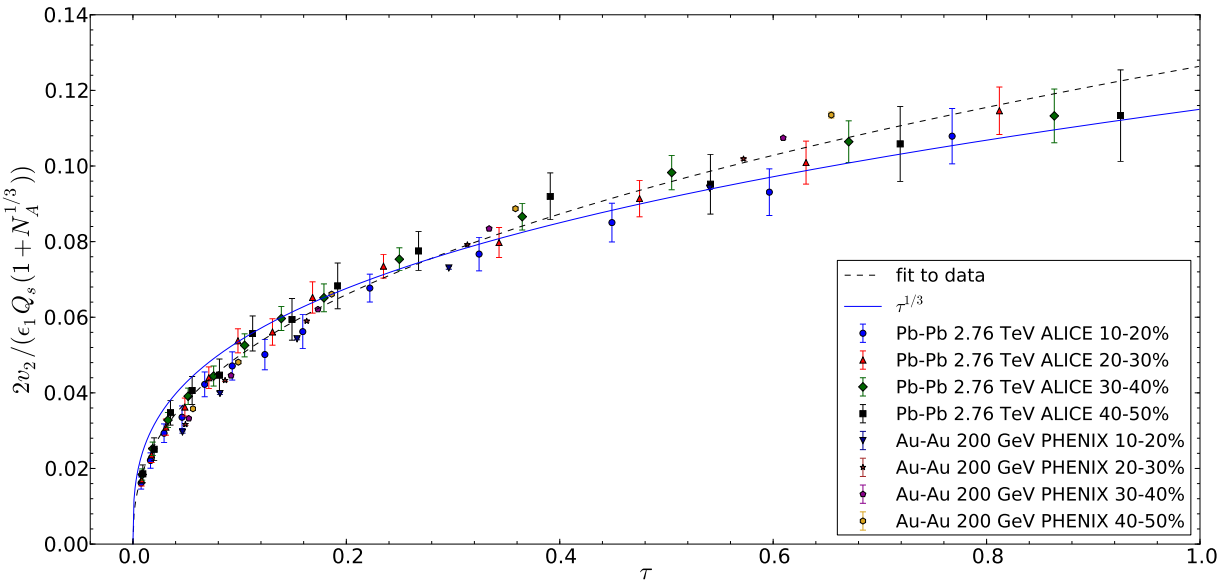

Figure 3.16: v_2 divided by the product $\epsilon_1 Q_s^A L$ for $10-20$ %, $20-30$ %, $30-40$, % and $40-50$ % Au-Au collisions at 200 GeV [262], for $10-20$ %, $20-30$ %, $30-40$ %, and $40-50$ % Pb-Pb collisions at 2.76 TeV [257] versus τ. The dashed black line is a fit to data according to $a\tau^b$ with $a = 0.1264 \pm 0.0076$ and $b = 0.404 \pm 0.025$. The solid blue curve corresponds to $\tau^{1/3}$.

In realistic events, the second term in brackets in Eq. (3.4.44) is small, so Eq. (3.4.44) can be approximated as

$$p_0 \;=\; p\,\left(1+\bar{\kappa}p^{-1/3}T^{4/3}l(\phi)\right)\;\;, \tag{3.4.45}$$

with $\bar{\kappa} = 3\kappa$. Hence, the distribution in p becomes

$$P(p,\phi) \;=\; C\,e^{-p/T}\;e^{-\bar{\kappa}p^{2/3}T^{1/3}l(\phi)}\;\;. \tag{3.4.46}$$

As it can be observed, the strength of the quenching is determined by the exponent in the second exponential in Eq. (3.4.46). This equation allows us to make a crude estimate of the elliptic flow coefficient, v_2. It is expected to be roughly proportional to the strength of the quenching – it vanishes in absence of any quenching. On the other hand, it vanishes when quenching is isotropic in the azimuthal angle, which happens if the nuclear overlap is completely isotropic, i.e, in central collisions. Then, from Eq. (3.4.46) it may be expected

$$v_2 \;\sim\; p^{2/3}\,T^{1/3}\,\epsilon\,L\;\;, \tag{3.4.47}$$

where ϵ is the eccentricity of the nuclear overlap, and L is the path travelled by the particle inside the nucleus averaged over the azimuthal angles. To a good approximation L is proportional to the average number of participants met by the particle on its path. Note that ϵ and L vary with the centrality in the opposite direction. At central collisions ϵ is small but L attains its maximal value, R_A. At peripheral collisions ϵ is large and L is small. As

a result, one expects a rather weak dependence on centrality; which has been confirmed by our previous calculations [254].

Taking – again roughly – $T \sim Q_S^A$ [282], it is found from Eq. (3.4.47) that

$$\frac{v_2}{Q_s^A \epsilon L} \sim \left(\frac{p}{Q_s^A}\right)^{2/3} = \tau^{1/3} . \tag{3.4.48}$$

In Fig. 3.16 the experimental data of PHENIX and ALICE are shown versus $\tau^{1/3}$. Also the best fit of the form $\propto \tau^b$ is shown, which gives a value of b of $b = 0.404$, not very different from 1/3. Taking into account the rather crude approximations in deriving our scaling equation, Eq. (3.4.48), we find this result quite remarkable. It confirms our assumptions about quenching of partons inside the nuclear overlap.

3.4.2 Discussion

The result obtained for the scaling of the elliptic flow indicates that the energy loss due to the interaction of the emitted parton with the color field of the strings is a possible explanation. This description can be extended to collisions of smaller sizes as p-A or p-p collisions. In the case of p-p collisions, from our scaling curve, the v_2 can be obtained once the profile function of the proton, and hence the eccentricity, is assumed. For a Gaussian profile function, for minimum bias p-p collisions at $\sqrt{s} = 13$ TeV, the results for the elliptic flow are the following: 0.03, 0.04, and 0.06 for the τ values: 0.04, 0.18, and 0.5, respectively. These τ values correspond to p_T's of 0.3, 0.6, and 1 GeV/c, respectively. These results on v_2 can be compared to the recent data from ATLAS. For the same p_T's, ATLAS Collaboration gives v_2 = 0.03, 0.035, and 0.05, respectively [283]. These values are for high multiplicity events, but ATLAS obtain a flat dependence of v_2 on multiplicity. CMS Collaboration obtains similar values [284]. Thus, it can be concluded that p-p data lie approximately on the scaling curve. A systematic comparison with more data should be done.

The scaling law $\propto \tau^{1/3}$ is found to be valid for $p_T < Q_s^A$. Notice that for central Pb-Pb collisions at the LHC, Q_s^A is close to 4 GeV/c [260], consequently, the scaling holds for not such low values of p_T. At high p_T, jet quenching and p_T-suppression mechanisms enter into play and the dependence $v_2 \propto p_T^{2/3}$ is not expected to be valid. In fact, the LHC data show that the transverse momentum dependence is proportional to p_T^b with b close to 1/2 [285,286]. This suggests that the scaling form would change from $\tau^{1/3}$ to $\tau^{1/4}$. This happens if at high transverse momenta quenching Eq. (3.4.44) changes into

$$p_0\left(p, l(\phi)\right) = p\left(1 + \kappa p^{-1/2} T^{3/2} l(\phi)\right)^2 . \tag{3.4.49}$$

Note that from this equation, it is concluded that at very large distance, l, the quenching grows as l^2 in agreement with the results obtained in the framework of the perturbative QCD [275]. From Eq. (3.4.49) at small κ and not so large distances, on purely dimensional

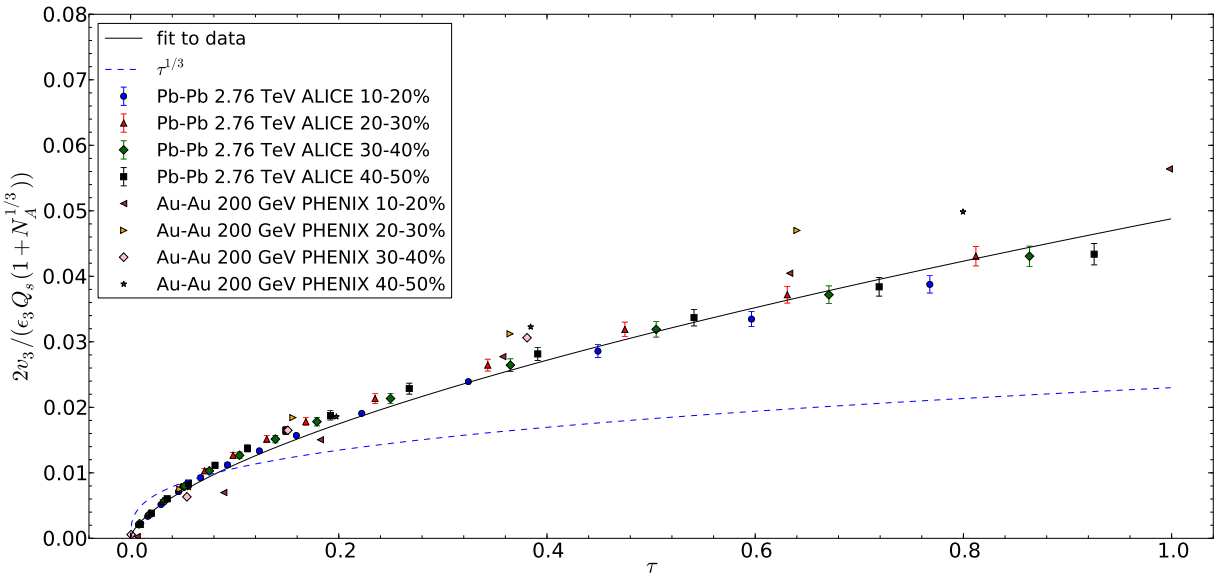

Figure 3.17: v_3 divided by the product $\epsilon_3 Q_s^A L$ for $10-20$ %, $20-30$ %, $30-40$ % and $40-50$ % Au-Au collisions at 200 GeV [287], for $10-20$ %, $20-30$ %, $30-40$ % and $40-50$ % Pb-Pb collisions at 2.76 TeV [288] versus τ. The solid black line is a fit to data. The dashed blue curve corresponds to $\tau^{1/3}$.

grounds, the scaling of Eq. (3.3.33) with $f(\tau) \propto \tau^{1/4}$ is, indeed, obtained.

In order to see whether the energy loss is the common origin of the elliptic flow at both low and high p_T's it would be interesting to perform a systematic comparison of Eq. (3.4.44) and its consequent scaling with experimental data.

Extension of this scaling to higher harmonics is questionable. It is known that v_4 and v_5 are not linear with their corresponding eccentricities, contrary to the v_2-scaling, Eq. (3.3.33). Neither v_3 nor v_5 are purely geometric and come from fluctuations, which implies some additional dynamics for their description. A possible scaling of v_3 in the simplest way, i.e., using eccentricity ϵ_3 in Eq. (3.3.33) has been explored. In Fig. 3.17 v_3 versus τ is plotted. PHENIX and ALICE data on v_3 are used [287, 288] and ϵ_3 is taken from [289] [6].

An approximate scaling is observed, although its quality is not so good as for v_2. However, v_3 does not grow as $\tau^{1/3}$, but considerably faster. This means that the energy loss alone cannot explain the scaling in v_3 and some additional dynamics, probably concerning the initial state, is necessary.

To summarize, energy loss may be regarded as the origin of the geometric scaling of the

[6] In the latter reference multiplicity fluctuations described by a negative binomial distributions are included. The parameter k of these distributions, which determines fluctuations, is related to the nuclear profile function.

elliptic flow obtained in Section 3.3. Possible extensions to smaller participants, such as p-p or p-A collisions, and to higher p_T, assuming that the energy loss mechanism is suitable in these cases, have been discussed. Application to higher harmonics has also been analyzed. In particular, it was shown that v_3 approximately satisfies a similar scaling, although in this case energy loss cannot be its cause.

USC
UNIVERSIDADE
DE SANTIAGO
DE COMPOSTELA

Chapter 4

Suppression of high-p_T particles in HICs

4.1 Jet quenching

Jet quenching is the suppression of high energy particles and jets in the hot nuclear medium formed in HICs. The standard theoretical picture of this phenomenon is that high energy particles lose energy through the multiple interactions with the medium and some of them may eventually thermalize becoming part of the medium and preventing their detection.

The energy loss that a jet or a hard particle experiences when traversing the medium has essentially two different origins: *collisional energy loss* and *radiative energy loss*.

4.1.1 Collisional energy loss

Collisional energy loss was the first mechanism proposed. Collisional energy loss due to soft elastic scatterings of a highly energetic parton with an uniform ideal QGP in thermal equilibrium (at temperature T) in the dominant t-channel was originally estimated by Björken [31] and Braaten-Thoma [290]. The cross sections reads

$$\frac{d\sigma_{js}}{dt} \;=\; 2\pi C_{js}\frac{\alpha_s^2}{t} \;\;, \tag{4.1.1}$$

with $C_{qq} = 4/9$, $C_{qg} = 1$, and $C_{gg} = 9/4$. The 4-momentum transfer squared is represented by the Mandelstam variable t. The energy loss per unit length can be calculated in terms of the flux and the cross section Eq. (4.1.1),

$$\frac{dE_{js}^{coll}}{dx} \;=\; \sum_s \int d^3k\, \rho_s(k)\, \Phi \int dt\, \frac{\sigma_{js}}{dt}\, \omega \;\;, \tag{4.1.2}$$

where Φ denotes the flux, ρ_s stands for the density of scatters, and $\omega = E - E'$ is the energy difference of the incoming and outgoing parton, whose energies are, respectively, E and E'.

Assuming that the energy of the propagating parton is much larger that the energy of the plasma constituents, $E, E' \gg k$, Björken obtained

$$\frac{dE^{\,coll}}{dx} \;=\; -2\pi\,\alpha_s^2 \left(\frac{2}{3}\right)^{\pm 1} \left(1+\frac{n_f}{6}\right) \ln\left(\frac{2\langle k\rangle E}{M^2}\right) \propto\; -\alpha_s^2\,T^2\,\ln E\;. \tag{4.1.3}$$

Here $\pm$ stands for an effective color charge of quarks an gluons, respectively. The only difference between the energy loss of quarks and gluons is the prefactor. Note that this expression is obtained in the fixed coupling approximation.

This was later improved, including running coupling, finite energy kinematics, and quark-mass effects by various authors [291–293]. Implementing the running coupling, for $E \gg M^2/T$, where M is the mass of the heavy quark, the collisional energy loss is given by [292]:

- Light quark, gluon:

$$\left.\frac{dE^{\,coll}}{dx}\right|_{q,g} \;=\; -\,\frac{C_R}{4}\,\alpha_s(ET) m_D^2 \ln\left(\frac{ET}{m_D^2}\right)\;, \tag{4.1.4}$$

- Heavy quark:

$$\left.\frac{dE^{\,coll}}{dx}\right|_{Q} \;=\; \left.\frac{dE^{\,coll}}{dx}\right|_{q} + \frac{2\pi\,C_R}{9}\,T^2\left[\alpha_s(M^2)\alpha_s(ET)\ln\left(\frac{ET}{M^2}\right)\right]\;. \tag{4.1.5}$$

Here m_D is the Debye mass, the inverse of the screening length, $m_D^2 = 4\pi\,\alpha_s T^2\left(1+\frac{n_f}{6}\right)$ [294] and $C_R = 4/3\,(3)$ is the quark (gluon) color factor. As a numerical example, taking $E = 20$ GeV, $M = 1.3$ GeV (charm quark) and a medium with $T = 0.4$ GeV and $m_D = 1$ GeV , the elastic energy losses per unit-length are $dE^{\,coll}/dx|_q = -2.3$ GeV/fm and $dE^{\,coll}/dx|_Q = -2.6$ GeV/fm.

4.1.2 Radiative energy loss

The dominant mechanism of energy loss of a fast parton in a QCD environment is radiative energy loss. The hard parton traversing the QGP suffers multiple scatterings with it, inducing extra gluon radiation with respect to vacuum – *medium-induced gluon radiation.*

Let us start by thin media, $L \ll \lambda$, being L the length of the media and λ the mean free path. In this case, the propagating particle suffers at most one single scattering and the QCD radiation spectrum is just given by the Bethe-Heitler (BH) bremsstrahlung expression, obtained in [295] [1]. The independent Bethe-Heitler gluon spectrum is $\omega dI_{rad}/d\omega \propto \omega^{-1}L^2$, where ω is the energy of the radiated gluon.

When the medium is thick, $L \gg \lambda$, *coherence* is a relevant effect that needs to be taken into account. When a high-energy parton traverses a medium, coherence effects between

[1] The BH formula was first obtained for QED bremsstrahlung in [296]

emitter and emitted quanta due to successive scattering centers with the medium show up. This leads to a destructive interference of gluon radiation with respect to the incoherent sum of scattering centers [297]. This effect was first derived in QED and it is known as LPM effect (Landau-Pomeranchuk-Migdal) [298, 299].

Coherence becomes important when the formation time of the radiated gluon, τ_f, is much larger than the mean free path, $\tau_f \gg \lambda$. The formation time is the time needed by the radiated gluon to decohere from the projectile. This time can be computed using the uncertainty principle,

$$\tau_f = \frac{\omega}{\mathbf{k}_\perp^2} \ , \tag{4.1.6}$$

where ω and $\mathbf{k}_\perp$ are, respectively, the energy and the transverse momentum of the gluon. The decoherence between the projectile and the gluon is achieved when the gluon becomes on-shell ($k^2 = 0$). In other words, when the phase, φ, – acquired through multiple scatterings by the gluon – is close to the unity [300]:

$$\varphi \ = \ \left\langle \frac{\mathbf{k}_\perp^2}{2\omega} \Delta l \right\rangle \ , \tag{4.1.7}$$

where Δl is the distance travelled by the gluon during its formation time.

The transport coefficient, which describes the medium-induced transverse momentum squared, $\langle \mathbf{k}_\perp^2 \rangle$, that the medium transfers to the parton per mean free path λ, can be written (for a static medium) as:

$$\hat{q} \ = \frac{\langle \mathbf{k}_\perp^2 \rangle}{\lambda} \ . \tag{4.1.8}$$

The limiting energy of the gluons that decohere from its parent parton is called the *characteristic gluon frequency*, ω_c. For a hard parton propagating through a finite path length L in the medium, ω_c can be easily obtained from Eq. (4.1.7)

$$\omega_c \ = \ \frac{1}{2} \hat{q} L^2 \ . \tag{4.1.9}$$

In medium, a *coherence time*, τ_{dec}, can be also defined as the *kicks* that the projectile receives from the medium until its decoherence from the parent parton,

$$\langle \mathbf{k}_\perp^2 \rangle \ = \ \hat{q} \tau_{dec} \ . \tag{4.1.10}$$

Using Eq. (4.1.6) and Eq. (4.1.10) and assuming that the coherence and the formation times are approximately the same, the coherence time can be obtained:

$$\tau_{dec} \ = \ \sqrt{\frac{\omega}{\hat{q}}} \ . \tag{4.1.11}$$

The gluon energy spectrum per unit length can be estimated qualitatively by taking just the coherent sum of all the scatterings,

$$\omega \frac{d^2 I^{rad}}{dz d\omega} \ \propto \ \alpha_s \sqrt{\frac{\hat{q}}{\omega}} \ , \tag{4.1.12}$$

for $\omega < \omega_c$. Note, that due to the destructive interference, the LPM spectrum – proportional to $\omega^{-1/2}$ – is suppressed in the infrared, i.e. for small ω's, compared to the independent Bethe-Heitler gluon spectrum, which was proportional to ω^{-1}.

The total energy loss can be obtained by integrating Eq. (4.1.12),

$$\Delta E^{rad} = \int_0^L dz \int_0^{\omega_c} d\omega\, \omega \frac{d^2 I}{dz d\omega} \propto \alpha_s\, \omega_c \propto L^2 \ . \tag{4.1.13}$$

The QCD energy loss shows a characteristic L^2-dependence which is also present in the case of Abelian (QED) plasmas, see, for instance, [301]. This is a general feature of the medium-induced energy loss of any in-medium newborn particle. The total collisional energy loss can be obtained, in first approximation, by integrating Eq. (4.1.3), which gives $\Delta E^{coll} \propto L \ln(L)$. Therefore, for an extended medium, the radiative energy loss is dominant with respect to the collisional (elastic) energy loss. A numerical illustration of this, to be compared with the elastic losses of $\mathcal{O}(2$ GeV/fm), would be to consider a gluon with $E =$ 20 GeV in a medium with $\hat{q} = 2\,\mathrm{GeV}^2/\mathrm{fm}$ and $L = 6$ fm, then dE^{rad}/dx is $\mathcal{O}(10$ GeV/fm).

Gluon emission off a heavy quark differs from that off a light quark, already in vacuum. Due to kinematics constraints, the radiation is suppressed at angles smaller than M/E, being M the mass of the heavy quark. This is known as the *dead cone effect* [302] and it results into a suppression of the total gluon radiation emitted off heavy quarks. In medium, this reduction is non-trivial [301] and the corrections are $\mathcal{O}(M/E)$ [303].

In summary, radiative energy loss is the dominant process of energy loss in the QGP. However, it has its limitations. Due to the dead cone effect, it predicts different amounts of energy loss for light and heavy quarks [302, 303].

4.1.3 Jet quenching models

The energy-loss expressions presented in the previous subsections refer to a static and uniform QGP traversed by an infinite-energy parton. However, the real situation is much more complicated. For instance, the temperature of the QGP, and therefore its Debye mass and transport coefficient, is position-dependent; the QGP evolves dynamically and, consequently, the medium properties ($\hat{q}$ and m_D) are also time dependent; and *energy loss fluctuations* show up due to the finite size of the medium. All these effects may produce significant deviations from the above-mentioned analytical energy loss formulas. Thus, more general approaches of jet quenching which compute parton energy loss within pQCD (regardless whether the properties of the medium itself can be treated perturbatively) have been developed. These main frameworks are: BDMPS-Z [275–277, 307, 308], ASW [278, 300, 303, 309], DGLV [279, 304, 310, 311], AMY [312–314] and Higher-Twist (HT) [315–318].

All these models are based on factorization. They all compute the radiative branching of a hard parton propagating through a colored dense medium. In order to do so, they all assume that hadronization takes place in vacuum and that only a global energy loss affects

the production of the fragmenting particles. Moreover, some other approximations are made in these models:

- The *eikonal approximation*: The energy of the radiated quanta, ω, and the energy of the emitter, E, are much larger than the transverse momentum exchanged with the medium, $\mathbf{q}_\perp$, i.e., $\omega, E \gg \mathbf{q}_\perp$. In addition, in general, only soft gluons are taken into account: $\omega \ll E$.

- The transverse momentum of the radiated parton, $\mathbf{k}_\perp$, is much smaller than its energy, ω: $\mathbf{k}_\perp \ll \omega$. That is, the gluon radiation is *collinear* with respect to the parent parton.

- The scattering in the medium occurs *locally*. This means that the mean free path of the propagating particle, λ, is much larger than the Debye screening length, m_D^{-1}: $\lambda \gg m_D^{-1}$.

These analysis differ in their assumptions about the relationships between the relevant scales (emitter energy E, virtuality Q^2, typical momentum $\mu \approx m_D$, and extent L of the medium), as well as by how they approximate the space-time profile of the medium. A brief description of each one is given here.

- **BDMPS-Z/ASW.** The BDMPS-Z model was the first to be developed. It uses the path integral formalism to calculate gluon radiation off an emitter. Energy loss in a colored medium is usually computed in a multiple soft-scattering approximation. A hard parton traversing the medium interacts with various scattering centers and splits into an outgoing parton as well as a radiated gluon. The ASW framework follows the same formalism, but it includes the interference effects between vacuum and medium-induced radiation.

  Both approaches define a density distribution of scattering centers, ρ, which depends on the time (to account for the characteristic dilution of a medium in expansion). Collisional energy loss is not considered. There are two possible approximations of these models: *multiple soft scattering* approximation (also called *dipole* or *saddle point* approximation), used by both formalisms, and the *opacity expansion*, only employed by ASW [309]. In the first one, the medium is described by only one parameter, the transport coefficient, $\hat{q}$. On the other hand, the medium is characterized in the second approximation by two parameters: the density of scattering centers, n, (or the mean free path λ) and the Debye screening mass, m_D. An expansion in terms of the number of scattering centers is made. Usually, this series is truncated at $\mathcal{N} = 1$, which corresponds to a single hard scattering. This second approximation results in exactly the same gluon spectra as the DGLV approach (see next).

  Multiple gluon emission is computed (in both approximations) by an incoherent sum of single emission giving rise to a Poisson distribution. This distribution is usually called Quenching Weights (QW) [300] and will be used in the present thesis to perform a study of the experimental data.

- **DGLV.** In the DGLV approach the medium consists of, as in the BDMPS-Z/ASW approach, almost static (heavy) scattering centers producing a screened Coulomb (Yukawa) potential. DGLV considers the single-hard radiation spectrum (opacity expansion). Despite most of the calculations only include the leading term ($\mathcal{N} = 1$), the behavior of gluon radiation at larger opacities were explored [279, 319]. Independent gluon emission is also considered to compute multiple gluon emission in a fashion similar to the QW.

- **AMY** describes parton energy loss through field theory considering a weakly-coupled QGP in equilibrium. The medium properties are encoded in the temperature, T, and the chemical potential, μ_B, and a hierarchy $T \gg gT \gg g^2T$ is assumed. The hard parton scatters off other partons in the medium, leading to momentum transfers of $\mathcal{O}(gT)$ and inducing collinear radiation. Rate equations between quarks and gluons are used to evolve the branching of the leading parton. This procedure allows to evolve the emission probability distribution as the leading parton loses its energy. It does not take into account neither vacuum radiation nor vacuum-medium interference.

- **Higher-Twist** describes the multiple scattering of a parton as power corrections to the leading-twist cross section. The medium properties are given by the higher-twist matrix element, that factorizes from nPDFs. The evolution of the parton branching is directed by the DGLAP equations [22–24] considering in this way the interference between vacuum and medium-induced radiation. These corrections are enhanced by the medium length L and suppressed by the power of the hard scale Q^2. Therefore, it is more appropriate for thin than thick media. Originally, this approach computed the medium corrections to nuclear DIS.

For further details and for a direct comparison among these formalisms, see reference [320].

Monte Carlo codes to simulate modification of the jet shower and, consequently, jet quenching, are also available. Some of these generators are: PYQUEN [321], which includes both collisional and radiative energy loss, but it does not modify the whole branching process. JEWEL [322, 323], which implements elastic scattering in DGLAP evolution plus radiative energy loss through a multiplicative constant in the infrared part of the splitting functions. Q-PYTHIA [324] that includes radiative energy loss of the ASW type. Elastic energy loss is neglected. And MARTINI [325], where the evolution is based on AMY rates. These all use PYTHIA [326] (or its more recent versions) as high energy generator of p-p collisions.

During the last five years, several extensions of the standard computations of energy loss have been developed. The $q\bar{q}$-antenna set-up [327–332] has been derived to account for interference between the different parton emitters. A new formalism based on soft collinear effective theory (SCET) that computes radiative energy loss has also started to be developed [333, 334].

4.2 Particle observables

4.2.1 Nuclear modification factor

Hard Probes are a successful tool to study the properties of the QGP. The simplest consequence of jet quenching in HICs is the suppression of the single inclusive high-p_T hadron spectrum relative to that in proton-proton collisions. The observable used to quantify this is the nuclear modification factor, R_{AA}, which characterizes how the number of hadrons, h, produced in the collision of two nuclei A-A varies with respect to the equivalent number of proton-proton, p-p, collisions. It is given by the ratio of the hadron spectrum in A-A, over, the same quantity in p-p, but scaled by the number of binary nucleon collisions, $\langle N_{coll} \rangle$:

$$R_{AA} = \frac{dN_{AA}/d^2p_T dy}{\langle N_{coll} \rangle dN_{pp}/dp_T^2 dy} \ . \tag{4.2.14}$$

This observable has information both from initial and final state, that is why nPDFs should be precisely determined. In the absence of nuclear modifications – of initial and final state – this observable would be equal to unity. By controlling nPDFs from pA collisions, where final state effects should be absent, we can disentangle both effects.

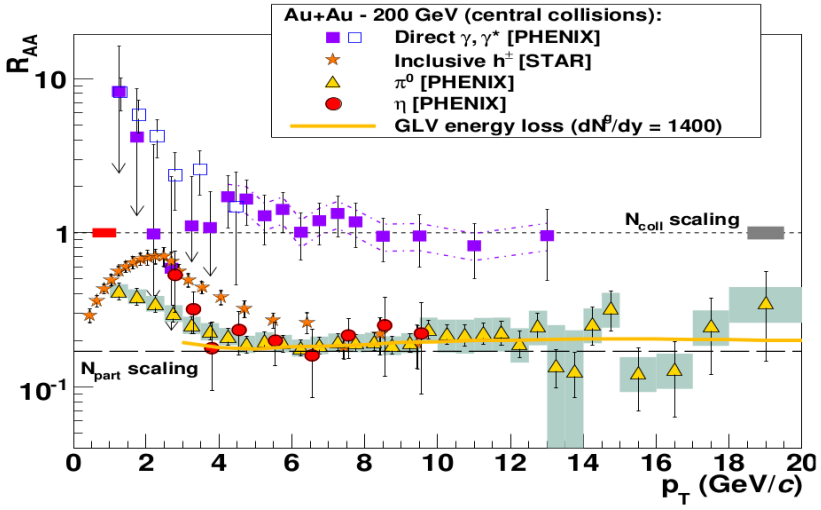

Figure 4.1: R_{AA} versus p_T measured in central Au-Au collisions at 200 GeV for π^0 [335], η mesons [336], charged hadrons [35], and photons [337, 338].

The nuclear modification factor depends, in general, on the identity, transverse momentum, p_T, and pseudorapity, η, of the particle, as well as on the energy and centrality of the collision.

As it can be seen in Fig. 4.1 for RHIC top energies, above $p_T \sim 5$ GeV, π^0 [335], η [336], and charged hadrons [34,35] show all a common $R_{AA} \approx 0.2$. This suppression is much larger

than the one expected from nPDFs, which indicates that jet quenching effects are present in the QGP. Direct photons, which do not interact with the medium, have an R_{AA} compatible with one [337]. The fact that $R_{AA} \approx 0.2$ irrespective of the nature of the produced hadron is consistent with the scenario where fragmentation into hadrons takes place in vacuum – but it is energy-rescaled.

The nuclear modification factor at RHIC was fitted using ASW, HT and AMY energy loss models using a common three-dimensional relativistic fluid dynamics [339]. However, the value of the jet quenching coefficient, $\hat{q}$, obtained in the three approaches by fitting the data differs significantly.

Let us move now from RHIC to the LHC, i.e., to $\mathcal{O}(10)$ times higher center of mass energy. As expected, the nuclear modification factor is now a bit smaller. For instance, for particles with $p_T \sim 6 - 7$ GeV, $R_{AA} \approx 0.13$ in the most central Pb-Pb collisions at the LHC . A more interesting feature of R_{AA} is its centrality- and p_T-dependence. At RHIC top energies, the nuclear modification factor remains relatively constant from 5 GeV up to the highest transverse momenta measured so far, $p_T \sim 20$ GeV (see Fig. 4.1). The much larger kinematical range opened at the LHC, allows us to observe an increase on R_{AA} for higher p_T's up to $R_{AA} \approx 0.4$ for $p_T \sim 50$ GeV in the most central collisions, see Fig. 4.2. As it is shown in the same figure, by moving from the most central to the most peripheral collisions the suppression is reduced. In a more peripheral collision, the overlap region where the QGP is formed is smaller and has lower density. This leads to a smaller path length, which is translated into a smaller amount of energy loss. Hence, the centrality dependence of the nuclear modification factor supports the picture of energy loss.

Single inclusive measurements and in particular the nuclear modification factor are very useful. However, they have their limitations. As it was explained before, a factorization between medium effects and fragmentation is needed. A more general approach, where this separation is not a requirement, such as fully reconstructed jets, is desirable.

Jet observables are very sensitive to jet quenching effects, but they will not be presented in this thesis, as they are not part of our analysis. Just to mention that the LHC has given us access to many jet measurements. Among them, there are the *Dijet asymmetry* for back-to-back jet pairs, A_J, measured in ATLAS [29] and CMS [30,42]; the *Dijet azimuthal distribution* [30], $\Delta\phi$; the *average missing transverse momentum*, $\langle \not{p}_T^{\parallel} \rangle$ [30]; the *jet fragmentation function* [340]; and *jet shapes* [341].

4.2.2 High-p_T flow harmonics

The almost perfect fluid QGP may be understood through two key experimental signatures: collective flow and jet quenching. Collective flow observables have been successfully described by means of event-by-event (EbyE) relativistic viscous hydrodynamics [342–346]. More recently, the effects of event-by-event fluctuations have been analyzed in the context of hard probes. Measuring the azimuthal asymmetry of hard particles was proposed for the first time

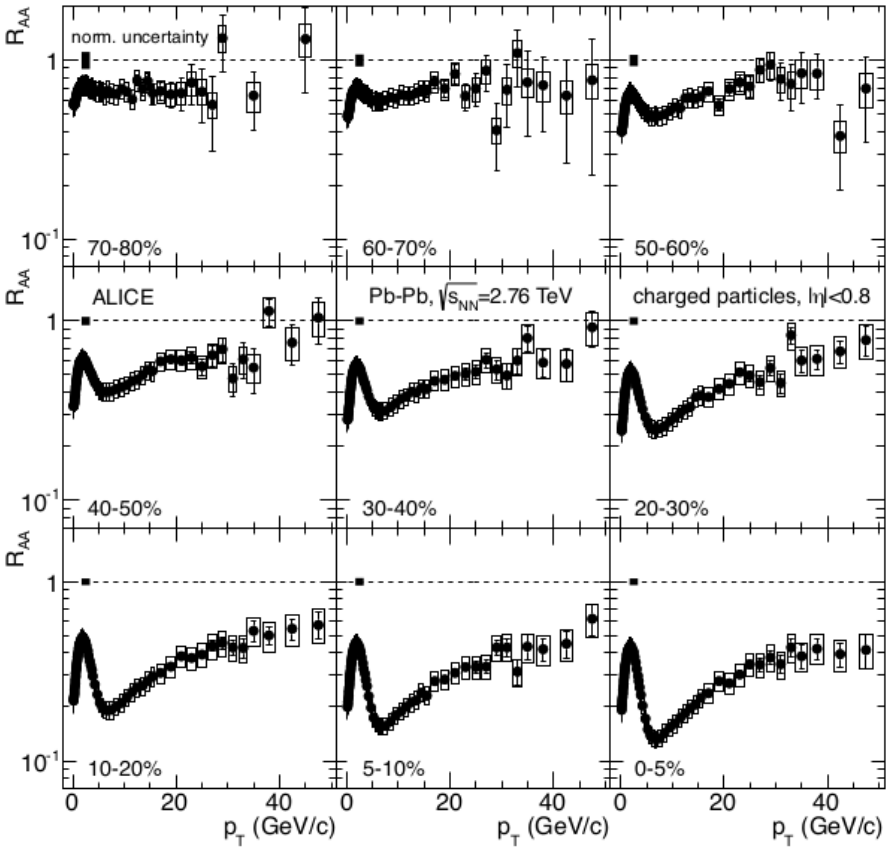

Figure 4.2: R_{AA} versus p_T for charged hadrons measured for different centralities in Pb-Pb collisions at 2.76 TeV from ALICE [205].

in [347, 348]. It was suggested in there that the path length dependence due to an initial anisotropy would lead to a non-zero elliptic flow, v_2, at high-p_T. The first measurement of high-p_T v_2 was published in 2006 by PHENIX Collaboration [349]. However, a simultaneous description of R_{AA} and high-p_T v_2 has been a puzzle during the last ten years. In fact, R_{AA} was reasonably described by all the energy loss models, but the computed high-p_T elliptic flow under-predicted the data [350]. Once EbyE fluctuations and more realistic initial conditions were implemented, a new theoretical high-p_T v_2 definition was proposed that might solve this puzzle [351].

First of all, EbyE relativistic hydrodynamics is mandatory to study the flow harmonics. For instance, all hydrodynamic simulations with averaged smooth initial conditions predict a triangular flow, v_3, equal to zero. Only in the case that event-by-event fluctuations are considered a non-zero v_3 can be obtained across all p_T's. However, until 2016 all the model calculations – energy loss approach plus relativistic hydrodynamic medium modeling – were incapable of computing both the nuclear modification factor and the high-p_T flow harmonics. It was suggested in [351] that this may be due to the fact that the theoretically computed

quantity, v_2^{hard}, was not the appropriate quantity to compare with the experimental data. In fact, the experimental $p_T > 10$ GeV flow coefficients $v_n^{exp}(p_T)$ are measured using the scalar product [352]

$$v_n^{exp}(p_T) \;=\; \frac{\langle v_n^{soft} v_n^{hard}(p_T) \cos\left[n\left(\psi_n^{soft} - \psi_n^{hard}(p_T)\right)\right]\rangle}{\sqrt{\left\langle \left(v_n^{soft}\right)^2 \right\rangle}} \;, \tag{4.2.15}$$

where v_n^{soft} and ψ_n^{soft} are the integrated soft flow harmonic and the corresponding event plane angle, and $v_n^{hard}(p_T)$ is the second Fourier coefficient of $R_{AA}(p_T, \phi)$,

$$v_n^{hard}(p_T) \;=\; \frac{\frac{1}{2\pi}\int_0^{2\pi} d\phi \, \cos\left[n\phi - n\psi_n^{hard}\right] \, R_{AA}(p_T,\phi)}{R_{AA}(p_T)} \tag{4.2.16}$$

where $\psi_n^{hard}(p_T)$ is given by

$$\psi_n^{hard}(p_T) \;= \frac{1}{n} \arctan\left(\frac{\int_0^{2\pi} d\phi \, \sin(n\phi)\, R_{AA}(p_T,\phi)}{\int_0^{2\pi} d\phi \, \cos(n\phi)\, R_{AA}(p_T,\phi)}\right) \;. \tag{4.2.17}$$

Hence, the calculation of high-p_T flow harmonics $v_n(p_T)$, requires modeling of both the soft and hard sectors of HICs. Note that in the case of smooth-averaged hydrodynamics there is only one "event" and, then, Eq. (4.2.15) is reduced to $v_n^{hard}(p_T)$, Eq. (4.2.16). In summary, EbyE fluctuations combined with the proper definition of v_2^{exp} at high-p_T could provide a solution to the $R_{AA} \otimes v_2$ puzzle. However, the energy loss model was implemented *ad hoc* in reference [351]. Therefore, a reliable energy loss model – combined with EbyE relativistic hydrodynamics – is mandatory to study the solution proposed in [351].

4.3 Energy loss in the ASW framework

In this section a brief summary of the path-integral formalism used to describe the propagation of hard particles through the QGP is given. Then the single-inclusive particle spectrum in the ASW approach (already introduced in Subsection 4.1.3) will be presented, as it is the formalism used in our analysis.

Jet quenching is usually described by considering an elementary hard collision, with a cross section computed by pQCD, which produces a high-energy parton with large transverse momentum, p_T, relative to the beam direction. In the high energy limit, as it was already explained, the dominant energy loss process is radiative (inelastic) energy loss. In this limit, the propagation time of the parton through the QGP is much smaller than the time scale of modifications of the medium. Consequently, the medium can be treated as a background field that interacts with the hard probe by means of very soft gluons [275, 277, 353], see Fig. 4.3. This limit can be summarized as

$$E \gg \omega \gg |\mathbf{k}|, |\mathbf{p}_\perp| \gg T, \Lambda_{QCD} \;, \tag{4.3.18}$$

where E is the (high) energy of the parton, ω and $\mathbf{k}$ are respectively the energy and momentum of the radiated gluons, and $\mathbf{p}_\perp$ is the transverse momentum (with respect to the initial parton) accumulated by the projectile due to the radiative interactions with the medium. T and Λ_{QCD} are the characteristic energy scales of the dense medium.

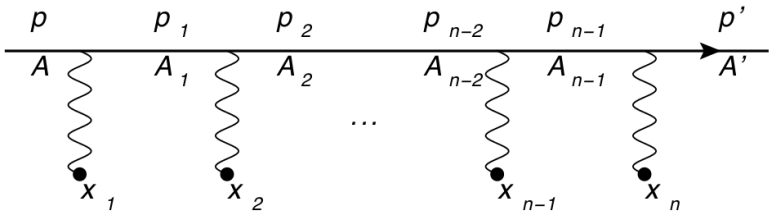

Figure 4.3: Representation of multiple scattering of a high energetic quark with static medium components, represented as a small dark blob.

The main effect of these inelastic interactions with the medium is the color rotation of the parton wave function, usually called *eikonal* phase [354]. As the energy of the parton is very high, in the reference frame where the parton is at rest, it traverses the target in such a small time that its transverse position does not vary during its propagation. This is known as *eikonal approximation*. Consequently, at ultrarelativistic energies, a color rotation on the parton wave function, due to the color field of the target, is induced. This effect is described by *Wilson lines*

$$W(x_{0+}, L_+; \mathbf{x}_\perp) = \mathcal{P}\exp\left\{ig\int_{x_{0+}}^{L_+} dx_+\, A_-(x_+, \mathbf{x}_\perp)\right\}, \tag{4.3.19}$$

where $\mathbf{x}_\perp$ is the transverse position of the projectile, x_{0+} and L_+ are the light-cone medium boundaries [2] and $A_- \equiv T^a A_-^a$ designs the medium color field components [3] in a given light-cone ordering $\mathcal{P}$. Wilson lines, therefore, are only valid to describe the propagation of partons that follow a straight line.

A simple derivation of the Wilson line can be obtained in terms of multiple scatterings [355], as shown in Fig. 4.3.

When the energy of the projectile is not as large, some subdominating terms with respect to the eikonal approximation can be incorporated, giving rise to a two dimensional path-integral. This is the *Green function*, which replaces the Wilson line, and that allows some Brownian perturbations in the transverse plane of the propagating parton,

[2] The light-cone variables are given by $x_\pm = (x_0 \pm x_3)/\sqrt{2}$ and $\mathbf{x}_\perp = (x_1, x_2)$.

[3] T^a is given in the fundamental or adjoint representation whether the radiated quanta is, respectively, a quark or a gluon.

$$G(x_{0+}, \mathbf{x_0}_\perp; L_+, \mathbf{x}_\perp|p_+) = \int_{\mathbf{r}_\perp(x_{0+})=\mathbf{x_0}_\perp}^{\mathbf{r}_\perp(L_+)=\mathbf{x}_\perp} \mathcal{D}\mathbf{r}_\perp(\xi) \exp\left\{\frac{ip_+}{2}\int_{x_{0+}}^{L_+} d\xi \left[\frac{d\mathbf{r}_\perp}{d\xi}\right]^2\right\} \times W(x_{0+}, L_+; \mathbf{r}_\perp(\xi)) \ , \quad (4.3.20)$$

where x_{0+} and L_+ are the longitudinal boundaries of the medium and $\mathbf{x_0}_\perp$ and $\mathbf{x}_+$ the respective transverse coordinates of the propagating parton. The path-integral corresponds to the motion of a free particle in a two dimensional space, at the same time that its color phase is modified according to Eq. (4.3.19). In the high-energy limit, i.e., when $p_+ \to \infty$, $dr_\perp/d\xi$ in Eq. (4.3.20) has to be zero. Consequently, partons propagate in a straight line and the Wilson line, Eq. (4.3.19), is recovered.

4.4 Medium induced gluon radiation

In this section the computation of medium-induced gluon radiation off a hard parton that propagates through a dense medium will be outlined. From this quantity, the amount of energy lost by the initial parton can be computed, and from that, extract the properties of the QGP (as the $\hat{q}$) created in the HIC. In the ASW model this is computed in the limit of soft gluon emissions: a very energetic quark radiates a gluon which carries a small fraction of the initial energy, $z \ll 1$. This is illustrated in Fig. 4.4, where p_+ and k_+ are, respectively, the energies of the quark and the radiated gluon, h represents the matrix element of the hard process that originated the propagating quark, and the black blobs symbolize scatterings with medium constituents.

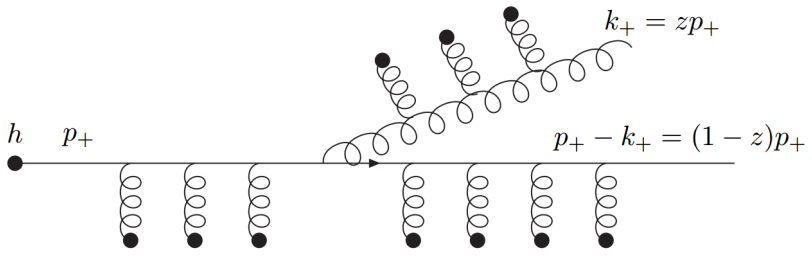

Figure 4.4: Medium-induced gluon radiation diagram taken from [355].

Since it is assumed that $z \ll 1$, the propagation of the initial and final quarks is considered eikonal, and so, described by Wilson lines, Eq. (4.3.19). The propagation of the gluon has to be described by a Green function, Eq. (4.3.20), as it has its propagation in the transverse plane corrected by Brownian motion. Two contributions need to be taken into account to compute the complete spectrum: when the gluon does not interact with the medium after

being emitted and when all the particles interact with the medium (as seen in Fig. 4.4). For technical details about how to compute these amplitudes, see [355]. This allows us to compute the medium-induced gluon radiation spectrum which is given by [300]

$$\omega \frac{dI^{(med)}}{d\omega} = \frac{\alpha_s C_R}{(2\pi)^2 \omega^2} 2\,Re \int_{\xi_0}^{\infty} dy_l \int_{y_l}^{\infty} d\bar{y}_l \int d\mathbf{u}_\perp \int_0^{\chi\omega} d\mathbf{k}_\perp\, e^{-i\mathbf{k}_\perp\cdot\mathbf{u}_\perp}\, e^{-\frac{1}{2}\int_{\bar{y}_l}^{\infty} d\xi\, n(\xi)\sigma(\mathbf{u}_\perp)} \times \frac{\partial}{\partial \mathbf{y}_\perp}\cdot\frac{\partial}{\partial \mathbf{u}_\perp} \int_{y=0}^{\mathbf{u}_\perp=\mathbf{r}_\perp(\bar{y}_l)} \mathcal{D}\mathbf{r}_\perp \exp\left[i\int_{y_l}^{\bar{y}_l} d\xi\, \frac{\omega}{2}\left(\dot{\mathbf{r}}_\perp^2 - \frac{n(\xi)\sigma(\mathbf{r}_\perp)}{i\omega}\right)\right] . \quad (4.4.21)$$

Without going through the details of this expression, let us emphasize a fundamental point. The properties of the medium in Eq. (4.4.21) appear as the product of the time-dependent density of scattering centers, $n(\xi)$, and the strength of one only elastic scattering $\sigma(\mathbf{r}_\perp)$. The latter is the dipole cross section and it can be written as

$$\sigma(\mathbf{r}_\perp = \mathbf{x}_\perp - \mathbf{y}_\perp) = \int \frac{d^2\mathbf{q}_\perp}{(2\pi)^2} |a_-(\mathbf{q}_\perp)|^2 \left(1 - e^{i\mathbf{q}_\perp\cdot\mathbf{r}_\perp}\right) , \quad (4.4.22)$$

where $|a_-(\mathbf{q}_\perp)|^2$ in the elastic cross section of one only scattering at high energy.

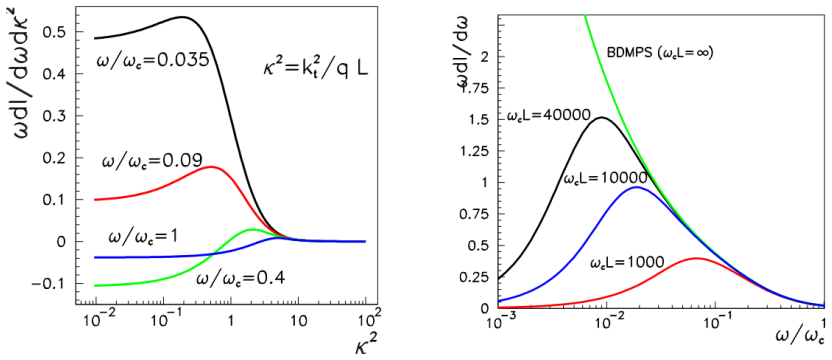

Figure 4.5: Double-differential medium-induced gluon radiation spectrum (left), and medium-induced radiation spectrum integrated in $\mathbf{k}_\perp$, Eq. (4.4.21) (right). Figure taken from [355].

In Fig. 4.5 numerical results for the double-differential medium-induced gluon radiation spectrum for a quark traversing a static medium are presented. These are presented in function of two variables, ω_c, given by Eq. (4.1.9), and $\kappa^2 \equiv k_\perp^2/\hat{q}L$.

As it can be observed, this spectrum does not present a collinear divergence. Furthermore, it corrects the characteristic BDMPS-Z infrared divergence, due to considering a finite medium instead of an infinite one. At high energies (large ω) ASW and BDMPS-Z spectra coincide and go to zero. This can be interpreted in terms of the formation time, Eq. (4.1.6).

At large ω, so, large formation time, the radiated gluon *sees* the medium as an only scattering center, suppressing the spectrum with respect to the case in which multiple incoherent scatterings are present.

The energy distribution, Eq. (4.4.21), is usually studied in two limit cases: *single hard scattering* (opacity expansion) and *multiple soft scattering*.

4.4.1 Opacity expansion

In the opacity expansion, a Yukawa-like potential with a Debye screening mass, m_D, is often employed in the dipole cross section, Eq. (4.4.22),

$$|a_-(\mathbf{q}_\perp)|^2 \;=\; \frac{m_D^2}{\mathbf{q}_\perp^2 + m_D^2} \;. \tag{4.4.23}$$

An expansion in powers of $[n(\xi)\sigma(\mathbf{r}_\perp]^N$ is done in Eq. (4.4.21). The $N = 0$ does not present any dependence on the medium parameters, and so, it corresponds to the vacuum contribution. The first order, $N = 1$, is the leading medium contribution and it is called the *single hard scattering approximation*. This first order approximation corresponds to a hard interaction of the parton with only one scattering center multiplied by the total number of scattering centers, $n_0 L = L/\lambda$, traversed by the parton. Higher order terms, $N > 1$ are corrections due to coherence effects among successive scattering centers.

4.4.2 Multiple soft scattering

In the multiple soft scattering approximation the medium is considered as a large number of soft scattering centers, instead of a few hard ones. In this kind of medium, the projectile performs a Brownian movement in the transverse plane. In consequence, the main contribution to the dipole cross section, Eq. (4.4.22), comes from the lowest order term in the Taylor expansion in Eq. (4.4.21) [356], $\sigma(\mathbf{r}_\perp) \propto \mathbf{x}_\perp^2$ with a logarithmic correction. Neglecting this logarithmic correction it can be approximated as [276, 308],

$$n(\xi)\sigma(\mathbf{r}_\perp) \;\simeq\; \frac{1}{2}\,\hat{q}(\xi)\,\mathbf{r}_\perp^2 \;, \tag{4.4.24}$$

where $\hat{q}(\xi)$ is the transport coefficient, given by Eq. (4.1.8) for a static medium. All the information about the medium is encoded in its length, L, and, in the jet quenching parameter, $\hat{q}$. The latter is the main parameter of this approximation and it is usually taken as a phenomenological parameter to be extracted from data [339, 357].

With this approximation, the path integral in Eq. (4.4.21) is that of a harmonic oscillator with imaginary (eventually time-dependent) frequency. The solutions of this path integral when $\hat{q}(\xi) \sim 1/\xi^\alpha$ can be found in [300]. The main difference between the two approximations, at the analytical level, is the presence of perturbative, power-law, tails in the opacity

expansion, which are absent in the multiple soft scattering one. Notice that the AMY approach would correspond to a resummation of the multiple scatterings with the correct cross section, Eq. (4.4.23), but without an interference between vacuum and medium radiation which turns out to be very relevant for finite medium lengths, making the soft part of the spectrum non-divergent when real angle emission is imposed for the emitted gluons.

Despite the two approximations presented in this section (single hard and multiple soft approximations) make different assumptions about the principal medium effects (one effective hard scattering or multiple soft scatterings) they lead to similar results for the medium-induced soft gluon radiation spectrum [300].

4.5 Quenching weights

Medium-induced soft gluon radiation modifies the correspondence between the initial and final momentum of the hadron. In the previous section, the medium-induced soft gluon radiation spectrum, Eq. (4.4.21), was obtained in the case of one gluon emission. The emission of more than one gluon is a complicated calculation which is not done yet. Starting with the proposal of independent gluon emission approximation [358], several groups have just iterated the one-gluon inclusive in an independent manner [279,300,359], which has been the most standard procedure to deal with the problem in the last years. This approximation leads to, in the eikonal case, a Poisson-like energy distribution of the probabilities of energy loss. In the ASW model these are the so-called *quenching weights* [300, 358]. When gluons are independently emitted, $P(\Delta E)$ is the normalized sum of the probability of emitting an arbitrary number n of gluons which carry a total energy ΔE

$$P(\Delta E) \;=\; \sum_{n=0}^{\infty} \frac{1}{n!} \left[\prod_{i=1}^{n} \int d\omega_i \, \frac{dI^{\,(med)}(\omega_i)}{d\omega} \right] \delta\left(\Delta E - \sum_{i=1}^{n} \omega_i \right) \exp\left[- \int_0^{\infty} d\omega \, \frac{dI^{\,(med)}}{d\omega} \right] \;. \tag{4.5.25}$$

In general, this distribution, $P(\Delta E)$, consists of two parts, the discrete one and the continuous one,

$$P(\Delta E) \;=\; p_0 \, \delta(\Delta E) + p(\Delta E) \;, \tag{4.5.26}$$

where the discrete weight, p_0, is interpreted as the probability of not having additional gluon radiation due to the scattering with the medium and, therefore, having medium-induced energy loss equal to zero. For a finite medium, there is always a finite probability, $p_0 \neq 0$, of the projectile not being affected by the presence of the medium.

Note that these quenching weights (QW) can be obtained from an iterative solution of the DGLAP evolution for medium-modified fragmentation functions in the soft limit [340].

Using Laplace transformations, the quenching weights, $P(\Delta E)$, can be computed for the medium induced soft gluon radiation, Eq. (4.4.21), in both approximations: multiple soft and single hard scattering [300], for a static medium. The numerical results of the QW are

tabulated in [360].

In the AMY framework, as it has been already mentioned, rate equations are employed to include the single-inclusive emission in a more sophisticated manner [313, 314]. This rate equation still assumed with no proof that subsequent emissions are independent. It is with a more developed study of the role of coherence in jet quenching [327, 361] that one can prove that in the limit of gluon formation times much smaller than the medium size, $\tau_{\rm form} \ll L$, a resummation is possible [362, 363] recovering, as a particular case, the rate equations by the AMY group. The main limitation of these resummations and the corresponding implementation in the AMY approach, is that they apply to arbitrarily large medium length L, leading to an enhanced energy loss, while finite length effects are relevant in phenomenological implementations, in particular to avoid over-representation of the soft part of the spectrum. The main advantage of the quenching weights is that these finite length effects can be included, although, as mentioned, with no formal proof.

4.5.1 Expanding medium

Up to now we have considered the medium as static. However, in HICs, the medium is rapidly expanding. The density of scattering centers is expected to have a maximum value, $\hat{q}_0$, when the formation time of the QGP, ξ_{0+}, is reached. Then, it is followed by a fast decrease, mainly caused by the longitudinal expansion of the created matter. In this case, the jet quenching parameter can be parameterized as [364]

$$\hat{q}(\xi) = \hat{q}_0 \left(\frac{\xi_{0+}}{\xi} \right)^{\alpha} , \tag{4.5.27}$$

where $\alpha = 0$ and $\alpha = 1$ correspond, respectively, to the static medium and to one-dimensional longitudinal expansion.

It has been shown than when $\hat{q}$ can be written as in Eq. (4.5.27), scaling laws can be used to relate the medium-induced soft gluon radiation in a collision with dynamic expansion with an equivalent static scenario [300]. This is valid both in the multiple soft approximation and in the single hard approach.

4.6 Energy and centrality dependence of the jet transport coefficient

The final goal of jet quenching studies is to obtain medium parameters that describe the QGP formed in high-energy nuclear collisions. In this section, RHIC and LHC data on the nuclear modification factor, R_{AA}, for inclusive particle production at high transverse momentum using the formalism of the *quenching weights* (presented in the previous section) are analyzed. This work has been done in collaboration with Nestor Armesto, Matthew Luzum, Carlos A. Salgado, and, Pia Zurita and corresponds to our publication [365]. The

main result of this study is an extraction of the value for the jet transport coefficient, $\hat{q}$, in a way which has been well tested, is easy to implement and can be combined with different hydrodynamic simulations of the medium (as done previously by some of the authors of this work in Ref. [357], see also [339,366,367]), and provides a good description of the experimental data, as it will be shown. In spite of the limitations of the formalism whose applicability is restricted to describing leading particle production in a jet, the main conclusions of the analysis are robust and surprising.

In our approach the jet quenching parameter, $\hat{q}$, is completely determined by the local – in position and time – energy density, ϵ, extracted from hydrodynamic models. Hence, the transport coefficient is defined as $\hat{q} = K 2\epsilon^{3/4}$, motivated by the ideal estimate $\hat{q}_{\rm ideal} \sim 2\epsilon^{3/4}$ [368], and the values of K are fitted to experimental data. No particular dependence of this K-factor on energy, centrality, temperature, etc. is imposed. On the contrary, K is the only free parameter in the fit of R_{AA} for each centrality at RHIC and LHC energies. Our main findings are that this K-factor is $\sim 2-3$ times larger at RHIC than for the LHC (larger values at RHIC than at the LHC have been found before [369]) and, surprisingly, this K-factor seems to be independent of the medium properties, e.g., its temperature. Instead, the K-factor looks like dependent on the center of mass energy of the collision. Indeed, these K-factors are found to be mostly independent of centrality both for RHIC and the LHC. Were the K-factor determined, say, by temperature, then the most central RHIC collisions should present a value similar to semi-peripheral LHC data. This is not the case. The study has been performed with various, quite different, smooth-averaged hydrodynamic simulations and these conclusions are independent of the profile used, while the values of K do present some dependencies and, interestingly, they dramatically change for some different assumptions for the dynamics at times before the starting of hydrodynamic evolution.

We do not have a straightforward interpretation of these results. Different theoretical restrictions of the technique that could affect this finding will be commented. A more detailed analysis of these limitations is not easy with present theoretical tools. If our result is not due to a restriction of the procedure, it would suggest that the properties of the QGP formed at RHIC and LHC are different in what refers to the jet quenching phenomenon. It would be important to check our conclusions with other jet quenching models.

4.6.1 Energy loss approach

The quenching weights (see Section 4.5) are used here to compute the energy loss of hard partons. This formalism is easy to carry out, permits to fit the transport coefficient, $\hat{q}$, once the geometry of the medium is known and, moreover, it has been extensively tested, principally for RHIC energies [279, 357, 370, 371] but also for the LHC, e.g. [367]. In addition, it is not only a phenomenological sound approach, but also it is theoretically motivated, see Section 4.5. Finally, it is worth stressing that QW include finite length effects, which are not included, for instance, in the AMY approach.

We use the quenching weights, $P(\epsilon)$, tabulated in [360], to model the amount of energy loss of highly energetic partons which will eventually fragment into a given hadron h in vacuum. The corresponding cross section reads

$$\frac{d\sigma^{AA\to h}}{dydp_T} = \int dq_T\, dz\, \frac{d\sigma^{AA\to k}}{dydq_T}\, P(\epsilon)\, D_{k\to h}(z,\mu_F^2)\, \delta\left(p_T - z(1-\epsilon)q_T\right) \ , \tag{4.6.28}$$

where the cross section for producing parton k is

$$\frac{d\sigma^{AA\to k}}{dydq_T} = \int dx_1\, dx_2\, x_1 f_i^A(x_1,\mu_F^2)\, x_2 f_j^A(x_2,\mu_F^2)\, \frac{d\hat{\sigma}^{ij\to k}}{d\hat{t}} \ . \tag{4.6.29}$$

Note that any difference between parton and hadron rapidities is neglected here, and that all renormalization, factorization and fragmentation scales are taken to be equal, $\mu_F = p_T$.

The partonic cross section is computed at NLO using the code in [372]. The free proton PDFs set CTEQ6.6M [373] with EPS09 [90] nuclear corrections is employed. Vacuum fragmentation functions DSS [374, 375] are used. The quenching weights, $P(\epsilon)$, are defined as in Eq. (4.5.25) and they are computed in the multiple soft scattering approximation, see Subsection 4.4.2.

It is worth emphasizing that this formalism is based on two main assumptions: i) the subsequent medium-induced gluon emissions are independent and ii) the fragmentation functions are not modified, i.e., fragmentation takes place in vacuum. Both of them find solid theoretical support in recent analyses of coherence effects in the medium. Beginning with the simplified setup of a QCD antenna [327, 330, 361, 376], a pair of color-correlated partons with opening angle Θ emitting a soft gluon, a simple picture of jet quenching arises [377]: a medium of length L and jet quenching parameter $\hat{q}$ has a typical transverse momentum scale for color correlations $\Lambda_\perp \sim 1/\sqrt{\hat{q}L}$; when the typical transverse size of the jet, $r_\perp \sim \Theta L$, is smaller than this scale, $r_\perp < \Lambda_\perp$, the medium cannot resolve the inner structure of the jet, which remains unmodified and radiates medium-induced gluons as a whole with the total charge of the jet. This is the *totally coherent case*. Clearly, this picture implies that the fragmentation function remains basically unchanged if color coherence is maintained. However, it still depends on the fraction of momentum, z, and only a global energy loss affects the production of the fragmenting particles. This picture of jet quenching dictated by color coherence is in qualitative agreement with the experimental findings at the LHC [30, 43, 341, 378–380] — see [381] for a quantitative analysis of some data.

4.6.2 From hydrodynamics to the transport coefficient

The quenching weights are tabulated in [360] for the case of a static medium of finite length L and transport coefficient $\hat{q}$, where

$$\omega_c = \frac{1}{2}\hat{q}L^2 \ , \quad R = \omega_c L \ . \tag{4.6.30}$$

For a medium in dynamic evolution, when the jet quenching parameter can be written as $\hat{q}(\tau) \sim 1/\tau^{\alpha}$, a dynamical scaling law was found [382] which relates the resulting spectra with an equivalent static scenario. Based on this scaling law, effective ω_c^{eff} and R^{eff} for an hydrodynamical medium profile are computed as

$$\omega_c^{eff}(x_0, y_0, \tau_{\rm prod}, \phi) \;=\; \int d\xi\, \xi\, \hat{q}(\xi) \;, \tag{4.6.31}$$

$$R^{eff}(x_0, y_0, \tau_{\rm prod}, \phi) \;=\; \frac{3}{2} \int d\xi\, \xi^2\, \hat{q}(\xi) \;, \tag{4.6.32}$$

that reproduces Eqs. (4.6.30) for the static case. Similar implementations of the hydrodynamic model have been used before [339,357,366,367], so it is a rather standard procedure[4].

The production point of the parton at time $\tau_{\rm prod}$ is distributed according to an $N_{\rm coll}$-scaling in the transverse plane and the azimuthal angle ϕ is taken as a random number in $[0, 2\pi]$. Each parton traverses the medium in a straight-line parameterized by the proper time ξ at each point in the transverse plane. Then, it is only needed to specify a relation between the local value of the hydrodynamical variables at $(x_\perp(\xi), y_\perp(\xi))$ and the local value of the transport coefficient $\hat{q}(\xi)$. Following [357],

$$\hat{q}(\xi) \;=\; K \cdot 2\epsilon^{3/4}(\xi) \;, \tag{4.6.33}$$

where $K \simeq 1$ corresponds to the ideal QGP, see the estimate in [368]. Other relations between the transport coefficient and the local thermodynamical quantities have been explored for instance in Ref. [339]. The local energy density $\epsilon(\xi)$ is taken from a hydrodynamic simulation of the medium. Several different options will be considered in the next section.

In an expanding medium like this one, there is an ambiguity on the value of the transport coefficient, defined by Eq. (4.6.33), for values smaller than the proper time, τ_0, when relativistic hydrodynamics is started. To quantify this uncertainty, three different extrapolations for the time from the production time to the proper time are considered:

- Case (i): $\hat{q}(\xi) = 0$ for $\xi < \tau_0$.
- Case (ii): $\hat{q}(\xi) = \hat{q}(\tau_0)$ for $\xi < \tau_0$.
- Case (iii): $\hat{q}(\xi) = \hat{q}(\tau_0)/\xi^{3/4}$ for $\xi < \tau_0$.

The $\hat{q}(\xi) = 0$-extrapolation is an extreme case. It considers no energy loss at all before the thermalization time. This is a strong assumption as neither thermalization nor isotropization is necessary in the quenching weights approach. The second case assumes a continuous interaction from the production time (taken to be $\tau_{\rm prod} \simeq 0.04$ fm/c) and the third one considers a free-streaming medium with energy density decreasing as $\epsilon(\xi) \sim 1/\xi$.

[4]Note that the prescription of R^{eff} is slightly modified here. Now, R^{eff} is the second moment of $\hat{q}(\xi)$. The results are similar with the old prescription (see Eqs. (4.2)-(4.4) in Ref. [357]) but with improved stability for functional dependencies of $\hat{q}(\xi)$ that are divergent in $1/\xi$.

The production point of the hard scattering is characterized by a production weight $w(x_0, y_0)$ calculated as

$$w(x_0, y_0) \;=\; T_A(x_0, y_0)\, T_A(\vec{b} - (x_0, y_0)) \;\;, \tag{4.6.34}$$

where T_A are the profile functions computed from a 3-parameter Fermi distribution at a given impact parameter $\vec{b}$ taken from [383]. The average fragmentation functions for a parton k which has propagated through the medium and hadronizes in the vacuum to a hadron h can be computed, in terms of these weights, as

$$D^{\rm med}_{k\to h}(z, \mu_F^2) \;=\; \frac{1}{N} \int d\phi\, dx_0\, dy_0\, w(x_0, y_0) \int \frac{d\zeta}{1-\zeta}\, P_k(x_0, y_0, \phi, \zeta)\, D^{\rm vac}_{k\to h}\left(\frac{z}{1-\zeta}, \mu_F^2\right) \;\;, \tag{4.6.35}$$

where $P_k(x_0, y_0, \phi, \zeta)$ is the quenching weight for parton k and the normalization is $N = 2\pi \int dx_0 dy_0 w(x_0, y_0)$. With this definition, the cross section, Eq. (4.6.28), is simply

$$\frac{d\sigma^{AA\to h}}{dy dp_T} \;=\; \int dq_T\, dz\, \frac{d\sigma^{AA\to k}}{dy dq_T}\, D^{\rm med}_{k\to h}(z, \mu_F^2)\, \delta\left(p_T - z q_T\right) \;\;. \tag{4.6.36}$$

4.6.3 Hydrodynamic modeling of the medium

The space-time distribution of the local energy density is obtained by solving the relativistic hydrodynamic equations. Such simulations require the specification of initial values for the energy momentum tensor, as well as parameters that describe medium properties, neither of which are accurately known. In order to test the robustness of our results and conclusions with respect to these uncertainties, we repeat all calculations using space-time profiles from various different smooth-averaged hydrodynamic descriptions.

The first, which we refer to as "Hirano", corresponds to the calculation described in [384–386], to which we refer the reader for details. In short, this simulation uses an optical Glauber model where the initial entropy density at initial proper time $\tau_0 = 0.6$ fm is given by a linear combination of the number density of participant nucleons, $\rho_{\rm part}$, and binary collisions, $\rho_{\rm bin}$:

$$s \propto (1-x)\rho_{\rm part} + x\rho_{\rm coll} \;\;, \tag{4.6.37}$$

with binary collision fraction $x = 0.15$. A bag model equation of state is used, with chemical freeze out enforced at $T_{ch} = 170$ MeV, and kinetic freeze out at $T_f = 100$ MeV, below which temperature the medium has frozen out and no energy loss occurs. This is an ideal hydrodynamic calculation, with vanishing viscosity.

The other two hydrodynamical models correspond exactly to the calculations in [387] (for 200 GeV Au-Au collisions at RHIC) and [388] (for 2.76 TeV Pb-Pb collisions at the LHC), to which we again refer the reader for all relevant details.

One calculation, which we refer to as "Glauber", uses as initial condition an energy density proportional to the density of binary collisions, $\rho_{\rm bin}$, while the ratio of shear viscosity to

entropy density is fixed to a constant value of $\eta/s = 0.08$.

The final calculation is referred to as "fKLN". This simulation takes its initial condition from a factorized Kharzeev-Levin-Nardi model [389], with the shear viscosity set to $\eta/s = 0.16$.

Both of the latter simulations begin at an initial proper time of $\tau_0 = 1$ fm and use an equation of state inspired by lattice QCD calculations. Each system is assumed to be in chemical equilibrium until it reaches a freeze out temperature of $T_f = 140$ MeV.

All of these calculations have been successfully tested against several experimental data, but use different choices for initial conditions, thermalization time, viscosity, equation of state, etc. Thus, we expect that the variation in our results from using these different models should give a reasonable indication of the uncertainty coming from the hydrodynamic background. It will be shown that such uncertainty is negligible with respect to our main conclusions.

4.6.4 Results

This analysis is restricted to single-inclusive suppression at RHIC [390] and the LHC [205]. Other observables are not considered here, as they may involve other effects related with fragmentation, mass effects on the energy loss mechanism, etc. Something new is, the centrality dependence of both RHIC and LHC data. Most of previous studies have analyzed the most central collisions or the centrality dependence only for one energy [339, 366, 367]. Therefore, this is the first study of both centrality and (center of mass) energy dependence of the nuclear modification factor.

In Fig. 4.6 our results for different values of K together with the experimental data from the PHENIX Collaboration [390] on suppression of inclusive neutral pions on Au-Au collisions at $\sqrt{s_{\rm NN}} = 200$ GeV (72 data points) are plotted. In Fig. 4.7 we plot the corresponding results for LHC Pb-Pb collisions at $\sqrt{s_{\rm NN}} = 2.76$ TeV from ALICE [205], 156 data points [5]. We restrict to $p_T > 5$ GeV/c to stay in a region where pQCD can be applied and no large contribution from other effects like flow is expected. In both figures "Hirano" hydrodynamic simulation was used. The results with the other two above-mentioned hydrodynamic profiles are very similar to these ones.

We have performed a χ^2 fit to the best value of K for each energy and centrality, and for each assumption of hydrodynamical profile or behavior of $\hat{q}$ at values of proper time smaller than the thermalization time, τ_0, assumed in each hydrodynamical simulation. For the case of ALICE data [205] we add the systematic and statistical errors in quadrature, as no particular instructions of how to include them in a fit are provided. For the case of RHIC, the latest analysis includes the contribution from several different error sources. The two methods lead

[5] Note that the plotted values of K are different in both figures.

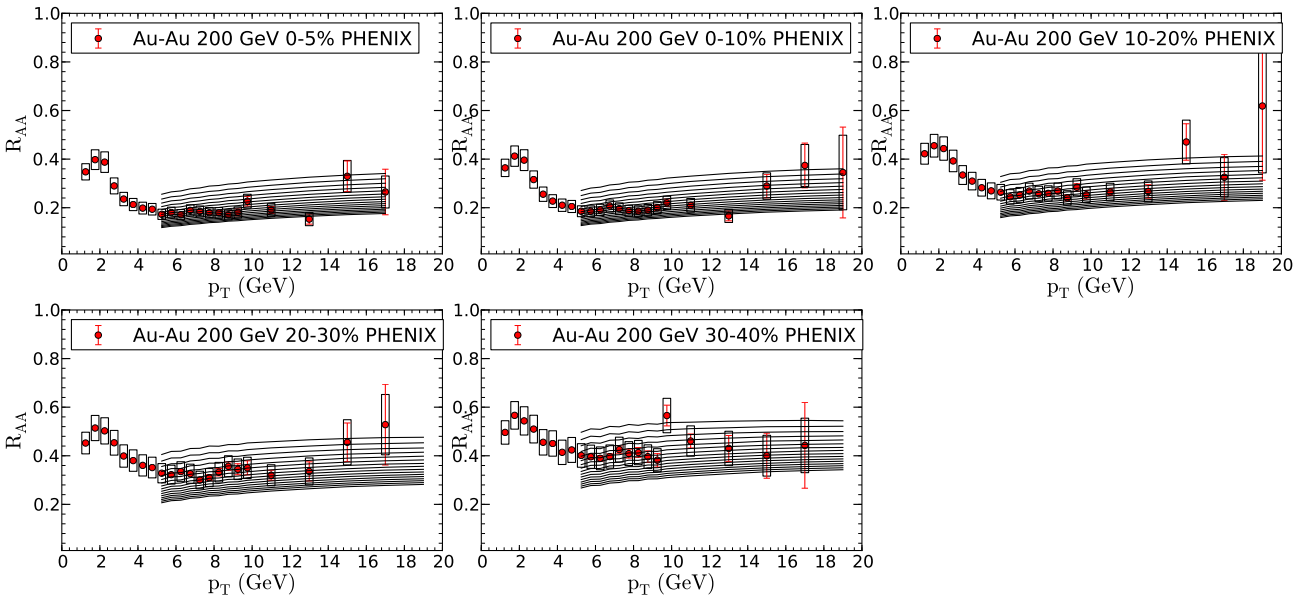

Figure 4.6: Suppression of inclusive π^0 in Au-Au collisions at $\sqrt{s_{\mathrm{NN}}} = 200$ GeV for different values of the parameter K (see Eq. (4.6.33)) compared with PHENIX data at different centralities [390]. Curves from top to bottom correspond to $K = K'/1.46$, with $K' = 2, 2.25, 2.5, \ldots, 6$, using the "Hirano" hydrodynamical model and the energy density prior to the start of hydrodynamical evolution taken as constant, see the previous subsection.

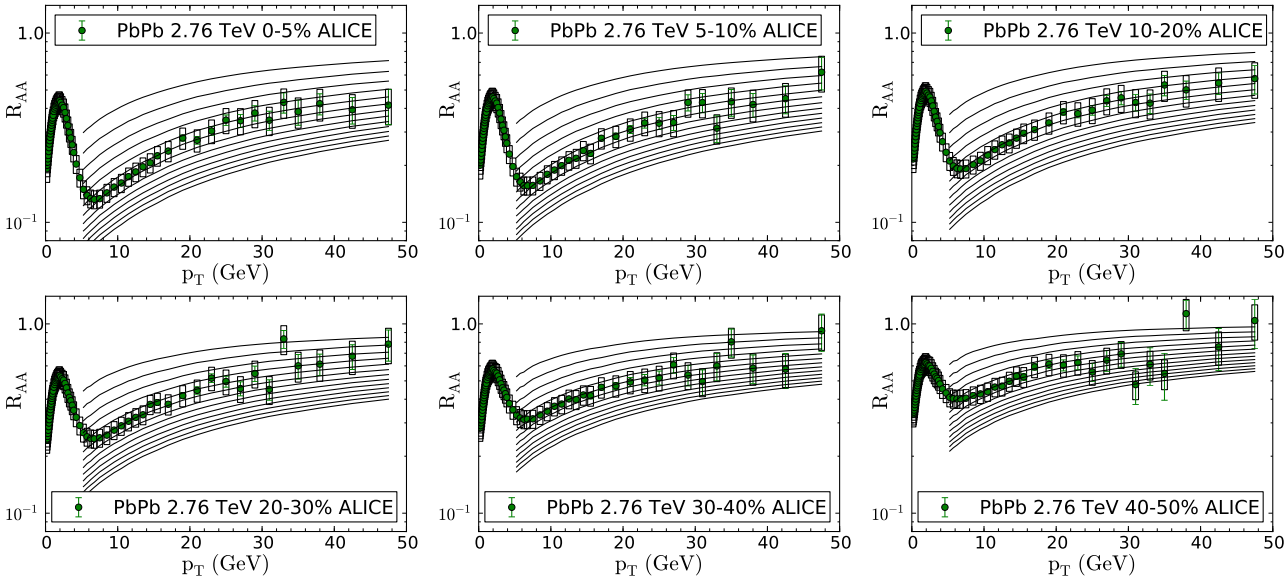

Figure 4.7: Suppression of inclusive charged particles in Pb-Pb collisions at $\sqrt{s_{\mathrm{NN}}} = 2.76$ TeV for different values of the parameter K (see Eq. (4.6.33)) compared to ALICE data at different centralities [205]. Curves from top to bottom correspond to $K = K'/1.46$, with $K' = 0.5, 0.7, 0.9, \ldots, 3.1$, using the "Hirano" hydrodynamical model and the energy density prior to the start of hydrodynamical evolution taken as constant, see the previous subsection.

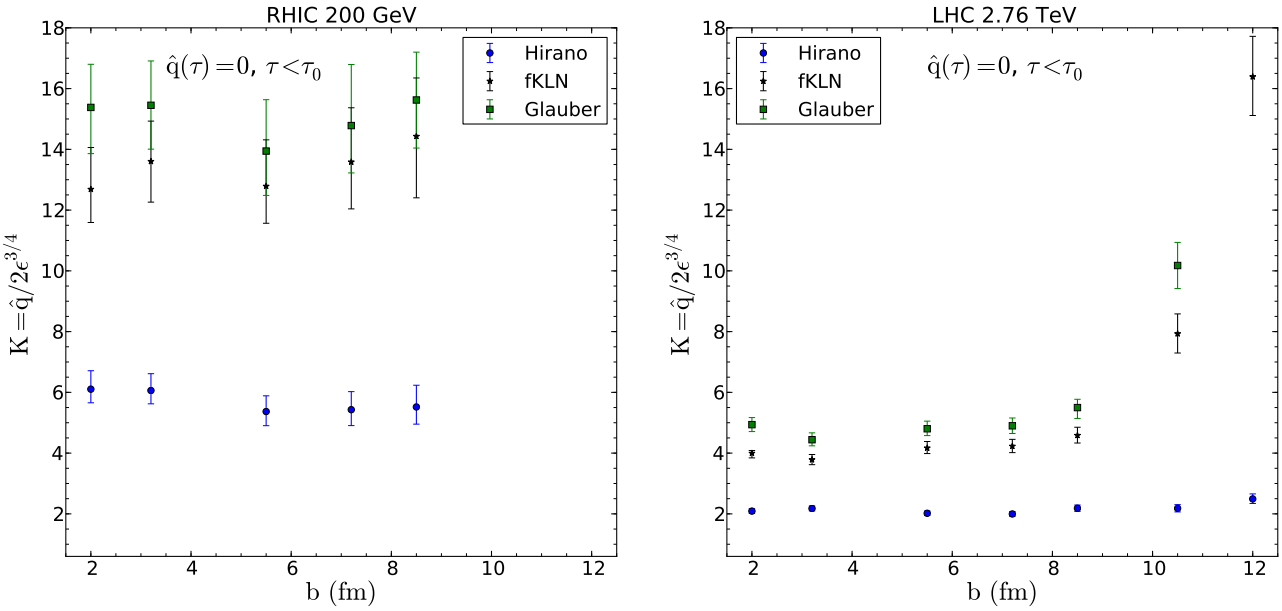

Figure 4.8: K-factors obtained from fits to PHENIX $R_{\rm AA}$ data [390] *(left panel)* and to ALICE $R_{\rm AA}$ data [205] *(right panel)* using different hydrodynamical profiles as a function of the average impact parameter for each centrality class and for $\hat{q}(\xi) = 0$ before thermalization, see the previous subsections.

to comparable values of K (differences $\sim 5\%$) except for the most peripheral bins, for which the K values in the case of errors added in quadrature are $\sim 30\%$ smaller. The uncertainty band is determined by $\Delta\chi^2 = 1$. In order to make the comparison between RHIC and the LHC, these issues need to be taken into account, although the conclusions do not change at the qualitative level. In the left panels of Fig. 4.8, Fig. 4.9 and Fig. 4.10 we plot the different values of the K-parameter fitted to the PHENIX data [390] for different combinations of hydrodynamic profiles and behavior before the proper time. The corresponding values for the LHC [205] are plotted in the right panels of the same figures.

Let us comment now on these results. First, the extracted values of K are compatible for the cases of either frozen energy density or free streaming before τ_0, and the results for the three different hydrodynamic models are similar. This is not the case when no quenching is assumed before τ_0; for this assumption, the two viscous hydrodynamic implementations which use a common (larger) τ_0 require a larger K than the ideal hydrodynamic model that considers a smaller τ_0, with actual values which become unrealistically large. Therefore, we do not consider the results obtained for this assumption for the discussion of the values of K, but the qualitative behavior that we find is in agreement with the two other assumptions. In any case they clearly illustrate the importance of the treatment of early times in jet quenching computations. Second, for the most peripheral collisions at the LHC, model "Glauber" demands a much larger K than the others, while model "Hirano" returns a rather flat value of K for all centralities. Third, the trend of the results at RHIC is a slight decrease with

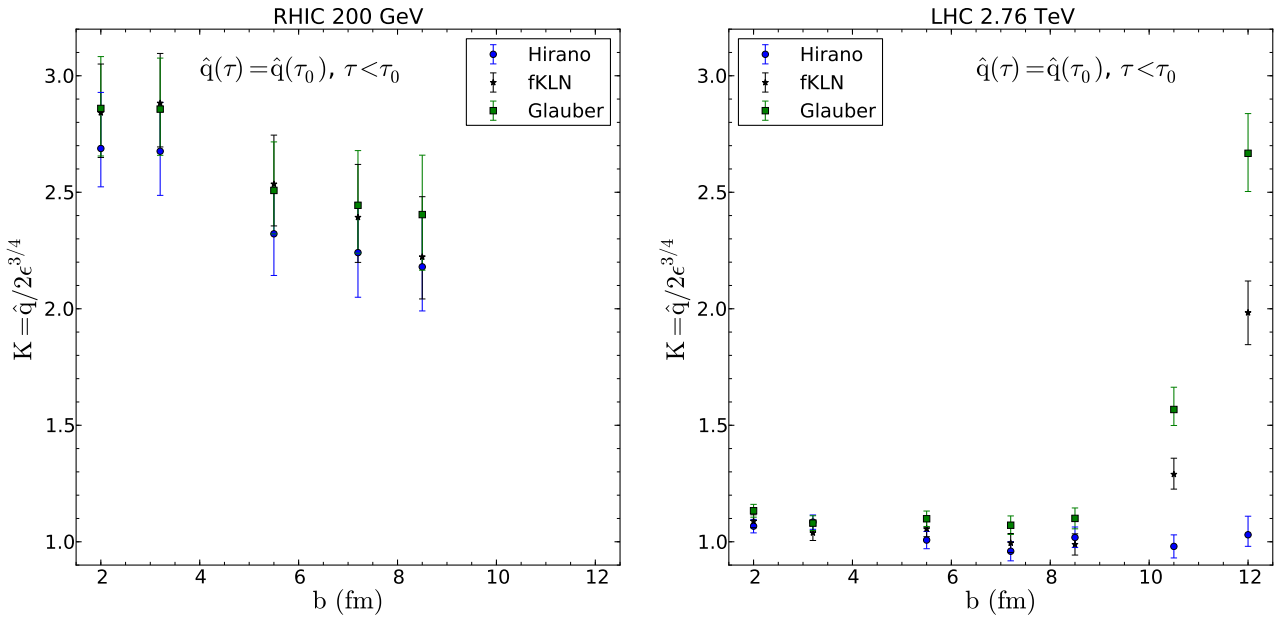

Figure 4.9: K-factors obtained from fits to PHENIX $R_{\rm AA}$ data [390] *(left panel)* and to ALICE $R_{\rm AA}$ data [205] *(right panel)* using different hydrodynamical profiles as a function of the average impact parameter for each centrality class and the energy density prior to the start of hydrodynamical evolution taken as constant, see the previous subsections.

decreasing centrality, although compatible with constant, while at the LHC the behavior is constant except for the smaller centralities, where the behavior, as it was mentioned above, depends very much on the hydrodynamic profile employed.

Finally, we would like to understand the systematics and relation of LHC and RHIC results for the K-factor that we obtain. First, we notice that, in principle, Eq. (4.6.33) determines how far or close the perturbative estimate $\hat{q} \simeq 2\epsilon^{3/4}$ is from our value fitted to experimental data. In this sense, we note that there is a clear departure from unity of this value for the case of RHIC. This fact was found several times [339, 357][6]. We also find that the corresponding value of K is smaller at the LHC, a fact which has been already found before by other groups [366] but with a smaller decrease (a factor ~ 25 % compared to our factor 2–3)[7]. The study of the centrality dependence is, nonetheless, more surprising. The extracted value of K seems to depend mainly on the energy of the collision and much less (if any) on the centrality. This is not the behavior one would expect from a naive interpreta-

[6]Note that the difference of the present extraction $K \sim 2$–3 and $K \sim 4$ from [357] comes mainly from the new definition of R in (4.6.32), indicating, again, the important role of the geometry in the extraction of $\hat{q}$.

[7]Nevertheless this comparison needs to be taken with caution as the values of $\hat{q}/T^3$ quoted in [366] are performed at a given temperature and no systematics with temperature is presented. Moreover, $\hat{q}$ is not the natural fitting parameter in the models studied in that reference but a derived quantity once the parameters of the different models are extracted from the data. In our case, $\hat{q}$ is the natural parameter, given by (4.4.24), and the K-factor has a well defined meaning.

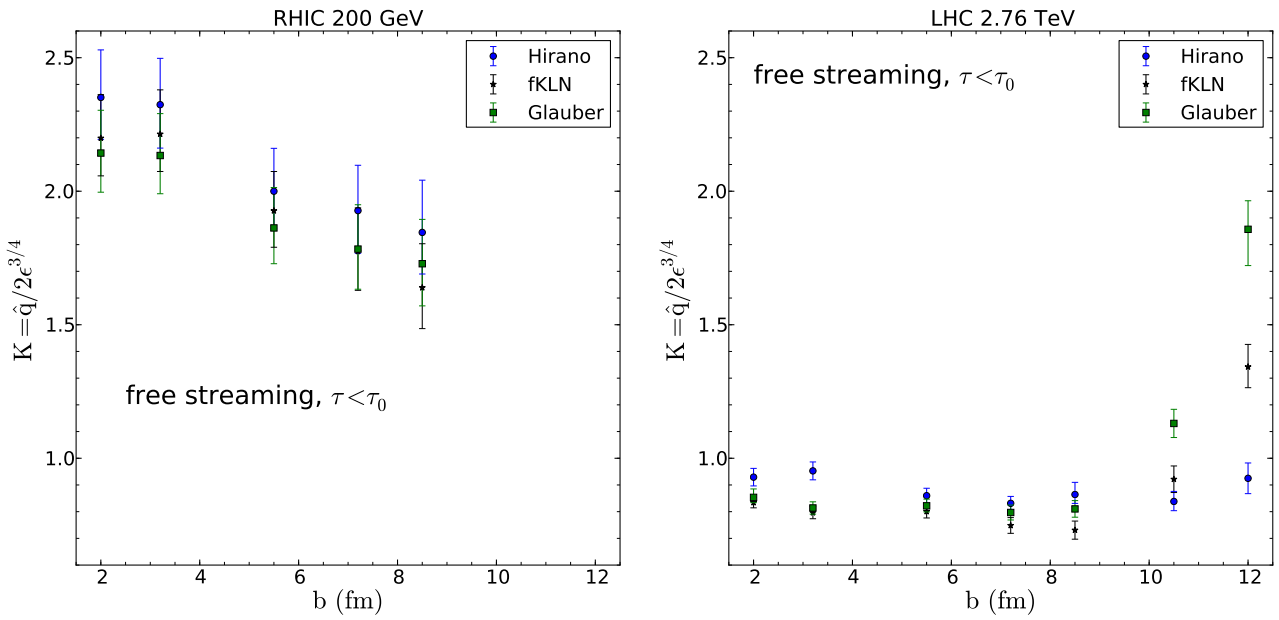

Figure 4.10: K-factors obtained from fits to PHENIX $R_{\rm AA}$ data [390] *(left panel)* and to ALICE $R_{\rm AA}$ data [205] *(right panel)* using different hydrodynamical profiles as a function of the average impact parameter for each centrality class and for the free-streaming extrapolation, see the previous subsections.

tion in which the K-factor only indicates the departure from the leading order perturbative estimate determined by temperature. In this naive interpretation, a medium with a smaller temperature (RHIC) would need higher orders of the perturbative series to be included, while a medium at higher temperature would be closer to the ideal limit. This simple interpretation does not correspond, notwithstanding, to the present findings as there is an overlap on typical energy densities between central Au-Au at RHIC and semi-peripheral Pb-Pb at the LHC, so their values of K should coincide in this naive interpretation. In order to provide an estimate of this overlap, we plot, in Figure 4.11, the K-factors obtained for different centralities and energies versus an energy density times formation time τ_0 extracted from the experimental data using Björken estimates [391, 392] – we have checked that the overlap is similar if we plot as a function of the maximum energy density of the hydrodynamical profiles that we have used to perform the fits.

4.6.5 Limitations and conclusions

One-particle inclusive suppression of particles produced at high transverse momenta at RHIC and the LHC as a function of centrality has been studied. By defining a constant K-factor with respect to the perturbative estimate $\hat{q} \simeq 2\epsilon^{3/4}$ we fit the corresponding experimental data at RHIC and LHC for different centralities. The fitted value at RHIC confirms previous estimates [339, 357] of large corrections to the ideal case, although the actual numerical

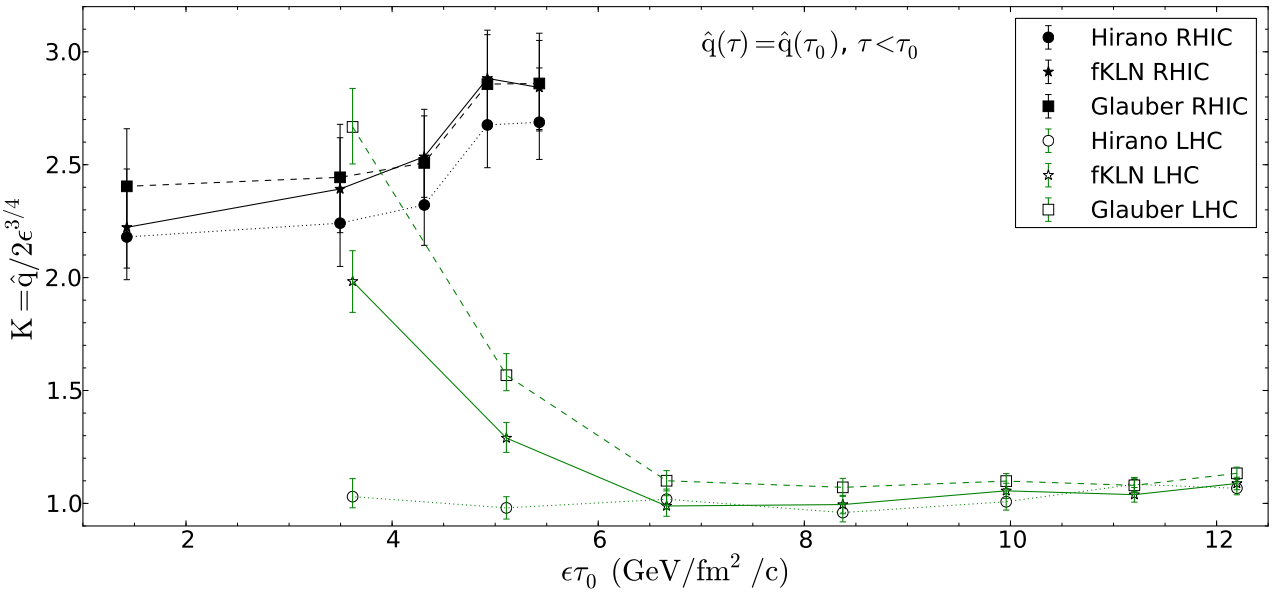

Figure 4.11: K-factor obtained from fits to R_{AA} data at RHIC and LHC energies for different centrality classes plotted as a function of an estimate of the energy density times formation time τ_0 of the QCD medium formed in each case. The $\epsilon\tau_0$ estimates are taken from [391,392].

value is a bit smaller, due to a new, more stable, definition of the effective values of the static scenario equivalent to the evolving medium, Eq. (4.6.32). For the case of the LHC, instead, the extracted value of K is close to unity. One would be tempted to make the naive interpretation that the medium created at the LHC, having a larger temperature, is closer to the ideal case than the one at RHIC, for which larger corrections or even a strongly coupling treatment, could be needed.

This naive interpretation finds difficulties to be accommodated, however, with the fact that the centrality dependencies at RHIC and the LHC separately are rather flat, that is, the change in the value of K is not simply due to the different temperature (or energy density), as there is a large region of overlap between RHIC and the LHC for different centralities. At this moment we do not have an interpretation for this finding which, in any case, should be checked by other model implementations of jet quenching. It is also worth noticing that the extraction of the value of K in the case of RHIC depends on a single set of experimental data, namely inclusive π^0 suppression measured by PHENIX. The corresponding results from STAR on $\pi^+ + \pi^-$ suppression [393] show a smaller suppression but the smaller range of transverse momentum studied makes our analysis to be not very reliable. For this reason we have chosen not to include this set of data in the fit. For the LHC, on the other hand, CMS [36] and ATLAS [394] have measured the suppression of inclusive charged particles with results almost identical to the ones from the ALICE collaboration[8].

[8]On the other hand, ALICE data are restricted to mid-rapidities where the boost invariant picture of

From a theoretical perspective, the formalism of the quenching weights presents several limitations which could influence the result. We quote some of them here: (i) the definition of $\hat{q}$ neglects the perturbative tails of the distributions which may enhance the energy loss and even change its angular dependence; (ii) as we have mentioned, the quenching weights rely on two assumptions which could fail if color coherence of the parton shower is broken during the path of the jet through the medium; (iii) the geometrical implementation of the hydrodynamical profiles relies on the relations (4.6.32) which have been proven only for a class of profiles $\hat{q}(\tau) \propto 1/\tau^{\alpha}$; (iv) finite length corrections to the independent gluon emission are not known in any of the implementations used at present; (v) finite energy corrections to the medium-induced gluon radiation could also affect the result; (vi) the jet quenching parameter $\hat{q}$ is taken to be energy or length independent, while evolution equations have been proposed [395–397]; (vi) finite energy corrections could also contain *collisional energy loss* which is neglected in our formalism and which may have a different parametric dependence with the medium properties. In spite of these limitations, it is difficult to imagine how a more refined implementation of the in-medium parton shower could qualitatively modify our finding of a mostly flat, in centrality, value of K and different for different collision energies. At the level of the partonic spectra, the main quantity affecting the suppression is a decreasing value of the slope with increasing energy: for a simple parametrization of $1/p_T^{\delta}$, δ varies in the range $5-7$ from the LHC to RHIC. This steeply falling spectrum introduces a bias in the probed energy loss distributions, so the typical energy of the partons at the LHC is larger than at RHIC for the same measured p_t. In this way, a softer part of the energy loss distribution is probed with increasing δ, so that the perturbative tails neglected in the multiple soft scattering approximation used may become relevant. Moreover, the typical jet could also be more collimated at lower energies (as the typical fraction of momentum probed in the fragmentation function is also larger). These details could modify the value of K extracted for a more realistic treatment of jet coherence and thermal cross sections. A better control on the initial times and the study of different experimental observables with refined methods will allow to clarify this issue.

4.6.6 One step forward: EbyE hydrodynamics

In the analysis shown in the previous section several smooth-averaged hydrodynamic simulations were used. It is shown here that these results are compatible with the ones obtained using an event-by-event hydrodynamics. The EbyE space-time distribution of the local energy density is obtained by solving the relativistic hydrodynamic equations with EKRT initial state, with constant shear viscosity $\eta/s = 0.2$ and starting time of viscous hydrodynamics $\tau_0 = 0.197$ fm [344]. This starting time is much smaller than that of the smooth-averaged hydrodynamic profiles (see Subsection 4.6.3), which reduces the ambiguity on the definition of the jet quenching parameter for times prior to thermalization. We have checked that using

the medium underlying the initial conditions for the hydrodynamic calculations should hold with very good accuracy, while ATLAS and CMS cover a much wider rapidity region. Further difficulties come from the modelling of the energy loss far from mid-rapidity. For these reasons, we restrict our study at the LHC to ALICE data.

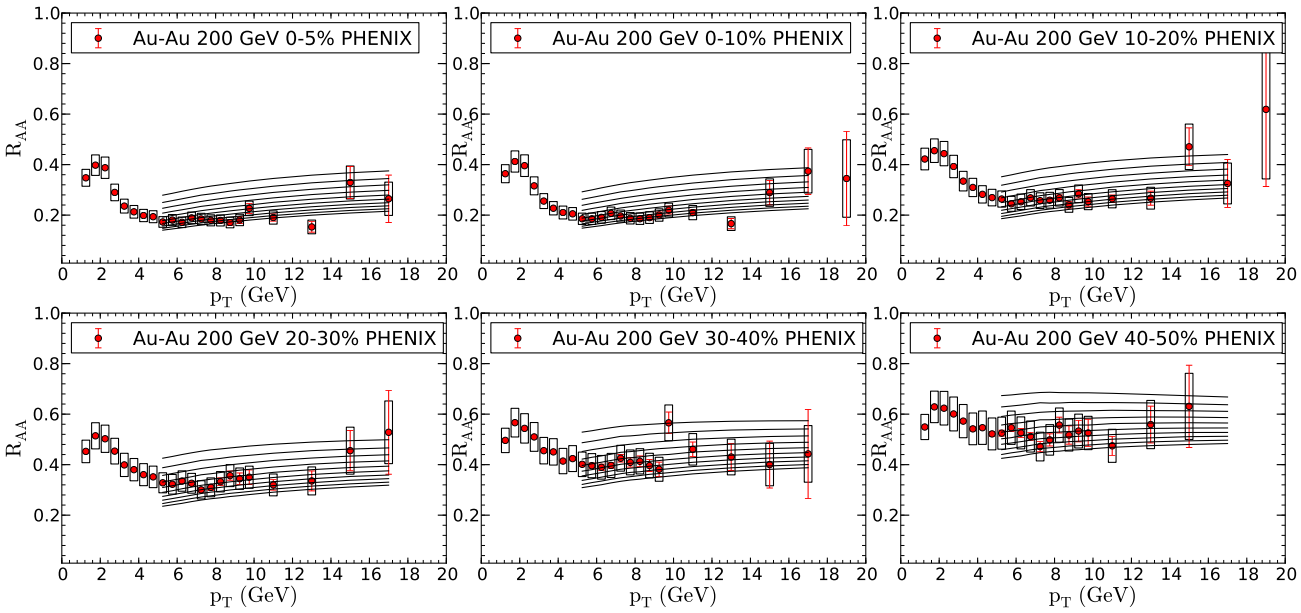

Figure 4.12: Suppression of inclusive π^0 in Au-Au collisions at $\sqrt{s_{\rm NN}} = 200$ GeV for different values of the parameter K (see Eq. (4.6.33)) compared with PHENIX data at different centralities [390]. Curves from top to bottom correspond to $K = 1.5, 1.75, 2, \ldots, 4$.

EKRT EbyE hydrodynamics the three extrapolations considered in the previous section for times smaller than the proper time, τ_0, give rise to similar results. Therefore, only the results for the case ii), i.e,

$$\hat{q}(\xi) \;=\; \hat{q}(\tau_0) \quad \text{for} \quad \xi < \tau_0 \;, \tag{4.6.38}$$

are presented in this section.

In Fig. 4.12 our results for different values of K together with the experimental data from the PHENIX Collaboration [390] on R_{AA} of Au-Au collisions at $\sqrt{s_{\rm NN}} = 200$ GeV are plotted. In Fig. 4.13 we plot the corresponding results for LHC Pb-Pb collisions at $\sqrt{s_{\rm NN}} = 2.76$ TeV from ALICE [205][9].

As for the study presented in the previous section for event-averaged hydrodynamical profiles, the fitted value at RHIC confirms large corrections to the ideal case, while the corresponding one at the LHC is close to unity. The K-factor obtained is $\sim 2-3$ times larger for RHIC than for the LHC, see Fig. 4.14. Second, the LHC results are rather constant except for the most peripheral collisions. Consequently, the fitted value of K seems to be mostly dependent on the (center of mass) energy of the collision rather than on its centrality, see Fig. 4.15.

In summary, this analysis, performed using the EbyE EKRT hydrodynamic descrip-

[9]Note that the plotted values of K are different in both figures and different to that on the previous section.

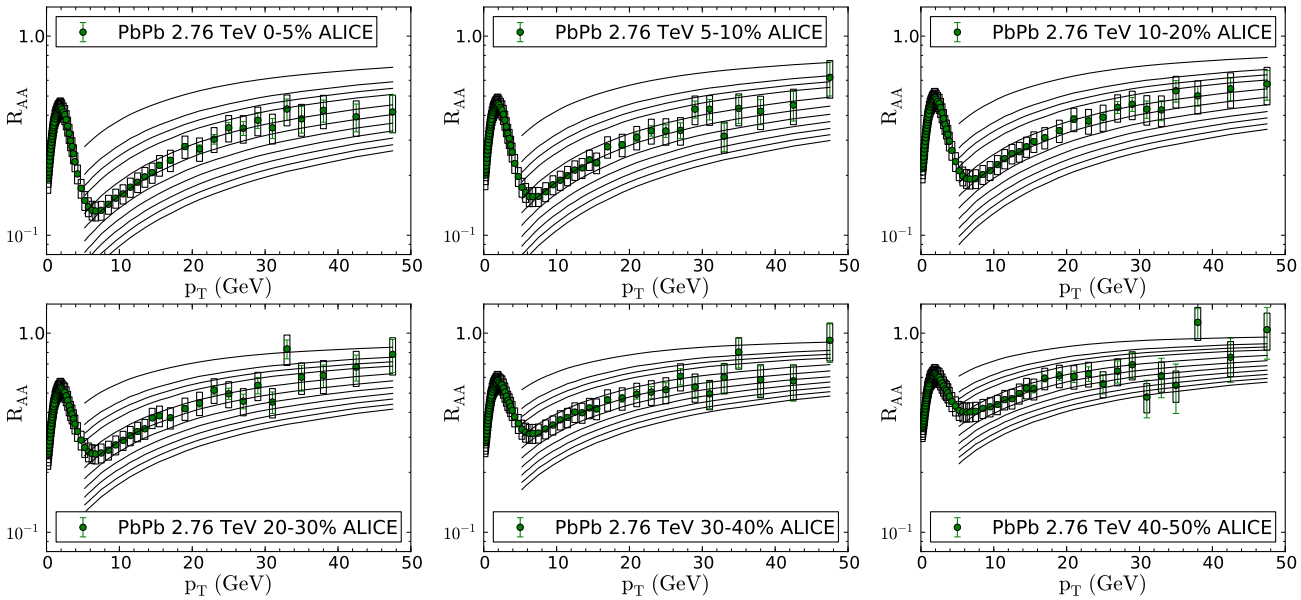

Figure 4.13: Suppression of inclusive charged particles in Pb-Pb collisions at $\sqrt{s_{\rm NN}} = 2.76$ TeV for different values of the parameter K (see Eq. (4.6.33)) compared to ALICE data at different centralities [205]. Curves from top to bottom correspond to $K = 0.5, 0.75, 0.875, 1, 1.125, 1.25, 1.5, 1.75, \ldots, 2.75$.

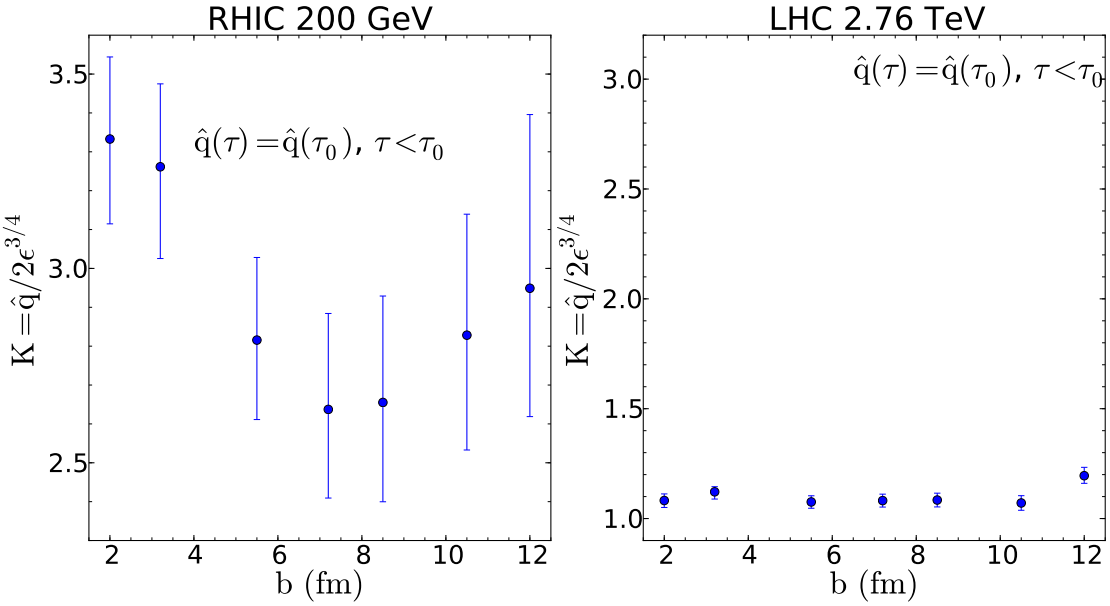

Figure 4.14: K-factors obtained from fits to PHENIX $R_{\rm AA}$ data [390] *(left panel)* and to ALICE $R_{\rm AA}$ data [205] *(right panel)* using EKRT EbyE hydrodynamics as a function of the average impact parameter for each centrality class.

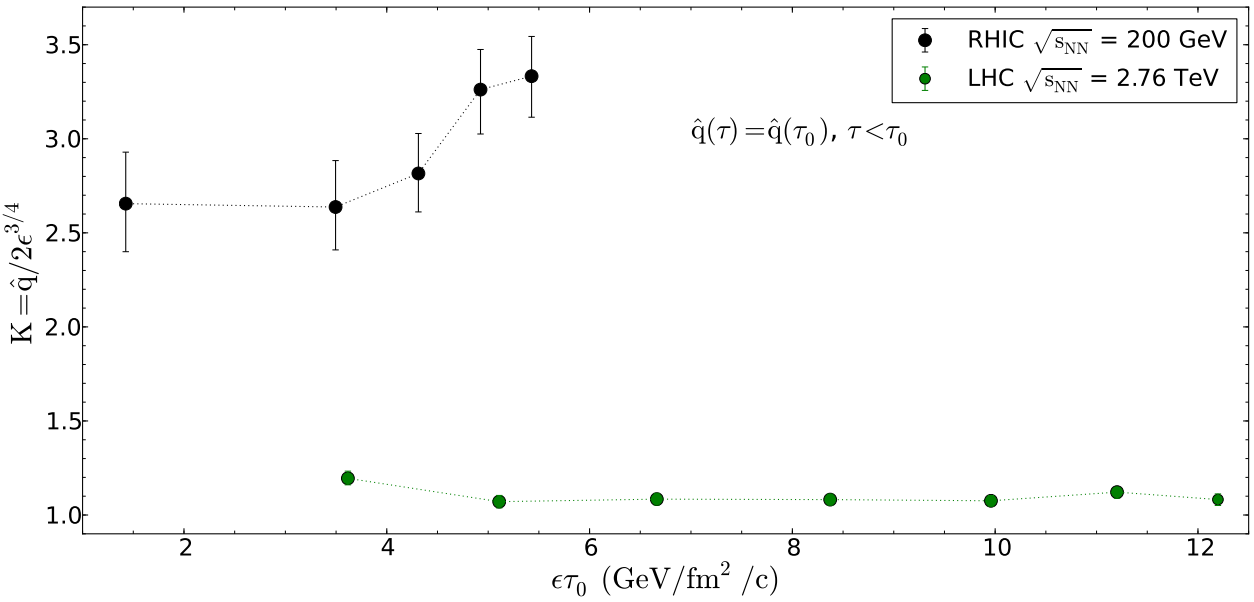

Figure 4.15: K-factor obtained from fits to R_{AA} data at RHIC and LHC energies for different centrality classes plotted as a function of an estimate of the energy density times formation time τ_0 of the QCD medium formed in each case. The $\epsilon\tau_0$ estimates are taken from [391,392].

tion [344], leads to the same conclusions that our previous analysis where smooth-averaged hydrodynamic simulations were employed.

As it was explained in Subsection 4.2.2 the description of high-p_T flow harmonics requires of the combination of EbyE fluctuations and a realistic model of jet quenching. We have shown here that by combining EbyE EKRT hydrodynamic simulation [344] and ASW Quenching Weights [300] we can fit the nuclear modification factor, R_{AA}, at different center of mass energies and centralities. This work was intended to serve as a first step towards a simultaneous description of the nuclear modification factor and the high-p_T flow harmonics within a complete and reliable treatement of both the hard and the soft sectors.

USC
UNIVERSIDADE
DE SANTIAGO
DE COMPOSTELA

Conclusions

This thesis is focused on the study of two different kind of effects arising in HICs: initial state effects (IS) and final state effects (FS). The former take place before the formation of the QGP and the latter occur once the dense medium is already created.

- **Initial state effects**

  Parton distribution functions (nPDFs)

  In chapter 2 a global analysis in NNLO in pQCD is presented. This is the first global fit at NNLO including a complete treatment of heavy quark effects within the *General Mass Variable Flavor Number scheme* (GM-VFNS). The analysis is performed in Mellin space and both data for charged-lepton DIS and neutrino DIS have been incorporated in it. It is worth emphasizing that among the neutral DIS data, deuterium data have been included, which are often excluded in nuclear global fits. We have also quantified the uncertainties by using the Hessian method. A central set of nPDFs and 24 error sets are presented.

  The results for the nuclear modification factors of the valence, sea, and gluon distributions turned out as expected. The valence distribution is the most constrained by DIS data. The sea and the gluon are only constrained by this kind of data in a very narrow region in x-space, therefore, their uncertainty bands are wider than those of the valence. Nevertheless, due to the sum rules and to the chosen parametrization, the uncertainties of the gluon are unrealistically small.

  Despite only DIS data have been included so far, this first attempt to compute in a complete way the nPDFs at NNLO is consistent with all the other available sets. This shows that this work sets the foundations for making a sizable improvement in the knowledge of nPDFs, once more data are incorporated. As we have entered an era of precision physics at the LHC, it is crucial to have nPDFs determined as precisely as possible. Furthermore, the future planned facilities such as the EIC, the LHeC, and the FCC make imperative this line of research. This work is in the process of being improved by including other types of data, as Drell-Yan, and by exploring different parametrizations.

Percolation of strings

The string percolation model (SPM) is a non-perturbative approach which captures some of the main features of the Color Glass Condensate (CGC). In the SPM, the multiplicity and the mean p_T-distributions result from the formation of clusters of strings which introduce correlations among the produced particles.

Several observables have been analyzed in chapter 3 within this framework. It has been shown that the geometric scaling observed both in HICs and in p-p collisions at different energies and centralities can be derived in the SPM. The anomalous dependence of the near-side ridge structure in Au-Au collisions at RHIC can be also naturally explained in this model. Moreover, the onset of this structure in high multiplicity events in proton-proton collisions is also described. Finally, experimental data of elliptic flow are shown to exhibit geometric scaling in Pb-Pb collisions at the LHC and Au-Au collisions at RHIC. This scaling law is also extended to the elliptic flow of identified particles: pions, kaons, and protons. It is suggested that this scaling may be due to the energy lost by the interaction of the parton with the color field of the strings.

- **Final state effects**

Regarding final state effects, hard probes and, more concretely, jet quenching has been studied in chapter 4. We have in there performed one of the most ample analysis of experimental data and its consequences for the QGP. Single-particle inclusive suppression of particles produced at high-p_T both at RHIC and at the LHC as a function of centrality has been presented. By defining a constant K-factor with respect to the perturbative estimate, $\hat{q} = K\, 2\epsilon^{3/4}$ – ϵ being the energy density – the corresponding nuclear modification factor data at RHIC and LHC for different centralities have been fitted. This is done by combining our energy loss model, the ASW Quenching Weights, with different smooth-averaged hydrodynamic simulations, to check that the outcome is independent of the hydrodynamic model employed.

The K-factor obtained at the LHC is approximately 1. The value at RHIC is $\sim 2-3$ times larger, confirming large corrections to the ideal case. However, its dependence on the centrality at RHIC and at the LHC separately is rather flat. Whether the K-factor was determined, by, for instance the temperature, the most central collisions at RHIC should present a value similar to semi-peripheral LHC data. Consequently, the K-factor would not depend on the local properties of the medium as energy density or temperature, but on global collision quantities such as the center of mass energy. This is a very unexpected result for which we cannot yet provide a clear interpretation.

Finally, an equivalent work to the one just described, but using now an *event-by-event* hydrodynamic profile, EKRT EbyE hydrodynamics, is shown. This analysis leads to the same conclusions that our previous one, where smooth-averaged hydrodynamic

simulations were used. It is worth stressing that this new study can be regarded as a first step towards the simultaneous description of the nuclear modification factor and the flow harmonics at high-p_T. Nowadays, there is not any realistic and reliable model of jet quenching which enable to compute both observables. However, recent works show the possibility of combining an *event-by-event* hydrodynamics and a complete formalism of jet quenching, as those implemented in our analysis. Therefore, this last study is a good starting point in this direction.

USC
UNIVERSIDADE
DE SANTIAGO
DE COMPOSTELA

Resumen

La fuerza fuerte es una de las cuatro interacciones fundamentales de la naturaleza. Dicha fuerza es la responsable de que los nucleones – protones y neutrones – permanezcan unidos formando los núcleos atómicos. La teoría que describe dicha interacción data de los años 1970 y se denomina Cromodinámica Cuántica (QCD, por sus siglas en inglés). La QCD describe las interacciones entre los quarks y gluones, partículas fundamentales que constituyen los hadrones. Actualmente la QCD es considerada uno de los pilares fundamentales del denominado Modelo Estándar de las partículas elementales y sus interacciones.

Entre las propiedades de la QCD cabe destacar dos de gran relevancia: la *libertad asintótica* y el *confinamiento*. La libertad asintótica es la reducción de la fuerza de las interacciones entre los quarks y gluones a medida que la escala de la energía de dichas interacciones aumenta, o lo que es lo mismo, la de distancia decrece. Por tanto, los quarks se mueven en el interior de los hadrones como partículas libres, lo que permite el uso de lo que se conoce como técnicas perturbativas. Sin embargo, a distancias largas, la fuerza de esta interacción aumenta confinando los quarks y gluones en el interior de los hadrones. Esta es la razón por la que quarks y gluones no existen de forma aislada en la naturaleza, sino que están formando parte de los hadrones.

Las colisiones de iones pesados (HICs, por sus siglas en inglés) son la herramienta fundamental para estudio de la Cromodinámica Cuántica bajo condiciones extremas de temperatura y densidad, muy distintas a las que existen en el interior del núcleo atómico. En estas colisiones nucleares de alta energía se alcanzan temperaturas y densidades críticas que permiten la formación del denominado quark-gluon plasma (QGP). La existencia de esta nueva forma de materia nuclear fue predicha por primera vez en los años 1970.

Bajo estas condiciones, las interacciones de distancia corta comienzan a dominar sobre las de distancia larga que empiezan a verse apantalladas por las fuentes de color a su alrededor. Las interacciones de distancia corta se caracterizan por una constante de acoplamiento pequeña debido a la libertad asintótica característca de la QCD. Por tanto, el QGP, está constituido por quarks y gluones – grados de libertad del lagrangiano de QCD – deconfinados. Este plasma es un líquido casi perfecto, cuyos componentes están estrechamente unidos. Por ello, su estudio nos puede ayudar a entender mejor la parte no perturbativa de la QCD, de la cual el conocimiento hoy en día es limitado.

Además, el QGP es descrito por los modelos cosmológicos actuales como el estado de la

materia durante los primeros microsegundos tras el Big-Bang. Por consiguiente, el estudio del QGP en colisiones de iones pesados, nos permite analizar la evolución de este estado de la materia (deconfinada) que existía en los inicios del Universo hacia la materia *normal* confinada. O lo que es lo mismo, nos pueden revelar información sobre el origen de la masa y del confinamiento. Las colisiones nucleares de alta energía son, en definitiva, una gran oportunidad de observar y entender el origen y la evolución de nuestro Universo. Esto ha llevado al desarrollo de diversos programas de física de iones pesados: en el Alternating Gradient Synchrotron (AGS) en Brookhaven National Laboratory (BNL), en el Super Proton Synchrotron (SPS) en el Conseil Européen pour la Recherche Nucléaire (CERN), en el Relativistic Heavy Ion Collider (RHIC) en BNL y en el Large Hadron Collider (LHC) en CERN.

Según cálculos en *Lattice QCD* la temperatura crítica para la formación del QGP es $T_c \simeq 154\,\mathrm{MeV}$, que se corresponde a una densidad crítica de energía de $\epsilon_c \sim 1\,\mathrm{GeV/fm^3}$. Los datos experimentales muestran desde hace mucho tiempo que la temperatura alcanzada en las colisiones relativistas de iones pesados es mayor que dicha temperatura crítica. En consecuencia, este tipo de colisiones son las propicias para estudiar las propiedades del QGP. Los sistemas producidos en estas colisiones se caracterizan por la presencia de fenómenos colectivos y efectos del medio (del QGP) que son accesibles experimentalmente. El estudio de procesos que son sensibles al grado de colectividad del sistema es el objetivo fundamental de las colisiones de iones pesados.

Sin embargo, la vida media del plasma de quarks y gluones producido en HICs es muy pequeña – del orden de 100 ys $= 10^{-24}$ s – y, por tanto, no puede ser detectado directamente. Las propiedades de este estado de la materia han de ser estudiadas indirectamente en el estado hadrónico final de la colisión. Generalmente, se utilizan distribuciones de partículas *soft* para ver indicios de comportamiento colectivo del QGP y tratar de dar una posible descripción hidrodinámica del mismo; al mismo tiempo que se usan *hard probes* para ver el efecto del medio sobre procesos que puedan ser calculados perturbativamente.

Esta memoria se centra en el análisis de dos tipos de efectos:

- **Efectos de estado inicial (IS)**. Son efectos previos a la termalización.
  - *Funciones de distribución partónicas nucleares (nPDFs).*

    Un ingrediente básico para entender las colisiones de iones pesados y poder describir, por tanto, el QGP formado en ellas, son las funciones de distribución partónicas nucleares (nPDFs, por sus siglas en inglés). Estas contienen la información de la estructura partónica (quarks y gluones) de los protones y neutrones que forman los núcleos que colisionan. Son, por tanto, contribuciones de distancia larga que no pertenecen al dominio perturbativo de la QCD. Su determinación precisa es crucial para la correcta interpretación de todos los observables utilizados en HICs. Gracias a su universalidad y al hecho de que su evolución respecto a una determinada escala inicial sí es perturbativa, las nPDFs son obtenidas mediante una técnica denominada análisis global. La extracción de estas distribuciones

mediante un análisis global a next-to-next-to leading order (NNLO) en QCD es el objeto del capítulo 2 de esta tesis.

La técnica del análisis global – o fit global – consiste en extraer las nPDFs a partir de diversos experimentos: dispersión inelástica profunda – DIS, por sus siglas en inglés –, Drell-Yan, etc. El procedimiento es el que sigue. Primero, se seleccionan los observables experimentales a usar y se computan a nivel partónico al orden deseado en QCD perturbativa, en nuestro caso a NNLO. A continuación, las nPDFs son parametrizadas a una escala inicial, Q_0. Para cada set de datos, las nPDFs son evolucionadas usando las conocidas como ecuaciones de Dokshitzer-Gribov-Lipatov-Altarelli-Parisi (DGLAP) (también a NNLO) desde la escala inicial a la escala del proceso, $Q > Q_0$. En nuestro caso esta evolución es realizada en el espacio Mellin. Después, se convoluciona la parte de pequeña distancia (*hard*) con la de larga distancia (*soft*) para obtener el observable en espacio Mellin. Posteriormente se realiza una inversión de Mellin para obtener la predicción teórica del observable en espacio x. Finalmente, se construye una distribución χ^2 y se extrae el valor de los parámetros minimizando iterativamente el χ^2.

En el capítulo 2 de esta tesis se presenta dicho fit global de nPDFs a NNLO. Este análisis incorpora un tratamiento íntegro de los efectos de quarks pesados siguiendo el denominado *Esquema General con Número Variable de Sabores* (GM-VFNS, por sus siglas en inglés). Este es el primer fit global hecho a NNLO en QCD con un tratamiento exhaustivo de los efectos de masa de los quarks. En este fit se utilizan datos de DIS con leptones cargados y de DIS con neutrinos. Cabe destacar que entre el primer tipo de datos, se incluyen datos donde el blanco es deuterio, tratando así los efectos nucleares del deuterio normalmente obviados en los análisis globales de funciones de distribución partónicas nucleares. Por otra parte, se han cuantificado las incertidumbres experimentales dando lugar a 24 sets de errores, además del set central de nPDFs.

Además de ser imprescendibles para entender las ya mencionadas colisiones de iones pesados que tiene lugar en el Large Hadron Collider (LHC) en CERN (Suiza) y en Relativistic Heavy-Ion Collider (RHIC) en Brookhaven (USA), el conocimiento preciso de las nPDFs será crucial para los futuros aceleradores, como el Electron Ion Collider (EIC) y el Large Hadron-Electron Collider (LHeC). Por ello su determinación cada vez más precisa es una línea de investigación imperativa no solo para la comunidad de iones pesados, sino para la física de altas energías actual y futura.

– *Percolación de cuedas.*

Otro tema de gran interés son los fenómenos colectivos que dan lugar a la producción del QGP. Estos son habitualmente analizados bajo el marco del Clolor

Glass Condensate (CGC) en HICs. Un modelo simplificado que captura varias de las propiedades del CGC es la percolación de cuerdas. Este enfoque y algunos de sus resultados comparados con los datos experimentales se presentan en el capítulo 3.

Las colisiones de iones pesados son descritas en este modelo mediante la formación de cuerdas que unen los partones del proyectil y del blanco de la colisión. Estas cuerdas de color pueden ser vistas como cilindros expandidos en la dirección longitudinal cuyas intersecciones con el plano transverso son pequeñas áreas llenas del campo de color de los partones colisionantes. Al crecer el número atómico o la energía de la colisión, el número de cuerdas crece y estas empiezan a solaparse formando agregados, usualmente denominados *clusters*. Esto da lugar a tres importantes consecuencias:
-La carga de color de un cluster de n cuerdas es $\sqrt{n}$ – y no n – veces la carga elemental de las cuerdas. Como consecuencia, la multiplicidad se reduce respecto al caso de cuerdas independientes.
-Las partículas son creadas vía producción de pares quark-antiquark en el campo de color mediante un mecanismo tipo Schwinger.
-La percolación es un fenómeno crítico: alcanzada una cierta densidad de cuerdas, denominada densidad crítica o de percolación, se forma un único cluster macroscópico que ocupa toda la superficie de solapamiento nuclear.

Diversos observables en HICs serán analizados en el capítulo 3 mediante dicho formalismo. Entre estos, se encuentra el denominado *escaleo geométrico* observado no solo en colisiones de iones persados, sino también en colisiones protón-protón. En dicho capítulo, se mostrará que este escaleo puede ser explicado mediante la percolación de cuerdas para distintas colisiones, energías y centralidades.

Otro fenómeno analizado es la llamada *near-side ridge structure*. La dependencia anómala de esta estructura encontrada en colisiones de núcleos de oro será explicada de forma natural en el contexto de la percolación de cuerdas. Además, la aparición de dicha estructura en eventos de alta multiplicidad en colisiones protón-protón también será descrita.

Por último, se mostrará que los datos experimetales de flujo elíptico en colisiones de plomo-plomo en el LHC y de oro-oro en RHIC también satisfacen una ley de escaleo. Dicha ley se extiende también al flujo elíptico de piones, kaones y protones. Se mostrará que dicho escaleo puede tener como origen la pérdida de energía debida a la interacción del partón emitido con el campo de color de las cuerdas.

- **Efectos de estado final (FS)**.

  Entre ellos, cabe destacar las *hard probes*, esto es, partículas caracterizadas por un alta

energía o masa cuyo estudio pertenece al régimen perturbativo de la QCD. El estudio de procesos tipo *hard* (hard probes) se ha convertido en uno de los campos más activos de investigación en colisiones de iones pesados debido al amplio rango de escalas de energía que engloba.

– *Supresión de jets*

Su comportamiento en vacío, esto es, en colisiones en las que no se forma un plasma, es conocido. En consequencia, se analizan las modificaciones debidas a la presencia de un medio nuclear, es decir, debidas a la fomación del QGP, permitiéndonos extraer así las propiedades de éste. Entre estas *hard probes* cabe destacar la supresión de jets (*jet quenching*). La supresión de jets, y más concretamente, la supresión inclusiva de partículas de alto momento en HICs será analizada en el capítulo 4.

El fenómeno supresión de jets se refiere más concretamente al conjunto de efectos que sufren las partículas tipo *hard* al propagarse por el QGP. Fue propuesto por Bjorken en 1982 y más tarde observado en RHIC y LHC. Hoy en día se trata de un fenómeno bien establecido del que se tienen muchos datos experimentales tanto de RHIC como del LHC. No obstante, desde el punto de vista teórico no ha sido todavía completamente entendido.

En una colisión de iones pesados los partones hard se forman con el QGP, el cual tienen que atravesar antes de dar lugar a las partículas finales detectadas en los experimentos. Durante dicha propagación sufren jet quenching. El objetivo fundamental de los analísis de dicho fenómeneno es extraer las propiedades del QGP a través del estudio de la modificación de la propagación de los partones debido a la presencia del plasma.

Uno de los estudios más extensos de datos experimentales y sus consecuencias para las propiedades del medio será presentado en capítulo 4. En dicho estudio, se analizan datos tanto de RHIC como de LHC del denomiado factor de modificación nuclear para producción *single-inclusive* de partículas de alto momento transverso. La pérdida de energía en el medio es analizada mediante los denominados *Quenching Weights* (QW) y la evolución dinámica del medio es tratada mediante distintas simulaciones hidrodinámicas. El resultado fundamental de este análisis es la extracción del denominado coeficiente de tranporte de jets, $\hat{q}$.

En nuestro estudio el coeficiente de tranporte de jets, $\hat{q}$, es determinadado por la densisdad de energía local, ϵ, extraida de diversos modelos hidrodinámicos. El coeficiente de transporte es definido como $\hat{q} = K2\epsilon^{3/4}$ y los valores de K son *fiteados* a los datos experimentales del factor de modificación nuclear a distintas centralidades y energías. El resultado obtenido es que este factor K es $\sim 2-3$ mayor para RHIC que para el LHC y que, sorprendentemente, este factor K parece no

depender de las propiedades locales del medio, como la temperatura. De hecho, K depende principalmente de la energía del centro de masa de la colisión y es básicamente independiente de la centralidad de la misma.

El formalismo de pérdida de energía utilizado en este trabajo, son los ya mencionados Quenching Weights. Estos son unas probabilidades de pérdida de energía tipo Poisson basadas en la emisión independiente de gluones inducida por el medio y calculados en el formalismo de Armesto-Salgado-Wiedemann (ASW). Para modelar la parte *soft* se utilizan primero tres perfiles hidrodinámicos *smooth-averaged* que usan diferentes ecuaciones de estado, condiciones iniciales, tiempo de termalización, etc., demostrando así que nuestras conclusiones son independientes del modelo hidrdinámico empleado. En el capítulo 4 este análisis, sus resultados, limitaciones y conclusiones son presentados en detalle.

Por último, se presenta un trabajo equivalente al anterior, pero usando una simulación hidrodinámica *event-by-event*. Este estudio lleva a las mismas conclusiones que el previo, en el que los modelos hidrodinámicos empleados eran *smooth-averaged*. Cabe destacar, además, que este nuevo análisis sirve como un paso previo hacia la descripción simultánea del factor de modificación nuclear y los armónicos a alto momento transverso. A día de hoy, ningún modelo realista de jet quenching ha sido capaz de determinar correctamente ambos observables. Sin embargo, estudios recientes muestran la posibilidad de calcular ambos mediante la combinación de un modelo hidrodinámico *event-by-event* y un formalismo completo para el jet quenching, como los que tenemos implementados en nuestro análisis. Por ello, este último trabajo sirve de punto de partida en esta dirección.

En resumen, en esta tesis se consideran diversos aspectos relacionados con los estados inicial y final en colisiones de iones pesados. En la introducción se presentan algunos aspectos generales de la Cromodinámica Cuántica motivando su estudio en colisiones de iones pesados. El el capítulo dedicado a las funciones de distribución partónicas nucleares, capítulo 2, se presenta un fit global a next-to-next-to leading order en QCD perturbativa. En el capítulo 3, se describe el formalismo de percolación de cuerdas y diversos observables en HICs son analizados mediante el uso de dicho modelo. Por último, en el capítulo 4 se presenta un análisis de la supresión inclusiva de partículas de alto momento a diversas energías y centralidades, cuyo resultado principal es la determinación del denominado coeficiente de tranporte de jets, $\hat{q}$.

Appendix A

About the Mellin technique in global analysis

The Mellin transform of a function $f(x)$ is given by

$$\hat{f}\,(N) \;=\; \int_0^1 dx\, x^{N-1} f(x) \;\;, \tag{A.1}$$

where N is an integer number. An analytic continuation to complex values of the argument can be done [398].

The DGLAP equations, Eqs. (2.1.12) and (2.1.13), where written in terms of a convolution of the PDFs (*soft* part) and the splitting functions (*hard* part). Here, it will be proven than this kind of convolution in the x-space, when a Mellin transform is applied, can be written as a product. The Mellin convolution is

$$f \otimes g\,(x) \;\equiv\; \int_x^1 \frac{dz}{z} f\,(z)\, g\left(\frac{x}{z}\right) \;\;, \tag{A.2}$$

a Mellin transform is applied,

$$\widehat{f \otimes g}\,(N) \;=\; \int_0^1 dx\, x^{N-1} \int_x^1 \frac{dz}{z} f\,(z)\, g\left(\frac{x}{z}\right) \;\;. \tag{A.3}$$

Changing the order of the integrals,

$$\widehat{f \otimes g}\,(N) \;=\; \int_0^1 \frac{dz}{z}\, f\,(z) \int_0^z dx\, x^{N-1} g\left(\frac{x}{z}\right) \tag{A.4}$$

Denoting by $y = x/z$ we have

$$\widehat{f \otimes g}\,(N) \;=\; \int_0^1 dz\, z^{N-1} f\,(z) \int_0^1 dy\, y^{N-1} g\,(y) = \hat{f}\,(N)\, \hat{g}\,(N) \tag{A.5}$$

This is what is done for the DGLAP equations. It is numerically useful, as instead of working with convolutions, it is possible to work with products in the Mellin-space. Therefore, the products of the Mellin moments of the PDFs and the splitting functions need to be

computed and then a Mellin inverse has to performed.

The moments of the splitting functions are usually called *anomalous dimensions*. They have been computed up to NNLO. The expressions of the anomalous dimensions (in Mellin-space) for the non-singlet up to NNLO can be found in [56]. For the anomalous dimensions appearing in the singlet sector, see [57].

Wilson coefficients in Mellin-space are needed to compute the structure functions. At LO the coefficients for F_2, F_L and F_3 are [399]

$$\begin{aligned} C_{2,q}^{(0)} &= C_{3,q}^{(0)} = 1 \\ C_{2,g}^{(0)} &= C_{L,q}^{(0)} = C_{L,g}^{(0)} = 0 \ . \end{aligned} \tag{A.6}$$

The expressions at NLO and NNLO can be found in [399, 400].

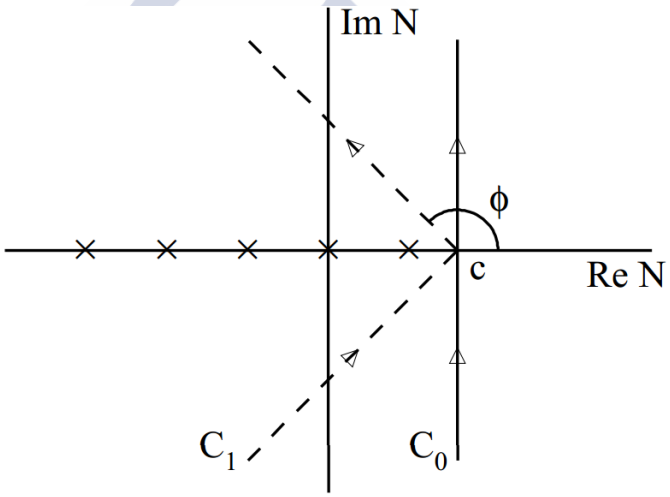

Figure A.1: Two integration contours, C_0 and C_1, for the Mellin inverse transformation Eq. (A.7). The crosses indicate the singularities, N_i, of $f(N)$.

The inverse transform of Mellin of the moments is given by

$$f\left(x\right) = \frac{1}{2\pi i}\int_{c+i\infty}^{c-i\infty} dN\, x^{-N} f\left(N\right) \tag{A.7}$$

where $f(x)$ is smooth for $x > 0$ (as in our case). The real number c has to be such that $\int_0^1 dx\, x^{c-1} f(x)$ is absolutely convergent [401]. Consequently, c has to lie on the right of the rightmost singularity N_{max} of $f(N)$. The contour of the integration in the complex plane in Eq. (A.7) is shown in Fig. A.1 denoted by C_0. Sometimes is useful to deform this contour, to improve the convergence. The route C_1, with $\phi > \pi/2$ displayed in the same figure, gives the same result for Eq. (A.7), provided that $f(N)$ has no singularities, N_i enclosed by

$C_0 - C_1$. This contour was suggested by [372]. In the case of (n)PDFs this requirement is fulfilled automatically as the singularities N_i are real with $N_i < N_{max} < c$. Specifically, the values $\phi = 3/4\,\pi$ and $c = 0.8$ are taken.

USC
UNIVERSIDADE
DE SANTIAGO
DE COMPOSTELA

List of Figures

List of Tables

USC
UNIVERSIDADE
DE SANTIAGO
DE COMPOSTELA

Bibliography

[1] T. D. Lee and G. C. Wick, "Vacuum Stability and Vacuum Excitation in a Spin 0 Field Theory," Phys. Rev. D **9** (1974) 2291.

[2] J. C. Collins and M. J. Perry, "Superdense Matter: Neutrons Or Asymptotically Free Quarks?," Phys. Rev. Lett. **34** (1975) 1353.

[3] N. Cabibbo and G. Parisi, "Exponential Hadronic Spectrum and Quark Liberation," Phys. Lett. **59B** (1975) 67.

[4] B. A. Freedman and L. D. McLerran, "Fermions and Gauge Vector Mesons at Finite Temperature and Density. 1. Formal Techniques," Phys. Rev. D **16** (1977) 1130.

[5] E. V. Shuryak, "Quark-Gluon Plasma and Hadronic Production of Leptons, Photons and Psions," Phys. Lett. **78B** (1978) 150 [Sov. J. Nucl. Phys. **28** (1978) 408] [Yad. Fiz. **28** (1978) 796].

[6] A. Bazavov [HotQCD Collaboration], "The QCD equation of state with 2+1 flavors of Highly Improved Staggered Quarks (HISQ)," Nucl. Phys. A **904-905** (2013) 877c [arXiv:1210.6312 [hep-lat]].

[7] J. Adams *et al.* [STAR Collaboration], "Experimental and theoretical challenges in the search for the quark gluon plasma: The STAR Collaboration's critical assessment of the evidence from RHIC collisions," Nucl. Phys. A **757** (2005) 102 [nucl-ex/0501009].

[8] K. Adcox *et al.* [PHENIX Collaboration], "Formation of dense partonic matter in relativistic nucleus-nucleus collisions at RHIC: Experimental evaluation by the PHENIX collaboration," Nucl. Phys. A **757** (2005) 184 [nucl-ex/0410003].

[9] U. W. Heinz and M. Jacob, "Evidence for a new state of matter: An Assessment of the results from the CERN lead beam program," nucl-th/0002042.

[10] T. Matsui and H. Satz, "J/ψ Suppression by Quark-Gluon Plasma Formation," Phys. Lett. B **178** (1986) 416.

[11] M. C. Abreu *et al.* [NA50 Collaboration], "Evidence for deconfinement of quarks and gluons from the J / psi suppression pattern measured in Pb + Pb collisions at the CERN SPS," Phys. Lett. B **477** (2000) 28.

[12] A. Adare *et al.* [PHENIX Collaboration], "J/ψ Production vs Centrality, Transverse Momentum, and Rapidity in Au+Au Collisions at $\sqrt{s_{NN}} = 200$ GeV," Phys. Rev. Lett. **98** (2007) 232301 [nucl-ex/0611020].

[13] L. V. Gribov, E. M. Levin and M. G. Ryskin, "Semihard Processes in QCD," Phys. Rept. **100** (1983) 1.

[14] A. H. Mueller and J. w. Qiu, "Gluon Recombination and Shadowing at Small Values of x," Nucl. Phys. B **268** (1986) 427.

[15] L. D. McLerran and R. Venugopalan, "Computing quark and gluon distribution functions for very large nuclei," Phys. Rev. D **49** (1994) 2233 [hep-ph/9309289].

[16] L. D. McLerran and R. Venugopalan, "Gluon distribution functions for very large nuclei at small transverse momentum," Phys. Rev. D **49** (1994) 3352 [hep-ph/9311205].

[17] M. A. Braun, J. Dias de Deus, A. S. Hirsch, C. Pajares, R. P. Scharenberg and B. K. Srivastava, "De-Confinement and Clustering of Color Sources in Nuclear Collisions," Phys. Rept. **599** (2015) 1 [arXiv:1501.01524 [nucl-th]].

[18] David J. Gross and Frank Wilczek, "Ultraviolet Behavior of Non-Abelian Gauge Theories," Phys. Rev. Lett. **30** (1973) 1343.

[19] R. K. Ellis, H. Georgi, M. Machacek, H. D. Politzer and G. G. Ross, "Perturbation Theory and the Parton Model in QCD," Nucl. Phys. B **152** (1979) 285.

[20] J. C. Collins, D. E. Soper and G. F. Sterman, "Factorization of Hard Processes in QCD," Adv. Ser. Direct. High Energy Phys. **5** (1989) 1 [hep-ph/0409313].

[21] R. Sassot, M. Stratmann and P. Zurita, "Fragmentations Functions in Nuclear Media," Phys. Rev. D **81** (2010) 054001 [arXiv:0912.1311 [hep-ph]].

[22] Yu. L. Dokshitzer, D. I. Dyakonov and S. I. Troyan, "Hard processes in quantum chromodynamics," Phys. Report. **58** (1980) 269.

[23] G. Altarelli and G. Parisi, "Asymptotic Freedom in Parton Language," Nucl. Phys. B **126** (1977) 298.

[24] V. N. Gribov and L. N. Lipatov, "e+ e- pair annihilation and deep inelastic e p scattering in perturbation theory," Sov. J. Nucl. Phys. **15** (1972) 675 [Yad. Fiz. **15** (1972) 1218].

[25] I. Arsene *et al.* [BRAHMS Collaboration], "Quark gluon plasma and color glass condensate at RHIC? The Perspective from the BRAHMS experiment," Nucl. Phys. A **757** (2005) 1 [nucl-ex/0410020].

[26] B. B. Back *et al.*, "The PHOBOS perspective on discoveries at RHIC," Nucl. Phys. A **757** (2005) 28 [nucl-ex/0410022].

[27] K. Aamodt *et al.* [ALICE Collaboration], "The ALICE experiment at the CERN LHC," JINST **3** (2008) S08002.

[28] K. Aamodt *et al.* [ALICE Collaboration], "Suppression of Charged Particle Production at Large Transverse Momentum in Central Pb-Pb Collisions at $\sqrt{s_{NN}} = 2.76$ TeV," Phys. Lett. B **696** (2011) 30 [arXiv:1012.1004 [nucl-ex]].

[29] G. Aad *et al.* [ATLAS Collaboration], "Observation of a Centrality-Dependent Dijet Asymmetry in Lead-Lead Collisions at $\sqrt{s_{NN}} = 2.76$ TeV with the ATLAS Detector at the LHC," Phys. Rev. Lett. **105** (2010) 252303 [arXiv:1011.6182 [hep-ex]].

[30] S. Chatrchyan *et al.* [CMS Collaboration], "Observation and studies of jet quenching in PbPb collisions at nucleon-nucleon center-of-mass energy = 2.76 TeV," Phys. Rev. C **84** (2011) 024906 [arXiv:1102.1957 [nucl-ex]].

[31] J. D. Bjorken, "Energy Loss of Energetic Partons in Quark - Gluon Plasma: Possible Extinction of High p(t) Jets in Hadron - Hadron Collisions," FERMILAB-PUB-82-059-THY, FERMILAB-PUB-82-059-T.

[32] K. Adcox *et al.* [PHENIX Collaboration], "Suppression of hadrons with large transverse momentum in central Au+Au collisions at $\sqrt{s_{NN}}$ = 130-GeV," Phys. Rev. Lett. **88** (2002) 022301 [nucl-ex/0109003].

[33] J. Adams *et al.* [STAR Collaboration], "Evidence from d + Au measurements for final state suppression of high p(T) hadrons in Au+Au collisions at RHIC," Phys. Rev. Lett. **91** (2003) 072304 [nucl-ex/0306024].

[34] S. S. Adler *et al.* [PHENIX Collaboration], "High p_T charged hadron suppression in Au + Au collisions at $\sqrt{s}_{NN} = 200$ GeV," Phys. Rev. C **69** (2004) 034910 [nucl-ex/0308006].

[35] J. Adams *et al.* [STAR Collaboration], "Transverse momentum and collision energy dependence of high p(T) hadron suppression in Au+Au collisions at ultrarelativistic energies," Phys. Rev. Lett. **91** (2003) 172302 [nucl-ex/0305015].

[36] S. Chatrchyan *et al.* [CMS Collaboration], "Study of high-pT charged particle suppression in PbPb compared to *pp* collisions at $\sqrt{s_{NN}} = 2.76$ TeV," Eur. Phys. J. C **72** (2012) 1945 [arXiv:1202.2554 [nucl-ex]].

[37] A. Adare *et al.* [PHENIX Collaboration], "Evolution of π^0 suppression in Au+Au collisions from $\sqrt{s_{NN}} = 39$ to 200 GeV," Phys. Rev. Lett. **109** (2012) 152301 [arXiv:1204.1526 [nucl-ex]].

[38] S. S. Adler *et al.* [PHENIX Collaboration], "Dense-Medium Modifications to Jet-Induced Hadron Pair Distributions in Au+Au Collisions at s(NN)**(1/2) = 200-GeV," Phys. Rev. Lett. **97** (2006) 052301 [nucl-ex/0507004].

[39] A. Adare *et al.* [PHENIX Collaboration], "Suppression of back-to-back hadron pairs at forward rapidity in *d*+Au Collisions at $\sqrt{s_{NN}} = 200$ GeV," Phys. Rev. Lett. **107** (2011) 172301 [arXiv:1105.5112 [nucl-ex]].

[40] J. Adams *et al.* [STAR Collaboration], "Distributions of charged hadrons associated with high transverse momentum particles in pp and Au + Au collisions at s(NN)**(1/2) = 200-GeV," Phys. Rev. Lett. **95** (2005) 152301 [nucl-ex/0501016].

[41] K. Aamodt *et al.* [ALICE Collaboration], "Particle-yield modification in jet-like azimuthal di-hadron correlations in Pb-Pb collisions at $\sqrt{s_{NN}} = 2.76$ TeV," Phys. Rev. Lett. **108** (2012) 092301 [arXiv:1110.0121 [nucl-ex]].

[42] S. Chatrchyan *et al.* [CMS Collaboration], "Jet momentum dependence of jet quenching in PbPb collisions at $\sqrt{s_{NN}} = 2.76$ TeV," Phys. Lett. B **712** (2012) 176 [arXiv:1202.5022 [nucl-ex]].

[43] S. Chatrchyan *et al.* [CMS Collaboration], "Measurement of jet fragmentation into charged particles in *pp* and PbPb collisions at $\sqrt{s_{NN}} = 2.76$ TeV," JHEP **1210** (2012) 087 [arXiv:1205.5872 [nucl-ex]].

[44] S. Salur [STAR Collaboration], "First Direct Measurement of Jets in s(NN)**(1/2) = 200-GeV Heavy Ion Collisions by STAR," Eur. Phys. J. C **61** (2009) 761 [arXiv:0809.1609 [nucl-ex]].

[45] A. Dainese [ALICE Collaboration], "Suppression of high-p_T heavy-flavour particles in Pb-Pb collisions at the LHC, measured with the ALICE detector," PoS ICHEP **2012** (2013) 417 [arXiv:1212.0995 [nucl-ex]].

[46] T. Lappi and L. McLerran, Nucl. Phys. A **772** (2006) 200 [hep-ph/0602189].

[47] M. B. Isichenko "Percolation, statistical topography, and transport in random media," Rev. Mod. Phys. **64** (1992) 961.

[48] G. E. Pike and C. H. Seager, "Percolation and conductivity: A computer study. I," Phys. Rev. B **10** (1974) 1421; E. T. Gawlinski and H. E. Stanley, J. Phys. A **10** (1977) 205; S. B. Lee, "Universality of continuum percolation," Phys. Rev. B **42**(1990) 4877 .

[49] U. Alon, A. Drory and I. Balberg, "Systematic derivation of percolation thresholds in continuum systems," Phys. Rev. A **42** (1990) 4634.

[50] C. Domb and N. F. Sykes, "Cluster Size in Random Mixtures and Percolation Processes," Phys. Rev. **122** (1960) 77.

[51] A. Rodrigues, R. Ugoccioni and J. Dias de Deus, "Percolation approach to phase transitions in high-energy nuclear collisions," Phys. Lett. B **458** (1999) 402 [hep-ph/9812364].

[52] H. Satz, "Extreme States of Matter in Strong Interaction physics," Lect. Not. Phys. **841** (2012) Springer.

[53] S. Fortunato and H. Satz, "Polyakov loop percolation and deconfinement in SU(2) gauge theory," Phys. Lett. B **475** (2000) 311 [hep-lat/9911020].

[54] G. Curci, W. Furmanski and R. Petronzio, "Evolution of Parton Densities Beyond Leading Order: The Nonsinglet Case," Nucl. Phys. B **175** (1980) 27.

[55] W. Furmanski and R. Petronzio, "Singlet Parton Densities Beyond Leading Order," Phys. Lett. **97B** (1980) 437.

[56] S. Moch, J. A. M. Vermaseren and A. Vogt, "The Three loop splitting functions in QCD: The Nonsinglet case," Nucl. Phys. B **688** (2004) 101 [hep-ph/0403192].

[57] A. Vogt, S. Moch and J. A. M. Vermaseren, "The Three-loop splitting functions in QCD: The Singlet case," Nucl. Phys. B **691** (2004) 129 [hep-ph/0404111].

[58] M. Botje, "QCDNUM: Fast QCD Evolution and Convolution," Comput. Phys. Commun. **182** (2011) 490 [arXiv:1005.1481 [hep-ph]].

[59] C. G. Callan, David J. Gross, "High-Energy Electroproduction and the Constitution of the Electric Current," Phys. Rev. Lett. **22** (1969) 156.

[60] R. Brock *et al.* [CTEQ Collaboration], 'Handbook of perturbative QCD: Version 1.0," Rev. Mod. Phys. **67** (1995) 157.

[61] J. D. Bjorken, "Asymptotic Sum Rules at Infinite Momentum," Phys. Rev. **179** (1969) 1547.

[62] SLAC-MIT Collaboration, G. Miller *et al.*, "Inelastic electron-Proton Scattering at Large Momentum Transfers," Phys. Rev. D **5** (1972) 528.

[63] H1 Collaboration, T. Ahmed *et al.*, "A measurement of the proton structure function F2(x, Q2)," Nuclear Physics B **439** (1995) 471.

[64] ZEUS Collaboration, M. Derrick *et al.*, Zeit. Phys. C **65** (1995) 379.

[65] K. Nakamura *et al.*, "Review of particle physics," J. Phys. G **37** (2010) 075021.

[66] R. D. Field, "Applications of Perturbative QCD, " Front. Phys. **77** (1989) 1.

[67] W. J. Marciano, "Dimensional regularization and mass singularities," Phys. Rev. D **12** (1975) 3861.

[68] G. Altarelli, R. K. Ellis and G. Martinelli, "Leptoproduction and Drell-Yan Processes Beyond the Leading Approximation in Chromodynamics," Nucl. Phys. B **143** (1978) 521 Erratum: [Nucl. Phys. B **146** (1978) 544].

[69] E. B. Zijlstra and W. L. van Neerven, "Order alpha-s**2 QCD corrections to the deep inelastic proton structure functions F2 and F(L)," Nucl. Phys. B **383** (1992) 525.

[70] Günther Dissertori, Ian G. Knowles, Michael Schmelling, "Quantum chromodynamics: high energy experiments and theory," Oxford University Press (2009).

[71] E. B. Zijlstra and W. L. van Neerven, "Order alpha-s**2 correction to the structure function F3 (x, Q**2) in deep inelastic neutrino - hadron scattering," Phys. Lett. B **297** (1992) 377,

[72] Andrzej J. Buras, "Asymptotic freedom in deep inelastic processes in the leading order and beyond," Rev. Mod. Phys. **52** (1980) 199.

[73] J. Blumlein y T. Riemann, "Deep inelastic scattering," Nucl. Phys. Proc. Supl. Bf 29A (1992).

[74] J. Tran Thanh Van, "Perturbative QCD and hadronic interactions," Proceedings, Hadronic Session of the 27th Rencontres de Moriond, 1992.

[75] W. L. van Neerven and E. B. Zijlstra, "Order alpha-s**2 contributions to the deep inelastic Wilson coefficient," Phys. Lett. B **272** (1991) 127.

[76] E. B. Zijlstra and W. L. van Neerven, 'Contribution of the second order gluonic Wilson coefficient to the deep inelastic structure function," Phys. Lett. B **273** (1991) 476.

[77] W. A. Bardeen and A. J. Buras, "Higher Order Asymptotic Freedom Corrections to Photon - Photon Scattering," Phys. Rev. D **20** (1979) 166 Erratum: [Phys. Rev. D **21** (1980) 2041].

[78] G. Altarelli, R. K. Ellis and G. Martinelli, "Large Perturbative Corrections to the Drell-Yan Process in QCD," Nucl. Phys. B **157** (1979) 461.

[79] S. D. Drell and T. M. Yan, "Massive Lepton Pair Production in Hadron-Hadron Collisions at High-Energies," Phys. Rev. Lett. **25** (1970) 316 Erratum: [Phys. Rev. Lett. **25** (1970) 902].

[80] R. D. Field, "Applications of perturbative QCD," Frontiers in Physics **77** (1989), Basic books.

[81] J. Kubar, M. Le Bellac, J. L. Meunier and G. Plaut, "QCD Corrections to the Drell-Yan Mechanism and the Pion Structure Function," Nucl. Phys. B **175** (1980) 251.

[82] W. Furmanski and R. Petronzio, "Lepton - Hadron Processes Beyond Leading Order in Quantum Chromodynamics," Z. Phys. C **11** (1982) 293.

[83] T. Matsuura, S. C. van der Marck and W. L. van Neerven, 'The Calculation of the Second Order Soft and Virtual Contributions to the Drell-Yan Cross-Section," Nucl. Phys. B **319** (1989) 570.

[84] W. L. van Neerven and E. B. Zijlstra, "The $O(\alpha_s^2)$ corrected Drell-Yan K factor in the DIS and MS scheme," Nucl. Phys. B **382** (1992) 11 Erratum: [Nucl. Phys. B **680** (2004) 513].

[85] N. Cabibbo and R. Petronzio, "Two Stage Model of Hadron Structure: Parton Distributions and Their Q^2 Dependence," Nucl. Phys. B **137** (1978) 395.

[86] M. Miyama and S. Kumano, "Numerical solution of Q**2 evolution equations in a brute force method," Comput. Phys. Commun. **94** (1996) 185 [hep-ph/9508246].

[87] R. Toldra, "A c++ code to solve the DGLAP equations applied to ultrahigh- energy cosmic rays," Comput. Phys. Commun. **143** (2002) 287 [hep-ph/0108127].

[88] G. P. Salam and J. Rojo, "A Higher Order Perturbative Parton Evolution Toolkit (HOPPET)," Comput. Phys. Commun. **180** (2009) 120 [arXiv:0804.3755 [hep-ph]].

[89] P. Santorelli and E. Scrimieri, "A Semianalytical method to evolve parton distributions," Phys. Lett. B **459** (1999) 599 [hep-ph/9807572].

[90] K. J. Eskola, H. Paukkunen and C. A. Salgado, "EPS09: A New Generation of NLO and LO Nuclear Parton Distribution Functions," JHEP **0904** (2009) 065 [arXiv:0902.4154 [hep-ph]].

[91] A. Cafarella, C. Coriano and M. Guzzi, "Nnlo logarithmic expansions and exact solutions of the DGLAP equations from x-space: New algorithms for precision studies at the lhc," Nucl. Phys. B **748** (2006) 253 [hep-ph/0512358].

[92] A. Vogt, "Efficient evolution of unpolarized and polarized parton distributions with QCD-PEGASUS," Comput. Phys. Commun. **170** (2005) 65 [hep-ph/0408244].

[93] W. Giele *et al.*, "The QCD / SM working group: Summary report," hep-ph/0204316.

[94] L. A. Harland-Lang, A. D. Martin, P. Motylinski and R. S. Thorne, "Parton distributions in the LHC era: MMHT 2014 PDFs," Eur. Phys. J. C **75** (2015) no.5, 204 [arXiv:1412.3989 [hep-ph]].

[95] W. K. Tung, H. L. Lai, A. Belyaev, J. Pumplin, D. Stump and C.-P. Yuan, "Heavy Quark Mass Effects in Deep Inelastic Scattering and Global QCD Analysis," JHEP **0702** (2007) 053 [hep-ph/0611254].

[96] H. Khanpour and S. Atashbar Tehrani, "Global Analysis of Nuclear Parton Distribution Functions and Their Uncertainties at Next-to-Next-to-Leading Order," Phys. Rev. D **93** (2016) no.1, 014026 [arXiv:1601.00939 [hep-ph]].

[97] M. Buza, Y. Matiounine, J. Smith, R. Migneron and W. L. van Neerven, "Heavy quark coefficient functions at asymptotic values Q**2 ¿¿ m**2," Nucl. Phys. B **472** (1996) 611 [hep-ph/9601302].

[98] M. Buza, Y. Matiounine, J. Smith and W. L. van Neerven, "Charm electroproduction viewed in the variable flavor number scheme versus fixed order perturbation theory," Eur. Phys. J. C **1** (1998) 301 [hep-ph/9612398].

[99] R. S. Thorne and W. K. Tung, "PQCD Formulations with Heavy Quark Masses and Global Analysis," arXiv:0809.0714 [hep-ph].

[100] "Low-energy manifestations of heavy particles: Application to the neutral current," J. Collins, F Wilczek and A. Zee, Phys. Rev. D **18** (1978) 242.

[101] J. C. Collins, "Hard scattering factorization with heavy quarks: A General treatment," Phys. Rev. D **58** (1998) 094002 [hep-ph/9806259].

[102] M. Kramer, 1, F. I. Olness and D. E. Soper, "Treatment of heavy quarks in deeply inelastic scattering," Phys. Rev. D **62** (2000) 096007 [hep-ph/0003035].

[103] R. S. Thorne and R. G. Roberts, "A Practical procedure for evolving heavy flavor structure functions," Phys. Lett. B **421** (1998) 303 [hep-ph/9711223].

[104] R. S. Thorne and R. G. Roberts, "An Ordered analysis of heavy flavor production in deep inelastic scattering," Phys. Rev. D **57** (1998) 6871 [hep-ph/9709442].

[105] A. Chuvakin, J. Smith and W. L. van Neerven, "Comparison between variable flavor number schemes for charm quark electroproduction," Phys. Rev. D **61** (2000) 096004 [hep-ph/9910250].

[106] W. K. Tung, S. Kretzer and C. Schmidt, "Open heavy flavor production in QCD: Conceptual framework and implementation issues," J. Phys. G **28** (2002) 983 [hep-ph/0110247].

[107] R. S. Thorne, "A Variable-flavor number scheme for NNLO," Phys. Rev. D **73** (2006) 054019 [hep-ph/0601245].

[108] E. Laenen, S. Riemersma, J. Smith and W. L. van Neerven", "Complete O(α_s) corrections to heavy-flavour structure functions in electroproduction," Nuc. Phys. B **392** (1993) 162.

[109] E. Laenen, S. Riemersma, J. Smith and W. L. van Neerven "O(α_s) corrections to heavy-flavour inclusive distributions in electroproduction," Nuc. Phys. B **392** (1993) 229.

[110] S. Riemersma, J. Smith and W. L. van Neerven, "Rates for inclusive deep inelastic electroproduction of charm quarks at HERA," Phys. Lett. B **347** (1995) 143 [hep-ph/9411431].

[111] J. Ablinger *et al.*, "The 3-Loop Non-Singlet Heavy Flavor Contributions and Anomalous Dimensions for the Structure Function $F_2(x, Q^2)$ and Transversity," Nucl. Phys. B **886** (2014) 733 [arXiv:1406.4654 [hep-ph]].

[112] J. Ablinger, A. Behring, J. Blümlein, A. De Freitas, A. von Manteuffel and C. Schneider, "The 3-loop pure singlet heavy flavor contributions to the structure function $F_2(x, Q^2)$ and the anomalous dimension," Nucl. Phys. B **890** (2014) 48 [arXiv:1409.1135 [hep-ph]].

[113] A. Behring, J. Blümlein, G. Falcioni, A. De Freitas, A. von Manteuffel and C. Schneider, "Asymptotic 3-loop heavy flavor corrections to the charged current structure functions $F_L^{W^+-W^-}(x,Q^2)$ and $F_2^{W^+-W^-}(x,Q^2)$," Phys. Rev. D **94** (2016) no.11, 114006 [arXiv:1609.06255 [hep-ph]].

[114] A. Behring, J. Blümlein, A. De Freitas, A. Hasselhuhn, A. von Manteuffel and C. Schneider, "O(α_s^3) heavy flavor contributions to the charged current structure function $xF_3(x,Q^2)$ at large momentum transfer," Phys. Rev. D **92** (2015) no.11, 114005 [arXiv:1508.01449 [hep-ph]].

[115] J. J. Aubert *et al.* [European Muon Collaboration], "The ratio of the nucleon structure functions $F2_n$ for iron and deuterium," Phys. Lett. **123B** (1983) 275.

[116] A. D. Martin, A. J. T. M. Mathijssen, W. J. Stirling, R. S. Thorne, B. J. A. Watt and G. Watt, "Extended Parameterisations for MSTW PDFs and their effect on Lepton Charge Asymmetry from W Decays," Eur. Phys. J. C **73** (2013) no.2, 2318 [arXiv:1211.1215 [hep-ph]].

[117] J. Gomez *et al.*, "Measurement of the A-dependence of deep inelastic electron scattering," Phys. Rev. D **49** (1994) 4348.

[118] M. R. Adams *et al.* [E665 Collaboration], "Shadowing in inelastic scattering of muons on carbon, calcium and lead at low x(Bj)," Z. Phys. C **67** (1995) 403 [hep-ex/9505006].

[119] P. Amaudruz *et al.* [New Muon Collaboration], "A Reevaluation of the nuclear structure function ratios for D, He, Li-6, C and Ca," Nucl. Phys. B **441** (1995) 3 [hep-ph/9503291].

[120] M. Arneodo *et al.* [New Muon Collaboration], "The A dependence of the nuclear structure function ratios," Nucl. Phys. B **481** (1996) 3.

[121] Stanley J. Brodsky, Francis E. Close, J. F. Gunion, "Phenomenology of Photon Processes, Vector Dominance, and Crucial Tests for Parton Models," Phys. Rev. D **6** (1972) 177.

[122] N. Armesto, "Nuclear shadowing," J. Phys. G **32** (2006) R367 [hep-ph/0604108].

[123] S. Kumano, "Nuclear shadowing in a parton recombination model," Phys. Rev. C **48** (1993) 2016 [hep-ph/9303306].

[124] S. J. Brodsky and H. J. Lu, "Shadowing and Antishadowing of Nuclear Structure Functions," Phys. Rev. Lett. **64** (1990) 1342.

[125] L. L. Frankfurt and M. I. Strikman, "Shadowing and Enhancement of Quark Distributions in Nuclei at Small X," Nucl. Phys. B **316** (1989) 340.

[126] M. Ericson and A. W. Thomas, "Pionic Corrections and the EMC Enhancement of the Sea in Iron," Phys. Lett. **128B** (1983) 112.

[127] C. H. Llewellyn Smith, "A Possible Explanation of the Difference Between the Structure Functions of Iron and Deuterium," Phys. Lett. **128B** (1983) 107.

[128] R. P. Bickerstaff, M. C. Birse and G. A. Miller, "Partons In Nuclei," Phys. Rev. D **33** (1986) 3228.

[129] O. Hen, D. W. Higinbotham, G. A. Miller, E. Piasetzky and L. B. Weinstein, "The EMC Effect and High Momentum Nucleons in Nuclei," Int. J. Mod. Phys. E **22** (2013) 1330017 [arXiv:1304.2813 [nucl-th]].

[130] N. Armesto, H. Paukkunen, J. M. Penín, C. A. Salgado and P. Zurita, "An analysis of the impact of LHC Run I proton–lead data on nuclear parton densities," Eur. Phys. J. C **76** (2016) no.4, 218 [arXiv:1512.01528 [hep-ph]].

[131] A. Kusina *et al.*, "Vector boson production in proton-lead and lead-lead collisions at the LHC and its impact on nCTEQ15 PDFs," arXiv:1610.02925 [nucl-th].

[132] W. T. Giele and S. Keller, "Implications of hadron collider observables on parton distribution function uncertainties," Phys. Rev. D **58** (1998) 094023 [hep-ph/9803393].

[133] R. D. Ball *et al.* [NNPDF Collaboration], "Reweighting NNPDFs: the W lepton asymmetry," Nucl. Phys. B **849** (2011) 112 [Erratum-ibid. B **854** (2012) 926] [Erratum-ibid. B **855** (2012) 927] [arXiv:1012.0836 [hep-ph]].

[134] R. D. Ball, V. Bertone, F. Cerutti, L. Del Debbio, S. Forte, A. Guffanti, N. P. Hartland and J. I. Latorre *et al.*, "Reweighting and Unweighting of Parton Distributions and the LHC W lepton asymmetry data," Nucl. Phys. B **855** (2012) 608 [arXiv:1108.1758 [hep-ph]].

[135] H. Paukkunen and P. Zurita, "PDF reweighting in the Hessian matrix approach," JHEP **1412** (2014) 100 [arXiv:1402.6623 [hep-ph]].

[136] K. J. Eskola, P. Paakkinen, H. Paukkunen and C. A. Salgado, "EPPS16: Nuclear parton distributions with LHC data," Eur. Phys. J. C **77** (2017) no.3, 163 [arXiv:1612.05741 [hep-ph]].

[137] M. Hirai, S. Kumano and T.-H. Nagai, "Determination of nuclear parton distribution functions and their uncertainties in next-to-leading order," Phys. Rev. C **76** (2007) 065207 [arXiv:0709.3038 [hep-ph]].

[138] D. de Florian, R. Sassot, P. Zurita and M. Stratmann, "Global Analysis of Nuclear Parton Distributions," Phys. Rev. D **85** (2012) 074028 [arXiv:1112.6324 [hep-ph]].

[139] K. Kovarik *et al.*, "nCTEQ15 - Global analysis of nuclear parton distributions with uncertainties in the CTEQ framework," Phys. Rev. D **93** (2016) no.8, 085037 [arXiv:1509.00792 [hep-ph]].

[140] S. S. Adler *et al.* [PHENIX Collaboration], "Centrality dependence of pi0 and eta production at large transverse momentum in s(NN)**(1/2) = 200-GeV d+Au collisions," Phys. Rev. Lett. **98** (2007) 172302 [nucl-ex/0610036].

[141] B. I. Abelev *et al.* [STAR Collaboration], "Inclusive π^0, η, and direct photon production at high transverse momentum in $p+p$ and d+Au collisions at $\sqrt{s_{NN}} = 200$ GeV," Phys. Rev. C **81** (2010) 064904 [arXiv:0912.3838 [hep-ex]].

[142] A. Kusina *et al.*, "LHC lead data and nuclear PDFs," Acta Phys. Polon. B **48** (2017) 1035 [arXiv:1705.06704 [hep-ph]].

[143] K. Kovarik, I. Schienbein, F. I. Olness, J. Y. Yu, C. Keppel, J. G. Morfin, J. F. Owens and T. Stavreva, "Nuclear corrections in neutrino-nucleus DIS and their compatibility with global NPDF analyses," Phys. Rev. Lett. **106** (2011) 122301 [arXiv:1012.0286 [hep-ph]].

[144] M. Arneodo *et al.* [New Muon Collaboration], "The Structure Function ratios F2(li) / F2(D) and F2(C) / F2(D) at small x," Nucl. Phys. B **441** (1995) 12 [hep-ex/9504002].

[145] M. Arneodo *et al.* [New Muon Collaboration], "The Q**2 dependence of the structure function ratio F2 Sn / F2 C and the difference R Sn - R C in deep inelastic muon scattering," Nucl. Phys. B **481** (1996) 23.

[146] J. Ashman *et al.* [European Muon Collaboration], "A Measurement of the ratio of the nucleon structure function in copper and deuterium," Z. Phys. C **57** (1993) 211.

[147] R. D. Ball *et al.* [NNPDF Collaboration], "Parton distributions for the LHC Run II," JHEP **1504** (2015) 040 [arXiv:1410.8849 [hep-ph]].

[148] J. P. Berge *et al.*, "A Measurement of Differential Cross-Sections and Nucleon Structure Functions in Charged Current Neutrino Interactions on Iron," Z. Phys. C **49** (1991) 187.

[149] G. Onengut *et al.* [CHORUS Collaboration], "Measurement of nucleon structure functions in neutrino scattering," Phys. Lett. B **632** (2006) 65.

[150] A. Airapetian *et al.* [HERMES Collaboration], "Measurement of R = sigma(L) / sigma(T) in deep inelastic scattering on nuclei," hep-ex/0210068.

[151] A. C. Benvenuti *et al.* [BCDMS Collaboration], "A High Statistics Measurement of the Nucleon Structure Function F(2) (X,Q^2) From Deep Inelastic Muon - Carbon Scattering at High Q^2," Phys. Lett. B **195** (1987) 91.

[152] J. Ashman *et al.* [European Muon Collaboration], "Measurement of the Ratios of Deep Inelastic Muon - Nucleus Cross-Sections on Various Nuclei Compared to Deuterium," Phys. Lett. B **202** (1988) 603.

[153] M. Arneodo *et al.* [European Muon Collaboration], "Shadowing in Deep Inelastic Muon Scattering from Nuclear Targets," Phys. Lett. B **211** (1988) 493.

[154] M. Arneodo *et al.* [European Muon Collaboration], "Measurements of the nucleon structure function in the range $0.002 - \mathrm{GeV}^2 < x < 0.17 - \mathrm{GeV}^2$ and $0.2 - GeV^2 < q^2 < 8 - GeV^2$ in deuterium, carbon and calcium," Nucl. Phys. B **333** (1990) 1.

[155] K. Abe *et al.* [E143 Collaboration], "Measurements of R = σ(L) / σ(T) for 0.03 ¡ x ¡ 0.1 and fit to world data," Phys. Lett. B **452** (1999) 194 [hep-ex/9808028].

[156] G. Bari *et al.* [BCDMS Collaboration], "A Measurement of Nuclear Effects in Deep Inelastic Muon Scattering on Deuterium, Nitrogen and Iron Targets," Phys. Lett. **163B** (1985) 282.

[157] A. Bodek *et al.*, "A Comparison of the Deep Inelastic Structure Functions of Deuterium and Aluminum Nuclei," Phys. Rev. Lett. **51** (1983) 534.

[158] P. Amaudruz *et al.* [New Muon Collaboration], "Measurements of R(d) - R(p) and R(Ca) - R(C) in deep inelastic muon scattering," Phys. Lett. B **294** (1992) 120.

[159] A. C. Benvenuti *et al.* [BCDMS Collaboration], "Nuclear Effects in Deep Inelastic Muon Scattering on Deuterium and Iron Targets," Phys. Lett. B **189** (1987) 483.

[160] A. Bodek *et al.*, "Electron Scattering from Nuclear Targets and Quark Distributions in Nuclei," Phys. Rev. Lett. **50** (1983) 1431.

[161] J. J. Aubert *et al.* [European Muon Collaboration], "A Detailed Study of the Nucleon Structure Functions in Deep Elastic Muon Scattering in Iron," Nucl. Phys. B **272** (1986) 158.

[162] M. R. Adams *et al.* [E665 Collaboration], "Saturation of shadowing at very low x_{BJ}," Phys. Rev. Lett. **68** (1992) 3266.

[163] J. J. Aubert *et al.* [European Muon Collaboration], "Measurements of the nucleon structure functions $F2_n$ in deep inelastic muon scattering from deuterium and comparison with those from hydrogen and iron," Nucl. Phys. B **293** (1987) 740.

[164] A. C. Benvenuti *et al.* [BCDMS Collaboration], "A High Statistics Measurement of the Deuteron Structure Functions F2 (X, Q^2) and R From Deep Inelastic Muon Scattering at High Q^2," Phys. Lett. B **237** (1990) 592.

[165] A. C. Benvenuti *et al.* [BCDMS Collaboration], "A Comparison of the Structure Functions F2 of the Proton and the Neutron From Deep Inelastic Muon Scattering at High Q^2," Phys. Lett. B **237** (1990) 599.

[166] M. R. Adams *et al.* [E665 Collaboration], "Measurement of the ratio σ_n/σ_p in inelastic muon - nucleon scattering at very low x and Q^2," Phys. Lett. B **309** (1993) 477.

[167] M. R. Adams *et al.* [E665 Collaboration], "Extraction of the ratio $F2_n/F2_p$ from muon - deuteron and muon - proton scattering at small x and Q**2," Phys. Rev. Lett. **75** (1995) 1466.

[168] M. R. Adams *et al.* [E665 Collaboration], "Proton and deuteron structure functions in muon scattering at 470-GeV," Phys. Rev. D **54** (1996) 3006.

[169] S. Dasu *et al.*, "Measurement of kinematic and nuclear dependence of R = sigma-L / sigma-t in deep inelastic electron scattering," Phys. Rev. D **49** (1994) 5641.

[170] M. Arneodo *et al.* [New Muon Collaboration], "Accurate measurement of F2(d) / F2(p) and R**d - R**p," Nucl. Phys. B **487** (1997) 3 [hep-ex/9611022].

[171] A. Airapetian *et al.* [HERMES Collaboration], "Inclusive Measurements of Inelastic Electron and Positron Scattering from Unpolarized Hydrogen and Deuterium Targets," JHEP **1105** (2011) 126 [arXiv:1103.5704 [hep-ex]].

[172] A. Accardi and J. W. Qiu, "Collinear factorization for deep inelastic scattering structure functions at large Bjorken x(B)," JHEP **0807** (2008) 090 [arXiv:0805.1496 [hep-ph]].

[173] A. B. Arbuzov, D. Y. Bardin and L. V. Kalinovskaya, "Radiative corrections to neutrino deep inelastic scattering revisited," JHEP **0506** (2005) 078 [hep-ph/0407203].

[174] F. James and M. Roos, "Minuit: A System for Function Minimization and Analysis of the Parameter Errors and Correlations," Comput. Phys. Commun. **10** (1975) 343.

[175] J. Pumplin, D. Stump, R. Brock, D. Casey, J. Huston, J. Kalk, H. L. Lai and W. K. Tung, "Uncertainties of predictions from parton distribution functions. 2. The Hessian method," Phys. Rev. D **65** (2001) 014013 [hep-ph/0101032].

[176] A. D. Martin, W. J. Stirling, R. S. Thorne and G. Watt, "Parton distributions for the LHC," Eur. Phys. J. C **63** (2009) 189 [arXiv:0901.0002 [hep-ph]].

[177] N. Armesto, M. A. Braun, E. G. Ferreiro and C. Pajares, "Percolation approach to quark - gluon plasma and J / psi suppression," Phys. Rev. Lett. **77** (1996) 3736 [hep-ph/9607239].

[178] E. Brezin and C. Itzykson, "Pair production in vacuum by an alternating field," Phys. Rev. D **2** (1970) 1191.

[179] T. S. Biro, H. B. Nielsen and J. Knoll, "Color Rope Model for Extreme Relativistic Heavy Ion Collisions," Nucl. Phys. B **245** (1984) 449.

[180] A. Bialas and W. Czyz, "Conversion of Color Field Into $Q\bar{Q}$ Matter in the Central Region of High-energy Heavy Ion Collisions," Nucl. Phys. B **267** (1986) 242.

[181] A. Casher, H. Neuberger and S. Nussinov, "Chromoelectric Flux Tube Model of Particle Production," Phys. Rev. D **20** (1979) 179.

[182] A. B. Kaidalov, "The Quark-Gluon Structure of the Pomeron and the Rise of Inclusive Spectra at High-Energies," Phys. Lett. **116B** (1982) 459; B. Andersson, G. Gustafson, G. Ingelman and T. Sjostrand, "Parton Fragmentation and String Dynamics," Phys. Rept. **97** (1983) 31; H. Sorge, H. Stoecker and W. Greiner, "Relativistic Quantum Molecular Dynamics Approach To Nuclear Collisions At Ultrarelativistic Energies," Nucl. Phys. A **498** (1989) 567C; X. N. Wang and M. Gyulassy, "A Systematic study of particle production in $p + p$ (anti-p) collisions via the HIJING model," Phys. Rev. D **45** (1992) 844.

[183] T. Regge, "Introduction to complex orbital momenta," Nuovo Cim. **14** (1959) 951.

[184] V. N. Gribov, Sov. Phys. JETP **26** (1968) 414 [Zh. Eksp. Teor. Fiz. **53** (1967) 654].

[185] K. Werner, "Strings, pomerons, and the venus model of hadronic interactions at ultrarelativistic energies," Phys. Rept. **232** (1993) 87.

[186] F. Antinori *et al.* [WA97 Collaboration], "Strangeness enhancement at mid-rapidity in Pb Pb collisions at 158-A-GeV/c: A comparison with VENUS and RQMD models," Eur. Phys. J. C **11** (1999) 79.

[187] M. M. Aggarwal *et al.* [WA98 Collaboration], "Scaling of particle and transverse energy production in Pb-208 + Pb-208 collisions at 158-A-GeV," Eur. Phys. J. C **18** (2001) 651 [nucl-ex/0008004].

[188] K. Adcox *et al.* [PHENIX Collaboration], "Centrality dependence of charged particle multiplicity in Au - Au collisions at S(NN)**(1/2) = 130-GeV," Phys. Rev. Lett. **86** (2001) 3500 [nucl-ex/0012008].

[189] M. Rybczynski and Z. Wlodarczyk, "Non-monotonic behavior of multiplicity fluctuations," J. Phys. Conf. Ser. **5** (2005) 238 [nucl-th/0408023].

[190] L. Cunqueiro, E. G. Ferreiro, F. del Moral and C. Pajares, "Multiplicity fluctuations in the string clustering approach," Phys. Rev. C **72** (2005) 024907 [hep-ph/0505197].

[191] M. A. Braun and C. Pajares, "Implications of percolation of color strings on multiplicities, correlations and the transverse momentum," Eur. Phys. J. C **16** (2000) 349 [hep-ph/9907332].

[192] J. Dias de Deus, E. G. Ferreiro, C. Pajares and R. Ugoccioni, "Universality of the transverse momentum distributions in the framework of percolation of strings," Eur. Phys. J. C **40** (2005) 229 [hep-ph/0304068].

[193] J. Dias de Deus, E. G. Ferreiro, C. Pajares and R. Ugoccioni, "Density saturation and the decrease of the normalised width of the multiplicity distribution in high energy pp collisions," Phys. Lett. B **601** (2004) 125 [hep-ph/0405116].

[194] G. N. Fowler, E. M. Friedlander, R. M. Weiner and G. Wilk, "High-energy Behavior of Multiparticle Distributions and Their Bounds," Phys. Rev. Lett. **56** (1986) 14.

[195] L. McLerran and M. Praszalowicz, "Saturation and Scaling of Multiplicity, Mean p_T and p_T Distributions from 200 GeV $< \sqrt{s} <$ 7 TeV," Acta Phys. Polon. B **41** (2010) 1917 [arXiv:1006.4293 [hep-ph]].

[196] M. Praszalowicz, "Improved Geometrical Scaling at the LHC," Phys. Rev. Lett. **106** (2011) 142002 [arXiv:1101.0585 [hep-ph]].

[197] I. Bautista, J. G. Milhano, C. Pajares and J. Dias de Deus, "Multiplicity in pp and AA collisions: the same power law from energy-momentum constraints in string production," Phys. Lett. B **715** (2012) 230 [arXiv:1204.1457 [nucl-th]].

[198] I. Bautista, C. Pajares, J. G. Milhano and J. Dias de Deus, "Rapidity dependence of particle densities in pp and AA collisions," Phys. Rev. C **86** (2012) 034909 [arXiv:1206.6737 [nucl-th]].

[199] J. Dias de Deus and C. Pajares, "String Percolation and the Glasma," Phys. Lett. B **695** (2011) 211 [arXiv:1011.1099 [hep-ph]].

[200] T. Lappi, "Energy dependence of the saturation scale and the charged multiplicity in pp and AA collisions," Eur. Phys. J. C **71** (2011) 1699 [arXiv:1104.3725 [hep-ph]].

[201] J. L. ALbacete and A. Dumitru, "A model for gluon production in heavy-ion collisions at the LHC with rcBK unintegrated gluon densities," arXiv:1011.5161 [hep-ph].

[202] E. Levin and A. H. Rezaeian, "Gluon saturation and energy dependence of hadron multiplicity in pp and AA collisions at the LHC," Phys. Rev. D **83** (2011) 114001 [arXiv:1102.2385 [hep-ph]].

[203] B. B. Back *et al.* [PHOBOS Collaboration], "Centrality dependence of charged hadron transverse momentum spectra in Au + Au collisions from s(NN)**(1/2) = 62.4-GeV to 200-GeV," Phys. Rev. Lett. **94** (2005) 082304 [nucl-ex/0405003]; B. B. Back *et al.* [PHOBOS Collaboration], "Charged hadron transverse momentum distributions in au + au collisions at (S(NN))**(1/2) = 200-GeV," Phys. Lett. B **578** (2004) 297 [nucl-ex/0302015].

[204] B. Alver *et al.* [PHOBOS Collaboration], "System size and centrality dependence of charged hadron transverse momentum spectra in Au + Au and Cu + Cu collisions at s(NN)**(1/2) = 62.4-GeV and 200-GeV," Phys. Rev. Lett. **96** (2006) 212301 [nucl-ex/0512016].

[205] B. Abelev *et al.* [ALICE Collaboration], "Centrality Dependence of Charged Particle Production at Large Transverse Momentum in Pb–Pb Collisions at $\sqrt{s_{\rm NN}} = 2.76$ TeV," Phys. Lett. B **720** (2013) 52 [arXiv:1208.2711 [hep-ex]].

[206] V. Khachatryan *et al.* [CMS Collaboration], "Transverse momentum and pseudorapidity distributions of charged hadrons in pp collisions at $\sqrt{s} = 0.9$ and 2.36 TeV," JHEP **1002** (2010) 041 [arXiv:1002.0621 [hep-ex]]; V. Khachatryan *et al.* [CMS Collaboration], "Transverse-momentum and pseudorapidity distributions of charged hadrons

in pp collisions at $\sqrt{s} = 7$ TeV," Phys. Rev. Lett. **105** (2010) 022002 [arXiv:1005.3299 [hep-ex]]; V. Khachatryan *et al.* [CMS Collaboration], "Charged particle multiplicities in pp interactions at $\sqrt{s} = 0.9$, 2.36, and 7 TeV," JHEP **1101** (2011) 079 [arXiv:1011.5531 [hep-ex]].

[207] G. Aad *et al.* [ATLAS Collaboration], "Charged-particle multiplicities in pp interactions at $\sqrt{s} = 900$ GeV measured with the ATLAS detector at the LHC," Phys. Lett. B **688** (2010) 21 [arXiv:1003.3124 [hep-ex]].

[208] B. Abelev *et al.* [ALICE Collaboration], "Transverse momentum distribution and nuclear modification factor of charged particles in p-Pb collisions at $\sqrt{s_{NN}} = 5.02$ TeV," Phys. Rev. Lett. **110** (2013) no.8, 082302 [arXiv:1210.4520 [nucl-ex]].

[209] B. Abelev *et al.* [ALICE Collaboration], "Pseudorapidity density of charged particles in p + Pb collisions at $\sqrt{s_{NN}} = 5.02$ TeV," Phys. Rev. Lett. **110** (2013) no.3, 032301 [arXiv:1210.3615 [nucl-ex]].

[210] A. H. Mueller, "Parton saturation at small x and in large nuclei," Nucl. Phys. B **558** (1999) 285 [hep-ph/9904404].

[211] E. Levin and K. Tuchin, "Solution to the evolution equation for high parton density QCD," Nucl. Phys. B **573** (2000) 833 [hep-ph/9908317]; E. Levin and K. Tuchin, "New scaling at high-energy DIS," Nucl. Phys. A **691** (2001) 779 [hep-ph/0012167]; E. Levin and K. Tuchin, "Nonlinear evolution and saturation for heavy nuclei in DIS," Nucl. Phys. A **693** (2001) 787 [hep-ph/0101275].

[212] E. Iancu and L. D. McLerran, "Saturation and universality in QCD at small x," Phys. Lett. B **510** (2001) 145 [hep-ph/0103032].

[213] N. Armesto and M. A. Braun, "Parton densities and dipole cross-sections at small x in large nuclei," Eur. Phys. J. C **20** (2001) 517 [hep-ph/0104038]; N. Armesto and M. A. Braun, "Nuclear structure functions and heavy flavor leptoproduction off the nucleus at small x in perturbative QCD," Eur. Phys. J. C **22** (2001) 351 [hep-ph/0107114].

[214] A. M. Stasto, K. J. Golec-Biernat and J. Kwiecinski, "Geometric scaling for the total gamma* p cross-section in the low x region," Phys. Rev. Lett. **86** (2001) 596 [hep-ph/0007192].

[215] E. Iancu, K. Itakura and L. McLerran, "Geometric scaling above the saturation scale," Nucl. Phys. A **708** (2002) 327 [hep-ph/0203137].

[216] L. Cunqueiro, J. Dias de Deus and C. Pajares, "Nuclear like effects in proton-proton collisions at high energy," Eur. Phys. J. C **65** (2010) 423 [arXiv:0806.0523 [hep-ph]].

[217] S. Vogel, P. B. Gossiaux, K. Werner and J. Aichelin, "Heavy Quark Energy Loss in High Multiplicity Proton Proton Collisions at LHC," Phys. Rev. Lett. **107** (2011) 032302 [arXiv:1012.0764 [hep-ph]].

[218] B. Abelev *et al.* [ALICE Collaboration], Eur. Phys. J. C **72** (2012) 2124 [arXiv:1205.3963 [hep-ex]].

[219] J. Schaffner-Bielich, D. Kharzeev, L. D. McLerran and R. Venugopalan, "Generalized scaling of the transverse mass spectrum at the relativistic heavy ion collider," Nucl. Phys. A **705** (2002) 494 [nucl-th/0108048].

[220] C. Pajares, "String and parton percolation," Eur. Phys. J. C **43** (2005) 9 [hep-ph/0501125].

[221] J. Adams *et al.* [STAR Collaboration], "Minijet deformation and charge-independent angular correlations on momentum subspace (eta, phi) in Au-Au collisions at s(NN)**(1/2) = 130-GeV," Phys. Rev. C **73** (2006) 064907 [nucl-ex/0411003].

[222] A. Adare *et al.* [PHENIX Collaboration], "Dihadron azimuthal correlations in Au+Au collisions at s(NN)**(1/2) = 200-GeV," Phys. Rev. C **78** (2008) 014901 [arXiv:0801.4545 [nucl-ex]].

[223] B. I. Abelev *et al.* [STAR Collaboration], "Long range rapidity correlations and jet production in high energy nuclear collisions," Phys. Rev. C **80** (2009) 064912 [arXiv:0909.0191 [nucl-ex]].

[224] B. Alver *et al.* [PHOBOS Collaboration], "High transverse momentum triggered correlations over a large pseudorapidity acceptance in Au+Au collisions at s(NN)**1/2 = 200 GeV," Phys. Rev. Lett. **104** (2010) 062301 [arXiv:0903.2811 [nucl-ex]].

[225] B. Alver *et al.* [PHOBOS Collaboration], "Non-flow correlations and elliptic flow fluctuations in gold-gold collisions at $\sqrt{s_{NN}} = 200$ GeV," Phys. Rev. C **81** (2010) 034915 [arXiv:1002.0534 [nucl-ex]].

[226] S. Chatrchyan *et al.* [CMS Collaboration], "Centrality dependence of dihadron correlations and azimuthal anisotropy harmonics in PbPb collisions at $\sqrt{s_{NN}} = 2.76$ TeV," Eur. Phys. J. C **72** (2012) 2012 [arXiv:1201.3158 [nucl-ex]].

[227] V. Khachatryan *et al.* [CMS Collaboration], "Observation of Long-Range Near-Side Angular Correlations in Proton-Proton Collisions at the LHC," JHEP **1009** (2010) 091 [arXiv:1009.4122 [hep-ex]].

[228] V. Khachatryan *et al.* [CMS Collaboration], "Measurement of long-range near-side two-particle angular correlations in pp collisions at $\sqrt{s}$ =13 TeV," Phys. Rev. Lett. **116** (2016) no.17, 172302 [arXiv:1510.03068 [nucl-ex]].

[229] S. Chatrchyan *et al.* [CMS Collaboration], "Observation of long-range near-side angular correlations in proton-lead collisions at the LHC," Phys. Lett. B **718** (2013) 795 [arXiv:1210.5482 [nucl-ex]].

[230] B. Abelev *et al.* [ALICE Collaboration], "Long-range angular correlations on the near and away side in p-Pb collisions at $\sqrt{s_{NN}} = 5.02$ TeV," Phys. Lett. B **719** (2013) 29 [arXiv:1212.2001 [nucl-ex]].

[231] A. Adare *et al.* [PHENIX Collaboration], "Quadrupole Anisotropy in Dihadron Azimuthal Correlations in Central d+Au Collisions at $\sqrt{s_{_{NN}}}$=200 GeV," Phys. Rev. Lett. **111** (2013) no.21, 212301 [arXiv:1303.1794 [nucl-ex]].

[232] B. B. Abelev *et al.* [ALICE Collaboration], "Long-range angular correlations of π, K and p in p-Pb collisions at $\sqrt{s_{\rm NN}}$ = 5.02 TeV," Phys. Lett. B **726** (2013) 164 [arXiv:1307.3237 [nucl-ex]].

[233] S. Chatrchyan *et al.* [CMS Collaboration], "Multiplicity and transverse momentum dependence of two- and four-particle correlations in pPb and PbPb collisions," Phys. Lett. B **724** (2013) 213 [arXiv:1305.0609 [nucl-ex]].

[234] I. M. Dremin and V. T. Kim, "Towards a common origin of the elliptic flow, ridge and alignment," Pisma Zh. Eksp. Teor. Fiz. **92** (2010) 720 [JETP Lett. **92** (2010) 652] [arXiv:1010.0918 [hep-ph]].

[235] K. Werner, I. Karpenko and T. Pierog, "The 'Ridge' in Proton-Proton Scattering at 7 TeV," Phys. Rev. Lett. **106** (2011) 122004 [arXiv:1011.0375 [hep-ph]].

[236] I. O. Cherednikov and N. G. Stefanis, "On correlations in high-energy hadronic processes and the CMS ridge: A manifestation of quantum entanglement?," Int. J. Mod. Phys. A **27** (2012) 1250008 [arXiv:1010.4463 [hep-ph]].

[237] S. Gavin, L. McLerran and G. Moschelli, "Long Range Correlations and the Soft Ridge in Relativistic Nuclear Collisions," Phys. Rev. C **79** (2009) 051902 [arXiv:0806.4718 [nucl-th]].

[238] A. Dumitru, K. Dusling, F. Gelis, J. Jalilian-Marian, T. Lappi and R. Venugopalan, "The Ridge in proton-proton collisions at the LHC," Phys. Lett. B **697** (2011) 21 [arXiv:1009.5295 [hep-ph]].

[239] A. Kovner and M. Lublinsky, "Angular Correlations in Gluon Production at High Energy," Phys. Rev. D **83** (2011) 034017 [arXiv:1012.3398 [hep-ph]].

[240] S. Gavin and G. Moschelli, "Fluctuation Probes of Early-Time Correlations in Nuclear Collisions," Phys. Rev. C **85** (2012) 014905 [arXiv:1107.3317 [nucl-th]].

[241] K. Dusling and R. Venugopalan, "Explanation of systematics of CMS p+Pb high multiplicity di-hadron data at $\sqrt{s}_{\rm NN}$ = 5.02 TeV," Phys. Rev. D **87** (2013) no.5, 054014 [arXiv:1211.3701 [hep-ph]].

[242] K. Dusling and R. Venugopalan, "Comparison of the color glass condensate to dihadron correlations in proton-proton and proton-nucleus collisions," Phys. Rev. D **87** (2013) no.9, 094034 [arXiv:1302.7018 [hep-ph]].

[243] A. Bzdak, B. Schenke, P. Tribedy and R. Venugopalan, "Initial state geometry and the role of hydrodynamics in proton-proton, proton-nucleus and deuteron-nucleus collisions," Phys. Rev. C **87** (2013) no.6, 064906 [arXiv:1304.3403 [nucl-th]].

[244] Y. V. Kovchegov and D. E. Wertepny, "Two-Gluon Correlations in Heavy-Light Ion Collisions: Energy and Geometry Dependence, IR Divergences, and k_T-Factorization," Nucl. Phys. A **925** (2014) 254 [arXiv:1310.6701 [hep-ph]].

[245] A. Kovner and M. Lublinsky, "Angular and long range rapidity correlations in particle production at high energy," Int. J. Mod. Phys. E **22** (2013) 1330001 [arXiv:1211.1928 [hep-ph]].

[246] G. Agakishiev *et al.* [STAR Collaboration], "Anomalous centrality evolution of two-particle angular correlations from Au-Au collisions at $\sqrt{s_{\rm NN}} = 62$ and 200 GeV," Phys. Rev. C **86** (2012) 064902 [arXiv:1109.4380 [nucl-ex]].

[247] A. Capella, U. Sukhatme, C. I. Tan and J. Tran Thanh Van, "Dual parton model," Phys. Rept. **236** (1994) 225.

[248] A. Capella, C. Pajares and A. V. Ramallo, "High-energy Nucleus-nucleus Collisions in the Dual Parton Model," Nucl. Phys. B **241** (1984) 75.

[249] A. B. Kaidalov and K. A. Ter-Martirosian, "Pomeron as Quark-Gluon Strings and Multiple Hadron Production at SPS Collider Energies," Phys. Lett. **117B** (1982) 247.

[250] K. Werner, T. Hirano, I. Karpenko, T. Pierog, S. Porteboeuf, M. Bleicher and S. Haussler, 'Gribov-Regge theory, partons, remnants, strings - and the EPOS model for hadronic interactions," Nucl. Phys. Proc. Suppl. **196** (2009) 36.

[251] C. Pajares and A. V. Ramallo, "Effects Of The Multiple Scattering Structure In The Propagation Of Hadronic Properties In Nucleus-nucleus Collisions," Phys. Rev. D **31** (1985) 2800.

[252] A. Dumitru, F. Gelis, L. McLerran and R. Venugopalan, "Glasma flux tubes and the near side ridge phenomenon at RHIC," Nucl. Phys. A **810** (2008) 91 [arXiv:0804.3858 [hep-ph]].

[253] M. A. Braun and C. Pajares, "Elliptic flow from color strings," Eur. Phys. J. C **71** (2011) 1558 [arXiv:1008.0245 [hep-ph]].

[254] M. A. Braun, C. Pajares and V. V. Vechernin, "Anisotropic flows from colour strings: Monte-Carlo simulations," Nucl. Phys. A **906** (2013) 14 [arXiv:1204.5829 [hep-ph]].

[255] M. A. Braun, C. Pajares and V. V. Vechernin, "Ridge from Strings," Eur. Phys. J. A **51** (2015) no.4, 44 [arXiv:1407.4590 [hep-ph]].

[256] R. L. Ray and M. Daugherity, "Applicability of Monte Carlo Glauber models to relativistic heavy ion collision data," J. Phys. G **35** (2008) 125106 [nucl-ex/0702039].

[257] K. Aamodt *et al.* [ALICE Collaboration], "Elliptic flow of charged particles in Pb-Pb collisions at 2.76 TeV," Phys. Rev. Lett. **105** (2010) 252302 [arXiv:1011.3914 [nucl-ex]].

[258] G. Torrieri, "Origin of long-range azimuthal correlations in hadronic collisions," Phys. Rev. C **89** (2014) no.2, 024908 [arXiv:1310.3529 [nucl-th]].

[259] M. Praszalowicz, "Geometrical scaling for identified particles," Phys. Lett. B **727** (2013) 461 [arXiv:1308.5911 [hep-ph]].

[260] C. Andres, A. Moscoso and C. Pajares, "Universal geometrical scaling for hadronic interactions," Nucl. Phys. A **901** (2013) 14 [arXiv:1212.3102 [nucl-th]].

[261] C. Klein-Bösing and L. McLerran, "Geometrical Scaling of Direct-Photon Production in Hadron Collisions from RHIC to the LHC," Phys. Lett. B **734** (2014) 282 [arXiv:1403.1174 [nucl-th]].

[262] A. Adare *et al.* [PHENIX Collaboration], "Scaling properties of azimuthal anisotropy in Au+Au and Cu+Cu collisions at s(NN) = 200-GeV," Phys. Rev. Lett. **98** (2007) 162301 [nucl-ex/0608033].

[263] B. Abelev *et al.* [ALICE Collaboration], "Centrality determination of Pb-Pb collisions at $\sqrt{s_{NN}}$ = 2.76 TeV with ALICE," Phys. Rev. C **88** (2013) no.4, 044909 [arXiv:1301.4361 [nucl-ex]].

[264] L. Cunqueiro, J. Dias de Deus, E. G. Ferreiro and C. Pajares, "Universal behavior of baryons and mesons transverse momentum distributions in the framework of percolation of strings," Eur. Phys. J. C **53** (2008) 585 [arXiv:0712.0509 [hep-ph]].

[265] S. S. Adler *et al.* [PHENIX Collaboration], "Identified charged particle spectra and yields in Au+Au collisions at S(NN)**1/2 = 200-GeV," Phys. Rev. C **69** (2004) 034909 [nucl-ex/0307022].

[266] J. Casalderrey-Solana and U. A. Wiedemann, "Eccentricity fluctuations make flow measurable in high multiplicity p-p collisions," Phys. Rev. Lett. **104** (2010) 102301 [arXiv:0911.4400 [hep-ph]].

[267] D. d'Enterria, G. K. Eyyubova, V. L. Korotkikh, I. P. Lokhtin, S. V. Petrushanko, L. I. Sarycheva and A. M. Snigirev, "Estimates of hadron azimuthal anisotropy from multiparton interactions in proton-proton collisions at $\sqrt{s}$ = 14 TeV," Eur. Phys. J. C **66** (2010) 173 [arXiv:0910.3029 [hep-ph]].

[268] V. Vechernin and I. Lakomov, "The dependence of the number of pomerons on the impact parameter and the long-range rapidity correlations in pp collisions," Proceedings of Science, Baldin ISHEPP XXI, 072 (2012) [arXiv:1212.2667 [nucl-th]].

[269] J. Adams *et al.* [STAR Collaboration], "Azimuthal anisotropy in Au+Au collisions at s(NN)**(1/2) = 200-GeV," Phys. Rev. C **72** (2005) 014904 [nucl-ex/0409033].

[270] D. Lohner [ALICE Collaboration], "Measurement of Direct-Photon Elliptic Flow in Pb-Pb Collisions at $\sqrt{s_{NN}}$ = 2.76 TeV," J. Phys. Conf. Ser. **446** (2013) 012028 [arXiv:1212.3995 [hep-ex]].

[271] B. B. Abelev *et al.* [ALICE Collaboration], "Elliptic flow of identified hadrons in Pb-Pb collisions at $\sqrt{s_{\rm NN}} = 2.76$ TeV," JHEP **1506** (2015) 190 [arXiv:1405.4632 [nucl-ex]].

[272] C. Andrés, J. Dias de Deus, A. Moscoso, C. Pajares and C. A. Salgado, "Universal geometrical scaling of the elliptic flow," Phys. Rev. C **92** (2015) no.3, 034901 [arXiv:1405.2177 [hep-ph]].

[273] A. Bialas, "Fluctuations of string tension and transverse mass distribution," Phys. Lett. B **466** (1999) 301 [hep-ph/9909417].

[274] J. Dias de Deus and C. Pajares, "Percolation of color sources and critical temperature," Phys. Lett. B **642** (2006) 455 [hep-ph/0607101].

[275] R. Baier, Y. L. Dokshitzer, A. H. Mueller, S. Peigne and D. Schiff, "Radiative energy loss of high-energy quarks and gluons in a finite volume quark - gluon plasma," Nucl. Phys. B **483** (1997) 291 [hep-ph/9607355]; R. Baier, Y. L. Dokshitzer, A. H. Mueller, S. Peigne and D. Schiff, "Radiative energy loss and p(T) broadening of high-energy partons in nuclei," Nucl. Phys. B **484** (1997) 265 [hep-ph/9608322].

[276] B. G. Zakharov, "Fully quantum treatment of the Landau-Pomeranchuk-Migdal effect in QED and QCD," JETP Lett. **63** (1996) 952 [hep-ph/9607440].

[277] B. G. Zakharov, "Radiative energy loss of high-energy quarks in finite size nuclear matter and quark - gluon plasma," JETP Lett. **65** (1997) 615 [hep-ph/9704255].

[278] U. A. Wiedemann, "Transverse dynamics of hard partons in nuclear media and the QCD dipole," Nucl. Phys. B **582** (2000) 409 [hep-ph/0003021].

[279] M. Gyulassy, P. Levai and I. Vitev, "Jet tomography of Au+Au reactions including multigluon fluctuations," Phys. Lett. B **538** (2002) 282 [nucl-th/0112071].

[280] A. I. Nikishov and V. I. Ritus, "Interaction of Electrons and Photons with a Very Strong Electromagnetic Field," Phys. Usp. **13** (1970) 303.

[281] A. Mikhailov, "Nonlinear waves in AdS / CFT correspondence," hep-th/0305196.

[282] D. Kharzeev, E. Levin and K. Tuchin, "Multi-particle production and thermalization in high-energy QCD," Phys. Rev. C **75** (2007) 044903 [hep-ph/0602063].

[283] M. Aaboud *et al.* [ATLAS Collaboration], "Measurements of long-range azimuthal anisotropies and associated Fourier coefficients for *pp* collisions at $\sqrt{s} = 5.02$ and 13 TeV and p+Pb collisions at $\sqrt{s_{\rm NN}} = 5.02$ TeV with the ATLAS detector," arXiv:1609.06213 [nucl-ex].

[284] V. Khachatryan *et al.* [CMS Collaboration], "Evidence for collectivity in pp collisions at the LHC," Phys. Lett. B **765** (2017) 193 [arXiv:1606.06198 [nucl-ex]].

[285] M. Spousta and B. Cole, "Interpreting single jet measurements in Pb + Pb collisions at the LHC," Eur. Phys. J. C **76** (2016) no.2, 50 [arXiv:1504.05169 [hep-ph]].

[286] M. Spousta, "On similarity of jet quenching and charmonia suppression," Phys. Lett. B **767** (2017) 10 [arXiv:1606.00903 [hep-ph]].

[287] A. Adare *et al.* [PHENIX Collaboration], "Measurements of Higher-Order Flow Harmonics in Au+Au Collisions at $\sqrt{s_{NN}} = 200$ GeV," Phys. Rev. Lett. **107** (2011) 252301 [arXiv:1105.3928 [nucl-ex]].

[288] K. Aamodt *et al.* [ALICE Collaboration], "Higher harmonic anisotropic flow measurements of charged particles in Pb-Pb collisions at $\sqrt{s_{NN}}$=2.76 TeV," Phys. Rev. Lett. **107** (2011) 032301 [arXiv:1105.3865 [nucl-ex]].

[289] A. Dumitru and Y. Nara, "KNO scaling of fluctuations in pp and pA, and eccentricities in heavy-ion collisions," Phys. Rev. C **85** (2012) 034907 [arXiv:1201.6382 [nucl-th]].

[290] E. Braaten and M. H. Thoma, "Energy loss of a heavy quark in the quark - gluon plasma," Phys. Rev. D **44** (1991) no.9, R2625.

[291] A. Peshier, "The QCD collisional energy loss revised," Phys. Rev. Lett. **97** (2006) 212301 [hep-ph/0605294].

[292] S. Peigne and A. Peshier, "Collisional energy loss of a fast heavy quark in a quark-gluon plasma," Phys. Rev. D **77** (2008) 114017 [arXiv:0802.4364 [hep-ph]].

[293] B. G. Zakharov, "Parton energy loss in an expanding quark-gluon plasma: Radiative versus collisional," JETP Lett. **86** (2007) 444 [arXiv:0708.0816 [hep-ph]].

[294] J. P. Blaizot and E. Iancu, "The Quark gluon plasma: Collective dynamics and hard thermal loops," Phys. Rept. **359** (2002) 355 [hep-ph/0101103].

[295] B. G. Zakharov, "On the energy loss of high-energy quarks in a finite size quark - gluon plasma," JETP Lett. **73** (2001) 49 [Pisma Zh. Eksp. Teor. Fiz. **73** (2001) 55] [hep-ph/0012360].

[296] H. Bethe and W. Heitler, "On the Stopping of fast particles and on the creation of positive electrons," Proc. Roy. Soc. Lond. A **146** (1934) 83.

[297] X. N. Wang, M. Gyulassy and M. Plumer, "The LPM effect in QCD and radiative energy loss in a quark gluon plasma," Phys. Rev. D **51** (1995) 3436 [hep-ph/9408344].

[298] L. D. Landau and I. Pomeranchuk, "Electron cascade process at very high-energies," Dokl. Akad. Nauk Ser. Fiz. **92** (1953) 735.

[299] A. B. Migdal, "Bremsstrahlung and pair production in condensed media at high-energies," Phys. Rev. **103** (1956) 1811.

[300] C. A. Salgado and U. A. Wiedemann, "Calculating quenching weights," Phys. Rev. D **68** (2003) 014008 [hep-ph/0302184].

[301] S. Peigne and A. V. Smilga, "Energy losses in a hot plasma revisited," Phys. Usp. **52** (2009) 659 [Usp. Fiz. Nauk **179** (2009) 697] [arXiv:0810.5702 [hep-ph]].

[302] Y. L. Dokshitzer, V. A. Khoze and S. I. Troian, "On specific QCD properties of heavy quark fragmentation ('dead cone')," J. Phys. G **17** (1991) 1602. Y. L. Dokshitzer and D. E. Kharzeev, "Heavy quark colorimetry of QCD matter," Phys. Lett. B **519** (2001) 199 [hep-ph/0106202].

[303] N. Armesto, C. A. Salgado and U. A. Wiedemann, "Medium induced gluon radiation off massive quarks fills the dead cone," Phys. Rev. D **69** (2004) 114003 [hep-ph/0312106].

[304] S. Wicks, W. Horowitz, M. Djordjevic and M. Gyulassy, "Elastic, inelastic, and path length fluctuations in jet tomography," Nucl. Phys. A **784** (2007) 426 [nucl-th/0512076].

[305] B. I. Abelev *et al.* [STAR Collaboration], "Transverse momentum and centrality dependence of high-p_T non-photonic electron suppression in Au+Au collisions at $\sqrt{s_{NN}} = 200\,\mathrm{GeV}$," Phys. Rev. Lett. **98** (2007) 192301 Erratum: [Phys. Rev. Lett. **106** (2011) 159902] [nucl-ex/0607012].

[306] B. Abelev *et al.* [ALICE Collaboration], "Suppression of high transverse momentum D mesons in central Pb-Pb collisions at $\sqrt{s_{NN}} = 2.76$ TeV," JHEP **1209** (2012) 112 [arXiv:1203.2160 [nucl-ex]].

[307] R. Baier, Y. L. Dokshitzer, A. H. Mueller and D. Schiff, "Medium induced radiative energy loss: Equivalence between the BDMPS and Zakharov formalisms," Nucl. Phys. B **531** (1998) 403 [hep-ph/9804212].

[308] B. G. Zakharov, "Light cone path integral approach to the Landau-Pomeranchuk-Migdal effect," Phys. Atom. Nucl. **61** (1998) 838 [Yad. Fiz. **61** (1998) 924] [hep-ph/9807540].

[309] U. A. Wiedemann, "Gluon radiation off hard quarks in a nuclear environment: Opacity expansion," Nucl. Phys. B **588** (2000) 303 [hep-ph/0005129].

[310] M. Gyulassy, P. Levai and I. Vitev, "Jet quenching in thin quark gluon plasmas. 1. Formalism," Nucl. Phys. B **571** (2000) 197 [hep-ph/9907461]; M. Gyulassy, P. Levai and I. Vitev, "Reaction operator approach to nonAbelian energy loss," Nucl. Phys. B **594** (2001) 371 [nucl-th/0006010].

[311] M. Djordjevic and M. Gyulassy, "Heavy quark radiative energy loss in QCD matter," Nucl. Phys. A **733** (2004) 265 [nucl-th/0310076].

[312] P. B. Arnold, G. D. Moore and L. G. Yaffe, "Transport coefficients in high temperature gauge theories. 1. Leading log results," JHEP **0011** (2000) 001 [hep-ph/0010177]; P. B. Arnold, G. D. Moore and L. G. Yaffe, "Photon emission from ultrarelativistic plasmas," JHEP **0111** (2001) 057 [hep-ph/0109064]; P. B. Arnold, G. D. Moore and L. G. Yaffe, "Photon emission from quark gluon plasma: Complete leading order results," JHEP **0112** (2001) 009 [hep-ph/0111107]; P. B. Arnold, G. D. Moore and L. G. Yaffe, "Photon and gluon emission in relativistic plasmas," JHEP **0206** (2002) 030 [hep-ph/0204343].

[313] S. Jeon and G. D. Moore, "Energy loss of leading partons in a thermal QCD medium," Phys. Rev. C **71** (2005) 034901 [hep-ph/0309332].

[314] S. Turbide, C. Gale, S. Jeon and G. D. Moore, "Energy loss of leading hadrons and direct photon production in evolving quark-gluon plasma," Phys. Rev. C **72** (2005) 014906 [hep-ph/0502248].

[315] X. f. Guo and X. N. Wang, "Multiple scattering, parton energy loss and modified fragmentation functions in deeply inelastic e A scattering," Phys. Rev. Lett. **85** (2000) 3591 [hep-ph/0005044].

[316] X. N. Wang and X. f. Guo, "Multiple parton scattering in nuclei: Parton energy loss," Nucl. Phys. A **696** (2001) 788 [hep-ph/0102230].

[317] B. W. Zhang and X. N. Wang, "Multiple parton scattering in nuclei: Beyond helicity amplitude approximation," Nucl. Phys. A **720** (2003) 429 [hep-ph/0301195].

[318] A. Majumder, R. J. Fries and B. Muller, "Photon bremsstrahlung and diffusive broadening of a hard jet," Phys. Rev. C **77** (2008) 065209 [arXiv:0711.2475 [nucl-th]].

[319] S. Wicks, "Up to and beyond ninth order in opacity: Radiative energy loss with GLV," arXiv:0804.4704 [nucl-th].

[320] N. Armesto *et al.*, "Comparison of Jet Quenching Formalisms for a Quark-Gluon Plasma 'Brick'," Phys. Rev. C **86** (2012) 064904 [arXiv:1106.1106 [hep-ph]].

[321] I. P. Lokhtin and A. M. Snigirev, "A Model of jet quenching in ultrarelativistic heavy ion collisions and high-p(T) hadron spectra at RHIC," Eur. Phys. J. C **45** (2006) 211 [hep-ph/0506189].

[322] K. Zapp, G. Ingelman, J. Rathsman, J. Stachel and U. A. Wiedemann, "A Monte Carlo Model for 'Jet Quenching'," Eur. Phys. J. C **60** (2009) 617 [arXiv:0804.3568 [hep-ph]].

[323] K. C. Zapp, "Geometrical aspects of jet quenching in JEWEL," Phys. Lett. B **735** (2014) 157 [arXiv:1312.5536 [hep-ph]].

[324] N. Armesto, L. Cunqueiro and C. A. Salgado, "Q-PYTHIA: A Medium-modified implementation of final state radiation," Eur. Phys. J. C **63** (2009) 679 [arXiv:0907.1014 [hep-ph]].

[325] B. Schenke, C. Gale and S. Jeon, "MARTINI: An Event generator for relativistic heavy-ion collisions," Phys. Rev. C **80** (2009) 054913 [arXiv:0909.2037 [hep-ph]].

[326] T. Sjostrand, S. Mrenna and P. Z. Skands, "PYTHIA 6.4 Physics and Manual," JHEP **0605** (2006) 026 [hep-ph/0603175].

[327] Y. Mehtar-Tani, C. A. Salgado and K. Tywoniuk, "Anti-angular ordering of gluon radiation in QCD media," Phys. Rev. Lett. **106** (2011) 122002 [arXiv:1009.2965 [hep-ph]].

[328] Y. Mehtar-Tani and K. Tywoniuk, "Jet coherence in QCD media: the antenna radiation spectrum," JHEP **1301** (2013) 031 [arXiv:1105.1346 [hep-ph]].

[329] Y. Mehtar-Tani, C. A. Salgado and K. Tywoniuk, "Jets in QCD Media: From Color Coherence to Decoherence," Phys. Lett. B **707** (2012) 156 [arXiv:1102.4317 [hep-ph]].

[330] Y. Mehtar-Tani, C. A. Salgado and K. Tywoniuk, "The radiation pattern of a QCD antenna in a dilute medium," JHEP **1204** (2012) 064 [arXiv:1112.5031 [hep-ph]].

[331] J. Casalderrey-Solana, J. G. Milhano and U. Wiedemann, "Jet quenching via jet collimation," J. Phys. G **38** (2011) 124086 [arXiv:1107.1964 [hep-ph]].

[332] N. Armesto, H. Ma, Y. Mehtar-Tani, C. A. Salgado and K. Tywoniuk, "Coherence effects and broadening in medium-induced QCD radiation off a massive $q\bar{q}$ antenna," JHEP **1201** (2012) 109 [arXiv:1110.4343 [hep-ph]].

[333] A. Idilbi and A. Majumder, "Extending Soft-Collinear-Effective-Theory to describe hard jets in dense QCD media," Phys. Rev. D **80** (2009) 054022 [arXiv:0808.1087 [hep-ph]].

[334] F. D'Eramo, H. Liu and K. Rajagopal, "Jet Quenching Parameter via Soft Collinear Effective Theory (SCET)," Int. J. Mod. Phys. E **20** (2011) 1610 [arXiv:1010.0890 [hep-ph]].

[335] S. S. Adler *et al.* [PHENIX Collaboration], "Suppressed π^0 production at large transverse momentum in central Au+ Au collisions at S(NN)**1/2 = 200 GeV," Phys. Rev. Lett. **91** (2003) 072301 [nucl-ex/0304022].

[336] S. S. Adler *et al.* [PHENIX Collaboration], "Common suppression pattern of η and π^0 mesons at high transverse momentum in Au+Au collisions at S(NN)**(1/2) = 200-GeV," Phys. Rev. Lett. **96** (2006) 202301 [nucl-ex/0601037].

[337] S. S. Adler *et al.* [PHENIX Collaboration], "Centrality dependence of direct photon production in s(NN)**(1/ 2) = 200-GeV Au + Au collisions," Phys. Rev. Lett. **94** (2005) 232301 [nucl-ex/0503003].

[338] A. Adare *et al.* [PHENIX Collaboration], "Enhanced production of direct photons in Au+Au collisions at $\sqrt{s_{NN}} = 200$ GeV and implications for the initial temperature," Phys. Rev. Lett. **104** (2010) 132301 [arXiv:0804.4168 [nucl-ex]].

[339] S. A. Bass, C. Gale, A. Majumder, C. Nonaka, G. Y. Qin, T. Renk and J. Ruppert, "Systematic Comparison of Jet Energy-Loss Schemes in a realistic hydrodynamic medium," Phys. Rev. C **79** (2009) 024901 [arXiv:0808.0908 [nucl-th]].

[340] N. Armesto, L. Cunqueiro, C. A. Salgado and W. C. Xiang, "Medium-evolved fragmentation functions," JHEP **0802** (2008) 048 [arXiv:0710.3073 [hep-ph]].

[341] S. Chatrchyan *et al.* [CMS Collaboration], "Modification of jet shapes in PbPb collisions at $\sqrt{s_{NN}} = 2.76$ TeV," Phys. Lett. B **730** (2014) 243 [arXiv:1310.0878 [nucl-ex]].

[342] F. G. Gardim, F. Grassi, M. Luzum and J. Y. Ollitrault, "Anisotropic flow in event-by-event ideal hydrodynamic simulations of $\sqrt{s_{NN}} = 200$ GeV Au+Au collisions," Phys. Rev. Lett. **109** (2012) 202302 [arXiv:1203.2882 [nucl-th]].

[343] C. Gale, S. Jeon, B. Schenke, P. Tribedy and R. Venugopalan, "Event-by-event anisotropic flow in heavy-ion collisions from combined Yang-Mills and viscous fluid dynamics," Phys. Rev. Lett. **110** (2013) no.1, 012302 [arXiv:1209.6330 [nucl-th]].

[344] H. Niemi, K. J. Eskola and R. Paatelainen, "Event-by-event fluctuations in a perturbative QCD + saturation + hydrodynamics model: Determining QCD matter shear viscosity in ultrarelativistic heavy-ion collisions," Phys. Rev. C **93** (2016) no.2, 024907 [arXiv:1505.02677 [hep-ph]].

[345] J. Noronha-Hostler, M. Luzum and J. Y. Ollitrault, "Hydrodynamic predictions for 5.02 TeV Pb-Pb collisions," Phys. Rev. C **93** (2016) no.3, 034912 [arXiv:1511.06289 [nucl-th]].

[346] J. E. Bernhard, J. S. Moreland, S. A. Bass, J. Liu and U. Heinz, "Applying Bayesian parameter estimation to relativistic heavy-ion collisions: simultaneous characterization of the initial state and quark-gluon plasma medium," Phys. Rev. C **94** (2016) no.2, 024907 [arXiv:1605.03954 [nucl-th]].

[347] X. N. Wang, "Jet quenching and azimuthal anisotropy of large p(T) spectra in noncentral high-energy heavy ion collisions," Phys. Rev. C **63** (2001) 054902 [nucl-th/0009019].

[348] M. Gyulassy, I. Vitev and X. N. Wang, "High p(T) azimuthal asymmetry in noncentral A+A at RHIC," Phys. Rev. Lett. **86** (2001) 2537 [nucl-th/0012092].

[349] S. S. Adler *et al.* [PHENIX Collaboration], "Measurement of identified pi0 and inclusive photon v(2) and implication to the direct photon production in s(NN)**1/2 = 200-GeV Au+Au collisions," Phys. Rev. Lett. **96** (2006) 032302 [nucl-ex/0508019].

[350] J. Xu, A. Buzzatti and M. Gyulassy, "Azimuthal jet flavor tomography with CUJET2.0 of nuclear collisions at RHIC and LHC," JHEP **1408** (2014) 063 [arXiv:1402.2956 [hep-ph]].

[351] J. Noronha-Hostler, B. Betz, J. Noronha and M. Gyulassy, "Event-by-event hydrodynamics + jet energy loss: A solution to the $R_{AA} \otimes v_2$ puzzle," Phys. Rev. Lett. **116** (2016) no.25, 252301 [arXiv:1602.03788 [nucl-th]].

[352] A. Bilandzic, R. Snellings and S. Voloshin, "Flow analysis with cumulants: Direct calculations," Phys. Rev. C **83** (2011) 044913 [arXiv:1010.0233 [nucl-ex]].

[353] M. Gyulassy and X. n. Wang, "Multiple collisions and induced gluon Bremsstrahlung in QCD," Nucl. Phys. B **420** (1994) 583 [nucl-th/9306003].

[354] A. Kovner and U. A. Wiedemann, "Eikonal evolution and gluon radiation," Phys. Rev. D **64** (2001) 114002 [hep-ph/0106240].

[355] J. Casalderrey-Solana and C. A. Salgado, "Introductory lectures on jet quenching in heavy ion collisions," Acta Phys. Polon. B **38** (2007) 3731 [arXiv:0712.3443 [hep-ph]].

[356] N. N. Nikolaev and B. G. Zakharov, "Color transparency and scaling properties of nuclear shadowing in deep inelastic scattering," Z. Phys. C **49** (1991) 607.

[357] N. Armesto, M. Cacciari, T. Hirano, J. L. Nagle and C. A. Salgado, "Constraint fitting of experimental data with a jet quenching model embedded in a hydrodynamical bulk medium," J. Phys. G **37** (2010) 025104 [arXiv:0907.0667 [hep-ph]].

[358] R. Baier, Y. L. Dokshitzer, A. H. Mueller and D. Schiff, "Quenching of hadron spectra in media," JHEP **0109** (2001) 033 [hep-ph/0106347].

[359] N. Armesto, A. Dainese, C. A. Salgado and U. A. Wiedemann, "Testing the color charge and mass dependence of parton energy loss with heavy-to-light ratios at RHIC and CERN LHC," Phys. Rev. D **71** (2005) 054027 [hep-ph/0501225].

[360] `http://csalgado.web.cern.ch/csalgado/swqw.html`.

[361] J. Casalderrey-Solana and E. Iancu, "Interference effects in medium-induced gluon radiation," JHEP **1108** (2011) 015 [arXiv:1105.1760 [hep-ph]].

[362] J. P. Blaizot, F. Dominguez, E. Iancu and Y. Mehtar-Tani, "Medium-induced gluon branching," JHEP **1301** (2013) 143 [arXiv:1209.4585 [hep-ph]].

[363] J. P. Blaizot, F. Dominguez, E. Iancu and Y. Mehtar-Tani, "Probabilistic picture for medium-induced jet evolution," JHEP **1406** (2014) 075 [arXiv:1311.5823 [hep-ph]].

[364] R. Baier, Y. L. Dokshitzer, A. H. Mueller and D. Schiff, "Radiative energy loss of high-energy partons traversing an expanding QCD plasma," Phys. Rev. C **58** (1998) 1706 [hep-ph/9803473].

[365] C. Andrés, N. Armesto, M. Luzum, C. A. Salgado and P. Zurita, "Energy versus centrality dependence of the jet quenching parameter $\hat{q}$ at RHIC and LHC: a new puzzle?," Eur. Phys. J. C **76** (2016) no.9, 475 [arXiv:1606.04837 [hep-ph]].

[366] K. M. Burke *et al.* [JET Collaboration], "Extracting the jet transport coefficient from jet quenching in high-energy heavy-ion collisions," Phys. Rev. C **90** (2014) 1, 014909 [arXiv:1312.5003 [nucl-th]].

[367] T. Renk, H. Holopainen, R. Paatelainen and K. J. Eskola, "Systematics of the charged-hadron p_T spectrum and the nuclear suppression factor in heavy-ion collisions from $\sqrt{s} = 200$ GeV to $\sqrt{s} = 2.76$ TeV," Phys. Rev. C **84** (2011) 014906 [arXiv:1103.5308 [hep-ph]].

[368] R. Baier, "Jet quenching," Nucl. Phys. A **715** (2003) 209 [hep-ph/0209038].

[369] W. A. Horowitz and M. Gyulassy, "The Surprising Transparency of the sQGP at LHC," Nucl. Phys. A **872** (2011) 265 [arXiv:1104.4958 [hep-ph]].

[370] K. J. Eskola, H. Honkanen, C. A. Salgado and U. A. Wiedemann, "The Fragility of high-p(T) hadron spectra as a hard probe," Nucl. Phys. A **747** (2005) 511 [hep-ph/0406319].

[371] A. Dainese, C. Loizides and G. Paic, "Leading-particle suppression in high energy nucleus-nucleus collisions," Eur. Phys. J. C **38** (2005) 461 [hep-ph/0406201].

[372] M. Stratmann and W. Vogelsang, "Towards a global analysis of polarized parton distributions," Phys. Rev. D **64** (2001) 114007 [hep-ph/0107064].

[373] P. M. Nadolsky, H. L. Lai, Q. H. Cao, J. Huston, J. Pumplin, D. Stump, W. K. Tung and C.-P. Yuan, "Implications of CTEQ global analysis for collider observables," Phys. Rev. D **78** (2008) 013004 [arXiv:0802.0007 [hep-ph]].

[374] D. de Florian, R. Sassot and M. Stratmann, "Global analysis of fragmentation functions for pions and kaons and their uncertainties," Phys. Rev. D **75** (2007) 114010 [hep-ph/0703242 [HEP-PH]].

[375] D. de Florian, R. Sassot and M. Stratmann, "Global analysis of fragmentation functions for protons and charged hadrons," Phys. Rev. D **76** (2007) 074033 [arXiv:0707.1506 [hep-ph]].

[376] Y. Mehtar-Tani, C. A. Salgado and K. Tywoniuk, "The Radiation pattern of a QCD antenna in a dense medium," JHEP **1210** (2012) 197 [arXiv:1205.5739 [hep-ph]].

[377] J. Casalderrey-Solana, Y. Mehtar-Tani, C. A. Salgado and K. Tywoniuk, "New picture of jet quenching dictated by color coherence," Phys. Lett. B **725** (2013) 357 [arXiv:1210.7765 [hep-ph]].

[378] G. Aad *et al.* [ATLAS Collaboration], "Measurement of the jet radius and transverse momentum dependence of inclusive jet suppression in lead-lead collisions at $\sqrt{s_{NN}}$= 2.76 TeV with the ATLAS detector," Phys. Lett. B **719** (2013) 220 [arXiv:1208.1967 [hep-ex]].

[379] S. Chatrchyan *et al.* [CMS Collaboration], "Measurement of jet fragmentation in PbPb and pp collisions at $\sqrt{s_{NN}}$ = 2.76 TeV," Phys. Rev. C **90** (2014) 2, 024908 [arXiv:1406.0932 [nucl-ex]].

[380] G. Aad *et al.* [ATLAS Collaboration], "Measurement of inclusive jet charged-particle fragmentation functions in Pb+Pb collisions at $\sqrt{s_{NN}}$ = 2.76 TeV with the ATLAS detector," Phys. Lett. B **739** (2014) 320 [arXiv:1406.2979 [hep-ex]].

[381] Y. Mehtar-Tani and K. Tywoniuk, "Jet (de)coherence in Pb D0Pb collisions at the LHC," Phys. Lett. B **744** (2015) 284 [arXiv:1401.8293 [hep-ph]].

[382] C. A. Salgado and U. A. Wiedemann, "A Dynamical scaling law for jet tomography," Phys. Rev. Lett. **89** (2002) 092303 [hep-ph/0204221].

[383] H. De Vries, C. W. De Jager and C. De Vries, "Nuclear charge and magnetization density distribution parameters from elastic electron scattering," Atom. Data Nucl. Data Tabl. **36** (1987) 495.

[384] T. Hirano, "Is early thermalization achieved only near mid-rapidity at RHIC?," Phys. Rev. C **65** (2002) 011901 [nucl-th/0108004].

[385] T. Hirano and K. Tsuda, "Collective flow and two pion correlations from a relativistic hydrodynamic model with early chemical freezeout," Phys. Rev. C **66** (2002) 054905 [nucl-th/0205043].

[386] `http://tkynt2.phys.s.u-tokyo.ac.jp/~hirano/parevo/parevo.html`.

[387] M. Luzum and P. Romatschke, "Conformal Relativistic Viscous Hydrodynamics: Applications to RHIC results at s(NN)**(1/2) = 200-GeV," Phys. Rev. C **78**, 034915 (2008) Erratum: [Phys. Rev. C **79**, 039903 (2009)] [arXiv:0804.4015 [nucl-th]].

[388] M. Luzum and P. Romatschke, "Viscous Hydrodynamic Predictions for Nuclear Collisions at the LHC," Phys. Rev. Lett. **103**, 262302 (2009) [arXiv:0901.4588 [nucl-th]].

[389] H. J. Drescher, A. Dumitru, A. Hayashigaki and Y. Nara, "The Eccentricity in heavy-ion collisions from color glass condensate initial conditions," Phys. Rev. C **74**, 044905 (2006) [nucl-th/0605012].

[390] A. Adare *et al.* [PHENIX Collaboration], "Suppression pattern of neutral pions at high transverse momentum in Au + Au collisions at s(NN)**(1/2) = 200-GeV and constraints on medium transport coefficients," Phys. Rev. Lett. **101** (2008) 232301 [arXiv:0801.4020 [nucl-ex]].

[391] A. Adare *et al.* [PHENIX Collaboration], "Transverse energy production and charged-particle multiplicity at midrapidity in various systems from $\sqrt{s_{NN}} = 7.7$ to 200 GeV," Phys. Rev. C **93** (2016) no.2, 024901 [arXiv:1509.06727 [nucl-ex]].

[392] J. Adam *et al.* [ALICE Collaboration], "Measurement of transverse energy at midrapidity in Pb-Pb collisions at $\sqrt{s_{\rm NN}} = 2.76$ TeV," Phys. Rev. C **94** (2016) no.3, 034903 [arXiv:1603.04775 [nucl-ex]].

[393] G. Agakishiev *et al.* [STAR Collaboration], "Identified hadron compositions in p+p and Au+Au collisions at high transverse momenta at $\sqrt{s_{_{NN}}} = 200$ GeV," Phys. Rev. Lett. **108** (2012) 072302 [arXiv:1110.0579 [nucl-ex]].

[394] G. Aad *et al.* [ATLAS Collaboration], "Measurement of charged-particle spectra in Pb+Pb collisions at $\sqrt{s_{\rm NN}} = 2.76$ TeV with the ATLAS detector at the LHC," JHEP **1509** (2015) 050 [arXiv:1504.04337 [hep-ex]].

[395] J. Casalderrey-Solana and X. N. Wang, "Energy dependence of jet transport parameter and parton saturation in quark-gluon plasma," Phys. Rev. C **77** (2008) 024902 [arXiv:0705.1352 [hep-ph]].

[396] J. P. Blaizot and Y. Mehtar-Tani, "Renormalization of the jet-quenching parameter," Nucl. Phys. A **929** (2014) 202 [arXiv:1403.2323 [hep-ph]].

[397] E. Iancu, "The non-linear evolution of jet quenching," JHEP **1410** (2014) 95 [arXiv:1403.1996 [hep-ph]].

[398] J. Blumlein, "Analytic continuation of Mellin transforms up to two loop order," Comput. Phys. Commun. **133** (2000) 76 [hep-ph/0003100].

[399] S. Moch and J. A. M. Vermaseren, "Deep inelastic structure functions at two loops," Nucl. Phys. B **573** (2000) 853 [hep-ph/9912355].

[400] J. A. M. Vermaseren, A. Vogt and S. Moch, "The Third-order QCD corrections to deep-inelastic scattering by photon exchange," Nucl. Phys. B **724** (2005) 3 [hep-ph/0504242].

[401] R. Courant and D. Hilbert, "Methods of Mathematical Physics," Interscience (New York) **1**, 1953.